TRAIL Therapy for Exploiting Mechanisms of Drug Resistance and Metastasis in Advanced Colorectal Cancer

By

Joshua Dale Greenlee

Dissertation

Submitted to the Faculty of the

Graduate School of Vanderbilt University

in partial fulfillment of the requirements

for the degree of

DOCTOR OF PHILOSOPHY

in

Biomedical Engineering

May 12, 2023

Nashville, Tennessee

Approved:

Michael R. King, Ph.D. (chair)

John Wilson, Ph.D.

Marjan Rafat, Ph.D.

Kamran Idrees, MD, MSCI, MMHC, FACS

To my family. Thank you for your unwavering love and for always believing in me. Each one of you has played a huge part in making this journey possible. I love you.

Acknowledgments

Thank you to my advisor Dr. Michael King, for always leading with “a lot of empathy, a little bit of confidence, and some good humor”. Graduate school has taken blood (literally), sweat, and tears, so I am extremely grateful to have been mentored by someone who cares so deeply about his students and their success. You have always shown patience and empathy, qualities that I aspire to have as a mentor. Thank you to my labmates, both former and current, for their support and friendship both inside and outside of the lab. Specifically, thank you to my undergraduate students Tejas Subramanian and Kevin Liu for their hard work and scientific contribution to this dissertation. Thanks to Maria Lopez-Cavestany for all the western blot help and Jenna Dombroski for being the lab mom. Thank you to former senior lab members Dr. Thong Cao, Dr. Nerymar Ortiz-Otero, Dr. Korie Grayson, and Dr. Jacob Hope for teaching me how to be a better scientist. Thank you to the friends I have made in Nashville: Paul Taufalele, Preston Hunt, Brandon Green, Aaron Williams and many others for their refreshing perspective and continuous support.

I would also like to acknowledge all my teachers and mentors. From high school science teachers Gary Dunfee and Dan Hendershott to college professors Dr. Valerie Young, Dr. Doug Goetz, and Dr. Monica Burdick, thank you for always believing in me and pushing me to become the critical thinker that I am today.

Thank you to the 13 deidentified cancer patients who donated blood samples for these research studies. Your altruism, selflessness and heroism are qualities that I reflect on daily, and your contribution to this work does not go unnoticed.

Finally, thank you to my family. To my mom and dad, Michael and Linda Greenlee, words cannot describe how grateful I am for all that you have done for me; I wouldn’t be where I am today if it were not for your unconditional love and guidance. To my sister Ashley Greenlee, thank you for always supporting me and being someone that I can confide in no matter the situation. To my beautiful wife Bre Greenlee, thank you for being my number one fan and for sticking by me all these years, through thick and thin, in sickness and in health. None of this would be possible without you by my side.

Thank you all for supporting me and encouraging me to follow my dreams.

Just a kid from Southeast Ohio.

Table of Contents

List Of Tables

List Of Figures

Abbreviations

3D-CRT	Three-dimensional conformal radiation therapy
5FU	5-fluorouracil
ALK	Anaplastic lymphoma kinase
AM	Acetoxymethyl ester
ANOVA	Analysis of variance
Apaf-1	Apoptotic protease activating factor 1
APC	Adenomatous polyposis
APC(-)	Acyl preservation negative control
ATCC	American Type Culture Collection
BAX	Bcl-2-associated X protein
Bcl-2	B-cell lymphoma 2
BEC	Blood endothelial cell
BID	BH3 interacting-domain death agonist
BSA	Bovine Serum Albumin
Ca	Calcium
Cas9	CRISPR associated protein 9
CASMER	Cluster of apoptotic signaling molecule-enriched rafts
CAV1	Caveolin-1
CBL	Casitas B-lineage lymphoma
CCL19	Chemokine (C-C motif) ligand 19
CCL21	Chemokine (C-C motif) ligand 21
CCR7	Chemokine (C-C motif) receptor 7
CEA	Carcinoembryonic antigen
c-FLIP	Cellular FLICE (FADD-like IL-1β-converting enzyme)-inhibitory protein
CIMP	CpG-island methylated phenotype
CIN	Chromosome instable
C_{max}	Maximum serum concentration
c-MET	Mesenchymal-epithelial transition factor
cPARP	Cleaved poly(ADP-ribose) polymerase
CRC	Colorectal cancer
CRISPR	Clustered regularly interspaced short palindromic repeats
CryoTEM	Cryo-transmission electron microscopy

CSC	Cancer stem cell
Ct	Cycle threshold
CTC	Circulating tumor cell
CTLs	Cytotoxic T lymphocytes
CTLA-4	Cytotoxic T-lymphocyte associated protein 4
CXCL12	C-X-C motif chemokine ligand 12
CXCR4	C-X-C chemokine receptor type 4
DAC	Division of Animal Care
DAPI	4′,6-diamidino-2-phenylindole
DC	Dendritic cell
DCIS	Ductal carcinoma in situ
DcR1	Decoy receptor 1
DcR2	Decoy receptor 2
DGS-NTA(Ni)	1,2-dioleoyl-sn-glycero-3-[(N-(5-amino-1-carboxypentyl)iminodiacetic acid)succinyl] (nickel salt)
DHA	Docosahexaenoic acid
DI	Deionized
DiR	DiIC18(7)(1,1'-Dioctadecyl-3,3,3',3'-Tetramethylindotricarbocyanine Iodide)
DISC	Death-inducing signaling complex
DLS	Dynamic light scattering
DMH	1,2-dimethylhydrazine dihydrochloride
DMSO	Dimethyl sulfoxide
DNA	Deoxyribose nucleic acid
DR4	Death receptor 4
DR5	Death receptor 5
DSPC	Distearoylphosphatidylcholine
DSPE-PEG	1,2-distearoyl-sn-glycero-3-phosphoethanolamine-N-[carboxy(polyethylene glycol)-2000]
EBRT	External-beam radiation therapy
ECM	Extracellular matrix
EDTA	Ethylenediaminetetraacetic acid
EGFR	Epidermal growth factor receptor
Egg PC	L-α-phosphatidylcholine (Egg)

EMT	Epithelial to mesenchymal transition
EPR	Enhanced permeability and retention effect
ER	Endoplasmic reticulum
ERK	Extracellular signal-regulated kinase
FACS	Fluorescence-activated cell sorting
FADD	Fas-associated death domain
FAK	Focal adhesion kinase
FAP	Familial adenomatous polyposis
FAPα	Fibroblast activation protein-α
FBS	Fetal bovine serum
FC	Fragment crystallizable region
FDA	Food and drug administration
FITC	Fluorescein isothiocyanate
FOLFIRI	5-fluorouracil + leucovorin + irinotecan
FOLFOX	5-fluorouracil + leucovorin + oxaliplatin
FOLFOXIRI	5-fluorouracil + leucovorin + oxaliplatin + irinotecan
FRET	Fluorescence resonance energy transfer
FSS	Fluid shear stress
GAPDH	Glyceraldehyde-3-phosphate dehydrogenase
GEMM	Genetically engineered mouse model
HBSS	Hank’s Balanced Salt Solution
HER2	Human epidermal growth factor receptor 2
HGF	Hepatocyte growth factor
HIF1	Hypoxia inducible factor 1
HIPEC	Hyperthermic intraperitoneal chemotherapy
HMEC/HMVEC	Human dermal microvascular endothelial cells
HNPPC	Hereditary non-polyposis colorectal cancer
HUVEC	Human umbilical vein endothelial cell
IACUC	Institutional Animal Care and Use Committee
IF	Interstitial flow
IFC	Input fraction controls
IFN-α	Interferon-alpha
IFN-γ	Interferon-gamma
IGF1	Insulin-like growth factor 1

IGFR	Insulin-like growth factor receptor
IL-4	Interleukin 4
IORT	Intraoperative radiation therapy
IP	Intraperitoneal
IV	Intravenous
IVIS	*In vivo* Imaging System
JC-1	5,5′,6,6′-tetrachloro-1,1′,3,3′-tetraethylbenzimi- dazolylcarbocyanine iodide
JNK	c-Jun N-terminal kinase
KO	Knockout
KRAS	Kirsten rat sarcoma virus proto-oncogene, GTPase
LEC	Lymphatic endothelial cell
LFA-1	Lymphocyte function-associated antigen 1
LIMK	LIM kinase
LN	Lymph node
LNPs	Lipid nanoparticles
LR	Lipid raft
LV	Leucovorin
LXR	Liver X receptor
mAb	Monoclonal antibody
MAPK	Mitogen-activated protein kinase
MCC	Manders’ Correlation Coefficient
met	Metastases
MFI	Median fluorescence intensity
MHC	Major histocompatibility complex
miRNA	microRNA
MLKL	Mixed lineage kinase domain-like pseudokinase
MMP	Matrix metalloprotease
MMR	Mismatch repair
MOMP	Mitochondrial outer membrane permeability
mRNA	Messenger RNA
MSC	Mechanosensitive ion channel
MSI	Microsatellite instable
MSI-H	Microsatellite instable high

MTT	(3-(4,5-dimethylthiazol-2-yl)-2,5-diphenyltetrazolium bromide) tetrazolium reduction assay
MW	Molecular weight
mβCD	Methyl-β-cyclodextrin
NHLF	Normal human lung fibroblasts
NK cell	Natural Killer cell
NSCLC	Non-small cell lung cancer
N-WASP	Neuronal Wiskott-Aldrich syndrome protein
ODE	Ordinary differential equation
OxR	Oxaliplatin resistant
P2X7	P2X purinoceptor 7
PBS	Phosphate-buffered saline
PDMS	Polydimethylsiloxane
PD-1	Programmed death protein 1
PD-L1	Programmed death ligand 1
PE	Phycoerythrin
PEG	Polyethylene glycol
PET	Polyethylene terephthalate
PET-CT	Positron emission tomography/computed tomography
PFA	Paraformaldehyde
PI	Propidium iodide
PIP2	Phosphatidylinositol 4,5-bisphosphate
PKB	Protein Kinase B
PMMA	Poly(methyl methacrylate)
PVDF	Polyvinylidene fluoride
RNA	Ribonucleic acid
RBC	Red blood cell
RNP	Ribonucleoprotein
ROCK	Rho-associated protein kinase
ROI	Region of interest
RRID	Research Resource Identifiers
RSV	Resveratrol
RT	Room temperature
RT-PCR	Reverse transcription polymerase chain reaction

SARS-Cov-2	Severe acute respiratory syndrome coronavirus 2
SD	Standard deviation
SDS	Sodium dodecyl sulfate
SEM	Standard error of the mean/Scanning electron microscopy
SFK	Src family kinases
sgRNA	Single-guide RNA
SLO	Streptolysin O
Smac	Second mitochondria-derived activator of caspase
STAT3	Signal transducer and activator of transcription 3
TAA	Tumor associated antigen
TAM	Tumor associated macrophage
TDLN	Tumor draining lymph node
TEK	Tyrosine kinase
TEM	Transendothelial migration
TGF-β	Transforming growth factor beta
TLR	Toll-like receptor
TME	Tumor microenvironment
TNBC	Triple negative breast cancer
TNF	Tumor necrosis factor
TRAIL	Tumor necrosis factor-related apoptosis-inducing ligand
TRPV4	Transient receptor potential cation channel subfamily V member 4
VEGF	Vascular endothelial growth factor
VEGFR	Vascular endothelial growth factor receptor
WB	Western blot
WD	Working distance
XIAP	X-linked inhibitor of apoptosis protein

Chapter 1:

Introduction

Colorectal cancer (CRC) is the second leading cause of cancer death in the United States, accounting for an estimated 55,000 deaths in the year 2022 alone [1]. Among men and women combined, CRC is the fourth most diagnosed cancer with over 150,000 new cases annually. It is expected that these numbers will continue to rise, specifically within the United States, with reports showing CRC risk and lethality being strongly associated with obesity [2], and a Western-style diet [3]. Despite its high mortality, CRC remains underfunded compared to other cancers such as prostate, breast, and leukemia [4]. Patient prognosis and 5-year survival varies dramatically depending upon stage at diagnosis. When identified at localized or regional stages, CRC remains treatable with a 5-year survival of 91% and 72%, respectively [1]. However, patients with Stage IV metastatic disease have only a 15% 5-year survival, making it one of the most lethal metastatic cancers. Despite the associated lethality of metastasis in CRC and other cancers, there remain a lack of effective FDA-approved anti-metastatic drugs on the market [5,6]. The stages of CRC progression are shown below in **Figure 1.1**.

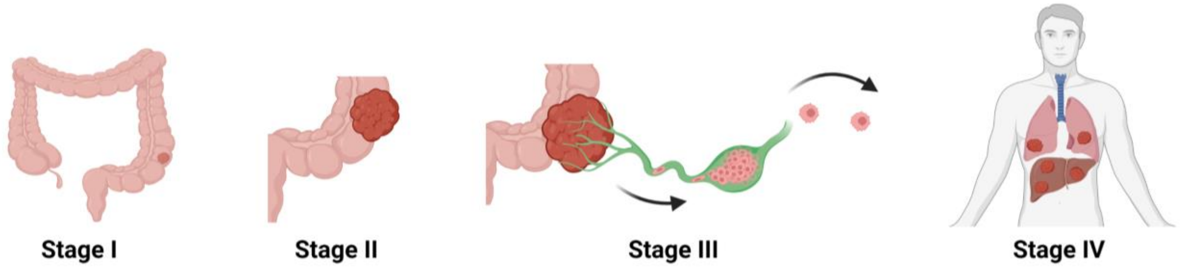

Figure 1.1. Stages of colorectal cancer. Stage I tumors are confined to the submucosal lining of the colon. Stage II tumors have spread through the outer wall of the colon and possibly to nearby tissues, but not to nearby lymph nodes. In Stage III, the cancer has spread into nearby (sentinel) lymph nodes. Stage IV, or metastatic disease, occurs when the cancer has spread to distant lymph nodes or other organs within the body, such as the lungs and liver.

1.1 Colorectal Carcinogenesis

A 1988 study by Vogelstein et al. first proposed the genetic alterations within CRC [7]. The majority of CRC cases are sporadic without genetic predisposition, however hereditary CRC takes two forms: familial adenomatous polyposis (FAP) caused by a mutation in the adenomatous polyposis (APC) gene, or hereditary non-polyposis colorectal cancer (HNPPC or Lynch Syndrome) from a defective DNA mismatch repair system [8]. Sporadic CRC can be divided by its molecular characteristics into three phenotypes: chromosome instable (CIN), high frequency microsatellite instable (MSI) and CpG-island methylated phenotype (CIMP). Over 85% of sporadic CRC is categorized as CIN, and its sequence of genetic aberrations have been well categorized in canonical adenoma-carcinoma progression. In this model of progression, an adenoma is first formed via mutations in APC causing upregulation of Wnt signaling, dysregulating the β-catenin destruction complex and initiating β-catenin accumulation in the cytosol. This is followed by mutations in oncogenes, specifically KRAS proto-oncogene GTPase (KRAS), and allelic loss of chromosome 18q containing vital tumor suppressor genes. The transition from adenoma to carcinoma is not complete until there is loss of function of tumor suppressor gene Tp53, widely recognized as the “guardian of the genome”. Mutations in Tp53 are found in nearly 75% of colorectal carcinomas, over three-fold of that found in adenomas, demonstrating its role in malignancy gatekeeping [9].

1.2 Cancer Metastasis

Metastasis is the process in which cancer cells travel from the organ of origin and successfully colonize a secondary site in the body. Hanahan and Weinberg first reported on “The Hallmarks of Cancer”, which characterize cancer cells as having the ability to create sustained proliferative signaling, resist cell death, evade growth suppression, induce angiogenesis, replicate indefinitely, and finally, metastasize [10]. Metastatic cancer cells also have unique hallmarks, including the ability to become increasingly motile through an epithelial to mesenchymal transition (EMT), intravasate into nearby vasculature through transendothelial migration (TEM), survive in the circulation, extravasate into a secondary site with a pre-metastatic niche, and colonize that site [11].

Metastasis accounts for nearly 90% of all cancer related death [12]. Despite the lethality of metastasis, it is an inefficient process that few cells survive. It’s estimated that less than 0.01% of cancer cells that enter the circulation, termed circulating tumor cells (CTCs), go on to colonize secondary tumors [13]. Even so, lymphatic and blood vessels act as highways to allow cancer cells to travel to distant organs within the body. Not all secondary sites are hospitable to cancer cells, and preferential metastasis to specific organs is not a random process. Paget’s “seed and soil” hypothesis demonstrates that, analogous to seeds needing proper soil to grow, cancer cells rely on specific pre-metastatic niches in order to successfully survive and proliferate [14].

In colorectal cancer, the most common metastatic locations are the liver, lungs and peritoneum [15]. Over the course of disease, approximately 50% of patients will develop metastases in the liver, 15% in the lungs, and 13% in the peritoneum [16]. While liver and lung metastases rely upon angiogenesis and hematogenous dissemination, peritoneal metastases do not metastasize via blood vessels but instead arise from shedding of the primary tumor into lymphatics [17]. Liver metastases rely upon EMT and have upregulation of cancer stem cell (CSC) hallmarks to make them more migratory and suitable for survival in the vasculature. On the other hand, peritoneal metastases can occur in an EMT-independent manner, where anoikis is avoided through cell clustering. This highlights how different metastatic mechanisms can be employed by cancer cells to meet the pressures associated with reaching a secondary site.

1.3 Standard of Care

Treatment strategies in CRC vary greatly depending upon the stage and severity of disease. While surgery and radiotherapy remain curative options for patients with localized disease, patients with Stage IV disease have poor prognosis even with systemic therapies.

1.3.1 Surgery and Radiotherapy

Patients with Stage 0 or Stage I disease will present with a polyp on the inner lining of the colon, usually detected through routine colonoscopy [18]. Even if malignant, these tumors can usually be removed through a colonoscope, and no further treatment is required if good margins are achieved during resection. In Stage II disease, the tumor has grown through the serosal space of the colon and possibly into nearby tissues, but without sentinel lymph node involvement. In this case, a partial colectomy with the removal of nearby lymph nodes is commonly curative, but adjuvant chemotherapy may be used in tandem to prevent recurrence in high grade tumors [19]. Stage III tumors have spread to nearby lymph nodes but no other parts of the body. In large tumors, neoadjuvant chemoradiation may be used to shrink tumors before surgery.

Radiation therapy is used less commonly in CRC compared to other cancers but has proven beneficial when used in combination with chemotherapy and surgery. Intraoperative radiation therapy (IORT) has demonstrated success in tumors with positive margins during surgical resection, improving disease free survival and reducing the risk of recurrence [20]. Outside of the operating room, external-beam radiation therapy (EBRT) is the most common radiotherapy used to treat CRC patients [21]. Newer techniques such as three-dimensional conformal radiation therapy (3D-CRT) allow for precise targeting of unresectable tumors as well as liver metastases [22,23]. Endocavitary or interstitial brachytherapy may be used in rectal patients for a more targeted radiation source that spares abdominal tissues [21]. Overall, radiotherapy is more commonly used to treat rectal cancer than colon cancer.

Surgery is unlikely to be curative for patients with Stage IV metastatic CRC but may improve quality of life and extend overall survival. It has been shown that primary tumor resection and mastectomy can extend overall survival to 36 months compared to just 13 months with palliative care in younger patients under 45 [24]. However, other results have shown no survival benefit to primary tumor removal in patients with an asymptomatic primary tumor and synchronous unresectable metastases [25]. Approximately 80% of Stage IV patients present with unresectable metastatic lesions at the time of diagnosis [26]. The risks and rewards of primary tumor removal in metastatic patients have not yet been fully resolved, and decisions are often made based on whether the metastatic tumors are also resectable [27].

1.3.2 Chemotherapy

For the majority of patients with metastatic CRC, the standard of care is combination front-line chemotherapy. These chemotherapy “cocktails” include multiple agents, typically 5-fluorouracil (FU)/leucovorin (LV) with either oxaliplatin (FOLFOX) or irinotecan (FOLFIRI) [28]. 5FU and LV work together to inhibit thymidylate synthase (TS) and block DNA/RNA synthesis, extending median survival in patients from 9 months (with palliative care) to over 12 months [29]. Oxaliplatin binds to adjacent guanine bases to form DNA adducts, causing irreversible replication errors and apoptosis [30]. The addition of oxaliplatin with 5FU/LV increases progression free survival from 6 months to 9 months and the response rate from 22% to 55% [31]. Irinotecan is a topoisomerase I inhibitor that induces lethal double stranded DNA breaks and subsequent mitotic arrest [32]. Irinotecan improves treatment response and increases median survival time from 14.1 to 17.4 months [33]. FOLOFX and FOLFIRI have shown similar therapeutic benefit in multiple studies [34,35]. FOLFOXIRI has also shown improved efficacy, but is only considered in younger patients due to toxicity concerns [19,36]

Chemotherapy can also be administered under surgical procedures for enhanced targeting while avoiding systemic toxicity. Hepatic artery infusion consists of surgically implanting a pump with a catheter into the hepatic artery to continuously administer chemotherapeutics such as floxuridine, FOLFOX or FOLFIRI directly into the liver to target unresectable liver metastases [37]. In patients with peritoneal metastasis, hyperthermic intraperitoneal chemotherapy (HIPEC) is commonly administered following cytoreductive surgery [38]. After removal of macroscopic cancerous tissue from the peritoneum, surgeons will perfuse 42°C chemotherapy, such as mitomycin-c or oxaliplatin, through the abdomen for 30-60 min. The combination of cytoreductive surgery and HIPEC has been shown to increase survival from 24 months to 63 months with a 5-year survival of over 50%.

1.3.3 Targeted Therapies and Immunotherapies

Treatment with FOLFOX or FOLFIRI is often combined with a monoclonal antibody (mAb) against vascular endothelial growth factor (VEGF) or epidermal growth factor receptor (EGFR) [28]. Bevacizumab (VEGF mAb) and cetuximab/panitumumab (EGFR mAb) have all been approved for front-line treatment of metastatic CRC in combination with FOLFOX/FOLFIRI. More nuanced treatment decisions are often determined on a case-by-case basis from molecular characteristics of tumors. For example, the EGFR mAb cetuximab in combination with FOLFOX is the gold standard for patients with KRAS wild type tumors, while KRAS mutant tumors have demonstrated therapeutic resistance to EGFR mAbs.

The majority of targeted therapies in CRC are anti-angiogenic agents or epidermal growth factor inhibitors. Besides VEGF antibodies such as bevacizumab, regorafenib is an oral small molecule tyrosine kinase inhibitor that also inhibits VEGFR2 [39]. Aflibercept is an FDA-approved fusion protein that acts as a decoy receptor to sequester VEGF and prevent angiogenic signaling [40].

In 2017, the first immunotherapy was approved for metastatic CRC. Pembrolizumab is a mAb against programmed death protein-1 (PD-1) that binds to cytotoxic T cells and prevents binding to PD-L1/PD-L2 ligands which are overexpressed on cancer cells. The checkpoint inhibition of the PD-1 complex prevents cancer cells from immunosuppressing T cell function, allowing T cells to recognize and kill otherwise evasive cancer cells. Nivolumab (another PD-1 inhibitor) and ipilimumab (a CTLA-4 inhibitor) are two other checkpoint mAb that are FDA-approved immunotherapies for CRC [41]. Importantly, checkpoint inhibitors have only proven effective for tumors with high microsatellite instability that are mismatch repair (MMR) deficient and are ineffective in MMR-proficient CRC. This is because MSI-H tumors are prone to overexpression of neoantigens that are readily recognized by the immune system as being foreign. As a result, these MSI tumors are reliant on overexpression of programmed death ligands to shield them from immune detection, making checkpoint blockade an effective therapy. In a phase II trial of Keytruda (pembrolizumab), patients with MMR-deficient, MSI-H tumors had a progression free survival rate of 78% compared to 11% in MMR-proficient tumors [42].

1.4 Chemoresistance

One of the greatest challenges in the treatment of metastatic CRC is therapeutic resistance. Despite initial success with the aforementioned chemotherapies, the survival rate for metastatic CRC patients is discouraging due to relapse and refractory disease. Cancer cells will develop resistance to chemotherapy via either intrinsic or acquired mechanisms.

Intrinsic resistance is associated with tumor heterogeneity; subpopulations of cancer cells will have fortuitously developed mutations to make them more suitable to survive initial treatment. In this Darwinian “survival of the fittest” model, these intrinsically resistant cells that started as a small subpopulation of the entire tumor, will go on to colonize the entire tumor as more sensitive cells are killed off [43]. Acquired resistance, also referred to as secondary resistance, results from genetic and phenotypic changes that arise during treatment to make cells more suitable for survival. In CRC, classic resistance mechanisms frequently involve the following: changes in drug metabolism [44], drug efflux [45], mutagenesis of drug targets [46], DNA damage repair [46], p53 mutations [47], and alterations within canonical apoptotic signaling [48]. The Warburg Effect and metabolic signaling also play an important role in chemoresistance, as increased glycolysis predicts resistance to multiple therapies [49]. Genetic and phenotypic hallmarks such as CIN, EMT, and cancer stem cells (CSC) are also strong predictors of both intrinsic and acquired resistance [50,51].

1.5 TRAIL and Death Receptor Signaling

Tumor Necrosis Factor-alpha related apoptosis inducing ligand (TRAIL) is a homotrimeric protein that initiates apoptosis (programmed cell death) in cells via the binding of transmembrane death receptors [52]. TRAIL acts as a transmembrane protein on the surface of many immune cells, notably NK cells and T cells [53], but can be proteolytically cleaved into its soluble form. Humans have two functional death receptors, death receptor 4 (DR4) and 5 (DR5) whereas mice only have one functional death receptor with homology closest to DR5 [52]. Upon binding to TRAIL, death receptors will recruit the intracellular death-inducing signaling complex (DISC), starting with binding of Fas-associated death domain (FADD) and recruitment of caspase-8. This is followed by an intracellular cascade that initiates the intrinsic (mitochondrial) or extrinsic apoptotic pathway.

The intrinsic apoptotic pathway is mitochondrial-dependent. In intrinsic apoptotic signaling, activated caspase-8 causes the cleavage of BH3 interacting-domain death agonist (BID), followed by Bcl-2-associated X protein (BAX) and BID binding to the outer membrane of the mitochondria [54]. This causes mitochondrial depolarization and increased permeability, initiating the release of pro-apoptotic factors such as cytochrome c into the cytosol. Upon binding of cytochrome c to apoptotic protease activating factor 1 (Apaf-1), the apoptosome is formed, activating caspase-9 which triggers cleavage of downstream caspases such as caspase-3 and caspase-7 to induce apoptotic arrest. In the extrinsic, mitochondrial-independent pathway, caspase-8 directly activates cleavage of caspase-3/7 [55].

TRAIL also binds two transmembrane decoy receptors, DcR1 and DcR2, which possess functional binding domains but are unable to transduce intracellular signaling as they lack a functional death domain [56]. Decoy receptors are highly expressed on healthy cells, where they primarily act as sequestering agents that inhibit the off-target apoptotic effects of TRAIL.

TRAIL's utility as a cancer therapeutic stems from its ability to selectively induce apoptosis in cancer cells, while leaving healthy resident cells unaffected. Cancer cells tend to not only have upregulated expression of death receptors 4/5, but also decreased expression of decoy receptors compared to healthy cells [57]. Additionally, the canonical TRAIL signaling pathway is able to initiate apoptosis in cancer cells independent of p53 mutation or deletion, making TRAIL an intriguing therapeutic for more robust cancers [58]. In CRC, studies have demonstrated that TRAIL acts synergistically with chemotherapies such as 5-FU, oxaliplatin, or irinotecan [59–61]. Chemotherapy treatment was shown to downregulate the caspase-8 inhibitor cellular FLICE-inhibitory protein (c-FLIP) and increase TRAIL-mediated apoptosis [59,62]. Besides c-FLIP, overexpression of DcR1 has also been implicated in inhibiting the synergistic anti-tumor response of TRAIL and oxaliplatin in CRC [63]. There is also evidence that chemoresistant side populations of CRC cells have increased sensitivity to TRAIL through increased expression of DR4 [64,65]. However, increased mRNA expression of death receptors alone is not an accurate gauge of sensitivity; TRAIL signaling in CRC is highly dependent upon death receptor transport to the cell membrane and subsequent DISC formation [66].

Compounds targeting TRAIL receptors have been used in multiple phase I, II, and III clinical trials. Recombinant TRAIL (dulanermin), TRAIL-R1 agonist Abs (mapatumumab), and TRAIL-R2 agonist Abs (lexatumumab) are the most notable compounds that have been explored in human trials either as monotherapies or in combination with chemotherapy [67]. Most clinical trials of TRAIL have shown similar results: despite the treatments being well tolerated with no substantial side effects, anti-cancer efficacy was poor and few patients achieved remission [68]. For CRC specifically, successful treatment with death receptor agonists in clinical trials remains limited. For example, a 2010 phase II study of mapatumumab reported minimal adverse events but no treatment response in patients with refractory colorectal cancer [69]. Overall, TRAIL has performed poorly in the clinic in part due to a lack of adequate systemic delivery mechanisms. To increase efficacy, many preclinical studies are engineering novel delivery methods to improve TRAIL targeting and increase half-life in the circulation.

1.6 Lipid Nanoparticles for Cancer

Lipid nanoparticles (LNPs) have emerged as promising delivery vehicles across the pharmaceutical industry. Liposomes are thought to be the earliest generation of LNP, and were discovered by observing that closed lipid bilayer structures self-assemble when suspended in water [70]. To date, film hydration is still a common means of liposome preparation; lipids (typically phospholipids or sphingolipids with stabilizers such as cholesterol) are dehydrated in an organic solvent, then resuspended in aqueous buffer [71]. Agitation followed by extrusion can yield monodispersed, unilamellar vesicles ranging from 20-1000 nm in diameter. Liposomes can be functionally modified for different applications, such as through the conjugation of ligands or antibodies to the liposome surface. Covalent attachment of poly(ethylene glycol) (PEG) to the liposome surface improves stability, increases circulation half-life, and decreases phagocytic clearance from immune cells [72]. Liposomes can also be used to encapsulate therapeutic payloads and formulated to respond to stimuli such as pH, which will cause a phase transition and increase membrane permeability for drug release [73]. Hydrophilic compounds can be encapsulated within the hollow liposome core, while hydrophobic drugs are sandwiched within the lipid bilayer, or alternatively, can be encapsulated in micelles which successfully carry water insoluble compounds.

Other forms of LNPs include solid lipid nanoparticles and nanostructured lipid carriers, which can be produced more easily on a large scale, have improved loading efficiency of therapeutic material, and have more predictable drug release profiles, overcoming some limitations of first-generation liposomes [70]. Cationic and ionizable LNPs are used to stably complex with negatively charged nucleic acids for delivery of genetic material, such as mRNA. Lipid nanocarriers are crucial vectors that prevent nucleic acid degradation, allowing for efficient endocytosis and delivery of mRNA into the cytosol [74]. The first two FDA approved COVID-19 vaccines from Moderna and Pfizer utilize LNP technology to delivery mRNA encoding for the SARS-Cov-2 spike protein. These LNPs simply consist of a proprietary ionizable lipid to stably complex RNA, a PEGylated lipid to decrease phagocytic clearance, cholesterol, and distearoylphosphatidylcholine (DSPC) to aid in cargo packaging [70].

LNPs have shown promising tumor targeting abilities through the enhanced permeability and retention (EPR) effect. Tumor angiogenesis gives rise to leaky neovasculature, allowing larger nanoparticles greater than 100 nm to pass more readily from blood vessels into the tumors harboring them. Tumors also have dysregulated lymphatic drainage, increasing nanoparticle retention and accumulation within tumors. Nanoparticle size is key for cancer delivery with optimal diameters ranging from 10-100nm, large enough to not leak into normal vasculature or be cleared by the kidneys, but small enough to avoid phagocytic clearance from immune cells [75]. There are currently more than 10 FDA-approved lipid nanoparticles therapies for the treatment of various cancers, including breast, pancreatic, ovarian, non-small cell lung (NSCLC), leukemia and prostate [76]. The majority of these clinically available therapies consist of chemotherapeutic agents such as doxorubicin, paclitaxel, or irinotecan encapsulated within a PEGylated “stealth” liposome or micelle [77].

1.7 Mechanosensitive Ion Channels

Cells translate physical stimuli into biochemical responses via the process of mechanotransduction [78]. One form of mechanotransduction is the opening of stretch-activated mechanosensitive ion channels (MSCs) in response to mechanical cues which cause deformations within the plasma membrane. These mechanical cues may arise from differences in substrate stiffness, changes in osmotic pressure, or response to fluid flow. MSCs allow for the intracellular transport of cations, such as calcium, which act as secondary messengers to facilitate downstream signaling processes. Recently, calcium-gated MSCs such as Transient Receptor Potential Cation Channel Subfamily V Member 4 (TRPV4), P2X purinoceptor 7 (P2X7), and Piezo1 have been implicated in many metastatic processes, such as angiogenic signaling, EMT, cell migration, TEM, and survival/apoptosis of cancer cells in the circulation [79,80]. For example, our lab discovered that circulatory shear stress induces calcium entry via Piezo1 opening, therapeutically sensitizing cancer cells to TRAIL-mediated apoptosis [81]. MSCs can also be activated by molecular agonists, locking the channel in an open state in lieu of physical stimuli. Yoda1 is an agonist of Piezo1 that binds within the transmembrane domain, acting as a molecular wedge to sustain channel activation [82]. Jedi1 is another Piezo1 agonist, but binds to the extracellular side of the Piezo1 blade, acting as a lever to induce pore opening [83]. More MSC agonists are being discovered as calcium-gated ion channels like Piezo1 have gained traction as therapeutic targets.

1.8 Conclusions

Colorectal cancer remains one of the deadliest cancers globally despite advancements in combination chemotherapy and FDA-approved immunotherapies. This is largely due to genetic, phenotypic, and epigenetic changes which drive mechanisms of therapeutic resistance, leaving patients with few treatment options. The research discussed herein aims to identify kinks in the armor of these robust CRC cell phenotypes, identifying how lipid rafts and fluid shear stress may be leveraged to exploit cancer cell weaknesses. Through this understanding, apoptosis-inducing nanoparticles are engineered to improve upon conventional treatment options in CRC.

Chapter 2:

Rafting Down the Metastatic Cascade: The Role of Lipid Rafts in Cancer Metastasis, Cell Death, and Clinical Outcomes

Joshua D Greenlee, Teja's Subramanian, Kevin Liu, and Michael R King

This chapter is adapted from *Rafting Down the Metastatic Cascade: The Role of Lipid Rafts in Cancer Metastasis, Cell Death, and Clinical Outcomes* published in *Cancer Research* and has been reproduced with permission of the publisher and co-authors Tejas Subramanian, Kevin Liu and Michael King [84].

Greenlee, J.D.; Subramanian, T.; Liu, K.; King, M.R. Rafting Down the Metastatic Cascade: The Role of Lipid Rafts in Cancer Metastasis, Cell Death, and Clinical Outcomes. Cancer Res 2021, 81, 5–17, doi:10.1158/0008-5472.CAN-20-2199.

2.1 Abstract

Lipid rafts are tightly packed, cholesterol- and sphingolipid-enriched microdomains within the plasma membrane that play important roles in many pathophysiological processes. Rafts have been strongly implicated as master regulators of signal transduction in cancer, where raft compartmentalization can promote transmembrane receptor oligomerization, shield proteins from enzymatic degradation, and act as scaffolds to enhance intracellular signaling cascades. Cancer cells have been found to exploit these mechanisms to initiate oncogenic signaling and promote tumor progression. This chapter highlights the roles of lipid rafts within the metastatic cascade, specifically within tumor angiogenesis, cell adhesion, migration, EMT, and transendothelial migration. Additionally, the interplay between lipid rafts and different modes of cancer cell death, including necrosis, apoptosis, and anoikis will be described. The clinical role of lipid raft-specific proteins caveolin and flotillin in assessing patient prognosis and evaluating metastatic potential of various cancers will be presented. Collectively, elucidation of the complex roles of lipid rafts and raft components within the metastatic cascade may be instrumental for therapeutic discovery to curb pro-metastatic processes.

2.2 Introduction

The presence and dynamic clustering of sphingolipid and cholesterol enriched “raft” domains within the plasma membrane was postulated in 1997 by Simons and Ikonen [85]. This discovery added complexity to the “fluid mosaic” model presented by Singer and Nicolson, which postulated that phospholipids and membrane proteins exhibited random lateral organization within a fluid lipid bilayer [86]. Lipid rafts are small arrangements enriched in specific lipids (such as saturated sphingolipids) and proteins (namely glycosylphosphatidylinositol (GPI)-anchored proteins) and the term is intended to convey the lateral heterogeneity that exists in cellular membranes [87]. Elevated concentrations of cholesterol and sphingolipids containing saturated hydrophobic chains allows for more densely packed, ordered lipid arrangements, in comparison to the surrounding bilayer [88]. Cholesterol in particular acts as both as a glue and a spacer between nonpolar regions of saturated lipids, and its presence has proven vital for raft assembly and integrity. Lipid rafts have more recently been defined as transient and dynamic, both in terms of their lateral fluidity within the membrane and their constant flux of assembly/disassembly [87]. The dynamic nature of rafts is highlighted by spatiotemporal changes of area and continuity between raft and non-raft regions as a result of cellular processes and stimuli. Heterogeneity also exists *within* lipid rafts between inner and outer leaflets of the lipid bilayer, governing biophysical properties of cellular membranes such as curvature and rigidity while also influencing the formation of vesicles for endo- and exocytosis [89].

The dynamic nature of lipid rafts along with their small size, short lifetime, and non-binary characterization of “raft” and “non-raft” regions confounds their experimental observation [87]. The presence of heterogeneous lipid microdomains within cellular plasma membranes has been demonstrated as early as 1982, through the use of fluorescence lifetime decay of 1,6-diphenyl-1,3,5-hexatriene (DPH) [90]. Evidence of lipid raft microdomains was further supported by discovery of high cholesterol and glycosphingolipid regions that remained insoluble in cold, non-ionic detergents [91]. While detergent insolubility is still commonly used to isolate lipids rafts, validation of fluorescently labeled probes and advances in super resolution microscopy has allowed for direct visualization of raft composition previously unseen using conventional confocal microscopy [87,92,93]. Mass spectrometry is used to detail protein and lipid composition of raft domains while Förster resonance energy transfer (FRET) has been instrumental in probing raft presence and size [87]. What remains a challenge, and what makes rafts somewhat controversial, are a lack of modalities for both live cell and *in vivo* observation over extended periods.

Nonetheless, advances in *in vitro* observation and characterization reinforce their importance in cellular biology.

Lipid rafts can exist in either non-planar (invaginated) or planar (flat) configurations [94]. Caveolins are associated proteins of non-planar lipid rafts, and are critical structural components of invaginated microdomains within the plasma membrane, known as caveolae [95]. There are three known isoforms in the caveolin family; caveolin-1 and caveolin-2 are expressed ubiquitously and abundantly in epithelial cells, while caveolin-3 is highly expressed in striated and smooth muscle cells [96]. On the contrary, planar rafts are smaller and remain as flat, ordered structures that are abundant in flotillin proteins (flotillin-1 and flotillin-2) [85,94]. Flotillin proteins are indispensable structural components to non-caveolae planar rafts and also function as signaling platforms in the compartmentalization of membrane receptors [97].

Lipid rafts play a vital role in receptor trafficking and signal transduction, largely through their capacity to act as concentrating platforms, prompting unique interactions between clustered proteins [98]. Through coalescing certain proteins, kinases and phosphatases while excluding others, a new lipid membrane environment is created. For example, lipid rafts protect receptors from enzymatic degradation or inactivation from non-raft enzymes. Specific receptors are predisposed to raft translocation, juxtaposing monomers to promote receptor oligomerization and supramolecular clustering which in turn amplifies downstream signaling [99]. This combination of signaling molecule concentration and exclusion of unwanted modulators make rafts master regulators of signal transduction. Within the context of cancer, these mechanisms of raft-mediated signal augmentation have been implicated in oncogenic and pro-metastatic signaling pathways [100]. This chapter summarizes the roles that lipid rafts play within cancer metastasis, cell death, and raft-associated clinical biomarkers.

2.3 Lipid Rafts in Cancer Metastasis

The metastatic dissemination of cancer cells from the primary tumor to distant organs is a process which few cells survive [13]. Successful metastatic colonization requires the following: creation of tumor neovasculature to support nutrient and oxygen demand, enhanced cellular motility through an epithelial-to-mesenchymal transition, directed migration and transendothelial migration into the vasculature, survival of aberrant shear conditions in circulation, endothelial rolling and extravasation, and a phenotypic switch back to a proliferative phenotype. Despite its inefficiencies, metastasis is responsible for approximately 90% of all cancer related death [101]. Understanding the complex protein interactions that allow for successful dissemination of specific subpopulations of cells is critical for discovery and development of anti-metastatic therapies. Herein, the roles of lipid rafts within the steps of cancer metastasis will be discussed (**Table 2.1**) and illustrated (**Figure 2.1)**.

	Important Proteins/Pathway	**LRs Effect on Stage**	**Cell Lines**	**LR Treatment**	**References**
Angiogenesis	TEK, RhoA	Promote	MDA-MB-231, MDA-MB-468, ZR 751, HUVECs, HMEC	Cerivastatin, mβCD, nystatin and filipin III (inhibitors)	[102–104]
	VEGF/VEGFR2 *Caveolin-1, CD82, CD24/Hsp90/STAT3*	Promote	PC-3, LNCaP, LLC-1, HT-29, SW480, HUVECs	CAV1 siRNA	[105–108]
	exosomal miR-205	Promote	HO-8910, SKOV-3	Filipin III, Simvastatin (inhibitors)	[109]
Epithelial-to Mesenchymal-Transition	**TGF-β/MAPK** *ERK, p38*	Promote	HaCaT, NMuMG	Nystatin	[110]
	Integrin-β3 *pFAK/pAkt/pERK/TGF-β*	Promote	A549, PC-9	Simvastatin	[111]
	HGF/c-Met *pAkt, mTOR*	Promote	MCF-7, MDA-MB-453, MDA-MB-231, BT-20	Osthole (inhibitor)	[112]
	Podoplanin *ROCK/ezrin/radixin/moesin*	Promote	MDCK type II	mβCD	[113]
	Caveolin-1/c-MET *CXCL12/CXCR4, Slug, PI3K/Akt*	Promote	T24, UMUC3, HT1376, 5637, MGC-803, SGC-7901, BGC-823	CAV1 siRNA, Nystatin	[114,115]
	Flotillin-2 *TGF-β/vimentin/N-cadherin*	Promote	GES-1, SGC-7901, NCI-N87, MGC-803	Flotillin-2 siRNA	[116]
	Snail, Slug	Inhibit	MDA-MB-231	DHA (LR stabilizer)	[117]
Migration	**Integrin β1/MMP-9/uPAR** *Src, FAK, Cav, Akt, ERK*	Promote	P29, MDA-MB-231, ZR-751, HMEC	mβCD, nystatin	[104,118]
	EGFR *Akt/PKB*	Promote	MDA-MB-231, MCF-7, T47D	mβCD	[119]
	CD133/Caveolin-1 *FAK, NF-κB*	Promote	MIA PaCa-2, Panc-1, SU.86.86	Lovastatin (inhibitor), CAV1 siRNA	[120]
	Flotillin-2 *PI3K/Akt*	Promote	MDA-MB-231, MCF-7	Flotillin-2 shRNA	[121,122]
	SK3/**Orai1** *Calpain/Talin*	Promote	MDA-MB-435	alkyl-lipid Ohmline (inhibitor)	[123]
	Squalene synthase/TNFR1 *MMP1/NF-κB*	Promote	A549, CL1-5	mβCD	[124]
	CXCL12/CXCR4 *Caveolin-1/C-met, EGFR,* $G_{\alpha i}$*/HER2/Src, PI4KIIIα*	Promote	C4-2B, LNCaP, PC3, MGC-803, SGC-7901, BGC-823	Nystatin, CAV1 siRNA	[115,125,126]
	Artificial crosslinking of GPI-anchored placental alkaline phosphatase	Promote	A375, HeLa	Ru-complex-based trefoil molecule	[127]
	TRPM8/**AR** *FAK*	Promote	PC3, LNCaP		[128]
Transendothelial Migration	**C1QBP/CD44vg** *IGF-1R/PI3K/MAPK*	Promote	H MIA-PaCa-2, PANC-1, SW1990, Capan-1, BxPC-3		[129]

	Caveolin-1/MT1-MMP *PI3K/Akt/mTOR*	Promote	MDA-MB-231, T47D, BT549, Hs578T, MDA-MB-453, SK-BR-3	mβCD, CAV1 siRNA, nystatin	[130,131]
	Caveolin-1/FAPα	Promote	CAFs		[132]
	Podoplanin *RhoC-GTPase/ROCK/LIMK/Cofilin*	Promote	HaCaT, SCC29, A253, Fadu, HN30, SCC13, HN5	mβCD	[133]
Adhesion	Fibronectin and vitronectin adhesion	Promote	MDA-MB-231, MDA-MB-468	mβCD	[103]
	Integrin-β1/Focal adhesion complex proteins	Promote	MDA-MB-231, HeLa, HSC5, HepG2, HCT-116	mβCD, simvastatin, emodin, gambogic acid (inhibitors)	[134–136]
	CD24 & **CD44/Src/Integrin β1** *FAK, paxillin*	Promote	U251, H1299, H23, H460, A569, SHP-77, AZ521, HT-29, MTLy, RKO, HCT-116	mβCD, Filipin, Simvastatin	[137–140]
	CD44 ezrin	Inhibit	MCF-10a, MDA-MB-231		[141]
	SFK	Promote	MCF-7, MDA-MB231	LRT-SIFP (inhibits the SFK activity in LRs)	[142]
	integrin α5β1/LFA-1/β3	Promote	Jurkat, F111, P-815	mβCD, 6- O-a-maltosyl-b cyclodextrin (inhibitor)	[143–145]
Necrosis	**MLKL** *TNFa/RIPK1/RIPK3*	Promote	HEK293T, L929, Jurkat, HeLa, CHO, SKOV3, TOV112D, A2780, A2780CP, PE01, PE04		[146–148]
Anoikis	**Integrin/FAK** *Bcl-xL, Akt, Src*	Inhibit	A431, PZ-HPV7, MCF-10A, MCF-7, MDA-MB-231, PC-3, LNCaP	Simvastatin, MβCD	[149,150]
	HIF-1a *EGFR/Akt/mTOR*	Inhibit	A431, HeLa	mβCD	[151]
Apoptosis	**DR4/DR5**	Promote	HT29, HCT116, SW480, SW620, H460, A549, A549, H1792, H596, CEM, HD-MyZ, I-83, JMV-3, NALM-6, BJAB	Nystatin	[152–156]
	Fas/**CD95**, *FADD, procaspase-8/10, JNK, Bid, Casp-3*	Promote	HL-60, Jurkat, MM1S, MM144, U266	mβCD, filipin	[157,158]
	Akt	Inhibit	NIH3T3	mβCD	[159]

Table 2.1. Lipid rafts in metastatic stages including angiogenesis, EMT, cell migration, transendothelial migration, and cell adhesion along with mechanisms of cell death including necrosis, apoptosis, and anoikis. Proteins in LRs are bolded, *associated pathways/proteins* are italicized.

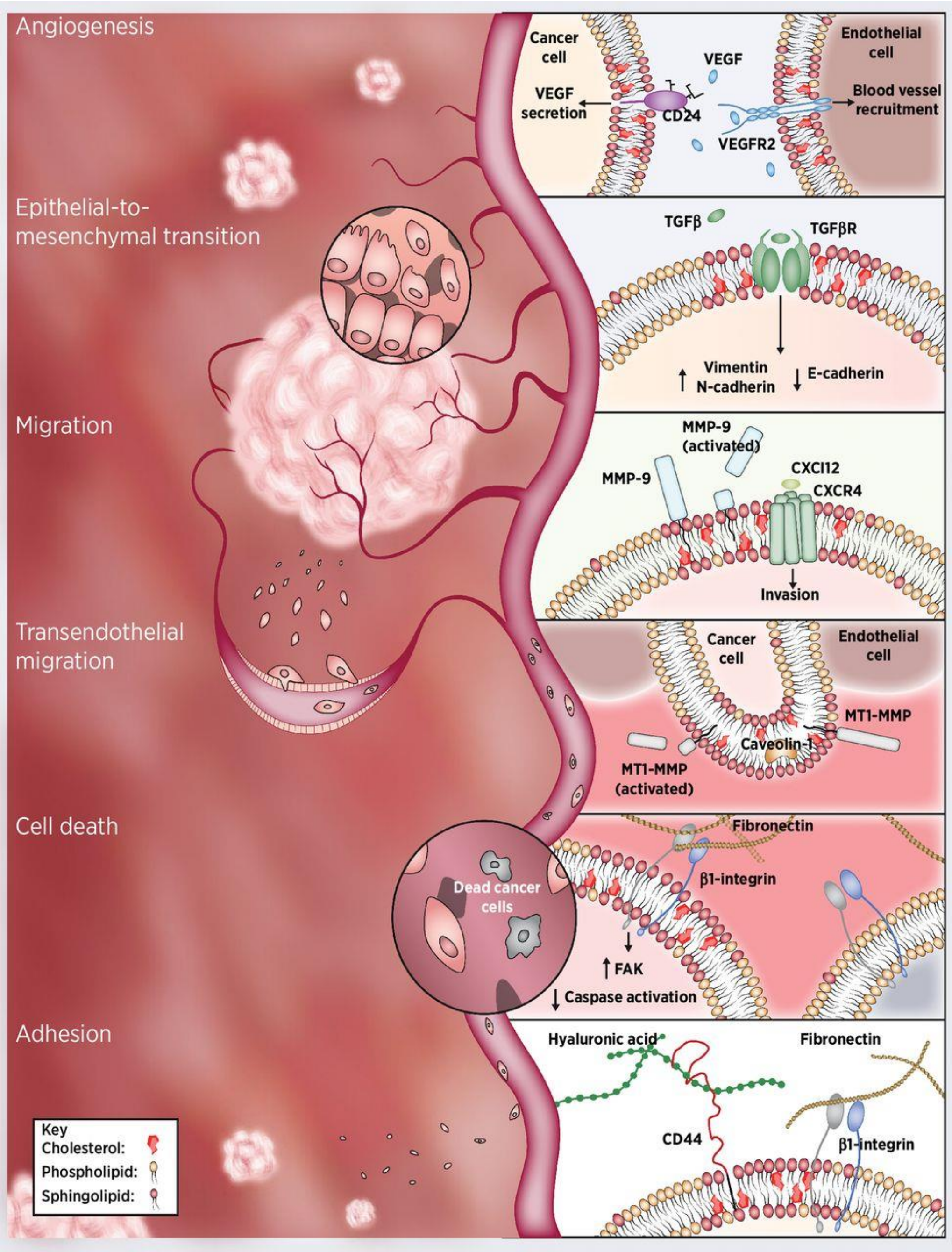

Figure 2.1. Lipid rafts play an important role in cancer cell metastasis and cell death. (Angiogenesis) CD24 raft colocalization promotes VEGF secretion of cancer cells while VEGFR2 raft colocalization enhances angiogenesis upon VEGF activation [106,108]. (Epithelial-to-Mesenchymal Transition) TGF-β receptor is reliant on localization with rafts to promote downstream EMT signaling pathways [110]. (Migration) Raft colocalization promotes MMP-9 activation and CXCR4-mediated cell migration [115,118]. (Transendothelial Migration) Lipid rafts are enriched at invadopodia where caveolin-1 colocalizes with MT1-MMP to promote TEM [130,131]. (Cell Death) Integrin-ECM detachment leads to FAK deactivation and the anoikis response [160]. (Adhesion) Colocalization of CD44 and β1 integrin enhance matrix-dependent cell adhesion to hyaluronic acid and fibronectin, respectively [103,137].

2.3.1 Angiogenesis

Lipid rafts play an important role in angiogenic signaling, as demonstrated in studies of raft antagonization. One study found that treatment with cerivastatin, an inhibitor of cholesterol biosynthesis which disrupts lipid rafts, attenuated angiogenesis by inhibiting endothelial cell migration and capillary formation [102]. Another study found that raft disruption in triple negative breast cancer (TNBC) cells via the cholesterol depleting agent methyl-beta-cyclodextrin (mβCD) inhibited angiogenic signaling through the suppression of proangiogenic markers, namely tyrosine protein kinase receptor [103]. Likewise, conditioned media from mβCD treated cancer cells decreased endothelial branching and capillary structures, demonstrating the obligatory roles of lipid rafts in tumor angiogenesis [104]. Lipid rafts have also been found to mediate and activate heparinase-induced protein kinase B (Akt/PKB) phosphorylation, a pro-angiogenic response in hyper-vascularized tumors [161].

The vascular endothelial growth factor (VEGF)/VEGFreceptor-2 axis is a pro-angiogenic signaling pathway employed by cancer cells via enhanced VEGF secretion [162]. Lipid rafts have proven to be important in endothelial cell VEGFR2 functionality. For example, one study found that affecting endothelial cholesterol homeostasis via liver X receptor (LXR) activation impaired VEGFR2 compartmentalization in lipid rafts, leading to defective VEGFR2 phosphorylation and downstream signaling upon VEGF-A stimulation [106]. Another study found that lipid raft marker caveolin-1 secreted by metastatic prostate cancer cells potentiated angiogenic signaling though colocalization and autophosphorylation of endothelial cell VEGFR2 [105]. Moreover, a separate study found that by inhibiting CD82 internalization and distribution into lipid rafts, VEGFR2 phosphorylation was reduced, attenuating angiogenic signaling [107].

Lipid rafts not only play a role in receptor signaling, but in cancer cell-secreted VEGF as well. Lipid raft-localized Hsp90 was found to stabilize CD24, necessary for STAT3 activation and VEGF angiogenic signaling in colorectal cancer cells [108]. Lipid rafts are also involved in exosome uptake, enabling non-coding microRNA communication between cancer cells, the endothelium, and stroma [163]. One study found that endothelial cell internalization of ovarian cancer-derived exosomal miR-205 occurred in a lipid raft-dependent manner. Inhibition of lipid raft-mediated endocytosis curbed miR-205 uptake, thereby inhibiting angiogenesis [109]. These studies demonstrate specific instances of raft-promoted tumor angiogenesis, making cholesterol-modulation an appealing target to prevent tumor vascularization.

2.3.2 Epithelial-to-Mesenchymal Transition (EMT)

Lipid raft disruption has been shown to attenuate EMT in cancer. One study found that disrupting lipid rafts with simvastatin suppressed integrin-β3/FAK signaling, reversing EMT and EMT-associated paclitaxel resistance in non-small cell lung cancer (NSCLC) cells [111]. Another study found that nystatin, a cholesterol sequestering agent, suppressed EMT markers in gastric cancer cells [115]. They further demonstrated that CXCL12/CXCR4-induced mesenchymal-epithelial transition factor (c-MET) activation and EMT are dependent on lipid raft caveolin-1 signaling. Nystatin treatment also attenuated EMT by disrupting TGF-β–signaling [110], which is strongly implicated in EMT and enhanced cancer cell motility [164]. Cholesterol was found to be essential for the TGF-β receptor activation of mitogen-activated protein kinase (MAPK) and subsequent EMT induction [110]. This TGF-β–EMT synergy was contingent upon TGF-β receptor localization into lipid rafts for efficient downstream signaling. Osthole, another lipogenic modulator, inhibits EMT via lipid raft depletion. A study found that osthole suppressed the hepatocyte growth factor (HGF)/c-Met signaling pathway in breast cancer cells, abrogating a mesenchymal phenotype though downregulation of vimentin and upregulation of E-cadherin [112]. Meanwhile, another study found that localization of the EMT-promoting glycoprotein podoplanin into lipid raft domains was necessary for podoplanin-mediated EMT and cell migration [113]. Treatment with mβCD impaired podoplanin lipid raft compartmentalization and impeded EMT.

The flotillin and caveolin families of proteins are also important drivers of EMT. One study found that upregulation of caveolin-1 is associated with enhanced EMT and aggressive, metastatic bladder cancer [114]. Caveolin-1 enhanced EMT by upregulating Slug, an EMT promoting transcription factor, through PI3K/AKT signaling. Knockdown of caveolin-1 reduced Slug expression, subsequently inhibiting EMT. Likewise, flotillin-2 is upregulated in gastric cancer cells and is required for TGF-β-induced EMT [116]. Inhibition of flotillin-2 reduced EMT markers vimentin and N-cadherin.

While much work has shown that disrupting lipid rafts prevents EMT signaling, other research shows that lipid raft destabilization is required for EMT. One study found that lipid raft stability *decreases* during EMT in breast cancer cells [117]. Stabilizing lipid rafts with docosahexaenoic acid (DHA) abrogated EMT hallmarks, prevented mesenchymal signaling, and inhibited metastasis. This demonstrates the complex interplay between rafts and EMT, warranting further validation before clinical implementation of raft destabilizers.

2.3.3 Migration

Since lipid rafts are closely tied to cytoskeletal components and receptor signaling, many studies have looked at their role within focal adhesions and cancer cell migration [165]. For example, disrupting lipid rafts in human melanoma decreased migration velocity and inhibited lamellipodia formation by inducing the formation of actin stress fibers, preventing the disassembly of focal adhesions [134]. One interesting study designed a ruthenium complex-based peptidic molecule that self-assembles into nanofibrils on lipid rafts [127]. The nanofibrils cross-linked lipid rafts, causing them to aggregate into large, chained structures. This raft constriction caused focal adhesion suppression and decreased cell migration. Another study found that the potassium channel SK3 associates with calcium channel Orai1 in lipid rafts to upregulate calcium influx and promote cell migration and bone metastasis [123]. Treating with the alkyl-lipid Ohmline translocated the SK3-Orai1 complex out of lipid rafts, impairing calcium entry and attenuating cell migration.

Matrix metallopeptidase proteins (MMPs) play a critical role in extracellular matrix degradation during cancer cell migration [166]. One study found that enhanced MMP-9 localization into lipid rafts augmented cell migration and metastatic potential in mouse Lewis lung cancer [118]. Disrupting rafts with mβCD significantly decreased MMP-9 secretion and suppressed invasiveness of these highly metastatic cells. Similarly, another study found that mβCD treatment reduced colocalization of the GPI-anchored membrane protein uPAR and MMP-9 in lipid rafts, decreasing migration of breast cancer cells [104]. MMP-1 is also important in promoting cancer cell migration. A study found that squalene synthase was upregulated in metastatic lung cancers and caused lipid raft enrichment of tumor necrosis factor receptor-1 (TNFR1), enhancing NF-κB activation leading to MMP-1 upregulation [124]. Treatment with mβCD inhibited TNFR1-lipid raft colocalization, abrogating promigratory signaling and reducing the metastatic potential of lung cancer cells.

Lipid rafts also influence chemotactic signaling of directed cell migration. The CXCL12/CXCR4 chemokine axis has been heavily studied for its role in driving cancer cell migration [167,168]. In metastatic prostate cancer, this signaling axis was found to transactivate EGFR, HER2 and Src selectively within lipid raft microdomains [125]. CXCR4 has been shown to colocalize with phosphatidylinositol 4-kinase IIIα (PI4KIIIα) within lipid rafts to promote CXCL12 stimulated cell invasion [126]. Likewise, CXCL12-induced c-MET activation and cell migration were found to be dependent on lipid raft caveolin-1, and inhibition of rafts with nystatin decreased activation of the CXCL12/CXCR4 axis [115]. Lipid rafts are also essential for androgen receptor and EGFR-mediated cell migration [119]. EGFR was found to colocalize into lipid rafts, while mβCD raft disruption inhibited EGF-induced chemotaxis and actin polymerization in breast cancer cells. In prostate cancer cells, low testosterone caused accumulation of transient receptor potential melastatin 8 (TRPM8) with androgen receptors in lipid rafts, thereby inhibiting TRPM8 and promoting cell migration [128].

Flotillin and caveolin are also implicated in driving cell migration. By reducing levels of flotillin-2 in breast cancer cells, tumor volume, metastatic capability, and proliferation decreased by inhibiting PI3K/Akt signaling [121,122]. Additionally, CD133, an oncogenic cancer stem cell marker, has been shown to colocalize with caveolin-1 in lipid rafts to increase invasiveness and chemoresistance in pancreatic tumor initiating cells [120].

2.3.4 Transendothelial Migration

Metastatic dissemination relies on the cell's ability to enter into (intravasation) and exit from (extravasation) the vasculature via transendothelial migration (TEM) [169]. The MUC1/intercellular adhesion molecule-1 (ICAM1) interaction activates a cascade through which physical barriers for transendothelial migration are abrogated [170]. MUC1 proteins, found to be concentrated in lipid rafts, bind to ICAM1 on endothelial cells to facilitate TEM [171]. In pancreatic cancer cells, one study found that IGF1 induces CD44/C1QBP complex formation in lipid rafts, activating PI3K/MAPK signaling pathways and promoting transendothelial migration. Knockdown of C1QBP inhibited complex formation in rafts, decreasing TEM [129].

Multiple studies have established that invadopodia formation is required for successful intravasation and extravasation [172,173]. For example, one study found that invadopodia formation through N-WASP-mediated actin cytoskeleton reorganization is required for cancer cell intravasation [174]. Another study found that cells extend invadopodia through the endothelium prior to extravasation; by inhibiting invadopodia formation, extravasation and metastatic tumor formations were decreased [175]. There is strong evidence that invadopodia formation in cancer cells relies on lipid raft enrichment. Proteases FAPα and MT1-MMP were found to colocalize with caveolin-1 in lipid rafts, recruiting invadopodia in cancer associated fibroblasts and breast cancer cells, respectively [130,132]. Disruption of lipid rafts via mβCD and CAV1 gene silencing impeded MT1-MMP activation and suppressed invadopodia formation [130]. Similarly, another study found that caveolin-1 activates MT1-MMP in invadopodia through the PI3K/Akt/mTOR pathway under low shear stress [131]. Treatment with mβCD inhibited MT1-MMP expression and prevented invadopodia formation, while CAV1 silencing curbed metastatic formation in animal models. An additional study revealed that podoplanin is recruited into invadopodia via lipid rafts and is essential for invadopodia stability by controlling the ROCK-LIMK-Cofilin pathway [133]. Taken together, these studies show that lipid rafts are important facilitators of TEM mechanisms and raft perturbation may be a viable therapeutic strategy to curb intravasation and extravasation.

2.3.5 Cancer Cell Adhesion

The likelihood of cancer cells surviving the disadvantageous stresses within the metastatic cascade is contingent upon their interactions with the extracellular matrix (ECM), fibroblasts, bloodborne cells, and the endothelium [176]. Cholesterol and sphingolipids, two integral components of lipid rafts, are necessary for the ECM adhesion of cancer cells [177,178]. Elevated cholesterol induces redistribution of integrins, resulting in increased cell attachment to fibronectin [143]. Conversely, membrane sphingolipid depletion prevents binding to fibronectin [179]. One study found that while lipid raft levels did not contribute to *de novo* synthesis of integrin, the depletion of lipid rafts with 6-O-α-maltosyl-β-cyclodextrin (mal-βCD) demonstrated that lipid raft levels were directly correlated with integrin activation and fibronectin adhesion [144]. A different study obtained similar results with human T cells. In both primary human T cells and Jurkat lymphoma cells, mβCD-induced raft depletion resulted in decreased integrin α5β1 and αLβ2 (LFA-1) mediated adhesion [145]. These reinforce the role that lipid rafts play in contributing to integrin-mediated ECM adhesion.

CD44 has been implicated in cancer progression and metastasis as a dynamic regulator of cell migration and adhesion, and its roles include initiating circulating tumor cell adhesion and rolling on the endothelium [180–182]. Similarly, integrins, particularly integrins of the β1 subtype, are critical for cancer cell adhesion and vasculature survival in transit [183–185]. The translocation of integrins and adhesion-related cluster of differentiation molecules to lipid rafts is critical for adhesion-related maintenance of cell migration. One study found that raft disruption of TNBC cells via mβCD treatment significantly decreased cell adhesion on fibronectin and vitronectin-coated substrates [103]. Likewise, cholesterol depletion caused CD44 shedding from lipid rafts in cancer cells, suppressing adhesion, migration, and endothelial cell rolling [139,140]. CD44 is known to interact with C1QBP in rafts to activate PI3K/MAPK downstream, a signaling pathway that also promotes cell adhesion and other pro-metastatic phenotypes [129]. Additionally, CD44 clustering in lipid rafts was found to activate Src family kinases (SFK), enriching β1 integrins into lipid rafts to promote cell adherence and matrix-derived survival [137]. By inhibiting SFK activity in lipid rafts, cancer cell adhesion of breast cancer cells was inhibited [142]. Similarly, CD24 was found to interact with, and promote c-Src translocation into lipid rafts, enhancing formation of focal adhesions, integrin-mediated adhesion, and cell spreading [138]. Using mβCD, emodin, and gambogic acid, studies have shown that blocking focal adhesion complex protein localization into lipid rafts inhibits tumor cell adhesion [135,136].

While many studies support the pro-migratory role of lipid raft-colocalized CD44, its role remains controversial. For example, one study demonstrated enhanced palmitoylation of CD44 drives colocalization with rafts, limiting associations with its cytoskeletal linker binding partner ezrin to suppress migration in invasive breast cancer subtypes [141]. Indeed, raft affinity of CD44 is largely regulated by one of two mechanisms: palmitoylation which enhances affinity and reduces binding to cytoskeletal linkers, and phosphatidylinositol 4,5-bisphosphate (PIP2) membrane concentration which decreases raft affinity thereby accelerating formation of the CD44-adaptor complex [186]. This confounding role of CD44 may be explained by the dynamic nature of protein-raft colocalization. That is, while palmitoylated CD44 may exist within rafts in an “inactive” state, rapid depalmitoylation may induce raft dissociation and subsequently promote cell adhesion. Meanwhile, CD44 shredding from rafts as a result of cholesterol depletion prevents the possibility of CD44 dissociation to “non-raft” PIP2 localized regions, thereby abrogating CD44 mediated cell adherence.

2.4 Lipid Rafts and Cell Death

Cell death is a vital function that occurs naturally in the body, one that mediates the removal of damaged or infected cells and maintains tissue homeostasis [187]. Mechanisms of cell death are especially important in the body’s response to cancer; most cells that develop DNA abnormalities and cell checkpoint mutations undergo programmed cell death before they can proliferate further [188]. Immunity to this process is one of the hallmarks of cancer, resulting in uncontrollable division and metastasis [189]. The roles of lipid rafts in various types of cell death including necrosis, apoptosis, and anoikis have been studied extensively in recent years (**Table 2.1**).

2.4.1 Necrosis

Necrosis is a form of unprogrammed cell death that occurs in response to trauma and other stress-inducing stimuli, resulting in an inflammatory cell death response [190]. More recently, it has been suggested that necrotic cell death proceeds in a programmed manner similar to apoptosis [191]. This pathway, termed “necroptosis”, acts through a caspase-independent signaling cascade. Several studies have evaluated the role of lipid rafts in this necroptotic pathway.

Mixed lineage kinase domain-like pseudokinase (MLKL) has been identified as a downstream protein in the TNF-α induced necroptosis signaling cascade [192]. One study demonstrated that oligomerization of MLKL proteins and translocation into lipid rafts is necessary for necroptosis in murine fibrosarcoma cells [146]. Translocation of the oligomerized MLKL complex into lipid rafts supported sodium influx, increased osmotic pressure, and cell rupture. Similarly, another study demonstrated MLKL-induced membrane permeabilization of PIP-containing liposomes [147]. Through selective mutation, it was discovered that binding of positive amino acids on the oligomerized MLKL complex to PIPs allows for recruitment to lipid rafts. Inhibiting PI5P and PIP2 led to decreased necroptosis in Jurkat and murine fibrosarcoma cells. A subsequent study evaluated the effect of ceramide nanoliposomes (CNLs) on MLKL expression, demonstrating that CNLs strongly promoted MLKL activation-driven necroptosis, but not apoptosis in ovarian cancer cells [148]. These results suggest that CNLs form lipid raft mimetics which promote MLKL translocation and necroptosis, supporting the role of lipid rafts in necroptosis. Given that many cancer cells display resistance to apoptosis, therapeutic targeting and activation of the necroptotic pathway presents an exploitable alternative to induce cell death.

2.4.2 Apoptosis

Apoptosis, is a noninflammatory, programmed cell death pathway [55,187]. External activation of death receptor in the TNF superfamily results in the recruitment of the death-inducing signaling complex (DISC), caspase activation, DNA fragmentation and cell death [193]. The majority of lipid raft-apoptosis synergism studies are in relation to the colocalization of CD95 (Fas) and death receptors 4/5 into rafts, forming cluster of apoptotic signaling molecule-enriched rafts (CASMER) to enhance apoptotic signaling [152–155,157,158]. Chemotherapeutic agents such as perifosine and lipid raft agonists such as resveratrol have been shown to promote death receptor translocation into rafts, warranting further investigation into combination treatments of chemotherapeutic raft synergism with death inducing ligands [61,156,158]. For additional information, studies of raft-mediated death ligand signaling have been extensively covered in recent reviews [100,194,195].

Apart from death receptor signaling, some studies have conversely implicated rafts as being pro-survival, apoptotic regulators. For example, one study demonstrated that mβCD-induced raft disruption resulted in G2-M phase arrest and eventual apoptosis in breast cancer cells [103]. Likewise, protein kinase B (Akt), an important pro-survival protein, was shown to localize into lipid rafts [159]. Lipid raft disruption using mβCD led to a decrease of Akt activity and increased apoptosis in mouse fibroblast cells.

2.4.3 Anoikis

Anoikis is a specialized type of apoptosis which is activated upon cell detachment, and developed resistance to anoikis is an essential step in cancer metastasis [160,196]. The loss of integrin attachment to matrix results in an inactivation of apoptosis inhibitor FAK, leading to caspase activation. Since lipid rafts facilitate integrin interactions and cell adhesion, depletion of lipid rafts has also been shown to directly result in anoikis-like death. When treated with cholesterol-inhibiting agents, human breast, prostate, and epidermoid carcinoma cells showed decreased lipid raft formation, Bcl-2 downregulation, caspase-3 activation, and Akt downregulation, inducing anoikis-like apoptosis [149]. Similarly, another study demonstrated that simvastatin-induced cholesterol depletion resulted in raft internalization and FAK downregulation, resulting in cell detachment, caspase-3 activation, and anoikis [150].

The lipid raft association of hypoxia inducible factor 1 (HIF1) in cell attachment has also been studied. HIF-1α is produced under hypoxic conditions and promotes cell survival. Interestingly, hypoxic conditions have been shown to correlate with decreased lipid rafts, suggesting that HIF-1α influences lipid raft production. Epidermoid carcinoma cells treated with mβCD under normoxic conditions demonstrated upregulated HIF-1α, suggesting that the cells underwent HIF-1α-mediated lipid raft production in response to cholesterol depletion [151]. Silencing of HIF-1α led to accelerated cell detachment and anoikis. These studies demonstrate the complexities of lipid raft involvement in mechanisms of cell death. Exploiting anoikis-like apoptosis mechanisms through lipid raft augmentation may be a viable method to prevent cancer cell survival upon detachment.

2.5 Lipid Raft-Associated Biomarkers of Cancer Progression and Metastasis

Apart from their roles in cancer metastasis and cell death, components of lipid rafts, namely caveolin and flotillin, have received much attention as clinical biomarkers. There are confounding oncogenic and tumor suppressing roles of these protein families surrounding different aspects of tumor growth and metastasis observed clinically. This section aims to elucidate the seemingly contradictory roles of caveolins and flotillins in metastatic progression and patient prognosis for a range of cancers. The prognostic roles of these proteins are summarized in **Table 2.2**.

Protein Family	Cancer Type	Summary	Protein	Prognosis	References
Flotillin	Breast Cancer	↑Flotillin-2 is significantly correlated with clinical stage, metastasis, and shorter overall survival	Flotillin-2	Poor	[197]
	Cervical Cancer	↑Flotillin-1 and Flotillin-2 corelates with pelvic lymph node metastasis, clinical stage, tumor differentiation and poor overall survival	Flotillin-1 and 2	Poor	[198,199]
	Colorectal Cancer	↑Flotillin-1 and flotillin-2 are associated with tumor volume, depth of invasion, lymph node metastasis, distant metastasis, increased proliferation and poor survival	Flotillin-1 and 2	Poor	[200,201]
	Liver (Hepatocellular and Intrahepatic Cholangio-Carcinoma)	↑Flotillin-1 and flotillin-2 in cancerous tissue and positively correlated with tumor size, clinical stage, vascular invasion, lymph node metastasis and relapse.	Flotillin-1 and 2	Poor	[202,203]
	Nasopharyngeal Carcinoma	↑Flotillin-2 promotes tumor progression and is positively associated with a metastatic phenotype and sorter overall survival	Flotillin-2	Poor	[204,205]
	Neuroblastoma	↓Flotillin-1 correlated with poor prognosis and mRNA expression inversely correlate with clinical malignancy grade	Flotillin-1	Favorable	[206]
	Small Cell Lung Cancer	↑Flotillin-1 is highly expressed in small cell lung cancer and strongly correlates with clinical stage, distant metastasis, and poor survival	Flotillin-1	Poor	[207]
	Various	↑Flotillin-1 and flotillin-2 are associated with shorter overall survival, decreased disease-free survival and increased lymph node metastasis	Flotillin-1 and 2	Poor	[208,209]
	Vulvar Squamous Cell Carcinoma	↑Flotillin-1 predicts poor overall and progressive free survival and is an oncogenic facilitator of inguinal/femoral lymph node metastasis	Flotillin-1	Poor	[210]
Caveolin	Bladder Cancer	↑Caveolin-1 in cancerous tissues and high-grade tumors	Caveolin-1	Poor	[211,212]
	Breast Cancer	↑Stromal Caveolin-1 in CAFs correlated with increased 5-year survival, low histological grade while absence or ↓stromal caveolin-1 increased risk of recurrence and predicted lymph node metastasis ↑Epithelial Caveolin-1 correlates with high histological grade, lack of hormone receptors and decreased survival Tumor+ Stromal- cancer subtypes had poor survival	Caveolin-1 (stromal and epithelial)	Favorable (stromal) Poor (tumoral)	[213–216]
	Breast Cancer (Brain metastases)	↑Caveolin-1 negatively regulates Stat3, inhibiting brain metastasis from breast cancer	Caveolin-1	Favorable	[217]
	Colorectal Cancer (Liver Metastases)	↓Stromal Caveolin-1 is associated with decreased disease free and overall survival after hepatectomy	Caveolin-1 (stromal)	Favorable	[218]
	Gastric Cancer	↑Caveolin-1 strong indicator of poor median overall survival, tumor grade, lymph node involvement and decreased relapse-free survival in resected gastric cancer	Caveolin-1	Poor	[219,220]
	Non-Small Cell Lung Cancer	↑Caveolin-1 expression correlated with pathological stage, chemoresistance and decreased overall and disease-free survival	Caveolin-1	Poor	[221,222]
	Prostate Cancer	↑Stromal Caveolin-1 associated with favorable prognosis, longer survival while expression decreased in malignant tissues and higher tumor stages	Caveolin-1 (stromal)	Favorable	[223]
	Thyroid Cancer	↑Stromal Caveolin-1, Caveolin-2 and Caveolin-3 in anaplastic carcinoma (poor prognosis) compared to papillary thyroid carcinoma and diffuse sclerosing variant of papillary carcinoma (more favorable prognosis)	Caveolin-1, 2 and 3 (stromal)	Poor	[224]

Table 2.2. The role of flotillin and caveolin families of proteins in metastatic progression and patient prognosis.

2.5.1 Flotillins

Flotillin-1 and flotillin-2 are widely believed to be metastatic drivers in a variety of tumors [225]. Two recent meta-analyses found that flotillin overexpression predicts poor overall survival, lymph node metastasis, and distant metastasis in a multitude of solid tumors [208,209]. In breast cancer, flotillin-2 mRNA and protein overexpression were indicative of poor prognosis in both early and late-stage disease [197]. Meanwhile, increased flotillin-1/flotillin-2 expression correlated with poor survival and enhanced pelvic, inguinal, and femoral lymph node metastasis in both cervical and vulvar squamous cell carcinoma [198,199,210]. High flotillin-1 and flotillin-2 levels were indicators of aggressive characteristics and poor prognosis of hepatocellular carcinoma and intrahepatic cholangiocarcinoma, respectively [202,203]. In both left and right colorectal cancer, flotillin-1 was overexpressed in cancerous tissue and was associated with tumor volume, differentiation and proliferation while flotillin-2 levels were associated with lymph node and distant metastasis [200,201]. Moreover, flotillin-1 and flotillin-2 were found to promote metastasis via TGF-β-mediated EMT induction in small cell lung cancer and nasopharyngeal carcinoma patients, respectively [204,205,207].

While mounting evidence implicates flotillin overexpression with tumor progression and metastasis, one study revealed that *low* expression of flotillin-1 correlates with poor prognosis in neuroblastoma patients [206]. Flotillin-1 regulated neuroblastoma progression by facilitating binding, endocytosis, and degradation of membrane-localizing anaplastic lymphoma kinase (ALK). Thus, it is possible that this conflicting, anti-metastatic role of flotillin-1 may be constrained to subsets of cancers that possess high levels of oncogenic ALK mutants, e.g. NSCLC and neuroblastoma [226].

2.5.2 Caveolins

While the oncogenic roles of flotillin-1 and 2 in the clinic are generally agreed upon, there remains contradictory evidence for the clinical role of caveolins, particularly caveolin-1. For example, multiple studies in bladder cancer have demonstrated high caveolin-1 expression is associated with cancer progression, high grade tumors, and poor patient prognosis [211,212]. Conversely, high stromal caveolin-1 in early prostate cancer was found to correlate with decreased malignancy, longer survival, and favorable prognosis when managed by watchful waiting [223]. In gastric cancers post-tumor resection, high caveolin-1 expression correlated with tumor relapse and lymph node metastasis [219,220]. However, in colorectal cancer-derived liver metastasis post-hepatectomy, weak stromal caveolin-1 expression was a predictor of poor prognosis [218]. Further, enhanced tumoral caveolin-1 correlated with gemcitabine drug resistance and advanced pathological stage and metastasis in NSCLC patients [221,222]. Taken collectively, these studies indicate tumoral caveolin-1 is an indicator of poor prognosis, while stromal caveolin-1 is favorable. While this is true for many studies, in thyroid cancer, expression of stromal caveolin was found to be upregulated in more aggressive carcinoma subtypes [224].

Breast cancer may be the most confounding cancer type when it comes to the clinical relevance of caveolin-1 [227]. Overexpression of caveolin-1 in cancer associated fibroblasts (CAFs) correlated with increased low histological grade and favorable prognosis, while absent or depleted stromal caveolin-1 increased the risk of recurrence and predicted lymph node metastasis in early ductal carcinoma in situ (DCIS) [213,214]. Additionally, high levels of epithelial caveolin-1 were correlated with more aggressive, triple negative breast cancer subtypes [215]. These findings are supported by a study that examined subgroups of breast cancer patients with high tumoral caveolin-1 (T++) and weak stromal expression (S-). T(++)/S(-) subgroups showed exceptionally poor clinical outcomes compared to T(++) and S(-) groups taken individually [216]. This is consistent with the differential roles of epithelial and stromal caveolin-1 in cancer prognosis discussed above. However, this may not always be the case. One study of metastatic breast cancer found caveolin-1 expression was *decreased* in brain metastases compared to primary DCIS [217]. Further, another study demonstrated that depletion of caveolin-1 in lipid rafts of breast tumors promoted cellular autophagy-mediated cell survival under starvation conditions [228]. This supports the multifaceted functionality of caveolins within breast cancer metastasis, warranting further investigation before implementation as a clinical biomarker.

2.6 Conclusions and Future Perspectives

Within the past few decades, numerous studies have implicated lipid rafts as drivers of oncogenic and pro-metastatic processes. However, the role of rafts in specific areas of metastasis has remained elusive. For example, little is known about how lipid rafts affect CTC survival in the vasculature. While we have presented studies that demonstrate that rafts are vital for anoikis resistance, endothelial cell rolling, and vasculature-related adhesion mechanisms, evidence of this in spontaneous CTCs in animal models remains nonexistent. This is likely a consequence of the aforementioned inadequacies of *in vivo* and real time lipid raft detection methods. Moreover, no known study has examined the presence or effect of lipid rafts in primary CTC's isolated from human patients. Given the heterogeneous landscape of CTCs, elucidating the undiscovered roles of rafts and raft-associated proteins may be instrumental in predicting CTC subpopulations that will survive in transit and proceed to colonize secondary tumors [229].

Studies have shown that excessive cholesterol in cancer cells is a biomarker of chemoresistance and stemness, but the role of raft microdomains in cancer stem cells (CSCs) remains largely unknown [230]. CD44 remains a prominent CSC marker in a variety of cancers, and we have discussed a multitude of studies demonstrating the propensity of CD44 to coalesce into raft fragments. However, other prominent CSC surface markers such as CD133 remain understudied despite recent methodologies for isolating CD133+ raft fractions [231]. It was recently demonstrated that CD133 localizes into lipid rafts in pancreatic cells to enhance chemoresistance, further supporting investigation into other CSC-related proteins [120]. Lipid rafts may be a vital missing link needed to fully understand the formation of cancer stem cell phenotypes, while also shedding light into mechanisms of senesce and therapeutic resistance. Further, abrogating the juxtaposition of lipid rafts and stemness-related proteins via raft antagonization may provide a means of reverting CSCs into more druggable cellular phenotypes.

While there has been substantial research done on the contribution of lipid rafts in apoptotic and anoikis pathways, the role of lipid rafts in necroptotic pathways has not been studied sufficiently. This review has discussed the importance of lipid rafts in the MLKL-mediated necroptotic pathway, in response to TNF superfamily ligands. However, it is important to note that necroptosis can also be induced by dsRNA and lipopolysaccharides, through TLR 3 and 4 [232,233]. Necroptosis can also be initiated through interferons [234]. It is currently unknown how and if lipid rafts play a role in this pathway, perhaps in an MLKL-independent fashion. Leveraging known mechanisms of raft associated apoptosis may be key for therapeutic exploitation. For example, it was mentioned that many chemotherapeutic agents have been shown to translocate death receptors into lipid rafts to enhance apoptotic signaling upon ligand activation. Clinical evaluation of combination treatments of chemotherapeutics and death-inducing ligands (TRAIL, Fas) may prove effective to overcome mechanisms of therapeutic resistance.

Moving forward, a major challenge will be developing targeted therapeutics and drug delivery strategies to selectively disrupt rafts that facilitate oncogenic and pro-metastatic processes. While FDA-approved cholesterol lowering drugs exist, they tend to be nonspecific and are not yet approved for cancer therapy [235]. Additionally, the off-target and downstream signaling implications following statin-mediated cholesterol depletion in cancer have yet to be fully elucidated. Given these translational challenges, we expect not only forthcoming research on raft antagonizing compounds, but raft-targeted delivery modalities as well. For example, one group designed mβCD-hyaluronic acid-ceramide nanoassemblies that selectively target and disrupt

CD44 positive lipid rafts [236]. Engineering novel drug delivery modalities for raft targeting and regulation will be critical for the development of anti-metastatic cancer therapies.

Chapter 3:

Oxaliplatin Resistance in Colorectal Cancer Enhances TRAIL Sensitivity Via Death Receptor 4 Upregulation and Lipid Raft Localization

Joshua D. Greenlee, Maria Lopez Cavestany, Nerymar Ortiz-Otero, Kevin Liu, Tejas Subramanian, Burt Cagir, Michael R. King

This chapter is adapted from *Oxaliplatin resistance in colorectal cancer enhances TRAIL sensitivity via death receptor 4 upregulation and lipid raft localization* published in *eLife* and has been reproduced with permission of the publisher and co-authors Maria Lopez Cavestany, Nerymar Ortiz-Otero, Tejas Subramanian, Kevin Liu, Burt Cagir, and Michael King [65].

Greenlee, J.D.; Lopez-Cavestany, M.; Ortiz-Otero, N.; Liu, K.; Subramanian, T.; Cagir, B.; King, M.R. Oxaliplatin Resistance in Colorectal Cancer Enhances TRAIL Sensitivity via Death Receptor 4 Upregulation and Lipid Raft Localization. *eLife* 2021, 10, e67750, doi:10.7554/eLife.67750.

3.1 Abstract

Colorectal cancer (CRC) remains a leading cause of cancer death, and its mortality is associated with metastasis and chemoresistance. We demonstrate that oxaliplatin-resistant CRC cells are sensitized to TRAIL-mediated apoptosis. Oxaliplatin-resistant cells exhibited transcriptional downregulation of caspase-10, but this had minimal effects on TRAIL sensitivity following CRISPR-Cas9 deletion of caspase-10 in parental cells. Sensitization effects in oxaliplatin-resistant cells were found to be a result of increased DR4, as well as significantly enhanced DR4 palmitoylation and translocation into lipid rafts. Raft perturbation via nystatin and resveratrol significantly altered DR4/raft colocalization and TRAIL sensitivity. Blood samples from metastatic CRC patients were treated with TRAIL liposomes, and a 57% reduction of viable CTCs was observed. Increased DR4/lipid raft colocalization in CTCs was found to correspond with increased oxaliplatin resistance and increased efficacy of TRAIL liposomes. To our knowledge, this is the first study to investigate the role of lipid rafts in primary CTCs.

3.2 Introduction

Colorectal cancer (CRC) is the second leading cause of cancer death and is responsible for over 50,000 deaths annually in the United States [237]. The probability of being diagnosed with CRC in one's lifetime is 1 in 24, and there are over 100,000 new cases diagnosed annually in the United States alone. While the 5-year survival rate of localized and regional disease is 90% and 71%, respectively, patients with metastatic disease have just a 14% 5-year survival rate [238]. Dissemination to other organs is the cause of high mortality in most cancers, as nearly 90% of all cancer death is attributed to metastasis [239]. The most common sites of CRC metastases include the liver, lungs, and peritoneum (peritoneal carcinomatosis). While surgery and radiation remain curative options for patients with localized disease, the standard of care for CRC patients with advanced metastatic disease is commonly combination front line chemotherapy treatment [240]. These chemotherapy regimens typically include fluorouracil (5-FU) and leucovorin (LV) in combination, which work together to inhibit DNA and RNA synthesis and modulate tumor growth, extending median survival in patients from 9 months (with palliative care) to over 12 months [29]. Oxaliplatin is a chemotherapeutic agent that upon binding to DNA, forms DNA adducts to cause irreversible transcriptional errors, resulting in cellular apoptosis. When oxaliplatin is administered with 5-FU/LV (FOLFOX), the objective response rate is 50% in previously untreated patients, increasing the median overall survival to 18 - 24 months [29,43].

While there have been incremental advances in extending survival using FOLFOX and other oxaliplatin-containing chemotherapeutics, patients who eventually succumb to the disease frequently develop chemoresistant subpopulations of cancer cells via intrinsic or acquired mechanisms [43,241]. Mechanisms of oxaliplatin resistance in tumors include alterations in responses to DNA damage, cell death pathways (e.g., apoptosis, necrosis), NF-κB signaling, and cellular transport [241]. Despite the robustness of these oxaliplatin-resistant cancer cells, multiple studies suggest that chemoresistant subpopulations may be increasingly susceptible to adjuvant therapies [64,241–245]. Tumor necrosis factor-related apoptosis-inducing ligand (TRAIL) is a member of the TNF family of proteins and induces apoptosis in cancer cells via binding to transmembrane death receptors [246]. The binding of TRAIL to trimerized death receptor 4 (DR4) and 5 (DR5) initiates an intracellular apoptotic cascade beginning with the recruitment of death domains and formation of the death-inducing signaling complex (DISC).

Lipid rafts (LRs) are microdomains in the plasma membrane lipid bilayer that are enriched in cholesterol and sphingolipids, with a propensity to assemble specific transmembrane and GPI-anchored proteins [98]. Mounting evidence has demonstrated that lipid rafts play major roles in tumor progression, metastasis and cell death [84]. Studies have shown that translocation into lipid rafts can augment signaling for a variety of cancer-implicated receptors, including growth factor receptors (IGFR and EGFR) and death receptors (Fas and Death receptors 4/5) [96,247–249]. Translocation of death receptors into rafts enhances apoptotic signaling through the formation of clusters of apoptotic signaling molecule-enriched rafts (CASMER), which act as scaffolds to facilitate trimerization and supramolecular clustering of receptors [248]. It has become increasingly evident that higher order oligomerization of death receptors is necessary for effective apoptotic signaling in cancer cells [250].

Studies have shown that combination treatment of chemotherapeutic agents with TRAIL may sensitize cancer cells to TRAIL-mediated apoptosis through a variety of mechanisms, including death receptor upregulation [251–253], suppression of apoptotic inhibitors within the intrinsic pathway [60], and redistribution of death receptors into lipid rafts [254]. However, no study has examined whether surviving oxaliplatin-resistant subpopulations of cancer cells have an enhanced sensitivity to TRAIL. In this study, we demonstrate that oxaliplatin-resistant cells show enhanced sensitivity to TRAIL-mediated apoptosis through lipid raft translocation of DR4. Moreover, we elucidate mechanisms which drive this sensitization using chemoresistant cell lines and blood samples collected from metastatic cancer patients. The response of oxaliplatin-resistant CRC to TRAIL-based therapeutics may prove critical to establishing promising new adjuvants for patients who have exhausted conventional treatment modalities.

3.3 Results

3.3.1 Oxaliplatin-resistant cell lines show enhanced TRAIL sensitivity

Cell viability of four colorectal cancer cell lines after 24 h treatment with 0.1-1000 ng/ml of TRAIL was measured and compared to the viability of oxaliplatin-resistant (OxR) cell lines (**Figure 3.1A**). Briefly, oxaliplatin-resistant cell lines were previously derived from exposure to increasing concentrations of oxaliplatin until a 10-fold increase in IC50 was achieved [255–257]. Parental and OxR cells were treated with a range of oxaliplatin concentrations to ensure that chemoresistance was conserved after multiple passages in culture (**Supplementary Figure 3.1A**). Moreover, oxaliplatin-resistant cells were found to have increased invasion and motility compared to parental cells, consistent with literature reporting their derivation (**Supplementary Figure 3.1B**). Interestingly, oxaliplatin-resistant HT29, SW620 and HCT116 cell lines showed increased maximum TRAIL sensitization levels compared to their parental counterparts, while

SW480 cells showed similar or decreased sensitization levels (**Supplementary Figure 3.2**). IC50 values demonstrate that a chemoresistant phenotype resulted in augmented TRAIL-mediated apoptosis in two cell lines (**Figure 3.1B**). Importantly, cells were not treated with any oxaliplatin in quantifying the level of TRAIL sensitization, and oxaliplatin was not supplemented in the cell culture media to exclude any possible effects from combination treatment. In SW620 cells, large differences in apoptosis were observed when treated with the highest concentration of TRAIL (1000 ng/ml) (**Figure 3.1C**). Only 33.3% of parental cells were found to be in late-stage apoptosis after 24 h, compared to 60.6% for OxR cells.

To determine if the observed differences in apoptosis were due to enhanced mitochondrial outer membrane permeability, a JC-1 dye was used. SW620 OxR cells exhibited over a 3-fold increase in the population of JC-1 red (-) cells, indicating increased mitochondrial depolarization (**Figure 3.1D**). Mitochondrial depolarization was significantly enhanced in OxR cells for TRAIL concentrations of 50 ng/ml and higher (**Figure 3.1E**). Similar TRAIL-induced mitochondrial effects were observed in HCT116 cells (**Supplementary Figure 3.3**). These results demonstrate that enhanced TRAIL mediated apoptosis is occurring, at least in part, via the intrinsic pathway and mitochondrial disruption.

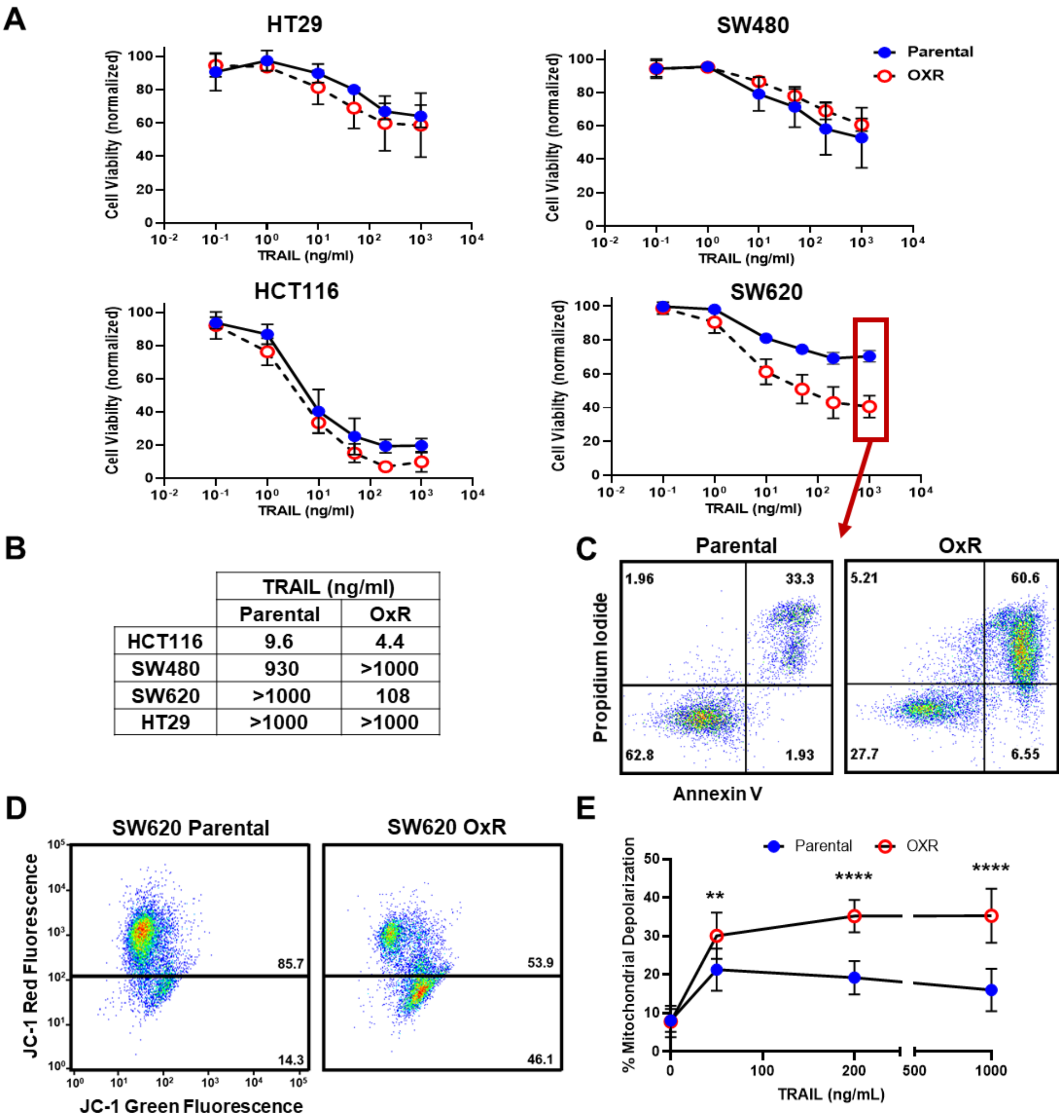

	TRAIL (ng/ml)	
	Parental	OxR
HCT116	9.6	4.4
SW480	930	>1000
SW620	>1000	108
HT29	>1000	>1000

Figure 3.1. Oxaliplatin-resistant CRC cell lines exhibit enhanced sensitization to TRAIL-mediated apoptosis via the intrinsic pathway and mitochondrial permeabilization. (A) Oxaliplatin-resistant SW620, SW480, HCT116 and HT29 colon cancer cell lines demonstrate similar or enhanced sensitivity to TRAIL compared to their parental counterparts after 24 h of treatment. N=3 (biological replicates); n=9 (technical replicates). **(B)** IC50 values were calculated using a variable slope four parameter nonlinear regression. **(C)** Representative Annexin V/PI flow plots comparing SW620 parental and OxR cell viability after 24 h of treatment with 1000 ng/ml TRAIL. The four quadrants represent viable cells (bottom left), early apoptosis (bottom right), necrosis (top left) and late apoptosis (top right). **(D)** Representative flow plots of JC-1 assay after treatment with 1000 ng/ml of TRAIL. Mitochondrial depolarization is evidenced by decreased red fluorescence and increased green fluorescence. **(E)** Mitochondrial depolarization as a function of TRAIL concentration for SW620 parental and OxR cell lines. N=3 (n=9). For all graphs, data are presented as mean±SD. $^{**}p<0.01$ $^{****}p<0.0001$ (unpaired two-tailed t-test).

3.3.2 Oxaliplatin-resistant derivatives have decreased CASP10 that has little consequence on TRAIL sensitization

Given that enhanced TRAIL-mediated apoptosis was found to occur via the mitochondrial pathway, gene expression of apoptotic transcripts was compared between the parental and OxR cells. RT-PCR human apoptosis profiler arrays were used to analyze transcripts within the SW620 and HCT116 cell lines, since these cells showed the highest degree of OxR TRAIL sensitization and exhibit different innate sensitivities to TRAIL (HCT116 cells are TRAIL-sensitive whereas SW620 cells are TRAIL-resistant). Interestingly, upon analyzing the RNA expression of 84 apoptotic transcripts, both cell lines shared similar profiles between parental and OxR derivatives. HCT116 OxR cells showed upregulated pro-apoptotic transcripts cytochrome-c and caspase-4 (**Figure 3.2A**). Cytochrome-c is released from the mitochondria into the cytosol after mitochondrial permeabilization, binding to adaptor molecule apoptosis-protease activating factor 1 (Apaf-1) to form the apoptosome and initiate downstream caspase signaling [54]. Caspase-4 is localized to the ER and initiates apoptosis in response to ER stress [258]. Interestingly, SW620 OxR cells had upregulated Fas, a cell surface death receptor that acts similarly in apoptotic signaling to DR4/DR5 via binding of Fas ligand [259], and osteoprotegerin, a soluble decoy receptor that sequesters TRAIL and inhibits apoptosis [260] (**Figure 3.2B)**. Upregulated Fas expression in SW620 OxR cells was confirmed via surface staining and flow cytometry, however, receptor neutralization with the ZB4 anti-Fas antibody had no effect on TRAIL sensitization when treated in combination with TRAIL (**Supplementary Figure 3.4A-C**). Notably, both HCT116 and SW620 OxR cell lines had caspase-10 as the most significantly downregulated transcript. To determine whether this was of consequence to the observed TRAIL sensitization, an SW620 caspase-10 knockout cell line was created using a multi-guide sgRNA CRISPR-Cas9 approach. Knock-out (KO) efficiency was found to be 93% **(Figure 3.2C)**. The TRAIL sensitivity of this caspase-10 KO cell line was compared to a control cell line treated with Cas9 only. Caspase-10 KO cells showed only a slight decrease in cell viability after 24 h of TRAIL treatment (**Figure 3.2D**). The number of late-stage apoptotic cells remained similar between cell lines (**Figure 3.2E**) and the maximum TRAIL sensitization observed was insignificant following caspase-10 KO (**Figure 3.2F)**.

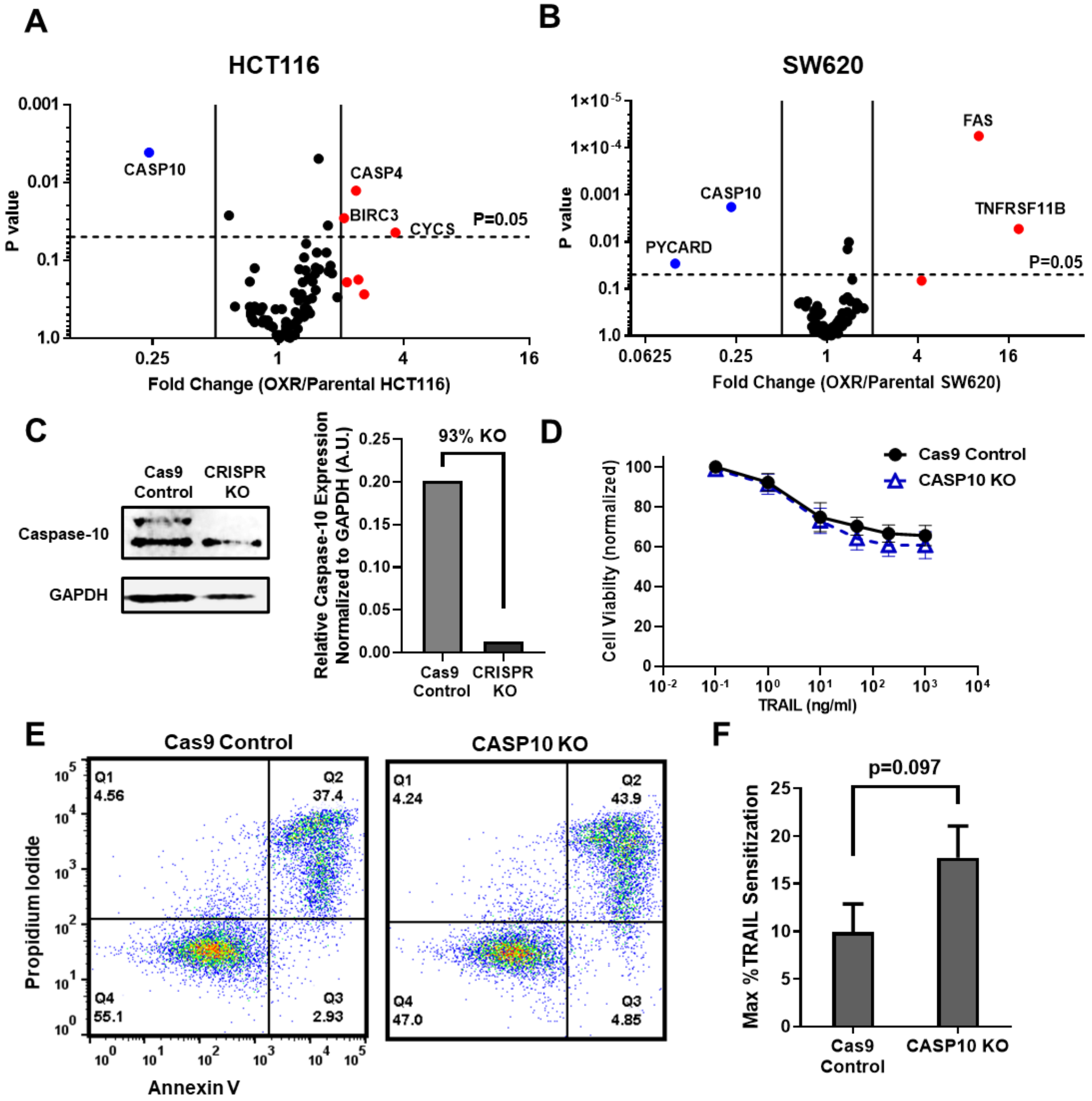

Figure 3.2. Microarray profiles show that parental and oxaliplatin-resistant CRC cell lines have similar expression of apoptotic transcripts while OxR derivatives have significantly downregulated CASP10. **(A-B)** Volcano plots of RT-PCR Apoptosis Profiler arrays demonstrate downregulation of CASP10 in OxR phenotypes. N=3. **(C)** CRISPR/Cas9 knockout of caspase-10 in SW620 parental cells was confirmed via western blot. sgRNA/Cas9 ribonucleoprotein complexes reduced caspase-10 expression by 93% compared to cells treated with Cas9 alone. **(D)** CASP10 KO cells demonstrate slight decreases in viability when treated with TRAIL compared to Cas9 control. Data are presented as mean±SD. N=3 (n=9). **(E)** Representative Annexin V/PI flow plots comparing SW620 parental (Cas9 only) and CASP10 KO cell viability after 24 h of treatment with 1000 ng/ml TRAIL. **(F)** Depletion of caspase-10 did not have a significant effect on TRAIL sensitization (unpaired two-tailed t-test). Data are presented as mean+SEM. N=3 (n=9).

3.3.3 TRAIL-sensitized OxR cell lines have upregulated DR4

While changes in death receptor expression were insignificant at a transcriptional level, studies have demonstrated that chemoresistance can alter receptor abundance via mechanisms of translational regulation [261,262]. Confocal microscopy showed that oxaliplatin-resistant cells have increased DR4 in both HCT116 (**Figure 3.3A**) and SW620 (**Figure 3.3B**) cell lines. To quantify receptor expression, total DR4 area per cell was analyzed for at least 70 cells. Analysis showed oxaliplatin-resistant derivative cell lines had significantly increased DR4 area per cell (**Figure 3.3C**). There were no differences in cell size between parental and OxR derivatives for all four cell lines (**Supplementary Figure 3.5**). Flow cytometry staining of non-permeabilized cells was used to determine if this death receptor increase was also observed on the cell surface. Both HCT116 OxR and SW620 OxR cells showed significant increases in DR4 surface expression (**Figure 3.3D**). Total and surface DR4 expression was similar between parental and OxR derivatives in mildly sensitized HT29 cells and unsensitized SW480 cells (**Supplementary Figure 3.6A-C**). To account for possible thresholding effects in area quantification, raw integrated density counts per cell were also measured and found to be consistent with changes in receptor area (**Supplementary Figure 3.7**). Increases in DR4 expression of OxR derivatives were also confirmed via western blot but were only significant in SW620 cells (**Figure 3.3E-F**). Oxaliplatin-resistant HCT116, SW620 and HT29 cells all displayed increases in DR5 area per cell, while SW480 OxR cells had significant decreases in total DR5 expression (**Supplementary Figure 3.8A-D**). However, total receptor area per cell was considerably lower for DR5 compared to DR4. Additionally, expression of surface DR5, analyzed via flow cytometry, was only significantly upregulated in SW620 OxR cells (**Supplementary Figure 3.8E**). This is further confounded by western blot data which show no change in DR5 expression in HCT116 OxR cells, and a significant decrease in SW620 OxR cells (**Supplementary Figure 3.9A-B**). Decoy receptors are surface receptors that, like death receptors, can bind to exogenous TRAIL. However, decoy receptor 1 (DcR1) and decoy receptor 2 (DcR2) are unable to activate the apoptotic pathway, making these receptors sequestering agents that competitively bind to TRAIL. While some studies have shown that chemotherapy-induced changes in TRAIL sensitivity have been linked to modulation or augmentation of decoy receptors [63], all cell lines exhibited no meaningful difference in surface DcR1 and DcR2 expression between parental and OxR derivatives (**Supplementary Figure 3.10**). Despite statistical significance in SW480 and HT29 cells, decoy receptor expression, especially DcR2, was expressed in negligible quantities in these cell lines.

Given the consistency in data suggesting DR4 upregulation in TRAIL-sensitized OxR cell lines, cells were treated with the DR4-agonist monoclonal antibody Mapatumumab to determine

DR4 specificity. SW620 OxR cells exhibited significant increases in the number of apoptotic cells after 24 hours of treatment, including a 3-fold increase in apoptosis at concentrations of 10 µg/ml (**Figure 3.3G**). Cell viability closely paralleled TRAIL treatments: parental cells remained resistant at high doses while OxR cells exhibited a dose-responsive decrease in cell viability (**Figure 3.3H**). HCT116 cell lines exhibited similar results, as OxR cells were significantly more apoptotic at concentrations exceeding 0.1 µg/ml (**Supplementary Figure 3.11A-B**). The maximum Mapatumumab sensitization was calculated to be greater than 40% for oxaliplatin-resistant HCT116 and SW620 cells (**Figure 3.3I**), providing more causal evidence for a DR4-associated mechanism.

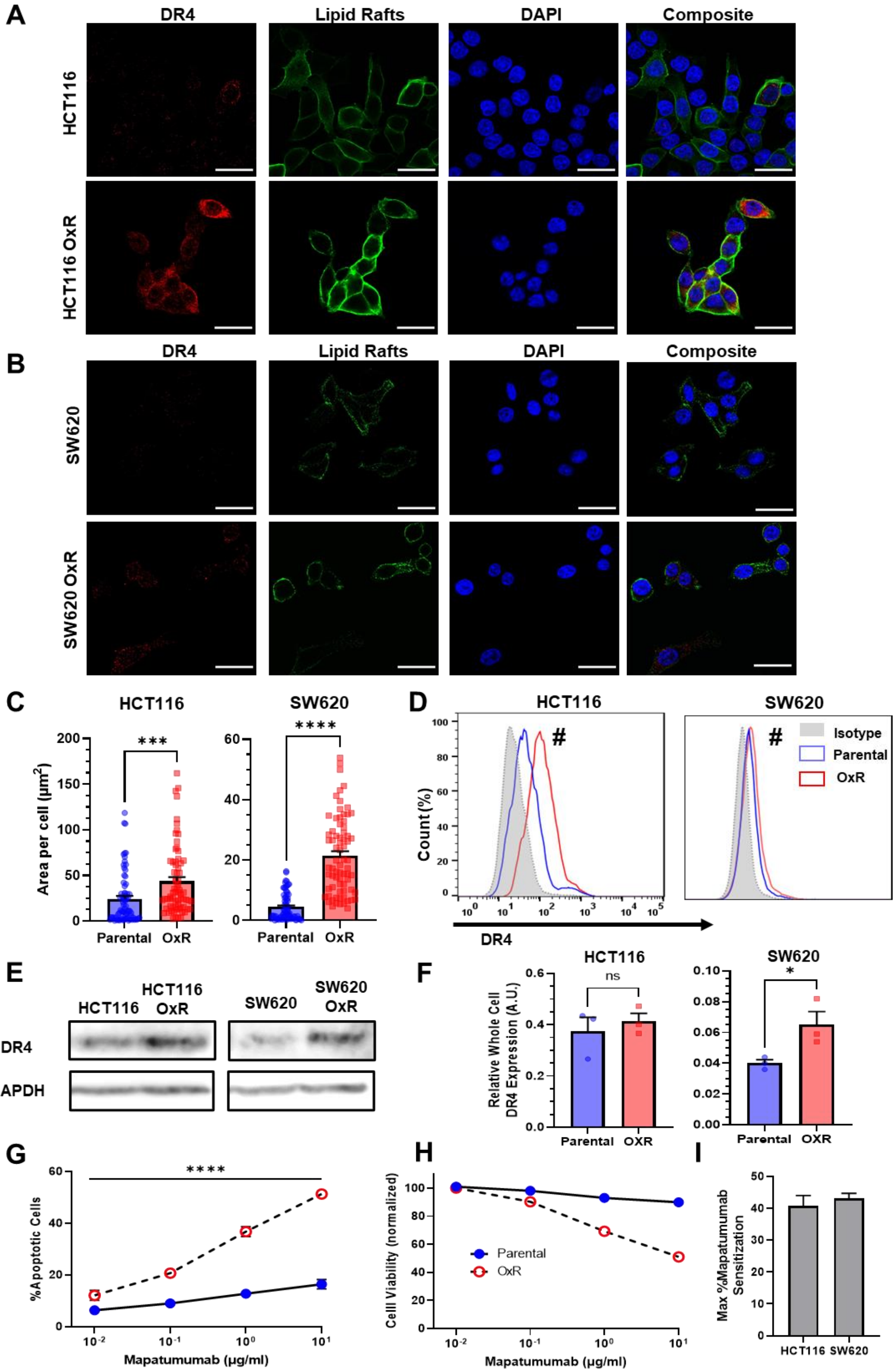

Figure 3.3. Oxaliplatin-resistant colon cancer cell lines have upregulated DR4 expression. (A-B) Confocal micrographs of HCT116 and SW620 cells, respectively. Red channel represents DR4, green is

lipid rafts and blue is DAPI (nuclei). Scale bar = 30 µm. **(C)** Quantification of DR4 area per cell in HCT116 and SW620 cells. For each cell line, N=75 cells were analyzed. Data are presented as mean+SEM from N=3 independent experiments. ***p<0.001 ****p<0.0001 (unpaired two-tailed t-test). **(D)** OxR cells had increased surface expression of DR4 in non-permeabilized cells analyzed via flow cytometry. $^{\#}$Significant according to a chi-squared test (see Supplementary Table 3.1). **(E)** Western blots for DR4 in whole cell lysates of parental and OxR cells. **(F)** Quantification of western blots from three independent experiments (N=3). Data are presented as mean+SEM. *p<0.05 (unpaired two-tailed t-test). **(G)** Percentage of apoptotic SW620 cells after treatment with 0.01-10 µg/ml Mapatumumab (sum of early and late-stage apoptotic cells from Annexin/PI staining). Data are presented as mean+SD. N=3 (n=9). ****p<0.0001 (multiple unpaired two-tailed t-tests). **(H)** Cell viability of SW620 cells after Mapatumumab treatment, determined by Annexin-V/PI staining. Data are presented as mean±SD. N=3 (n=6). **(I)** Maximum Mapatumumab sensitization within OxR cell lines compared to their parental counterparts. Data are presented as mean+SEM.

3.3.4 TRAIL-sensitized OxR cell lines have enhanced colocalization of DR4 into lipid rafts

Binary projections of colocalization events between DR4 and lipid rafts demonstrate that OxR phenotypes had enhanced DR4 translocation into lipid rafts in HCT116 and SW620 cells **(Figure 3.4A)**. Quantification of total area of colocalization events showed that HCT116 OxR and SW620 OxR cells have significantly enhanced DR4 localized into lipid rafts, each with an over four-fold increase (**Figure 3.4B**). The areas of DR4/LR colocalized events per cell were not significantly different in HT29 and SW480 cells (**Supplementary Figure 3.6D)**. Other methods of colocalization analysis, including calculation of the Manders' Correlation Coefficient (MCC), supported these results, specifically in HCT116 and SW620 cell lines where the Manders' overlap was significantly greater in OxR cells (**Supplementary Figure 3.12**). The fold change in DR4/LR colocalization area between OxR and parental cells exhibited a strong linear correlation (0.86) with TRAIL sensitization (**Figure 3.4C**). Colocalization of lipid rafts with DR5 was significantly enhanced only in HCT116 and HT29 cells, and analysis of the correlation between DR5 colocalization and TRAIL sensitization resulted in a weaker correlation of 0.48 (**Supplementary Figure 3.13A-C).** Quantification of lipid raft area per cell revealed insignificant changes between parental and OxR derivatives in all cell lines except for HT29 cells, where parental cells showed significantly more rafts (**Supplementary Figure 3.14)**.

To confirm DR4 redistribution into rafts, western blots for DR4 were run on plasma membrane-derived lipid raft fractions, isolated using non-ionic detergent and centrifugation. Isolated lipid raft fractions exhibited significant increases in DR4 for both HCT116 OxR and SW620 OxR cells (**Figure 3.4D-E**). β-actin was used as a loading control to compare relative DR4 expression between parental and OxR cell lines [263]. There were no detectable levels of DR5 in western blots from lipid raft isolated fractions (**Supplementary Figure 3.13D)**. This is consistent with studies in hematological cancers that demonstrate raft localization of DR4 but not DR5 [247,264]. To further examine the proximity of DR4 and lipid rafts between phenotypes, Förster resonance energy transfer (FRET) efficiency was measured using a previously described flow cytometry protocol and calculated via a donor quenching method [265]. Both HCT116 and SW620 OxR cells had significantly increased FRET efficiencies compared to their parental counterparts, with an over two-fold and five-fold increase, respectively **(Figure 3.4F**).

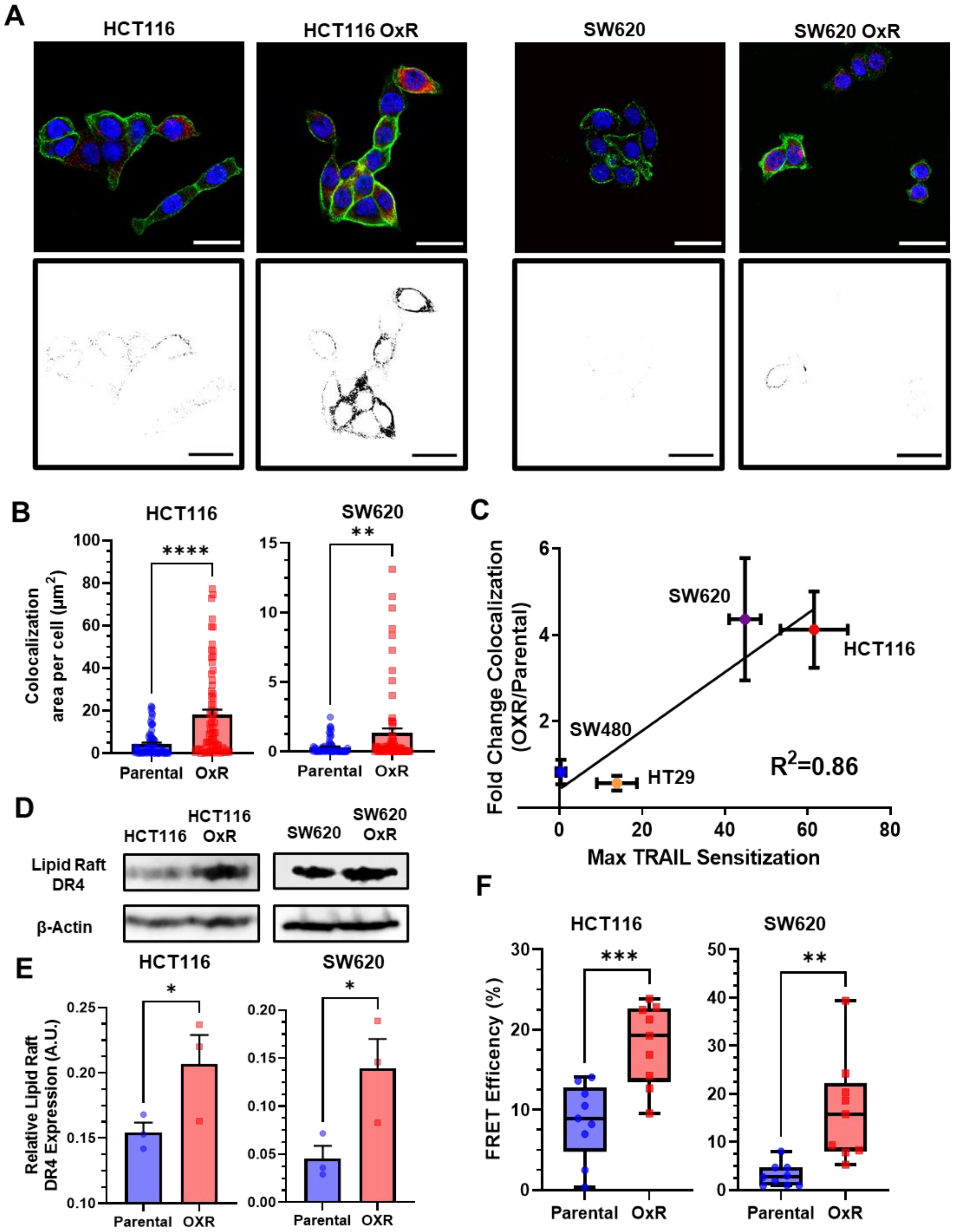

Figure 3.4. Oxaliplatin-resistant colon cancer cell lines have enhanced colocalization of DR4 into lipid rafts. (A) Composite images and binary projections of DR4/LR colocalization areas in HCT116 and SW620 cell lines. Lipid raft and DR4 binary images were generated for a specified threshold, then multiplied by one another to generate images with positive pixels in double positive areas. Red is DR4, green is lipid rafts and blue is DAPI. Scale bar = 30 µm. **(B)** Quantification of DR4 and lipid raft colocalization area per cell in HCT116 and SW620 cells. For each cell line, N=75 cells were analyzed. $^{**}p<0.01$ $^{****}p<0.0001$

(unpaired two-tailed t-test). (**C)** Correlation between the fold change in DR4/LR colocalization (OxR phenotype/parental) and maximum TRAIL sensitization observed by the OxR phenotype for each of the four cell lines (simple linear regression analysis). **(D)** Lipid raft fractions were isolated and analyzed for DR4 via western blot in parental and OxR cells. **(E)** Quantification of lipid raft DR4 blots in (D). *p<0.05 (unpaired two-tailed t-test). For all graphs, data are presented as mean+SEM. **(F)** FRET efficiencies of FITC-labeled DR4 (donor) and Alexa 555-labeled lipid rafts (acceptor) in parental and OxR cells analyzed via flow cytometry. **p<0.01 ***p<0.001 (unpaired two-tailed t-test).

3.3.5 Altering lipid raft composition affects DR4/LR colocalization and has consequential effects on TRAIL sensitization

To probe the effects of LR modulation on DR4 clustering and TRAIL sensitization, SW620 OxR and HCT116 OxR cells were treated with 5 µM of nystatin, a cholesterol-sequestering agent that inhibits LR formation, in combination with TRAIL for 24 h (**Figure 3.5A, G**). Nystatin inhibited TRAIL-mediated apoptosis in SW620 OxR cells, significantly decreasing the maximum TRAIL sensitization from 45% to 23%. (**Figure 3.5B**). Nystatin treatment was found to decrease DR4/LR colocalization by over 20-fold (**Figure 3.5C, M).** Similar results were found in HCT116 OxR cells, as nystatin treatment decreased TRAIL sensitization from 62% to 1% (**Figure 3.5H)** and decreased DR4/LR colocalization by over nine-fold **(Figure 3.5I)**. To demonstrate that enhancing LR formation would have pro-apoptotic effects, parental cells were treated with 70 µM of resveratrol in combination with TRAIL for 24 h (**Figure 3.5D, J**). Resveratrol has been shown to stabilize liquid-ordered domains in the plasma membrane and promote cholesterol/sphingolipid enriched lipid rafts [266]. Resveratrol significantly sensitized parental SW620 cells to TRAIL irrespective of TRAIL concentration with a maximum TRAIL sensitization of 68% (**Figure 3.5E**). Treatment with resveratrol coincided with significant augmentation of DR4/LR colocalization area, an increase of over six-fold **(Figure 3.5F, N)**. Similarly, parental HCT116 cells treated with resveratrol were sensitized 59% **(Figure 3.5K)**, corresponding with a nearly seven-fold increase in DR4/LR colocalization area per cell **(Figure 3.5L)**. Resveratrol and nystatin had no significant effects on DR5 lipid raft colocalization, except in SW620 OxR cells where nystatin treatment surprisingly resulted in a slight increase in colocalization (**Supplementary Figure 3.15A-B)**.

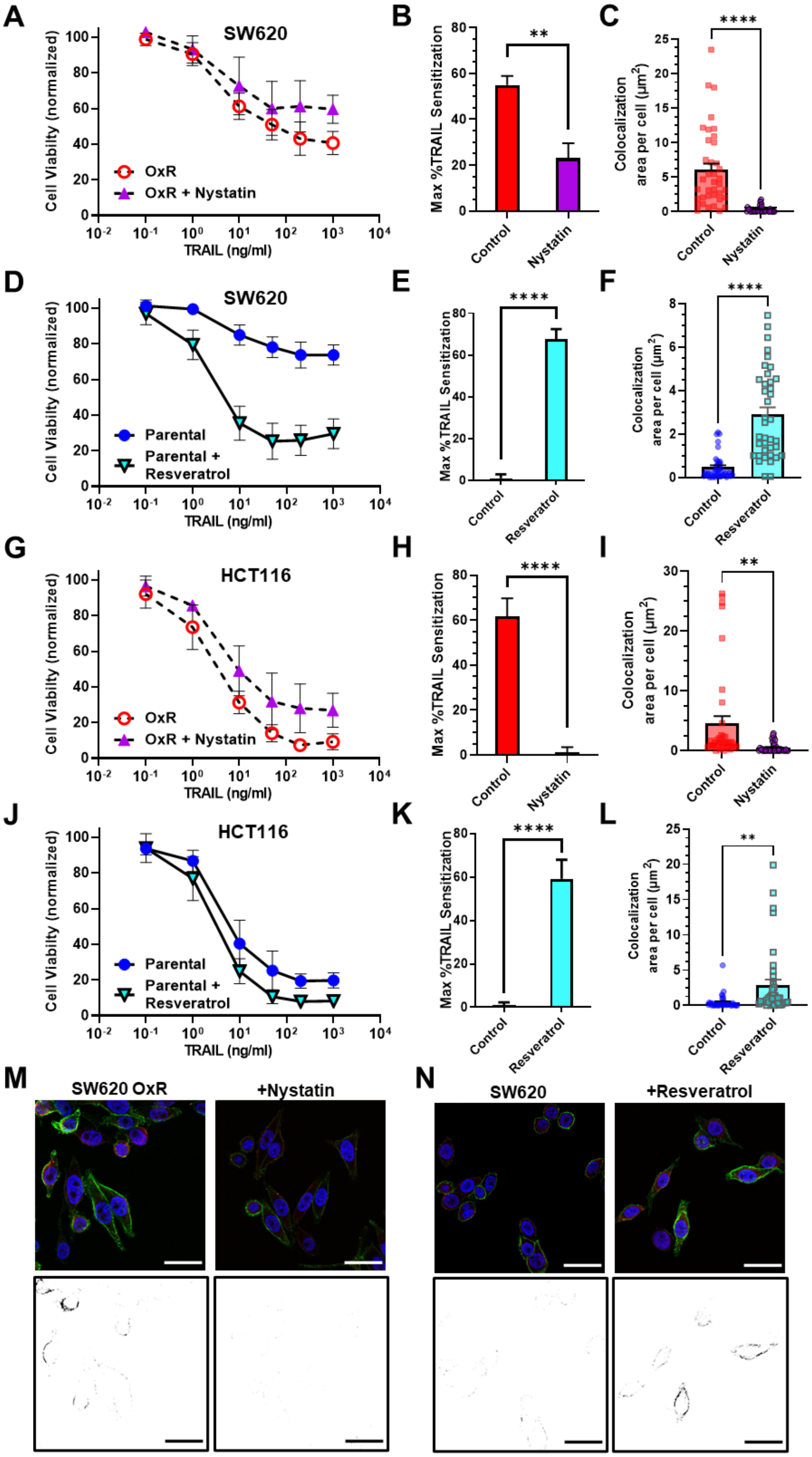
A
SW620
Cell Viability (normalized)
100
80
60
40
20
0
OxR
OxR + Nystatin
10^{-2} 10^{-1} 10^{0} 10^{1} 10^{2} 10^{3} 10^{4}
TRAIL (ng/ml)
B
Max %TRAIL Sensitization
**
Control
Nystatin
C
Colocalization area per cell (μm^2)
****
Control
Nystatin
D
SW620
Parental
Parental + Resveratrol
TRAIL (ng/ml)
E
****
Max %TRAIL Sensitization
Control
Resveratrol
F
****
Colocalization area per cell (μm^2)
Control
Resveratrol
G
HCT116
OxR
OxR + Nystatin
TRAIL (ng/ml)
H
****
Max %TRAIL Sensitization
Control
Nystatin
I
**
Colocalization area per cell (μm^2)
Control
Nystatin
J
HCT116
Parental
Parental + Resveratrol
TRAIL (ng/ml)
K
****
Max %TRAIL Sensitization
Control
Resveratrol
L
**
Colocalization area per cell (μm^2)
Control
Resveratrol
M
SW620 OxR
+Nystatin
N
SW620
+Resveratrol

Figure 3.5. Pharmacological perturbation of DR4 localization in lipid rafts significantly alters cellular apoptosis in response to TRAIL. (A, G) SW620 OxR and HCT116 OxR cells, respectively, treated for 24 h with a combination of TRAIL and 5 µM nystatin. **(B, H)** SW620 OxR and HCT116 OxR cells, respectively, showed a significant decrease in TRAIL sensitization when treated in combination with nystatin. N=3 (n=9). **(C, I)** Treatment with 5 µM nystatin significantly decreased DR4/LR colocalization area in SW620 OxR and HCT116 OxR cells, respectively. For each cell line, N=40 cells were analyzed. **(D, J)** SW620 Par and HCT116 Par cells, respectively, treated for 24 h with a combination of TRAIL and 70 µM resveratrol. N=3 (n=9). **(E, K)** SW620 Par and HCT116 Par cells, respectively, showed a significant increase in TRAIL sensitization when treated in combination with resveratrol. N=3 (n=9). **(F, L)** Treatment with 70 µM nystatin significantly increased DR4/LR colocalization area in SW620 Par and HCT116 Par cells, respectively. For each cell line, N=40 cells were analyzed. **(M)** Representative composite images and binary projections of DR4/LR colocalization in SW620 OxR cells before and after nystatin treatment. **(N)** Representative composite images and binary projections of DR4/LR colocalization in parental SW620 cells before and after resveratrol treatment. Red represents DR4, green is lipid rafts and blue is DAPI. Scale bar = 30 µm. **p<0.01 ****p<0.0001 (unpaired two-tailed t-test for all graphs). (A, D, G, J) Data are presented as mean±SD. (B, C, E, F, H, I, K, L) Data are presented as mean+SEM.

3.3.6 S-Palmitoylation of DR4 is enhanced in oxaliplatin-resistant cells

Palmitoylation is the reversible, post-translational addition of the saturated fatty acid palmitate to the cystine residue of proteins. Palmitoylation of DR4 has proven to be critical for receptor oligomerization and lipid raft translocation, both obligatory for effective TRAIL-mediated apoptotic signaling [267]. S-palmitoylation of DR4 in SW620 parental and OxR cells was analyzed via protein precipitation, free thiol blocking, thioester cleavage of palmitate linkages, and exchange with a mass tag label to quantify the degree of palmitoylated protein. We discovered that DR4 has four distinct palmitoylated sites, the degree of which was enhanced in the oxaliplatin-resistant phenotype (**Figure 3.6A**). Quantifying the percentage of palmitoylated protein in relation to input fraction (IFC) and non-mass tag preserved controls (APC-) validated that oxaliplatin-resistant cells had a significantly higher percentage of DR4 that was palmitoylated (55% compared to 43%) **(Figure 3.6B**). To determine whether enhanced palmitoylation was specific to DR4 and not a ubiquitous characteristic of the OxR phenotype, total cellular protein palmitoylation was measured and analyzed via flow cytometry (**Supplementary Figure 3.16A**). Fluorescent azide labeling of palmitic acid confirmed that total cellular palmitoylation was unchanged between parental and OxR cells (**Supplementary Figure 3.16B**).

To further examine the relationship between DR4 palmitoylation and TRAIL sensitization in OxR cells, the irreversible palmitoylation inhibitor 2-bromopalmitate (2BP) was used. 2BP is a commonly used palmitate analog that is thought to bind to palmitoyl acyl transferase, forming an inhibitory enzyme complex [268]. Treating SW620 OxR cells with 3.5 µM 2BP in combination with TRAIL significantly reduced TRAIL sensitization and increased the IC50 to over 1000 ng/ml (**Figure 3.6C, E**). 2BP significantly reduced the number of apoptotic cells in both parental and OxR cells, demonstrating the importance of DR4 palmitoylation in TRAIL signaling, particularly in chemoresistant cells (**Figure 3.6D**). These data suggest a novel mechanism for enhanced lipid raft-DR4 colocalization in OxR cells via enhanced DR4 palmitoylation **(Figure 3.6F**).

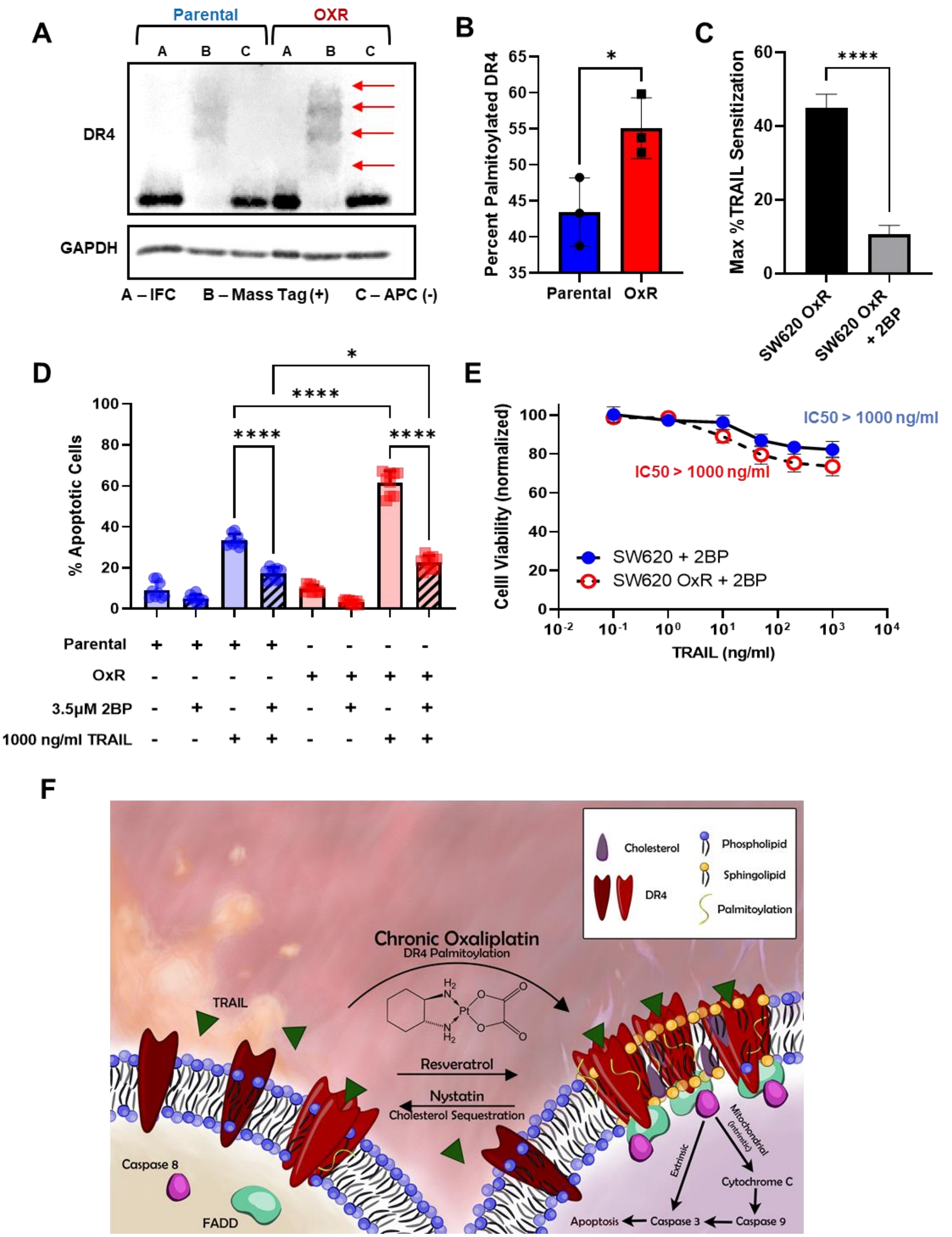

Figure 3.6. Oxaliplatin resistance enhances palmitoylation of DR4, selectively. (A) Death receptor palmitoylation was determined by protein precipitation, thioester cleavage, and conjugation of a mass tag to enumerate and quantify the degree of S-palmitoylation between cellular phenotypes. Samples with a mass tag “B” have distinct bands of equivalent increasing mass, with each mass shift indicating a

palmitoylated site. Input fraction control (IFC) samples “A” were collected before thioester cleavage, while the acyl preservation negative control (APC) samples were incubated with an acyl-preservation reagent to block free thiols in place of the mass tag reagent. Arrows show palmitoylation bands. **(B)** Quantification of the percentage of palmitoylated DR4, calculated by dividing the total palmitoylated mass shift intensity by the average intensity of IFC and APC for each sample. Data are presented as mean±SD (N=3). $*p<0.05$ (unpaired two-tailed t-test). **(C)** Treatment with the irreversible palmitoylation inhibitor 2BP in combination with TRAIL significantly reduced TRAIL sensitization in SW620 OxR cells. Data are presented as mean+SEM. N=3 (n=9). $*p<0.0001$ (unpaired two-tailed t-test). **(D)** Percentage of apoptotic SW620 parental and OxR cells after treating with 1000 ng/ml TRAIL and 3.5 μM 2BP in combination (sum of early and late-stage apoptotic cells from Annexin/PI staining). Data are presented as mean+SD. N=3 (n=9). $*p<0.05$ $****p<0.0001$ (ordinary one-way ANOVA–Tukey’s multiple comparison test). **(E)** Cell viability determined by Annexin-V/PI staining for cells treated with 0.1-1000 ng/ml TRAIL and 3.5 μM 2BP. IC50 values were calculated using a variable slope four parameter nonlinear regression. Data are presented as mean±SD. N=3 (n=9). **(F)** Proposed mechanism of enhanced TRAIL-mediated apoptosis in oxaliplatin-resistant cells.

3.3.7 Metastatic CRC patients show sensitivity to TRAIL liposomes despite chemoresistance

Despite promising specificity for cancer cells and low off-target toxicity, TRAIL’s translational relevance has been confounded by a short half-life and ineffective delivery modalities [68]. In recent studies, our lab has demonstrated that TRAIL-coated leukocytes via the administration of liposomal TRAIL can be effective in eradicating circulating tumor cells (CTCs) in the blood of metastatic cancer patients [269]. Briefly, liposomes were synthesized as previously described using a thin film hydration method, stepwise extrusion to 100 nm in diameter, and decoration with E-selectin and TRAIL via his-tag conjugation [270] (**Figure 3.7A**). Undecorated “control” liposomes, soluble TRAIL (290 ng/ml; at equivalent concentrations as TRAIL liposomes) and oxaliplatin (at peak plasma concentrations of 5 μM) were used as controls. Blood was collected from 13 metastatic CRC patients who had previously undergone or were currently undergoing an oxaliplatin chemotherapy regimen (**Table 3.1**). Of these, five patients were analyzed at two to three timepoints over their respective treatment regimens, representing 21 total samples. Blood samples were treated with TRAIL liposomes or control treatments under hematogenous circulatory shear conditions in a cone-and-plate viscometer. TRAIL liposomes significantly decreased the average percentage of viable CTCs in patient blood to 43%, compared to just 86% when treated with oxaliplatin (**Figure 3.7B**). Interpatient variation was dominant in response to TRAIL liposome treatment, as the between-patient coefficient of variation was twice as high (CoV=0.55) as the average within-patient variation (CoV=0.28). Viable CTCs were categorized as cells that were cytokeratin(+), DAPI(+), CD45(-) and propidium iodide(-) (**Figure 3.7C**). TRAIL liposomal therapy reduced total viable CTC counts by 58% compared to control liposomes, and over 32% compared to oxaliplatin after just 4 h in circulation (**Supplementary Figure 3.17**). Notably, in two patients (P10 and P11), there were no detectable viable CTCs in blood samples treated with TRAIL liposomes. When categorizing patients by location of metastasis, patients that presented with metastases in the liver or bone showed a greater reduction in viable CTCs (69% and 71%, respectively) than patients with both lung and liver metastases (32%) (**Figure 3.7D**). Patients had similar CTC reductions regardless of their treatment at the time of blood draw, while those undergoing FOLFOX or capecitabine + oxaliplatin had the highest reduction in CTCs (65% and 60%, respectively) (**Figure 3.7E**). When categorizing patients as either oxaliplatin-sensitive or resistant, based on their response to 5 μM oxaliplatin under hematogenous circulatory-shear conditions (threshold 80% CTC viability), there was no significant difference in CTC response to TRAIL liposomes (**Supplementary Figure 3.18A**). Likewise, grouping patients by those undergoing oxaliplatin chemotherapy and those who had failed oxaliplatin previously, there was no significant difference in reduction of viable CTCs from the administration of liposomal TRAIL (**Supplementary Figure 3.18B**). This demonstrates the utility of TRAIL liposomes to eradicate CTCs in both oxaliplatin-sensitive and oxaliplatin-resistant patients.

3.3.8 CTC DR4-lipid raft colocalization corresponds with TRAIL liposome treatment efficacy and oxaliplatin resistance

Patient CTCs were also stained for DR4 and lipid rafts to examine the relationships between raft colocalization, treatment efficacy and oxaliplatin resistance. Decreasing lipid raft colocalization with DR4 coincided with reduced efficacy of TRAIL liposomes (higher percentage of viable CTCs after treatment), with a negative slope that significantly deviated from zero (**Figure 3.7F)**. Additionally, increasing lipid raft DR4 corresponded with increasing resistance to oxaliplatin (higher percentage of viable CTCs after oxaliplatin treatment), with a positive slope that significantly deviated from zero (**Figure 3.7G)**. These same trends were observed for total DR4 area (**Supplementary Figure 3.18C-D**). Despite the small size of the patient cohort, these results are encouraging and support our *in vitro* data in OxR cell lines. Five patients provided multiple blood samples over the course of their treatment, as shown in **Table 3.1.** Of these, P07 was the only patient being treated with oxaliplatin (FOLFOX) over the course of all three blood draws. Patient 7 was undergoing the 1st cycle of FOLFOX at the time of draw one and progressed while on FOLFOX for draws two and three. However, DR4 and lipid raft staining of CTCs revealed increased DR4/LR colocalization despite progression (**Figure 3.7H**). This same trend of enhanced CTC DR4/LR colocalization with treatment was observed in patients undergoing 5FU+Avastin (P01) and FOLFIRI (P09), while P06 (FOLFIRI) exhibited a bimodal response

(**Supplementary Figure 3.18E**). Interestingly, P12 exhibited decreased colocalization in CTCs over the course of treatment. This is hypothesized to be a result of a switch in treatment (FOLFIRI + Avastin to cetuximab + encorafenib) due to progression after the first draw.

Patient	Age	Sex	Cancer	Metastatic Location	Treatment History at Draw 1	Draw 2	Draw 3
P01	59	F	Colon	Paraaortic Lymph Nodes	# FOLFOX (2016), FOLFIRI, 5-FU+Avastin	+2months 5-FU+Avastin	* +7months 5-FU+Avastin
P02	83	F	Colon	Liver	# FOLFOX, FOLFIRI, FOLFOX+Avastin		
P04	53	F	Rectal	Pelvis, mesenteric lymph nodes	FOLFOX+Avastin, Capecitabine+Radtiaion, Regorafenib+ Nivolumab		
P05	68	M	Rectal	Pulmonary	Capecitabine+Oxaliplatin		
P06	68	F	Rectal	Lung, bone	FOLFOX, FOLFIRI	+6months FOLFIRI	+7months FOLFIRI
P07	64	M	Cecum	Peritoneal Carcinomatosis	FOLFOX (1st cycle)	+7months FOLFOX (progression)	+10months FOLFOX (progression) Started FOLFIRI
P08	69	M	Colon	Lung, abdomen	FOLFOX+Avastin (progression) Capecitabine+Avastin, 5FU+Cetuximab+ Panitumumab		
P09	73	M	Sigmoid	Liver, mesentery	FOLFOX, Capecitabine, FOLFIRI, Lonsurf	+7months FOLFIRI	N/A (patient deceased)
P10	52	M	Rectal	Lung	Radiation+ Capecitabine Capecitabine+Oxaliplatin		
P11	70	M	Colon	Liver	FOLFOX		
P12	59	M	Colon	Liver, lungs, R adrenal	FOLFOX+Avastin, FOLFIRI +Avastin	cetuximab + encorafenib (progression)	+3 months cetuximab + encorafenib (progression)
P13	63	F	Colon	Adnexa Pelvis	FOLFOX, Irinotecan+Panitumumab, Capecitabine+Oxaliplatin		
P15	79	M	Colon	Liver	FOLFOX (1st cycle)		

Table 3.1. Demographic and clinical information of metastatic CRC patients enrolled in this study. *Denotes missing treatment analysis for this sample. #Denotes missing DR4/LR analysis for this sample.

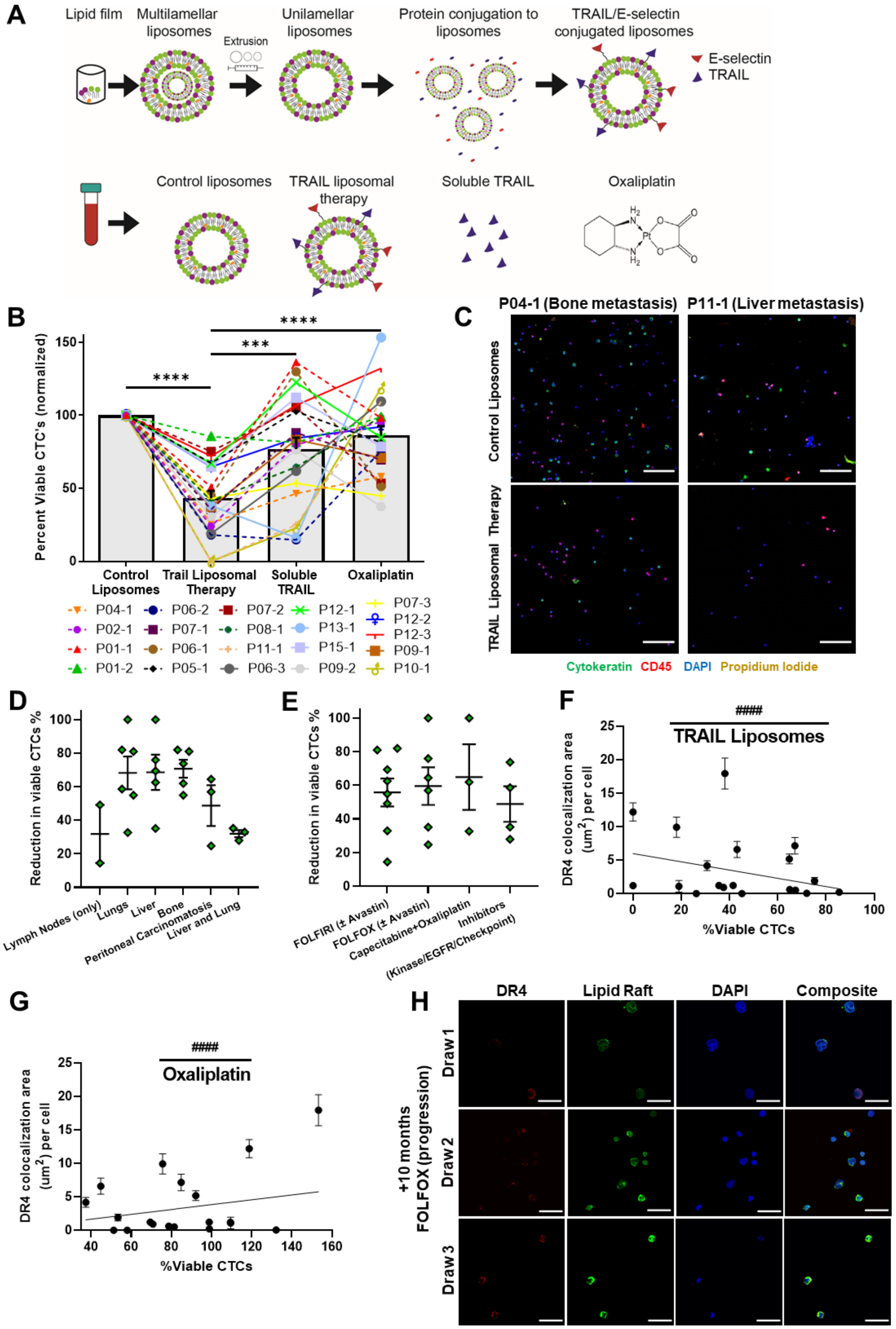
A
Lipid film
Multilamellar liposomes
Extrusion
Unilamellar liposomes
Protein conjugation to liposomes
TRAIL/E-selectin conjugated liposomes
E-selectin
TRAIL
Control liposomes
TRAIL liposomal therapy
Soluble TRAIL
Oxaliplatin
B
Percent Viable CTC's (normalized)
150
100
50
0
****
***
****
Control Liposomes
Trail Liposomal Therapy
Soluble TRAIL
Oxaliplatin
P04-1
P02-1
P01-1
P01-2
P06-2
P07-1
P06-1
P05-1
P07-2
P08-1
P11-1
P06-3
P12-1
P13-1
P15-1
P09-2
P07-3
P12-2
P12-3
P09-1
P10-1
C
P04-1 (Bone metastasis)
P11-1 (Liver metastasis)
Control Liposomes
TRAIL Liposomal Therapy
Cytokeratin
CD45
DAPI
Propidium Iodide
D
Reduction in viable CTCs %
100
80
60
40
20
0
Lymph Nodes (only)
Lungs
Liver
Bone
Peritoneal Carcinomatosis
Liver and Lung
E
Reduction in viable CTCs %
FOLFIRI (± Avastin)
FOLFOX (± Avastin)
Capecitabine+Oxaliplatin
Inhibitors (Kinase/EGFR/Checkpoint)
F
####
TRAIL Liposomes
DR4 colocalization area (um^2) per cell
25
20
15
10
5
0
0
20
40
60
80
100
%Viable CTCs
G
####
Oxaliplatin
DR4 colocalization area (um^2) per cell
40
60
80
100
120
140
160
%Viable CTCs
H
DR4
Lipid Raft
DAPI
Composite
+10 months FOLFOX (progression)
Draw 1
Draw 2
Draw 3

Figure 3.7. TRAIL-conjugated liposomes neutralize CTCs from the blood of patients with metastatic, oxaliplatin-resistant colorectal cancer. (A) Liposomes were synthesized using a thin film hydration method, followed by extrusion and his-tag conjugation of TRAIL and E-selectin protein. Patient blood samples were treated in a cone-and-plate viscometer under circulatory shear conditions with either control liposomes, TRAIL liposomes, soluble TRAIL, or oxaliplatin. **(B)** Effects of TRAIL liposomes and control treatments on the number of viable CTCs, normalized to control liposome treatment. Bars represent the average of all patients and time points. (N=21) **p<0.001 ****p<0.0001 (ordinary one-way ANOVA–Tukey's multiple comparison test). **(C)** Representative micrographs of 2 patients showing neutralization of CTCs in TRAIL liposomes compared to control liposomes, stained for cytokeratin (green), DAPI (blue), CD45 (red), and propidium iodide (yellow). Scale bar = 100 µm. **(D, E)** Reduction in viable CTCs categorized by location of metastasis and treatment administered at the time of blood draw, respectively. **(F)** DR4/LR colocalization area of patient CTCs plotted against the percentage of viable CTCs following TRAIL liposome treatments. Each point corresponds with one patient draw. $^{\#\#\#\#}$p<0.0001 (simple linear regression to confirm significant deviation from zero). **(G)** DR4/LR colocalization area of patient CTCs plotted against the normalized percentage of viable CTCs following oxaliplatin treatment. Each point corresponds with one patient draw. $^{\#\#\#\#}$p<0.0001 (simple linear regression to confirm significant deviation from zero). **(H)** CTCs of Patient 7, stained for DR4 (red) and lipid rafts (green), demonstrating increased DR4/LR colocalization over the course of 10 months of FOLFOX treatment (with progressive disease despite treatment). Scale bar = 30 µm. For all graphs, data are presented as mean±SEM.

3.4 Discussion

Our lab has demonstrated the utility of TRAIL nanoparticles to treat a variety of cancer types *in vitro* [270], *in vivo* [271], and in clinical samples [269]. While frontline chemotherapy remains a viable option for patients with metastatic CRC, long term treatment frequently leads to chemoresistance, consequently yielding a more aggressive, robust phenotype that is unresponsive to many systemic treatments [241]. Our results demonstrate that OxR colorectal cancer cells are particularly susceptible to TRAIL-mediated apoptosis. Additionally, the ability to eradicate over 57% of oxaliplatin-resistant CTCs in patient blood demonstrates the utility of TRAIL liposomes clinically. Moreover, two patient samples exhibited 100% neutralization of all viable CTCs following *ex vivo* TRAIL liposomal treatment. This demonstrates the natural cancer cell targeting ability and low toxicity of TRAIL-based therapeutics, presenting a promising cancer management strategy for patients who have exhausted traditional treatment modalities. TRAIL's apoptotic affect has been shown to be sensitized by circulatory shear stress, further supporting its use as an anti-metastatic therapy in the blood of patients [272]. Multiple other studies have demonstrated that platin-based chemotherapeutics, including oxaliplatin, are able to sensitize cancer cells to TRAIL-mediated apoptosis when treated in combination [63,245,251,252]. However, no study has investigated the effects of oxaliplatin resistance on TRAIL-mediated apoptosis, and importantly, no study has demonstrated that oxaliplatin-resistant cancers can be exploited with TRAIL therapies.

Elucidating the mechanisms that drive OxR TRAIL sensitization will be key in establishing personalized treatment strategies in patients. Interestingly, genetic analysis of TRAIL-sensitized OXR cells demonstrated that OxR cells consistently exhibited downregulated caspase-10. This may seem counterintuitive generally since caspase-10 is a caspase-8 analog that initiates the apoptotic pathway after binding to FADD. However, studies have demonstrated the potential anti-apoptotic effects of high caspase-10 expression [273,274]. One recent study in particular demonstrated that upon activation with Fas ligand, caspase-10 reduced DISC association and activation of caspase-8, rewiring DISC signaling toward the NF-κB pathway and cell survival [275]. However, this non-canonical caspase-10 signaling was found to have an insignificant effect on TRAIL sensitization as evidenced in experiments where caspase-10 was depleted in parental cells. This establishes that the observed augmentation of TRAIL sensitivity is likely a result of a translational or post-translational effect induced by oxaliplatin resistance, rather than a transcriptional change within the apoptotic pathway.

We have demonstrated that augmentation of death receptors, particularly DR4, in oxaliplatin resistant cells is one of the drivers of enhanced sensitization. One study found that cisplatin and 5-FU resistant side populations of colon cancer cells had upregulated DR4, consistent with our results [64]. While microscopy data suggest that DR5 is upregulated in TRAIL-sensitized oxaliplatin-resistant cell lines, DR5 area per cell was considerably lower than DR4. Additionally, conflicting western blot and flow cytometry data make the case for DR5 augmentation in OxR cells less convincing. Treatment with the DR4 agonist antibody Mapatumumab validated the role of DR4 in the TRAIL-sensitization of OxR cells, as the differential treatment responses were analogous to that observed from TRAIL treatment. Interestingly, DR4 augmentation appears to be independent from transcriptional upregulation, as there was no significant change in mRNA expression between OxR and parental cell lines. Increasing evidence demonstrates that chemoresistance affects small non-coding microRNA (miRNA) expression, which modulates transcriptional and translational processes [261,262]. More specifically, studies have shown that oxaliplatin treatment and subsequent resistance in colorectal cancer cells alter miRNA expression, affecting signaling pathways within p53, epithelial-to-mesenchymal transition, and cell migration [257,276,277]. Moving forward, future studies should examine the role of miRNA attenuation post-oxaliplatin resistance on the expression of death receptors, particularly DR4.

While sufficient DR4 expression is important for sustained apoptotic signaling, DR4 localization and compartmentalization within lipid rafts is unequivocally vital. Lipid rafts enhance the signaling capacity of surface receptors through a multitude of mechanisms [84]. For example, LRs promote death receptor trimerization which is needed for signal transduction, act as concentrating platforms for DISC assembly and the recruitment of death domains, and protect DRs from internalization or enzymatic degradation [98]. Additionally, juxtaposition of multiple DR trimers forms supramolecular entities, recently termed "CASMER" [248], capable of multivalent TRAIL signaling via extracellular pre-ligand assembly domains (PLADs) [250]. Altering raft integrity via cholesterol sequestration using nystatin had profound impacts on reducing TRAIL sensitization within the OxR phenotype. Moreover, raft stabilization with resveratrol was able to enhance TRAIL sensitization within the parental phenotype, mirroring that observed in OxR cells. These changes in sensitivity were confirmed to coincide specifically with enhanced clustering of DR4 within rafts. These results are consistent with other studies which have shown that pharmacological alterations of lipid rafts have profound impacts on Fas and TRAIL toxicity [249,278]. Other studies have demonstrated that DR4 localization into lipid rafts is obligatory for TRAIL-induced apoptosis in hematological malignancies and non-small cell lung cancer, whereas DR5 has no dependence on raft translocation [247,250,279,280], consistent with our correlative data and receptor contents from lipid raft isolated membrane fractions. Additionally, one study found that oxaliplatin combination treatment with TRAIL in gastric cancer cells enhances apoptotic signaling through casitas B-lineage lymphoma (CBL) regulation and death receptor redistribution into lipid rafts [254]. While it is evident that rafts promote CASMER formation, death receptor oligomerization, and TRAIL-mediated apoptosis, the mechanism linking the oxaliplatin-resistant phenotype and enhanced DR4 localization within rafts has yet to be studied.

We have demonstrated that a mechanism for this phenomenon is via enhanced DR4 palmitoylation. Palmitoylation is the post-translational covalent attachment of a fatty acid tail to cysteine residues in the protein transmembrane domain, influencing protein trafficking and signaling. There is evidence that both Fas receptor and DR4 are palmitoylated, while DR5 is not [267,281]. Furthermore, this post-translational modification has proven to be mandatory for DR4 oligomerization, lipid raft localization, and TRAIL-mediated apoptotic signaling [267]. Interestingly, in a sensory neuron study in rats, palmitoylation of δ-Catenin in dorsal root ganglion was significantly increased after chronic oxaliplatin treatment [282]. This is analogous to our results, as oxaliplatin-resistant colorectal cancer cells that have undergone chronic oxaliplatin treatment exhibited a higher percentage of palmitoylated DR4. Inhibiting palmitoylation with 2BP abrogated the TRAIL sensitizing effects within OxR cells, demonstrating the mandatory role palmitoylation has on DR4-mediated TRAIL signaling. Additionally, the fact that palmitoylation is inherent to DR4 and not DR5 explains why TRAIL sensitization of oxaliplatin-resistant cells strongly correlated with lipid raft translocation of DR4, but not DR5. Further studies probing the differences in palmitoylation between parental and OxR phenotypes are warranted to provide a more detailed understanding of oxaliplatin-induced palmitoylation of specific membrane proteins.

We have also shown that these results translate clinically, as DR4 expression and lipid raft colocalization of patient CTCs coincided with increased oxaliplatin resistance and increased neutralization of CTCs from TRAIL liposome treatment. Additionally, some metastatic CRC patients exhibited increased DR4/LR colocalization with ongoing chemotherapy cycles despite metastatic progression and worsening prognosis. To our knowledge, this is the first study investigating lipid raft/protein interactions in primary CTCs [84]. Overall, our results demonstrate a novel mechanism for TRAIL sensitization in chemoresistant colorectal cancer cells via death receptor upregulation and localization within lipid rafts. However, since this sensitization was only observed in two of the four CRC cell lines tested, future studies should investigate genetic and phenotypic differences between these cell lines that may make some more susceptible than others to DR4 palmitoylation, augmentation, and localization. For the scope of this study, we chose to focus on the use of TRAIL treatment alone given its low toxicity and given our previous work in engineering TRAIL-conjugated delivery vehicles. However, since patients are treated with combination therapies, it would be valuable to investigate other therapeutics, such as curcumin or oxaliplatin, that synergize with TRAIL to treat oxaliplatin-resistant cancer cells [60,244]. Additionally, future studies should examine the TRAIL sensitization of oxaliplatin-resistant cells *in vivo* in orthotopic models of colorectal cancer metastasis [283]. Examining the efficacy of TRAIL and TRAIL-conjugated nanoparticles to curb metastasis of oxaliplatin-resistant cells in humanized mouse models will provide translational evidence to support the mechanisms elucidated in this study. Moving forward, leveraging the enhanced signaling of death receptors in lipid rafts through mechanisms of drug delivery and lipid raft antagonization will be instrumental in therapeutic development for chemoresistant cancers.

3.5 Materials and Methods

Key Resources Table				
Reagent type (species) or resource	**Designation**	**Source or reference**	**Identifiers**	**Additional information**
cell line (*Homo-sapiens*)	SW620 Adenocarcinoma, Colorectal, Dukes' type C	ATCC	#CCL-227	RRID:CVCL_0547 L15 Media

cell line (*Homo-sapiens*)	SW480 Adenocarcinoma, Colorectal, Dukes' type B	ATCC	#CCL-228	RRID:CVCL_0546 L15 Media
cell line (*Homo-sapiens*)	HT29 Adenocarcinoma, Colorectal	ATCC	#HTB-38	RRID:CVCL_0320 McCoy's 5a Media
cell line (*Homo-sapiens*)	HCT116 Carcinoma, Colorectal	ATCC	#CCL-247	RRID:CVCL_0291 McCoy's 5a Media
cell line (*Homo-sapiens*)	SW620 OxR Adenocarcinom,Colorectal, Dukes' type C	Kobe Pharmaceutical University	#CCL-227	RRID:CVCL_4V77 L15 Media
cell line (*Homo-sapiens*)	SW480 OxR Adenocarcinoma, Colorectal, Dukes' type B	MD Anderson Cancer Center Characterized Cell Line Core	#CCL-228	RRID:CVCL_AU18 L15 Media
cell line (*Homo-sapiens*)	HT29 OxR Adenocarcinoma, Colorectal	MD Anderson Cancer Center Characterized Cell Line Core	#HTB-38	RRID:CVCL_ 5949 McCoy's 5a Media
cell line (*Homo-sapiens*)	HCT116 OxR Carcinoma, Colorectal	MD Anderson Cancer Center Characterized Cell Line Core	#CCL-247	RRID:CVCL_4V73 McCoy's 5a Media
chemical compound, drug	Oxaliplatin	MedChemExpress	Cat# HY-17371	CAS No: 61825-94-3
commercial assay or kit	MTT Assay Kit	Abcam	Cat# ab211091	
peptide, recombinant protein	Recombinant Human sTRAIL/Apo2L	PeproTech	Cat# 310-04	
antibody	Mouse Anti-TNFRSF10A Recombinant Antibody (clone mAY4)	Creative Biolabs	Cat# HPAB-1616-FY	Mapatumumab (0.01-10 ug/ml)
commercial assay or kit	FITC Annexin V Apoptosis Detection Kit I	BD Pharmingen	Cat# 556547	Includes Propidium Iodide
software, algorithm	FlowJo v10.7.1	FlowJo	RRID:SCR_008520	
commercial assay or kit	JC1 – Mitochondrial Membrane Potential Assay Kit	Abcam	Cat# ab113850	
commercial assay or kit	RNeasy Plus Mini Kit	Qiagen	Cat# 74134	
commercial assay or kit	RT2 First Strand Kit	Qiagen	Cat# 330404	
commercial assay or kit	RT2 Profiler PCR Human Apoptosis Array	Qiagen	Cat# PAHS-012Z	

software, algorithm	CFX Maestro Software	Bio-Rad	RRID:SCR_018064	
software, algorithm	GeneGlobe Data Analysis Center	Qiagen	RRID:SCR_021211	
commercial assay or kit	Gene Knockout Kit v2 – Human CASP10 with Cas9 2NLS Nuclease	Synthego		sgRNA:Cas9 (90pmol:10pmol)
commercial assay or kit	Vybrant Alexa Fluor 488 Lipid Raft Labeling Kit	Invitrogen	Cat# V34403	
commercial assay or kit	Vybrant Alexa Fluor 555 Lipid Raft Labeling Kit	Invitrogen	Cat# V34404	
antibody	Mouse anti-human CD261 (DR4) Monoclonal Antibody (clone DJR1)	Invitrogen	Cat# 14-6644-82	RRID:AB_468188 (1:50 IF)
antibody	Mouse anti-human CD262 (DR5) Monoclonal Antibody (Clone DJR2-4)	Invitrogen	Cat# 14-9908-82	RRID:AB_468592 (1:50 IF)
antibody	Alexa Fluor 555 goat anti-mouse IgG (H+L)	Invitrogen	Cat# A28180	RRID:AB_2536164 (1:1000 IF)
other	DAPI	Invitrogen	Cat# D1306	RRID:AB_2629482 (1 µg/mL)
software, algorithm	Fiji - ImageJ	FIJI		RRID:SCR_002285 JaCOP plugin
antibody	Human TruStain FcX	Biolegend	Cat# 422301	RRID:AB_2818986
antibody	PE mouse anti-human CD261 (DR4) (Clone DJR1)	Biolegend	Cat# 307206	RRID:AB_2287472 (5 µl per sample, FC)
antibody	PE mouse anti-human CD262 (DR5) (Clone DJR2-4)	Biolegend	Cat# 307406	RRID:AB_2204926 (5 µl per sample, FC)
antibody	PE mouse anti-human TRAILR3 (DcR1) (Clone DJR3)	Biolegend	Cat# 307006	RRID:AB_2205089 (5 µl per sample, FC)
antibody	PE mouse anti-human TRAILR4 (DcR2) (Clone 104918)	Biolegend	Cat# FAB633P	RRID:AB_2205217 (5 µl per sample, FC)
antibody	PE Mouse IgG1 κ Isotype Control (clone MOPC-21)	Biolegend	Cat# 400114	RRID:AB_326435 (5 µl per sample, FC)
antibody	FITC mouse anti-human DR4 (Clone DR-4-02)	Thermo Fisher Scientific	Cat# MA1-19757	RRID:AB_1955203 (5 µl per sample, FC)

chemical compound, drug	Resveratrol	Sigma-Aldrich	Cat# R5010-100MG	RRID:AB_309682 CAS: 501-36-0
chemical compound, drug	Nystatin	Thermo Fisher Scientific	Cat# BP29495	CAS: 1400-61-9
chemical compound, drug	2- Bromopalmitate	Sigma-Aldrich	Cat# 21604-1G	CAS: 18263-25-7
antibody	Mouse Anti-Fas Antibody (human, neutralizing) (clone ZB4)	Sigma-Aldrich	Cat# 05-338	RRID:AB_309682 500 ng/ml (Neutralization)
commercial assay or kit	Minute™ Plasma Membrane-Derived Lipid Raft Isolation Kit	Invent Biotechnologies	Cat# LR-042	
antibody	DR4 Rabbit monoclonal antibody (clone D9S1R)	Cell Signalling Technologies	Cat# 42533	RRID:AB_2799223 (1:500 WB)
antibody	DR5 Rabbit polyclonal antibody	Thermo Fisher Scientific	Cat# PA1-957	RRID:AB_2303474 (1:500 WB)
antibody	Caspase-10 Rabbit polyclonal antibody	Thermo Fisher Scientific	Cat# PA5-29649	RRID:AB_2547124 (1:1000 WB)
antibody	Mouse anti-human GAPDH (clone 6C5)	Millipore Sigma	Cat# MAB374	RRID:AB_2107445 (1:2000 WB)
antibody	Mouse Anti-β-Actin monoclonal antibody (clone C4)	Santa Cruz	Cat# sc-47778	RRID:AB_2714189 (1:1000 WB)
antibody	IRDye 800CW goat anti-rabbit secondary antibody	LICOR	Cat# 926-32211	RRID:AB_621843 (2:15000 WB)
antibody	IRDye 800CW goat anti-mouse secondary antibody	LICOR	Cat# 926-32210	RRID:AB_621842 (2:15000 WB)
software, algorithm	LICOR housekeeping protein normalization protocol	LICOR Odyssey Fc	RRID:SCR_013715	
commercial assay or kit	SiteCounter™ S-Palmitoylated Protein Kit	Badrilla	Cat# K010312	
commercial assay or kit	EZClick™ Palmitoylated Protein Assay Kit	BioVision	Cat# K416-100	
commercial assay or kit	CD45 magnetic beads (human)	Mylteni Biotech	Cat# 130-045-801	
antibody	Biotin mouse anti-human CD45 Antibody (Clone HI30)	Biolegend	Cat# 304004	RRID:AB_314392 (1:50 IF)
antibody	Streptavidin-conjugated Alexa Fluor 647	Thermo Fisher Scientific	Cat# S21374	RRID:AB_2336066 (1:200 IF)

antibody	FITC Mouse Anti-Human Cytokeratin (Clone CAM5.2)	BD Pharmingen	Cat# 347653	(20 µl per sample, IF)
antibody	Goat anti-mouse Alexa Fluor 647	Thermo Fisher Scientific	Cat# A21235	RRID:AB_2535804 (1:200 IF)

Table 3.2. List of key resources and materials.

3.5.1 Cell Culture

Colorectal cancer cell lines SW620 (ATCC, #CCL-227), SW480 (ATCC, #CCL-228), HCT116 (ATCC, #CCL-247), and HT29 (ATCC, #HTB-38), were purchased from American Type Culture Collection. SW620 and SW480 cells were cultured in Leibovitz's L-15 cell culture medium (Gibco). HCT116 and HT29 cells were cultured in McCoy’s 5A cell culture medium (Gibco). Media was supplemented with 10% (v/v) fetal bovine serum and 1% (v/v) PenStrep, all purchased from Invitrogen. SW480 OxR, HCT116 OxR and HT29 OxR cells were obtained from MD Anderson Cancer Center Characterized Cell Line Core, supplied and generated by the Dr. Lee Ellis laboratory. SW620 OxR cells were obtained from Dr. Mika Hosokawa at Kobe Pharmaceutical University in Japan. Oxaliplatin-resistant derivative cell lines were cultured in the same medium as their parental counterparts. To prevent phenotypic drift of OxR lines, cells were used within 6 passages from the time they were received. To prevent chemotherapy-induced cytotoxicity in downstream experiments, oxaliplatin was not supplemented in OxR cell culture media. All cell lines were maintained in a humidified incubation chamber at 37°C and 5% CO_2. All cell lines were screened for mycoplasma contamination and tested negative.

3.5.2 MTT Assay

SW620, SW620 OxR, HCT116, HCT116 OxR, HT29, HT29 OxR, SW480 and SW480 OxR cell lines were plated into tissue culture 96-well black-walled plates, at a concentration of 3,000 cells/well and incubated overnight at 37°C. A 10mM stock oxaliplatin suspension was created by dissolving oxaliplatin (MedChemExpress) in molecular grade water via sonication and heating. Cell culture media was replaced with oxaliplatin treatments ranging from 0-1000µM and incubated for 72 h. Following treatments, an MTT assay (Abcam) was carried out according to the manufacturer’s protocol. The plates were then read using a plate reader (BioTek µQuant) at 590nm absorbance using gen5 software. Control wells containing the MTT solution without cells were used for background subtraction.

3.5.3 Transwell Assay

Transwell inserts (6-well with 8 µm pores) (Greiner Bio-one) were evenly coated with 75 µL of a 1 mg/mL collagen solution composed of 3 mg/mL rat tail collagen (Gibco), serum free media, and 0.2% 1N NaOH for crosslinking. Inserts were incubated for 20 min at 37°C. After crosslinking, 2.5 mL of 10% FBS media was added to the bottom of the well plate while the top was filled with 1 mL of serum free media until cells were ready for seeding. Parental and oxaliplatin-resistant SW480, SW620, HT29, HCT116 cells were seeded in the collagen-coated inserts at a concentration of 200,000 cells/mL in serum-free media. The transwell inserts were replaced with new serum-free media after two days. On day four, the number of cells that had migrated into the bottom plate were counted using a Thermo Fisher Countess II Automated Cell Counter.

3.5.4 Annexin-V/PI Apoptosis Assay

Parental and OxR cell lines were plated at 100,000 cells/well onto 24-well plates and incubated overnight at 37°C. Wells were treated in triplicate with soluble human TRAIL (PeproTech) or treated with the anti-DR4 agonist antibody Mapatumumab (Creative Biolabs, clone mAY4) and incubated for 24 h. All cells were collected by recovering the supernatant and lifting the remaining adhered cells using 0.25% Trypsin-EDTA (Gibco). Cells were washed thoroughly with HBSS with calcium and magnesium (Gibco). Cells were incubated for 15 min with FITC-conjugated Annexin-V and propidium iodide (PI) (BD Pharmingen) at room temperature (RT) in the absence of light and immediately analyzed using a Guava easyCyte 12HT benchtop flow cytometer (MilliporeSigma). Viable cells were identified as being negative for both Annexin-V and PI, early apoptotic cells as positive for Annexin-V only, late apoptotic cells were positive for both Annexin-V and PI, and necrotic cells were positive for PI only. Flow cytometry plots were analyzed using FlowJo v10.7.1 software. Control samples included: unstained negative control with no Annexin-V/PI to adjust for background and autofluorescence, and Annexin V only and PI only samples for gating apoptotic and necrotic populations.

The change in cell viability in response to TRAIL treatments between parental and OxR cells for each of the four CRC cell lines was calculated using the following TRAIL Sensitization equation:

$$\text{TRAIL Sensitization} = \frac{(\%\text{Viable Parental Cells}) - (\%\text{Viable OxR Cells})}{(\%\text{Viable Parental Cells})} * 100\%$$

where the percentage of viable cells was normalized to untreated controls for each trial. TRAIL sensitization was calculated for each concentration of TRAIL, where the “Maximum TRAIL Sensitization” was the highest sensitization observed among all concentrations. Since this sensitization equation is based on a percent reduction formula, small changes in viability can yield large TRAIL sensitizations when cell viability is low. To account for this, both cell viability and TRAIL sensitization are reported to provide a complete perspective on treatment responses between cell lines.

3.5.5 JC-1 (Mitochondrial Membrane Potential) Assay

SW620 and HCT116 cells (parental and OxR) were plated at 100,000 cells/well onto 24-well plates and incubated overnight. Cells were treated in triplicate with TRAIL for 24 h. Following treatment, cells were collected, washed thoroughly with HBSS without calcium and magnesium, and incubated for 15 min with JC-1 dye (Abcam) in accordance with the manufacturer’s protocol. JC-1 fluorescence was assessed via flow cytometry. Cells with healthy mitochondria were identified as having higher red fluorescence while those with depolarized mitochondria had lower red JC-1 fluorescence.

3.5.6 RT-PCR Profiler Array

2×10^6 SW620 and HCT116 (parental and OxR) cells were seeded into a 100 mm diameter cell culture dish for 24 h. Cells were lifted using a cell scraper and washed with HBSS with calcium and magnesium. RNA was isolated using the RNeasy Plus Mini Kit (Qiagen) according to the manufacturer’s protocol. RNA yield following isolation was determined using a UV5Nano spectrophotometer (Mettler Toledo). cDNA synthesis was completed using the RT^2 First Strand Kit (Qiagen, 330404) using 0.5µg RNA per sample. RNA expression of 84 apoptotic genes was analyzed using the RT2 Profiler PCR Human Apoptosis Array (Qiagen, PAHS-012Z). Arrays were prepared according to the manufacturer’s protocols applied to the prepared cDNA samples. Profiler array plates were run on a CFX96 Touch Real Time PCR (Bio-Rad) using the following protocol: 1 cycle for 10 min at 95°C, 40 cycles of 95 °C for 15 s followed by 60°C for 60 s at a rate of 1°C/s. Melt curves were generated immediately following the PCR protocol. Cycle threshold (Ct) values were calculated using CFX Maestro Software (Bio-Rad). Data analysis was completed using the GeneGlobe Data Analysis Center (Qiagen). Volcano plots were generated in GraphPad Prism using calculated fold changes in gene expression between OxR and parental cells and their corresponding p-values.

3.5.7 CRISPR-Cas9 Knockout

Knockout of the CASP10 gene in SW620 cells was completed using the Gene Knockout Kit v2 – Human CASP10 kit with Cas9 2NLS Nuclease (Synthego). Ribonucleoprotein (RNP) complexes were made at a 9:1 ratio of sgRNA:Cas9 (90pmol:10pmol) in Gene Pulser® Electroporation Buffer (Bio-Rad, 1652677) and incubated for 10 min at RT. Cas9 control samples consisted of 10 pmol Cas9 with no sgRNA. RNP complexes were added to 200,000 cells in 200µL electroporation buffer (0.2 cm cuvette) and electroporated via the Gene Pulser Xcell™ Electroporation System (Bio-Rad) using exponential decay pulses (145V, 500µF, 1000ohm). Cells were immediately cultured in 12-well plates and allowed to recover for 7 days before measuring knockout efficiency.

3.5.8 Confocal Microscopy and Image Analysis

Parental and OxR cells were seeded onto polystyrene cell culture slides (Thermo Fisher Scientific). Cells were allowed to grow for 48 h at 37°C. In samples treated with nystatin or resveratrol, cells were plated for 24 h then treated for 24 h before staining. Cells were washed and lipid rafts were stained using the Vybrant Alexa Fluor 488 Lipid Raft Labeling Kit (Invitrogen, V34403) according to the manufacturer's protocol. Briefly, cells were incubated with Alexa488-conjugated cholera toxin subunit B (CT-B) followed by an anti-CT-B antibody to crosslink CT-B labeled rafts. Slides were fixed for 15 min with 4% paraformaldehyde (PFA) (Electron Microscopy Sciences) in PBS (Gibco) and then permeabilized using 1% Triton X-100 (MilliporeSigma) in PBS at RT. Slides were blocked for 2 h with 5% goat serum (Thermo Fisher Scientific) and 5% bovine serum albumin (BSA, Sigma) in HBSS. Primary staining was done overnight at 4°C with either DR4 monoclonal antibody (Invitrogen, Clone DJR1) or DR5 monoclonal antibody (Invitrogen, Clone DJR2-4) in the blocking serum at a ratio of 1:50. Secondary staining was carried out with Alexa Fluor 555 goat anti-mouse IgG (H+L) (Invitrogen, A28180) for 30 min at RT (1:1000). Slides were stained with DAPI (Invitrogen, D1306) for 30 min at RT in the blocking solution at 1:1000. Washes were done twice between each step for 5 min each using 0.02% Tween20 in PBS. Slides were assembled using 10 µl of Vectrashield antifade mounting media (Vector Laboratories). Confocal imaging was performed using an LSM 880 (Carl Zeiss) with a 63x/1.40 Plan-Apochromat Oil, WD = 0.19 mm objective. At least five images were taken per sample.

Image analysis was performed in FIJI using a macro to automate quantification of raft and DR contents per cell. Briefly, all images were adjusted for background using the same thresholding specifications. The "analyze particles" feature was used to quantify the total area of lipid rafts and DR per outlined cell. Colocalization events were quantified by creating binary masks of DR and lipid raft events. For each gated cell, the lipid raft and DR binary masks were multiplied to create a binary projection of colocalized events. Raw integrated density and cell area (ROI area) were also measured. Cells with areas outside of three times the standard deviation from the mean were considered outliers and not included in the analysis. Colocalization analysis was also performed using the JACoP plugin in FIJI [284]. The Manders' Correlation Coefficient was calculated as the fraction of lipid raft colocalized DR4.

3.5.9 Flow Cytometry

Surface DR Expression

Parental and OxR cell lines were cultured to 70% confluency upon collection and split into 250,000 cells per sample. Cells were fixed in 4% PFA in HBSS for 15 min at RT, then blocked in a 100 µL 1% BSA solution for 30 min at 4°C, with 2X HBSS washes between each step. Cells suspensions of 100 µL were incubated for 15 min at RT with 2 µL Human TruStain FcX (Biolegend, 422301) to prevent nonspecific Fc receptor binding. Samples were immediately stained with 5µL of either PE anti-human CD261 (DR4) (Biolegend, Clone DJR1), PE anti-human CD262 (DR5) (Biolegend, Clone DJR2-4), PE anti-human TRAILR3 (DcR1) (Biolegend, Clone DJR3), PE anti-human TRAILR4 (DcR2) (R&DSystems, Clone 104918) or PE Mouse IgG1 κ Isotype Control (Biolegend, Clone MOPC-21) for 30 min at 4°C. Samples were washed twice with HBSS and analyzed using a Guava easyCyte flow cytometer. A chi-squared test was performed using FlowJo v10.7.1, where significance in histogram distribution was confirmed if T(x) between parental and OxR stained samples was greater than T(x) between background (unstained) parental and OxR samples (see **Supplementary Table 3.1**).

FRET

Cells were prepared as described above, but without fixation or permeabilization. Samples were stained for lipid rafts using the Vybrant Alexa Fluor 555 Lipid Raft Labeling Kit (Invitrogen, V34404). Samples were then stained with 5 µL FITC anti-human DR4 (Thermo Fisher Scientific, Clone DR-4-02) for 30 min at 4°C. Samples were washed twice with HBSS and analyzed using a Guava easyCyte flow cytometer. Donor quenching FRET efficiency was calculated using the following formula:

$$\mathrm{E} = 1 - \frac{\mathrm{FI}_{\mathrm{LR+DR}} - \mathrm{FI}_{\mathrm{B}}}{\mathrm{FI}_{\mathrm{DR}} - \mathrm{FI}_{\mathrm{B}}}$$

Where E is the FRET efficiency, $\mathrm{FI_{LR+DR}}$ is the mean fluorescence intensity of the double stained lipid raft/DR4 sample (acceptor + donor), $\mathrm{FI_{DR}}$ is the mean fluorescence intensity of the DR4 only stain (donor only) and $\mathrm{FI_B}$ is the fluorescence intensity of an unstained sample (background). Fluorescence intensity was recorded in the donor (FITC) channel.

3.5.10 TRAIL Combination Treatments

Resveratrol

Parental SW620 and HCT116 cells were plated at 100,000 cells/well onto 24-well plates and incubated overnight at 37°C. Cells were treated with 70 µM resveratrol (Sigma) in combination with 0.1-1000 ng/ml of TRAIL for 24 h. Following treatment, cells were collected for Annexin-V/PI apoptosis assay. TRAIL sensitization was calculated using the following equation:

$$\text{TRAIL Sensitization}_{resveratrol} = \frac{(\%\text{Viable Parental Cells}) - (\%\text{Viable Parental Cells}_{\text{+resv}})}{(\%\text{Viable Parental Cells})} * 100\%$$

where TRAIL + resv treatments were normalized to resveratrol treatment in the absence of TRAIL to account for any resveratrol-associated cytotoxicity.

Nystatin

SW620 OxR and HCT116 OxR cells were plated at 100,000 cells/well onto 24-well plates and incubated overnight at 37°C. Cells were treated with 5 µM nystatin (Thermo Fisher Scientific) in combination with 0.1-1000 ng/ml of TRAIL. Following treatment, cells were collected for Annexin-V/PI apoptosis assay. TRAIL sensitization was calculated using the following equation:

$$\text{TRAIL Sensitization}_{\text{nystatin}} = \frac{\left(\%\text{Viable OxR Cells}_{\text{+nys}}\right) - (\%\text{Viable OxR Cells})}{(\%\text{Viable OxR Cells}_{\text{+nys}})} * 100\%$$

where TRAIL + nys treatments were normalized to nystatin treatment in the absence of TRAIL to account for any nystatin associated cytotoxicity.

2-Bromopalmitate

SW620 parental and OxR cells were plated at 100,000 cells/well onto 24-well plates and incubated overnight at 37°C. Cells were treated with 3.5 µM 2BP (Millipore Sigma) in combination with 0.1-1000 ng/ml of TRAIL. Following treatment, cells were collected for Annexin-V/PI apoptosis assay. TRAIL sensitization was calculated as described above.

Anti-Fas (ZB4)

SW620 OxR cells were plated at 100,000 cells/well onto 24-well plates and incubated overnight at 37°C. Cells were treated with 500 ng/ml human anti-Fas (Millipore Sigma, Clone ZB4) with and without 1000 ng/ml of TRAIL. Following treatment, cells were collected for Annexin-V/PI apoptosis assay. TRAIL sensitization was calculated as described above.

3.5.11 Western Blot

Lipid rafts were isolated according to manufacturer's protocol using the Minute™ Plasma Membrane-Derived Lipid Raft Isolation Kit (Invent Biotech, LR-042). Cell lysates and lipid raft protein isolates were prepared by sonication in 4x Laemmli sample buffer (Bio-Rad, 1610747) and then loaded into 10% SDS-polyacrylamide gels for electrophoresis. Protein transfer onto a PVDF membrane was carried out overnight, and then blocked with Intercept (TBS) Blocking Buffer (LICOR, 927-60001) at RT for an hour. Primary antibody incubation occurred overnight at 4ºC for DR4 (Cell Signaling Technology, 42533) and DR5 (Thermo Fisher Scientific, PA1-957) at 1:500 dilution and caspase-10 (Thermo Fisher Scientific, PA5-29649) at a 1:1000 dilution in LICOR buffer. Cell lysate protein bands were normalized to GAPDH (EMD Millipore, MAB347) at 1:2000 dilution, while lipid raft isolates were normalized to β-actin (Santa Cruz, 47778) at 1:1000 dilution in LICOR blocking buffer. Western blots were quantified using the Licor Odyssey Fc with IRDye 800CW goat anti-rabbit secondary antibody (LICOR, 926-32211) and IRDye 800CW goat anti-mouse secondary antibody (LICOR, 926-32210) at a dilution of 2:15000. Quantification was done following the LICOR housekeeping protein normalization protocol.

3.5.12 Palmitoylation Assay

Cells were grown to 70% confluency in a 100 mm tissue culture dish. Palmitoylation of DR4 was measured using the SiteCounter™ S-Palmitoylated Protein Kit (Badrilla, K010312) according to the manufacturer's protocol. Input fraction controls (IFC) were obtained prior to thioester cleavage. Acyl preservation negative controls (APC-) were obtained by using an acyl preserving reagent instead of mass-tag conjugation. Western blots were run for DR4 following the "Western Blot" protocol described above. The percentage of DR4 palmitoylation was calculated by dividing the total intensity of all palmitoylated bands (mass tag) divided by the average intensity of the IFC and APC(-) bands for that sample.

To measure the amount of total palmitoylated protein, cells were cultured in 96-well plates at a concentration of 20,000 cells/well. The EZClick™ Palmitoylated Protein Assay Kit (BioVision, K416-100) was used in accordance with the manufacturer's protocol. Cells were incubated overnight with either 1x EZClick™ Palmitic Acid label in media or culture media with no label (background control). Cells were recovered and stained using EZClick™ Fluorescent Azide, then analyzed via flow cytometry for shifts in FL2-H intensity. Median fluorescence intensity (MFI) was calculated by subtracting the background intensity from each sample (Palmitic Acid label [**-**]/ Fluorescent Azide [**+**]).

3.5.13 Patient Blood Samples

Peripheral whole blood samples of 10 mL were collected from 13 metastatic CRC patients after informed consent. Patient criteria for this study included the following: presenting with metastatic CRC at the time of blood draw and undergone (or undergoing) oxaliplatin-containing chemotherapy (i.e. FOLFOX). Additionally, 5 patients had samples collected through their respective chemotherapy regimens. De-identified blood samples were transported from the Guthrie Clinic to Vanderbilt University and processed within 24 h. Blood samples were split for treatment (8 ml) and death receptor/lipid raft staining (1-2 ml).

<u>Ex-vivo treatment of colorectal cancer patient blood samples</u>

For the treated samples, 2 mL of blood were treated with either 40 µL of control liposomes, 40µl TRAIL/E-selectin conjugated liposomes (290 ng/mL of TRAIL), 6 µL (290 ng/mL) of soluble TRAIL or 2 µL (5 µM) of oxaliplatin. Liposomes were synthesized using a thin film hydration method followed by extrusion and his-tag conjugation as described previously [270]. The aliquots were sheared for 4 h in a cone-and-plate viscometer (Brookfield) at a shear rate of 120 s^{-1}. Prior to incubation, the cone-and-plate viscometers were blocked using 5% BSA for 30 min. After 4 h, the blood aliquots were washed from the viscometer's spindle and cup by using twice the volume of HBSS without calcium and magnesium. Blood aliquots were placed over twice the volume of Ficoll (GE Healthcare) to separate out mononuclear cells within the buffy coat. CTCs were enriched using a negative selection kit with CD45 magnetic beads (Mylteni Biotech, 130-045-801) following the manufacturer's protocol [269].

The resulting isolated CTCs were placed in cell culture overnight using RPMI media supplemented with 10% FBS. After 1 day in culture, the cells were recovered from the tissue culture plate and stained with 100 µL of propidium iodide for 15 min. Cells were washed, fixed with 4% PFA and cytospun onto microscope slides using a Cytospin 3 (Shandon). Samples were then permeabilized and blocked with 100 µL of 0.25% Triton-X (Sigma) for 15 min and 100 µL of blocking solution (5% BSA and 5% goat serum) for 1 h, respectively. Cells were stained with anti-CD45 conjugated with biotin (Biolegend, Clone HI30) for 45 min at 1:50 dilution. Finally, cells were stained with 100 µL of streptavidin-conjugated Alexa Fluor 647 (Thermo Fisher Scientific, S21374) at 1:200 dilution and 20 µl per sample of anti-cytokeratin conjugated with FITC (BD Pharmingen, Clone CAM5.2) for 45 min. Cells were washed 3X after each staining incubation using 200 µL of 0.02% Tween20 in PBS. Cells were stained with 10 µL of DAPI mounting media (Vector Laboratories), covered with a coverslip (No. 1.5, VWR), and sealed with nail polish.

Five images per sample were taken at random locations using an LSM 710 (Carl Zeiss) with a 20x/0.8 objective. The cell number in the sample was scaled up by multiplying by the relative area (slide area/frame area). Viable tumor cells were identified using the following criteria: (i) positive for DAPI, (ii) negative for CD45, (iii) positive for cytokeratin and (iv) negative for propidium iodide.

<u>Staining of lipid raft and death receptors in primary CTCs</u>

CTCs from the remainder of the patient blood were isolated and cytospun onto slides as described above. Death receptors and lipid rafts were stained and analyzed as detailed above in "Confocal Microscopy and Image Analysis". Lipid rafts were stained using the Vybrant Alexa Fluor 555 Lipid Raft Labeling Kit (Invitrogen, V34404) after CTCs were spun onto slides. Secondary staining for DR4 and DR5 was completed using goat anti-mouse Alexa Fluor 647 (Thermo Fisher Scientific, A21235) at a 1:200 dilution. Cells were also stained with FITC-conjugated cytokeratin, as described above, to positively identify CTCs for analysis.

3.5.14 Statistical Analysis

Data sets were plotted and analyzed using GraphPad Prism 9. When comparing two groups, a symmetric unpaired t-test was used with $p < 0.05$ considered significant. One-way ANOVA with multiple comparisons was used for multiple groups with $p < 0.05$ considered significant. At least three independent biological replicates were used for each experiment unless otherwise stated.

3.6 Supplementary Figures

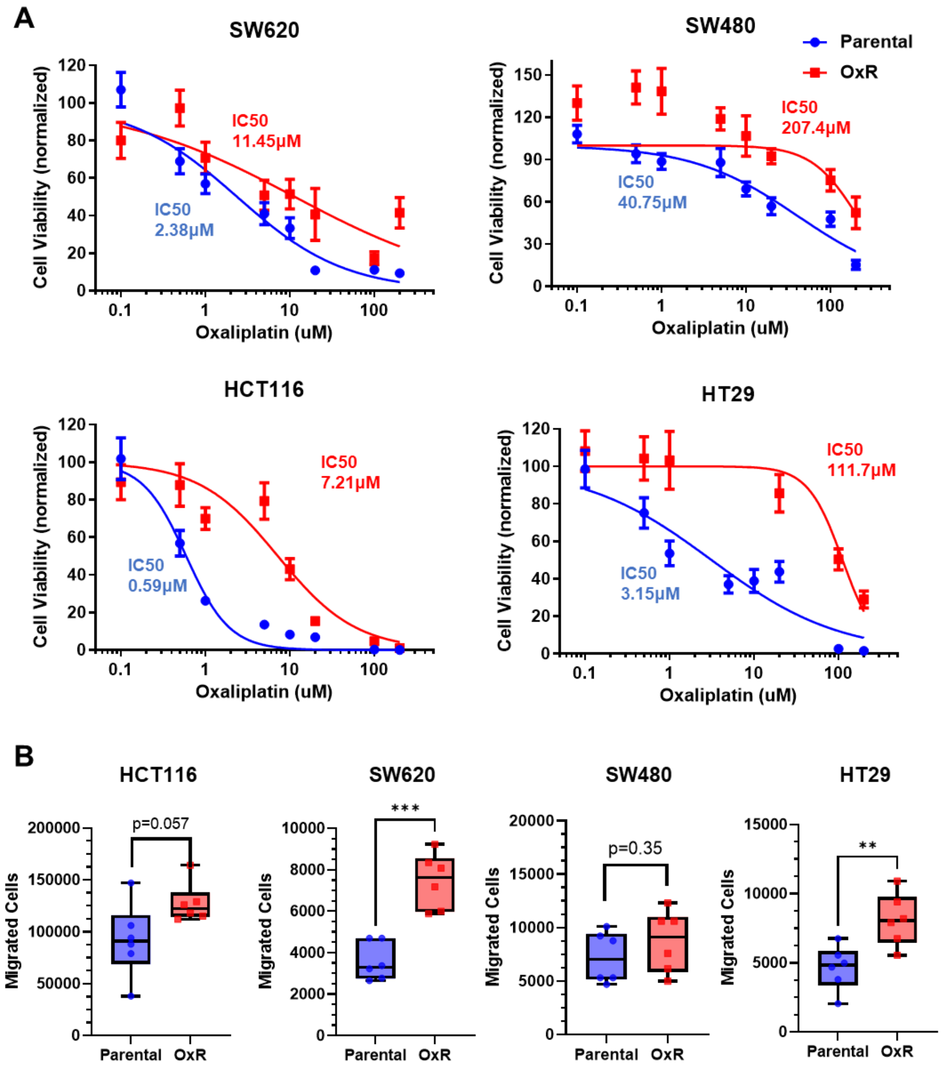

Supplementary Figure 3.1. Oxaliplatin-resistant CRC cells retain their increasingly chemoresistant and invasive phenotypes in culture. (A) SW620, SW480**,** HCT116, and HT29 cells were treated with various concentrations of oxaliplatin for 72 h and cell viability was measured using an MTT assay. IC50 values were calculated using a variable slope four parameter nonlinear regression. Data are presented as mean±SEM. N=2 (n=12). **(B)** Counts of successfully invasive cells after a four-day Transwell assay with an initial seeding of 200,000 cells. N=2 (n=6). * p<0.05 **p<0.01 (unpaired two-tailed t-test).

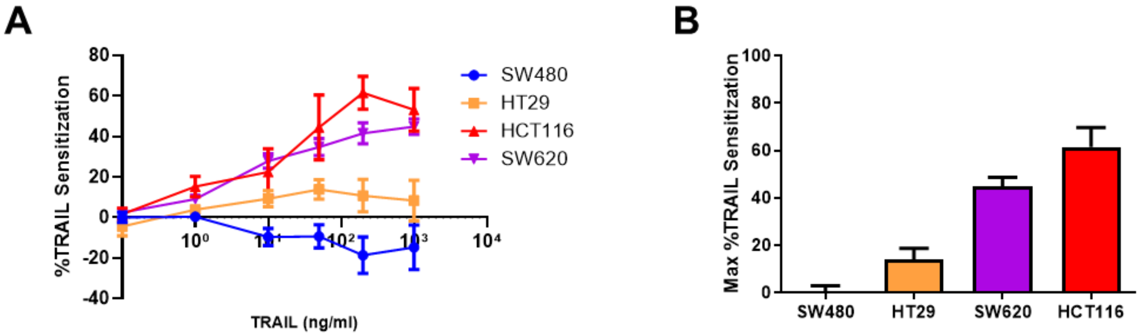

Supplementary Figure 3.2. Sensitization of oxaliplatin-resistant CRC cell lines to TRAIL. (A) Sensitization of oxaliplatin-resistant SW620, HCT116, HT29 and SW480 cell lines compared to their parental counterparts as a function of TRAIL concentration. **(B)** Maximum TRAIL sensitization for each cell line between the tested concentrations of 0.1-1000 ng/ml. Data are presented as mean±SEM.

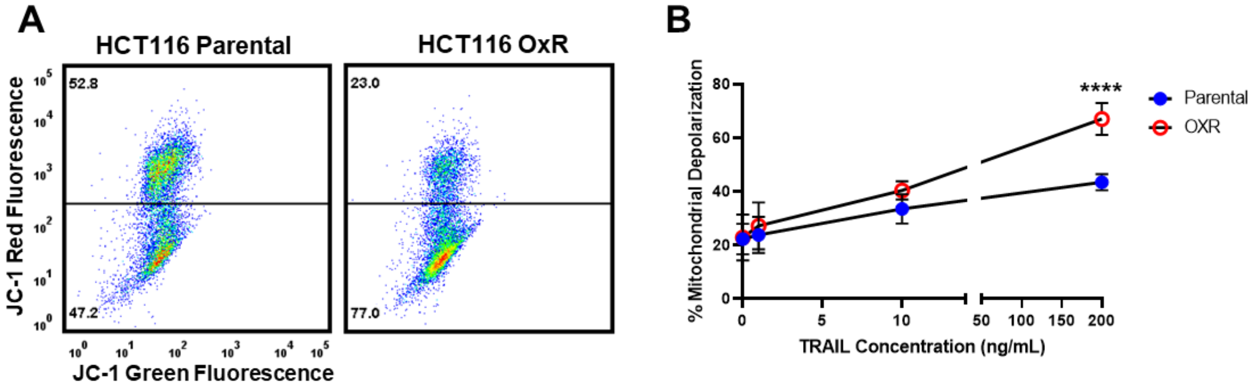

Supplementary Figure 3.3. HCT116 OxR cells have increased mitochondrial depolarization and activation of the intrinsic apoptotic pathway when treated with TRAIL. (A) Representative flow plots of JC-1 assay after treatment with 200 ng/ml of TRAIL. Mitochondrial depolarization is evidenced by decreased red fluorescence and increased green fluorescence. **(B)** Mitochondrial depolarization as a function of TRAIL concentration for HCT116 parental and OxR cell lines. Data are presented as mean±SD. N=3 (n=9). ****p<0.0001 (unpaired two-tailed t-test).

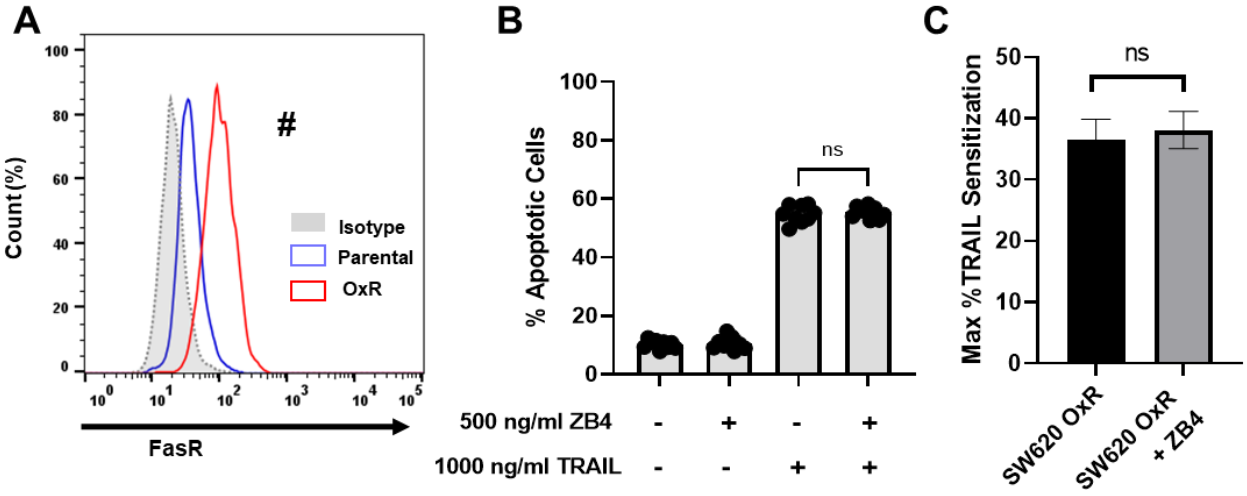

Supplementary Figure 3.4. Upregulated FasR in SW620 OxR cells has no effect on TRAIL sensitivity. (A) Flow cytometry staining confirms increased surface expression of Fas receptor. #Significant according to a chi-squared test (see Supplementary Table 3.1). **(B)** Percentage of apoptotic SW620 OxR cells after treating with 1000 ng/ml TRAIL and 500 ng/ml of the anti-FasR neutralizing antibody ZB4 (sum of early and late-stage apoptotic cells from Annexin/PI staining). Data are presented as mean+SD. N=3 n=9. Significance was measured using an ordinary one-way ANOVA–Tukey's multiple comparison test. **(C)** Neutralizing FasR has no effect on TRAIL sensitization. Data are presented as mean+SEM. N=3 (n=9). Significance was measured using an unpaired two-tailed t-test.

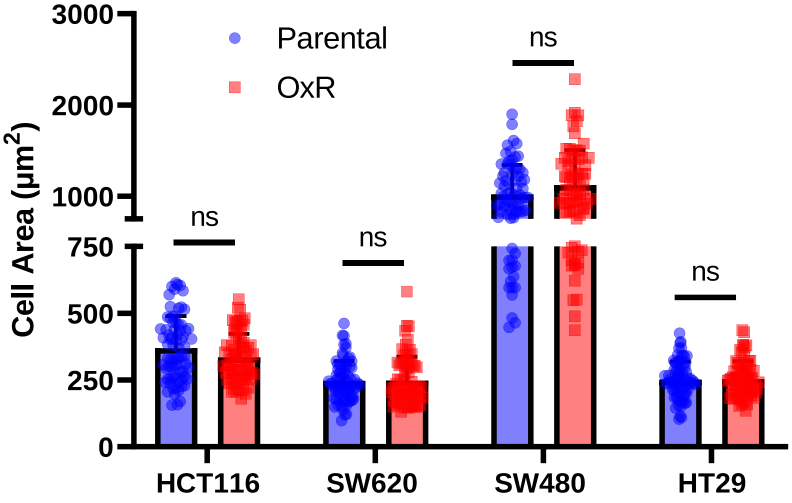

Supplementary Figure 3.5. Parental and OxR cell lines have no significant changes in cell area, analyzed from confocal microscopy images. Data are presented as mean+SD. For each cell line, N=75 cells were analyzed. An unpaired two-tailed t-test was used to measure significance between groups.

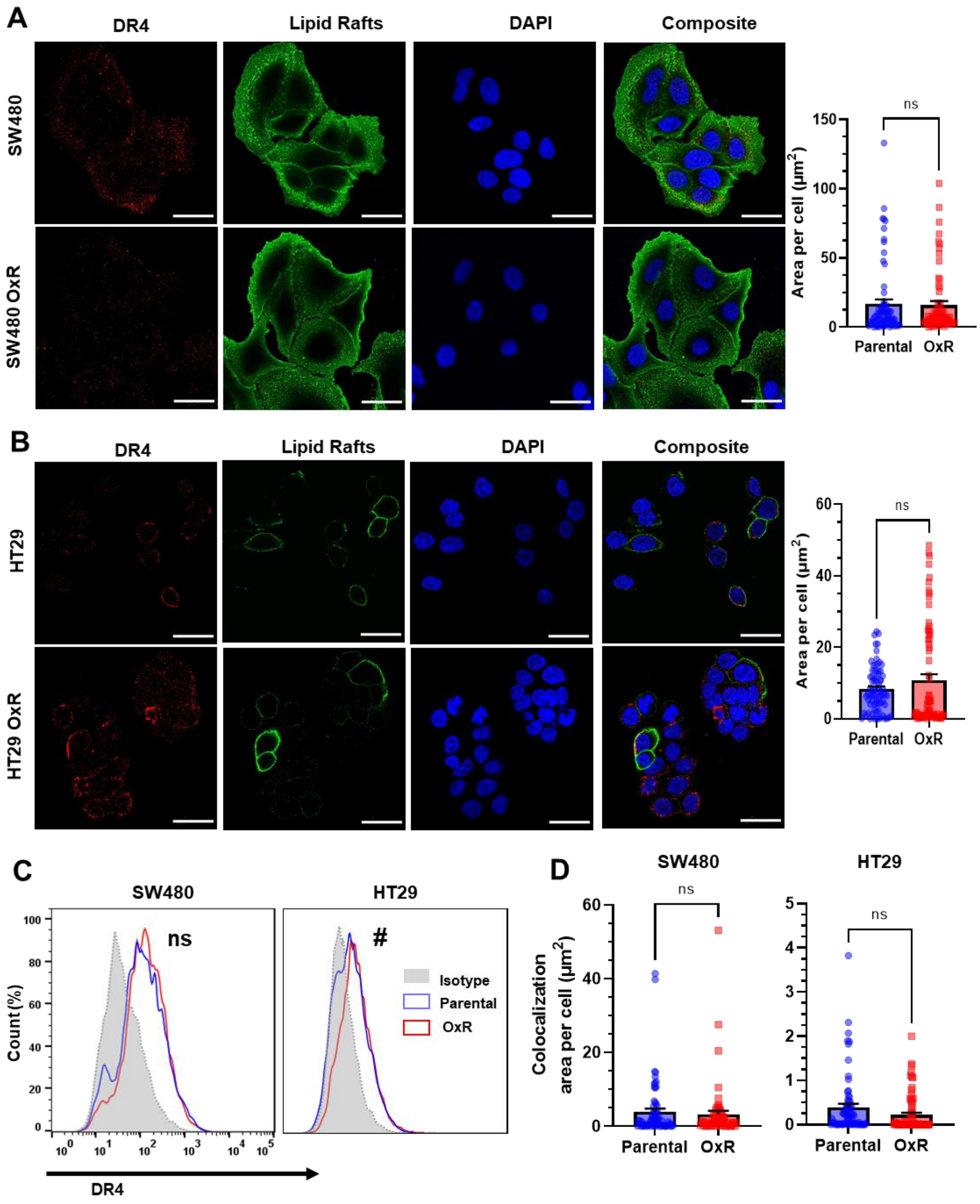

Supplementary Figure 3.6. Unsensitized SW480 and HT29 OxR cell lines show no significant changes in DR4 expression or lipid raft colocalization relative to their parental counterparts. (A-B) Confocal micrographs and DR4 quantification of SW480 and HT29 cells, respectively. Red channel is DR4, green is lipid rafts and blue is DAPI (nuclei). Scale bar = 30 μm. **(C**) Surface expression of DR4 in non-permeabilized cells analyzed via flow cytometry. $^{\#}$Significant according to a chi-squared test (see Supplementary Table 3.1). **(D)** DR4/LR colocalization area per cell for SW480 and HT29 was found to be insignificant between parental and OxR phenotypes. Data are presented as mean+SEM. An unpaired two-tailed t-test was performed for panels A, B and D. For each cell line, N=75 cells were analyzed.

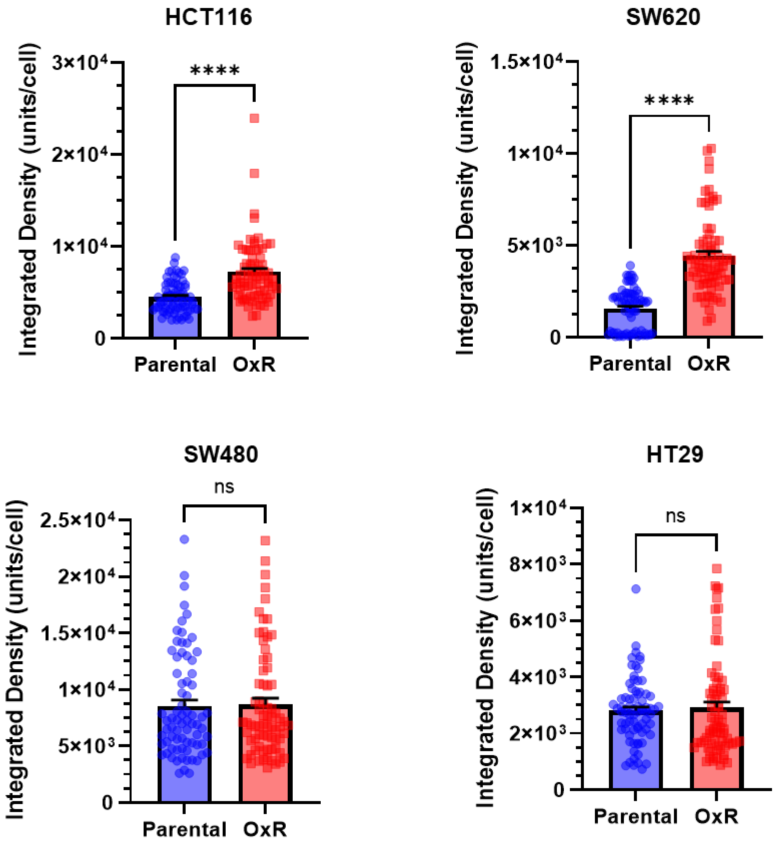

Supplementary Figure 3.7. Sensitized oxaliplatin-resistant cell lines have significantly increased DR4 integrated density per cell. Data are presented as mean+SEM. For each cell line, N=75 cells were analyzed. ****p<0.0001 (unpaired two-tailed t-test).

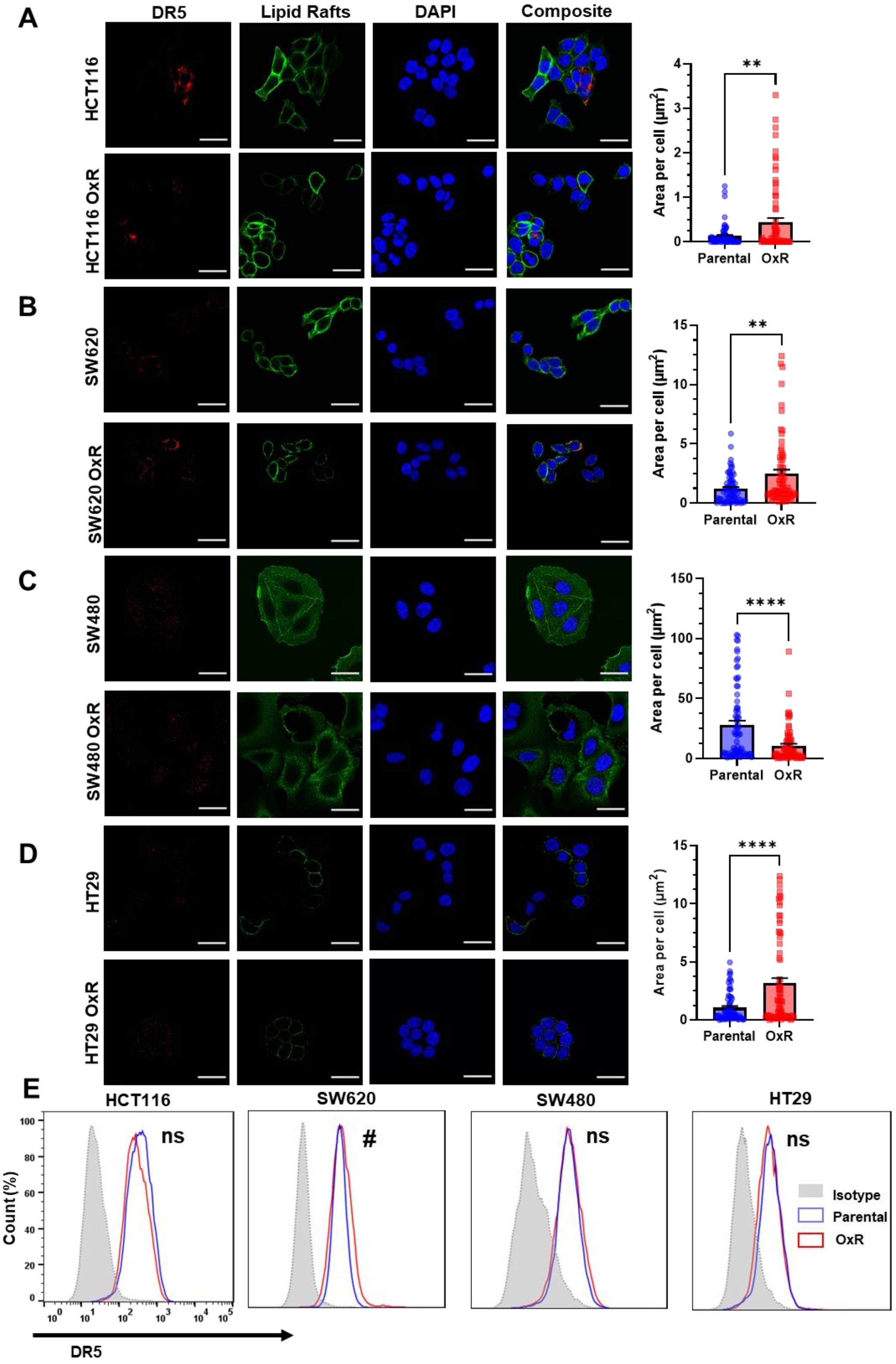
A
DR5
Lipid Rafts
DAPI
Composite
HCT116
HCT116 OxR
Area per cell (μm^2)
4
3
2
1
0
**
Parental
OxR
B
SW620
SW620 OxR
Area per cell (μm^2)
15
10
5
0
**
Parental
OxR
C
SW480
SW480 OxR
Area per cell (μm^2)
150
100
50
0
****
Parental
OxR
D
HT29
HT29 OxR
Area per cell (μm^2)
15
10
5
0
****
Parental
OxR
E
HCT116
SW620
SW480
HT29
ns
#
ns
ns
Count (%)
100
80
60
40
20
0
10^0
10^1
10^2
10^3
10^4
10^5
DR5
Isotype
Parental
OxR

Supplementary Figure 3.8. Chemoresistant HCT116, SW620 and HT29 cells have upregulated DR5 while in chemoresistant SW480 cells, DR5 is decreased. (A-D) Confocal micrographs and DR5 quantification of HCT116, SW620, SW480 and HT29 cells, respectively. Red channel is death receptor 5, green is lipid rafts and blue is DAPI (nuclei). Scale bar = 30 μm. ** $p<0.01$ ****$p<0.0001$ (unpaired two-tailed t-test). Data are presented as mean+SEM. For each cell line, N=75 cells were analyzed. **(E**) OxR cells only demonstrate increased surface expression of DR5 in non-permeabilized SW620 cells. $^{\#}$Significant according to a chi-squared test (see Supplementary Table 3.1).

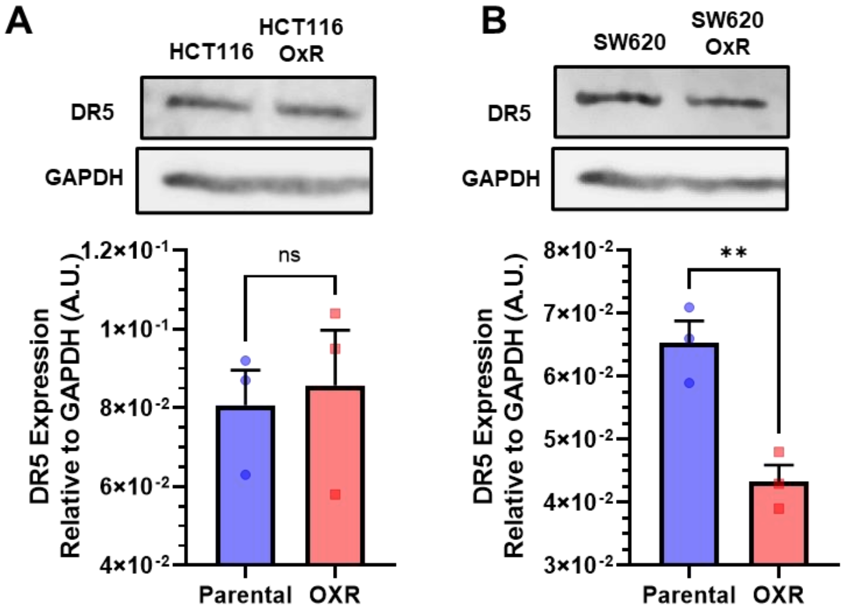

Supplementary Figure 3.9. Western blots show TRAIL-sensitized HCT116 (A) and SW620 (B) OxR cells have no increases in DR5. Data are presented as mean+SEM. N=3. ** $p<0.01$ (unpaired two-tailed t-test).

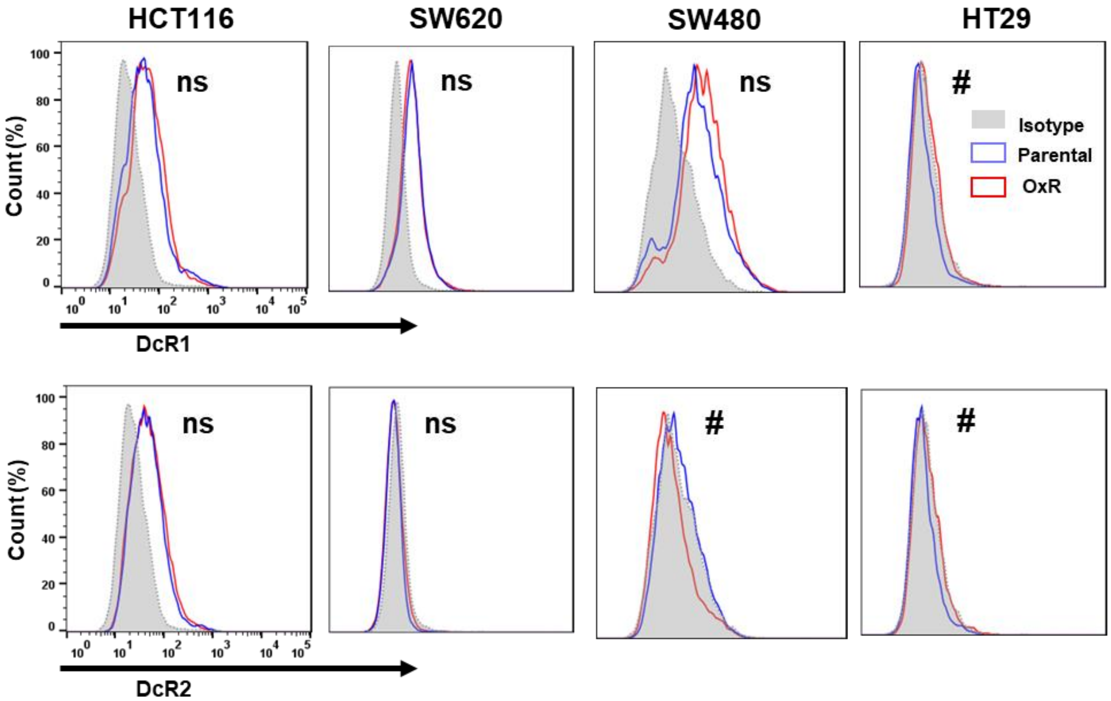

Supplementary Figure 3.10. Flow cytometry analysis of the surface expression of decoy death receptors 1 (DcR1) and 2 (DcR2) on nonpermeabilized parental and OxR cell lines. #Significant according to a chi-squared test (see Supplementary Table 3.1).

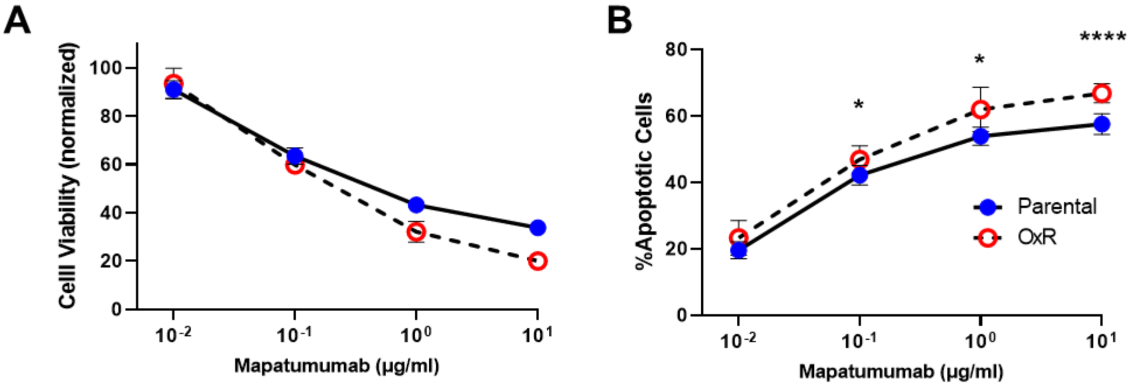

Supplementary Figure 3.11. HCT116 OxR cells are increasingly sensitive to DR4 agonist antibody treatment. (A) Cell viability of HCT116 cells after 0.01-10 µg/ml Mapatumumab treatment, determined by AnnexinV/PI staining. **(B)** Percentage of apoptotic SW620 cells after Mapatumumab treatment (sum of early and late-stage apoptotic cells from Annexin/PI staining). For all graphs, data are presented as mean+SD. N=3 (n=6). *p<0.05 ****p<0.0001 (multiple unpaired two-tailed t-tests).

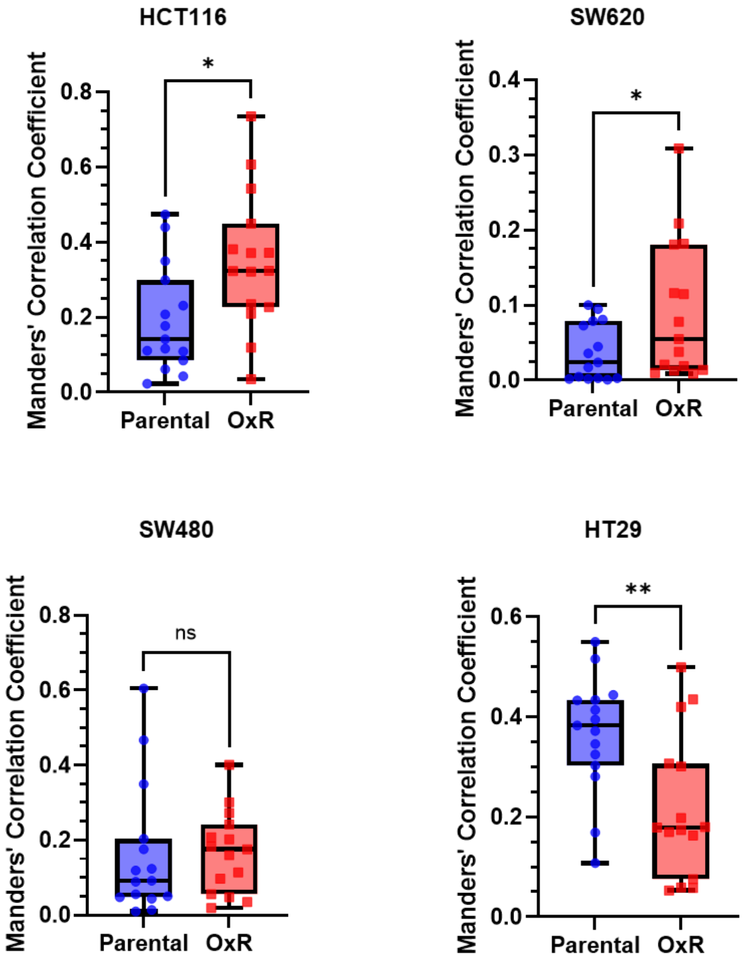

Supplementary Figure 3.12. TRAIL-sensitized OxR cells have significantly increased colocalization of DR4 with lipid rafts according to Manders' Correlation Coefficient. N=15 analyzed micrographs across three independent trials. *p<0.05 *p<0.001 (unpaired two-tailed t-test).

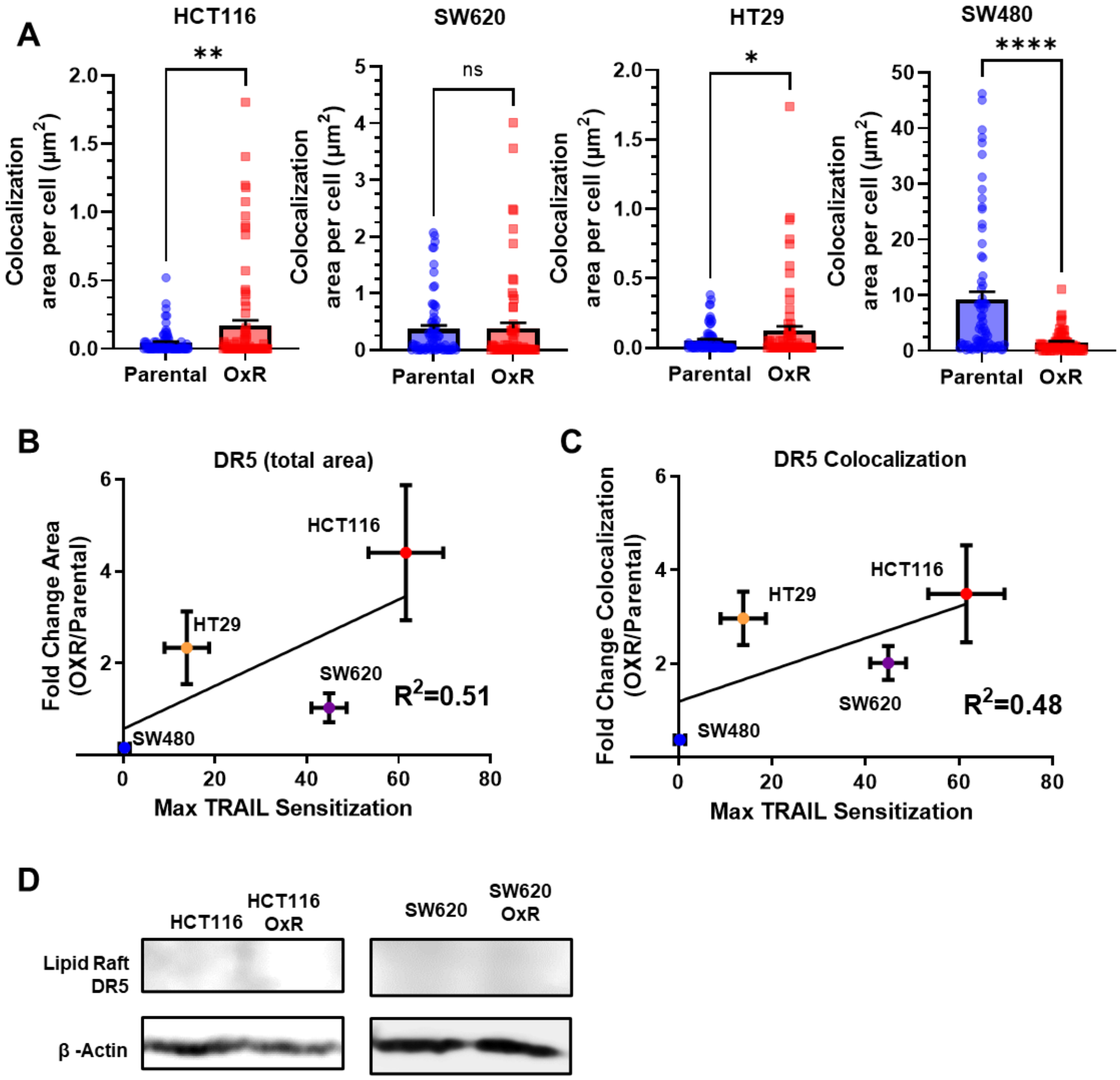

Supplementary Figure 3.13. Sensitization to TRAIL in OxR cell lines poorly correlates with DR5 expression while lipid raft fractions have no detectable DR5. (A) Quantification of DR5/LR colocalization in HCT116, SW620, SW480 and HT29 cells. $*p<0.05$ $**p<0.01$ $****p<0.0001$ (unpaired two-tailed t-test). For each cell line, N=75 cells were analyzed. **(B)** Correlation of total DR5 area per cell and **(C)** DR5/LR colocalization with maximum TRAIL sensitization observed in OxR cells (linear regression analysis). For all graphs, data are presented as mean+SEM. **(D)** Western blots show DR5 was undetectable in lipid raft isolated fractions.

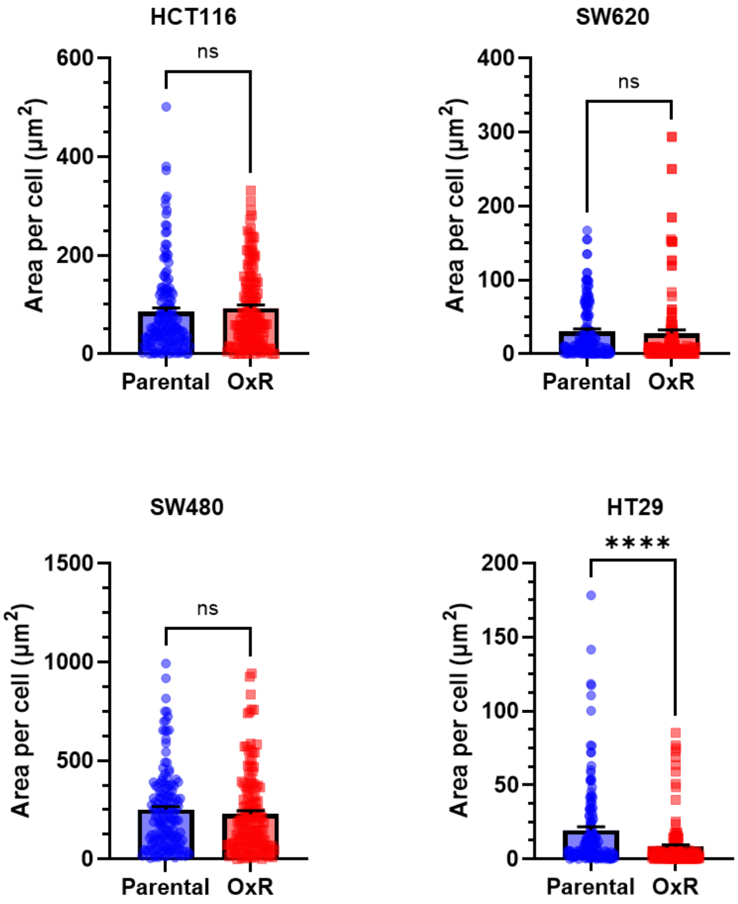

Supplementary Figure 3.14. Quantification of lipid raft area per cell. For each cell line, N=150 cells were analyzed. Data are presented as mean+SEM. ****$p<0.0001$ (unpaired two-tailed t-test).

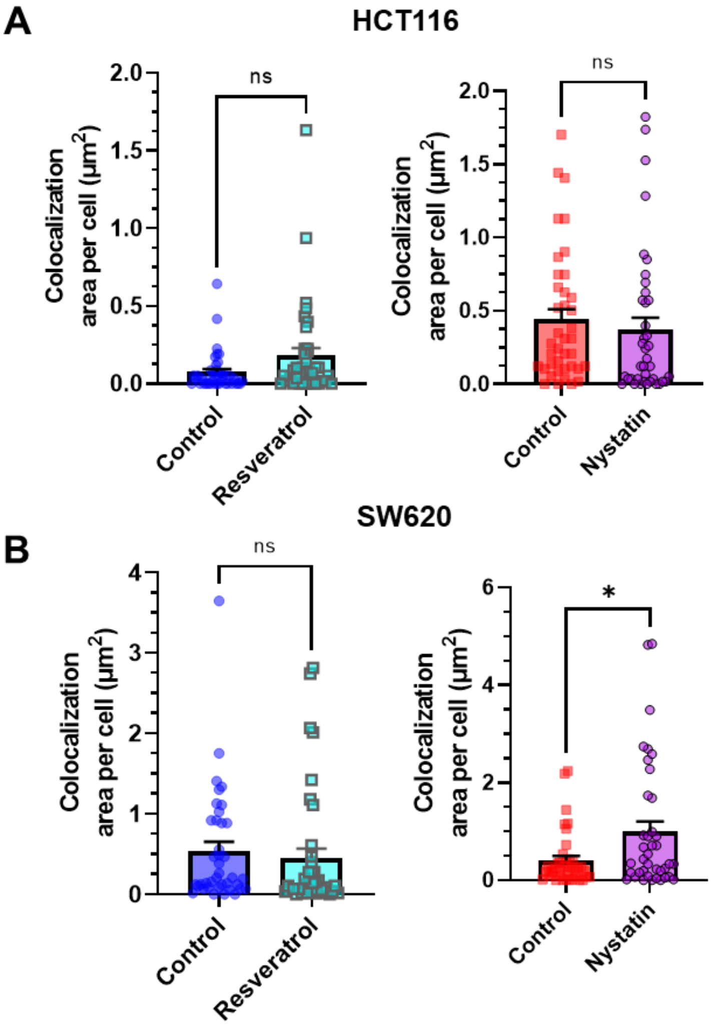

Supplementary Figure 3.15. Quantification of the effects of resveratrol and nystatin on DR5 colocalization with lipid rafts in HCT116 (A) and SW620 cells (B). For each cell line, N=40 cells were analyzed. Data are presented as mean+SEM. *$p<0.05$ (unpaired two-tailed t-test).

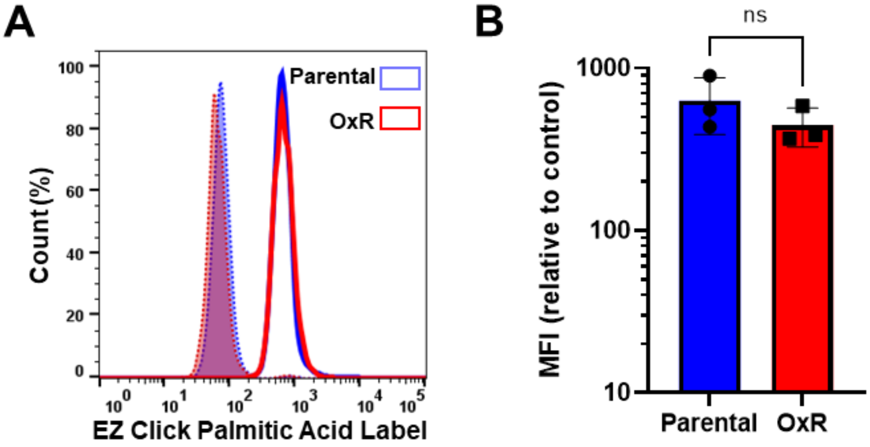

Supplementary Figure 3.16. Total palmitoylation remains unchanged between SW620 parental and OxR cells. (A) Parental and OxR SW620 cells were labeled with EZClick™ Palmitic Acid/ Fluorescent Azide staining kit and analyzed via flow cytometry to determine total protein palmitoylation between cell lines. Blue histograms represent parental SW620 cells and red histograms are SW620 OxR cells. Shaded histograms are background controls for each cell line (Palmitic Acid (**-**)/ Fluorescent Azide (**+**). **(B)** Quantification of median fluorescence intensity (MFI) shows no significant change in total palmitoylation between cellular phenotypes (unpaired two-tailed t-test). Data are presented as mean±SD. N=3. Significance was measured using an unpaired two-tailed t-test.

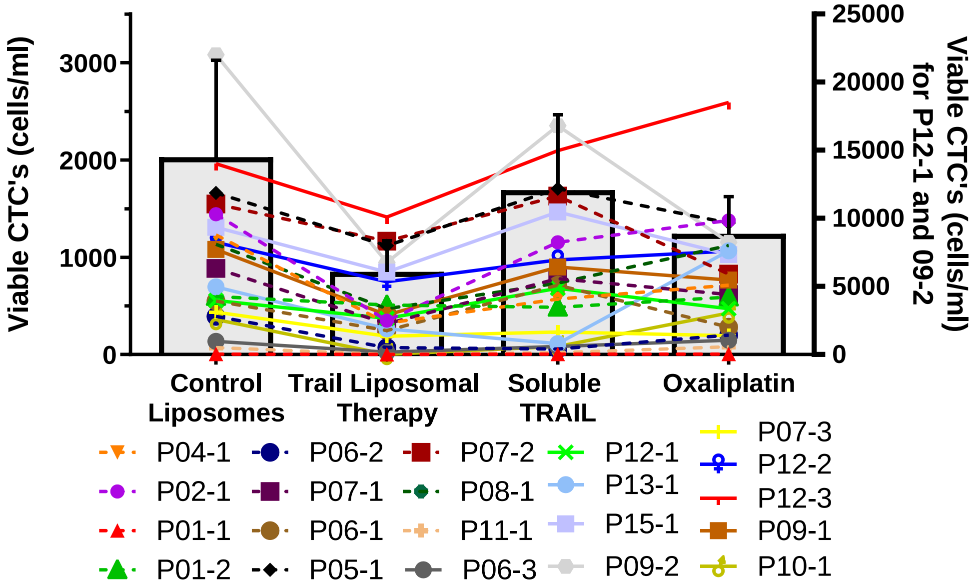

Supplementary Figure 3.17. Absolute numbers of viable CTCs per ml of blood following TRAIL liposomal therapy and control treatments. Bars represent mean of all patient samples and error bars represent SEM. Samples 12-1 and 09-2 showed very large CTC concentrations and were plotted using the alternative scale shown on the right. All other samples (and average) were plotted using the scale shown on the left.

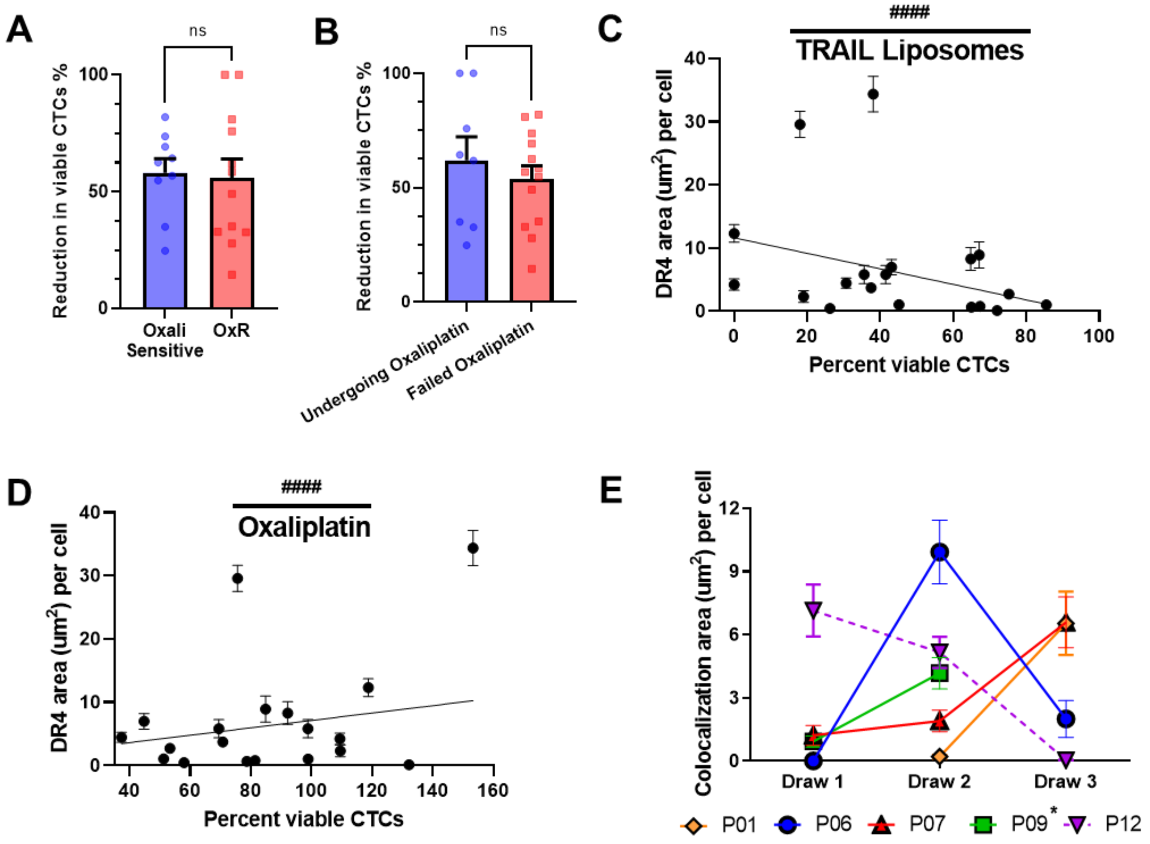

Supplementary Figure 3.18. TRAIL liposomes are effective in oxaliplatin sensitive and refractory patients. (A) Patients were categorized as either oxaliplatin-sensitive (viability <80%, N=9) or oxaliplatin resistant (viability >80%, N=12) to compare changes in the reduction of viable CTCs (unpaired two-tailed t-test). **(B)** Patients undergoing oxaliplatin chemotherapy at the time of blood draw (N=8) showed insignificant changes in viable CTC reduction compared to patients that have previously failed oxaliplatin (N=13) (unpaired two-tailed t-test). **(C)** DR4 area of patient CTCs plotted against the percentage of viable CTCs following TRAIL liposome treatments. Each point corresponds with one patient draw. $^{\#\#\#\#}$p<0.0001 (simple linear regression to confirm significant deviation from zero). **(G)** DR4 area of patient CTCs plotted against the normalized percentage of viable CTCs following oxaliplatin treatment. Each point corresponds with one patient draw. $^{\#\#\#\#}$p<0.0001 (simple linear regression to confirm significant deviation from zero). **(E)** Lipid raft/DR4 analysis of repeat patients, analyzing the changes in DR4 colocalization over the course of therapy. *Patient 9 died after draw 2, precluding further blood collection. For all graphs, data are presented as mean± SEM.

Cell line	**Stain**	**Chi-Squared T(x) Background (OxR vs Parental)**	**Chi-Squared T(x) Sample (OxR vs Parental)**	**Significance**
SW620	DR4	43.54	106.74	**Yes**
SW620	DR5	43.54	307.20	**Yes**
SW620	DcR1	43.54	11.70	**No**
SW620	DcR2	43.54	35.37	**No**
SW620	FasR	2.95	271.82	**Yes**
HCT116	DR4	443.32	1182.10	**Yes**
HCT116	DR5	443.32	95.20	**No**
HCT116	DcR1	443.32	53.28	**No**
HCT116	DcR2	443.32	11.32	**No**
SW480	DR4	88.47	26.34	**No**
SW480	DR5	88.47	17.46	**No**
SW480	DcR1	88.47	46.67	**No**
SW480	DcR2	88.47	99.23	**Yes**
HT29	DR4	54.33	76.58	**Yes**
HT29	DR5	54.33	29.15	**No**
HT29	DcR1	54.33	95.81	**Yes**
HT29	DcR2	54.33	68.73	**Yes**

Supplementary Table 3.1. Statistical reporting of Chi-Squared T(x) values for comparing distribution differences in flow cytometry staining.

Chapter 4:

Piezo1 Mechano-Activation is Augmented by Resveratrol and Differs between Colorectal Cancer Cells of Primary and Metastatic Origin

Joshua D. Greenlee, Kevin Liu, Maria Lopez Cavestany, Michael R. King

This chapter is adapted from *Piezo1 Mechano-Activation is Augmented by Resveratrol and Differs between Colorectal Cancer Cells of Primary and Metastatic Origin* published in *Molecules* and has been reproduced with permission of the publisher and co-authors Kevin Liu, Maria Lopez Cavestany, and Michael King [285].

Greenlee, J.D.; Liu, K.; Lopez-Cavestany, M.; King, M.R. Piezo1 Mechano-Activation Is Augmented by Resveratrol and Differs between Colorectal Cancer Cells of Primary and Metastatic Origin. *Molecules* 2022, 27, 5430, doi:10.3390/molecules27175430.

4.1 Abstract

Cancer cells must survive aberrant fluid shear stress (FSS) in the circulation to metastasize. Herein, we investigate the role that FSS has on colorectal cancer cell apoptosis, proliferation, membrane damage, calcium influx, and therapeutic sensitization. We tested this using SW480 (primary tumor) and SW620 cells (lymph node metastasis) derived from the same patient. The cells were exposed to either shear pulses, modeling millisecond intervals of high FSS seen in regions of turbulent flow, or sustained shear to model average magnitudes experienced by circulating tumor cells. SW480 cells were significantly more sensitive to FSS-induced death than their metastatic counterparts. Shear pulses caused significant cell-membrane damage, while constant shear decreased cell proliferation and increased the expression of CD133. To investigate the role of mechanosensitive ion channels, we treated cells with the Piezo1 agonist Yoda1, which increased intracellular calcium. Pretreatment with resveratrol further increased the calcium influx via the lipid-raft colocalization of Piezo1. However, minimal changes in apoptosis were observed due to calcium saturation, predicted via a computational model of apoptosis. Further, SW480 cells had increased levels of Piezo1, calcium influx, and TRAIL-mediated apoptosis compared to SW620 cells, highlighting differences in the mechano-activation of metastatic cells, which may be a necessary element for successful dissemination in patients.

4.2 Introduction

Colorectal cancer (CRC) remains the second leading cause of cancer-related death in the United States [286]. As true for most cancers, the primary cause of CRC-related death is attributed to metastasis [239]. Metastasis is the process in which cancer cells undergo an epithelial to mesenchymal transition (EMT) to become increasingly motile, which then allows them to migrate toward the vasculature and then intravasate into vessels through endothelial junctions. For successful tumor dissemination to occur, once cancer cells access blood or lymphatic vessels, they must survive inhospitable environments comprised of surveying immune cells and harsh physical forces from flow. For example, in lymphatic vessels, cancer cells have been shown to experience pulses of shear stress ranging from 4-12 dyne/cm^2 compared to less than 0.1 dyne/cm^2 within the solid tumor [287,288]. Within the blood, cancer cells experience magnitudes of circulatory shear stress ranging from 0.5-30 dyne/cm^2 within veins and arteries, to magnitudes greater than 1000 dyne/cm^2 for brief periods of time at arterial bifurcations and within the heart. [289,290]. These harsh fluid environments explain why less than 0.01% of circulating tumor cells (CTCs) that enter the circulation survive to colonize secondary sites in the body [14,291]. However, the presence and survival of CTCs is a strong predictor of secondary tumor colonization, poor prognosis and mortality in most cancer types [269,292,293].

Our lab has recently demonstrated that prostate cancer cell lines have different sensitivities to fluid shear stress (FSS) dependent upon their metastatic location [294]. Cells derived from a brain met (having been exposed to high magnitudes of FSS from the heart) were much more resistant to FSS-induced apoptosis than cells derived from the lymph node. However, these cell lines were isolated from different patients, making it more difficult to interpret mechanisms of FSS resistance. Using an isogenic cellular model, consisting of cell lines derived from different tissues within the same patient, could provide mechanistic insight into how cancer cells evolve to evade apoptosis within the circulation. Recent studies have shown that physiological levels of FSS stress can promote a mesenchymal phenotype and enhance CTC survival in the circulation [295–298]. For example, one study demonstrated that lung cancer cells exposed to fluid shear stress show side population enrichment, hallmarks of EMT, and upregulation of cancer stem cell (CSC) marker CD44 [298]. However, no study has compared the response to FSS between cells isolated from the primary tumor with those that have successfully disseminated to a metastatic site. We hypothesize that cancer cells of metastatic origin will be increasingly impervious to FSS through mechanisms of intrinsic (subpopulation selection) or acquired resistance.

Cancer cells are able to sense and respond to FSS and other mechanical stimuli through the process of mechanotransduction. One type is the stimuli-induced opening of mechanosensitive ion channels that allows for the influx of calcium, acting as a secondary effector to propagate intracellular signaling cascades. Calcium-gated ion channels, such as transient receptor potential cation channel subfamily V member 4 (TRPV4), P2X purinoceptor 7 (P2X7) and Piezo1 have recently been implicated as integral components in mechanisms of cancer metastasis and cell death [79,80]. For instance, we have recently determined that cancer cells can be sensitized to tumor necrosis factor-related apoptosis inducing ligand (TRAIL)-mediated apoptosis through activation of Piezo1, either through FSS or chemical agonists such as Yoda1 [81,272]. There is evidence suggesting that both lipid composition and biophysical properties of the membrane influence mechanosensitive ion channel activation [299,300]. The concentration of membrane cholesterol has effects on cell stiffness, tension and rigidity, consequently affecting membrane deformation and the force “perceived” by channels following mechanical stimuli. For example, depletion or disruption of membrane cholesterol has been shown to inhibit activation of mechanosensitive ion channels, including Piezo1 [301,302]. If the cell membrane can be considered a spring, increasing the membrane rigidity via cholesterol (higher spring constant) will make the applied force greater for equivalent membrane deformations.

Cholesterol is an integral component of lipid rafts (LRs), which are densely packed, organized, detergent-insoluble areas within the lipid bilayer [86,303]. Lipid rafts have been shown to facilitate mechanisms of cancer metastasis by acting as protein scaffolds and receptor oligomerization platforms to augment downstream signal transduction [98]. While the role of LRs in many forms of signal transduction, including apoptotic death receptor signaling, has been well described [65], the role of rafts in mechanosensation via ion channels remains elusive. We hypothesize that similarly to cholesterol, the presence of lipid rafts will have an amplifying effect on Piezo1 activation and calcium influx. In this chapter, we examine the role that lipid rafts, and the raft-stabilizing polyphenol resveratrol (RSV) have on mechanical and chemical activation of Piezo1 in order to sensitize cancer cells to therapeutics. Additionally, using two CRC cell lines (SW480 and SW620) derived from the same patient, we demonstrate that metastatic cells are increasingly resistant to different types of FSS. Understanding how cells respond to different types of physiological FSS and mechanosensitive ion channel agonists may prove useful in leveraging calcium-dependent metastatic processes for therapeutic benefit.

4.3 Results

4.3.1 SW480 cells from the primary tumor are increasingly sensitive to FSS

For this study, two CRC cell lines derived from the same patient were used. SW480 cells were isolated from a primary adenocarcinoma of the colon in a 50-year-old male, while SW620 cells were isolated from a lymph node metastasis one year later. Through metastasizing from lymphatic vessels into a lymph node, SW620 cells would have been exposed to higher magnitudes of FSS than SW480 cells in the body. SW620 cells have been well characterized as being increasingly mesenchymal, tumorigenic and metastatic compared to SW480 cells, which appear more epithelial in culture [304]. However, no study to date has compared how these cell lines respond to FSS. To measure the sensitivity of these cell lines to FSS, cells were exposed to three different physiological flow conditions: static (0 dyne/cm^2), shear pulses (10 pulses of 3950 dyne/cm^2; total strain = 39.5 dyne×s/cm^2) and constant shear (2.5 h of 10 dyne/cm^2; total strain = 90,000 dyne×s/cm^2) (**Figure 4.1**). Shear pulses were used to model brief intervals of high-intensity FSS in areas such as the heart, whereas constant shear was used to model average magnitudes and durations CTCs experience in the circulation [294,305,306]. After FSS, cells were incubated for 24 h and then analyzed for apoptosis via Annexin-V/propidium iodide (PI) staining. SW480 cells had a significant decrease in cell viability from both forms of FSS compared to SW620 cells (**Figure 4.2A, E**)**.** Decreases in viability coincided with increases in the percentage of cells undergoing early and late-stage apoptosis (**Figure 4.2B, C**). Metastatic SW620 cells demonstrated no significant change in cell viability in response to FSS. To determine if the FSS-induced apoptosis was associated with enhanced mitochondrial outer membrane permeability (MOMP), cells were stained with a JC-1 dye after FSS. Both SW480 and SW620 cells showed no changes in depolarized mitochondria following FSS, suggesting that increases in apoptosis were likely due to the extrinsic apoptotic pathway (**Figure 4.2D**).

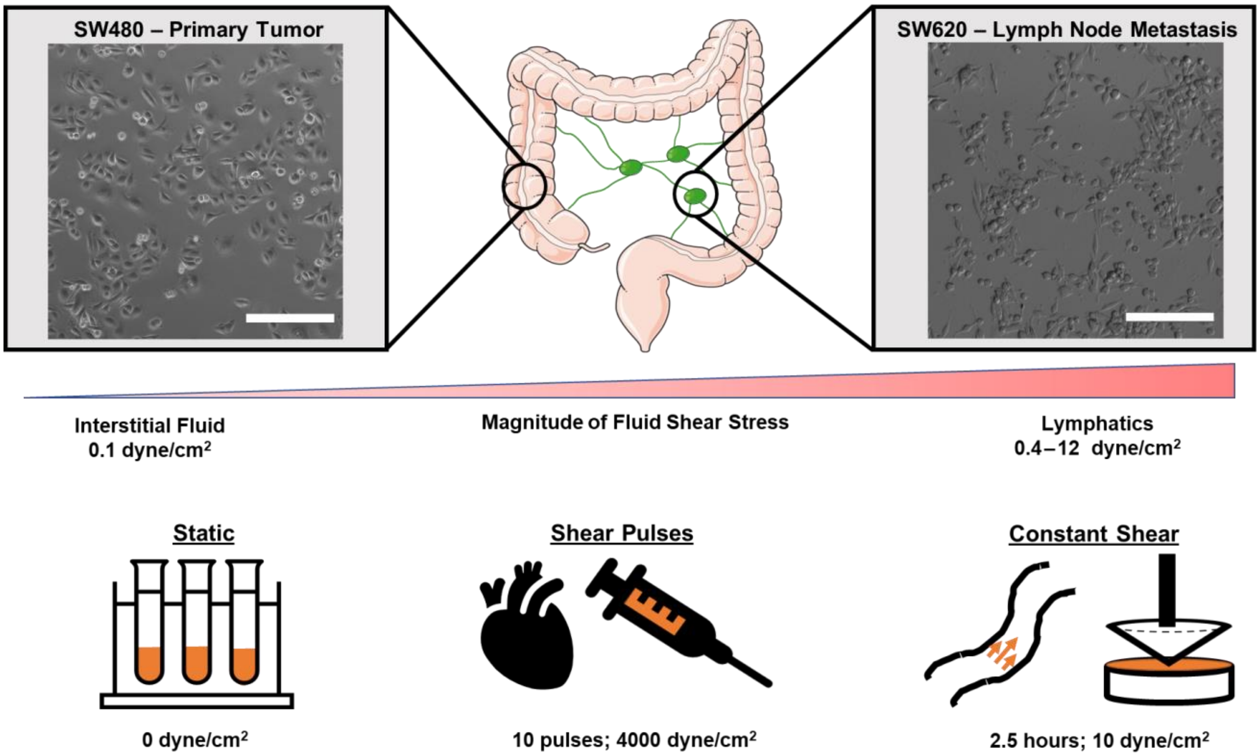

Figure 4.1. Isogenic colorectal cancer cellular model with different exposures to FSS *in situ*. FSS conditions were chosen to model flow conditions experienced by CTCs at brief intervals of turbulence (shear pulses) and average magnitudes and durations in the vasculature (constant shear).

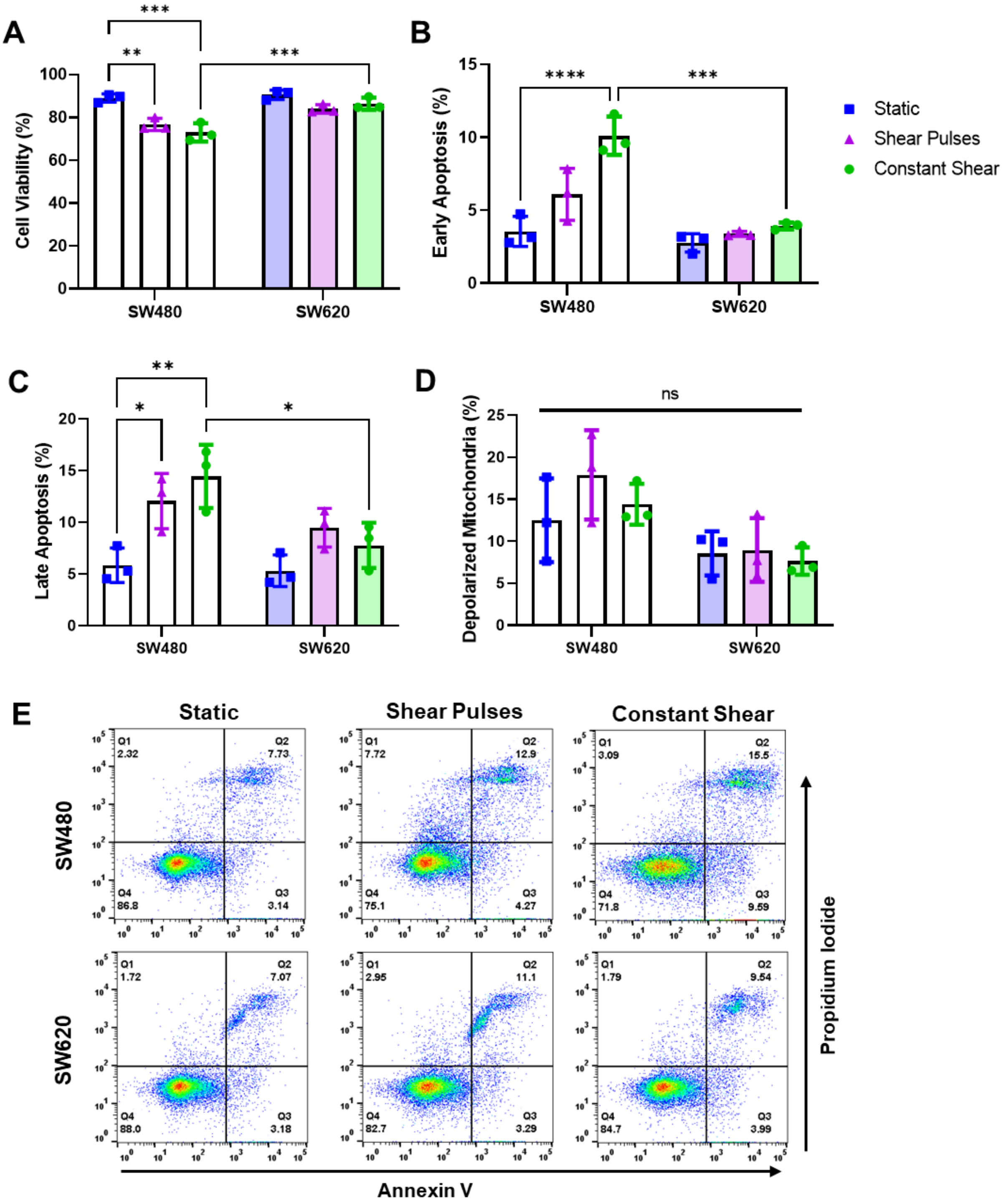

Figure 4.2. SW480 cells are more sensitive to FSS compared to SW620 cells. (A-C) Cell viability and apoptosis measured via Annexin V/PI staining 24 h after FSS treatments. **(D)** Percentage of cells with depolarized mitochondria measured via a JC-1 assay after FSS. N=3; ns = not significant, *p<0.05 **p<0.01 ***p<0.001 (two-way ANOVA with multiple comparisons). Error bars represent mean ± SD. **(E)** Representative flow cytometry plots showing necrotic cells (Q1), late apoptotic cells (Q2), early apoptotic cells (Q3), and viable cells (Q4).

4.3.2 Moderate levels of constant FSS decrease cell proliferation and increase CD133 expression

To measure changes in proliferation and cell cycle after FSS, cells were analyzed for Ki67 expression and total DNA content, respectively. Interestingly, cell proliferation was significantly decreased after constant shear stress but not shear pulses in SW480 cells (**Figure 4.3A**). SW620 cells also saw a 20% decrease in proliferation from constant shear, but this was not found to be significant. Despite decreases in proliferation, there was no significant change in cell cycle. (**Figure 4.3B**). Studies have shown that exposing suspended cancer cells to fluid flow can alter expression of mesenchymal and CSC markers [298]. Twenty-four hours post-FSS, cells were analyzed for CSC markers CD133 and CD44. To exclude dead cells, samples were counterstained with propidium iodide before analyzing, where debris and propidium iodide (+) cells were excluded from analysis (**Figure 4.3C**). SW480 cells were found to be high expressors of CD44 but low CD133, whereas SW620 cells had low CD44 expression and high CD133. While CD44 expression remained unchanged from FSS (**Figure 4.3D**), constant FSS increased the expression of CD133+ SW480 cells by over two-fold (**Figure 4.3E**). CD133 is a transmembrane protein and CSC marker in many cancer types, and is a predictor of cancer cell survival, tumorigenicity and metastasis [307]. This increase in CD133 expression in SW480 cells more closely mimics expression in metastatic SW620 cells, possibly highlighting a mechanism by which cells in transit become more metastatic though a response to sustained fluid forces.

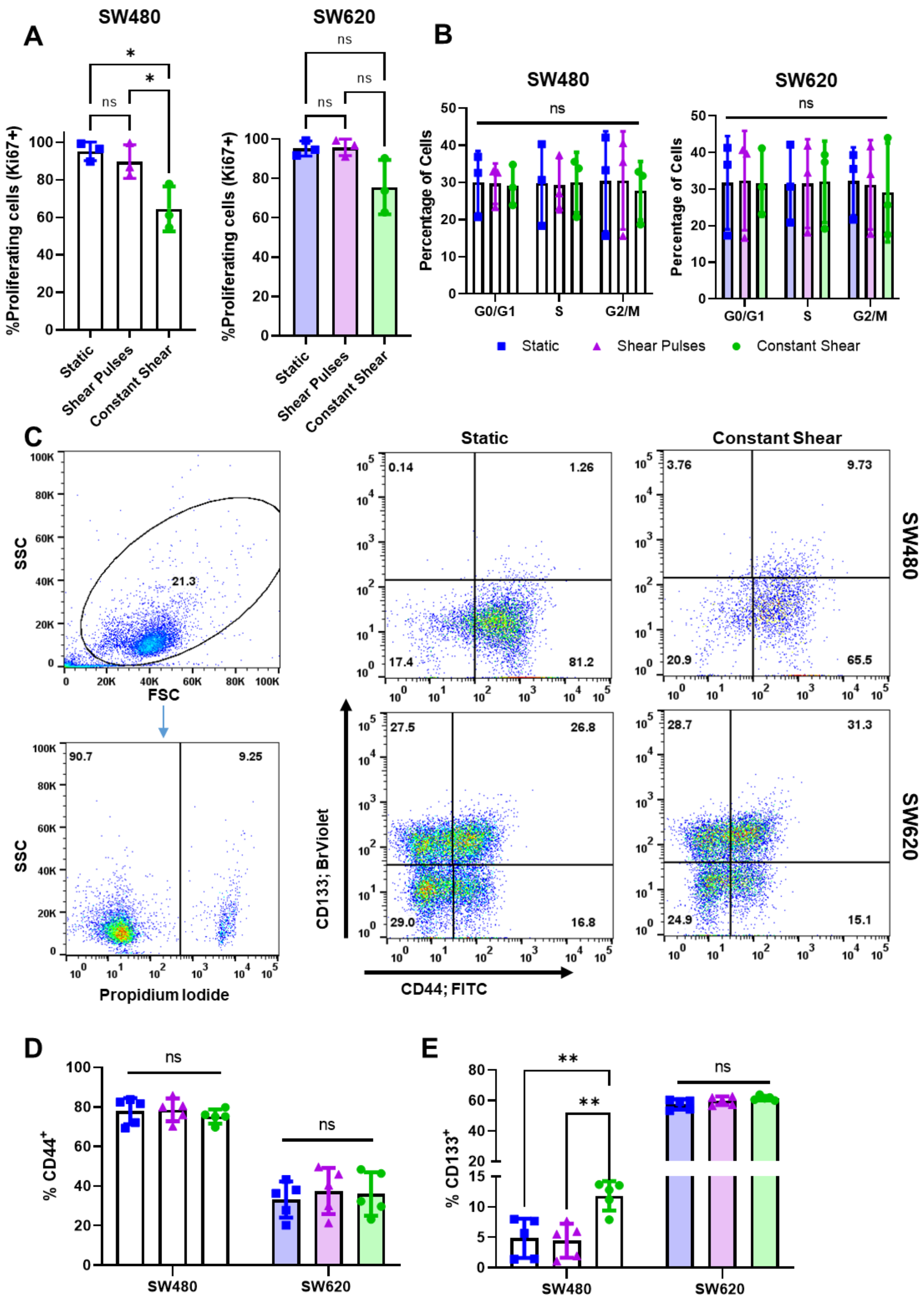

Figure 4.3. Constant shear stress decreases cell proliferation and increases CD133 expression in SW480 cells. (A) Percentage of proliferating cells 24 h post-FSS exposure, determined by the percentage of Ki67+ cells. N=3, *p<0.05 (one-way ANOVA with multiple comparisons). Error bars represent mean ± SD. **(B)** Cell cycle distribution based on total DNA content from DAPI staining analyzed via flow cytometry. A Watson (Pragmatic) model was used in FlowJo to determine the percentage of cells in each stage of the cell cycle. N=3. **(C)** Expression of CSC markers CD44 and CD133 post-FSS. Cells were gated from debris using forward and side scatter. PI+ cell populations were considered dead and excluded from analysis. Intact, PI- cells were appropriately compensated and gated for expression of CD44 and CD133 using single stained controls. (**D-E**) Quantification of CSC markers CD44 and CD133 for different conditions of FSS. N=5, ns = not significant, **p<0.01 (two-way ANOVA with multiple comparisons). Error bars represent mean ± SD.

4.3.3 High magnitude FSS pulses causes cell membrane damage and pores that are rapidly repaired

We have previously demonstrated that pulses of high magnitude FSS cause membrane damage in prostate cancer cells [294]. To investigate the role of the cell membrane in relation to apoptosis during FSS, cells were incubated with fluorescently-conjugated dextran of 3kD and 10kD MW during FSS exposure. These 3kD and 10kD MW dextran molecules have an estimated hydrodynamic radius of 1.4 nm and 2.3 nm, respectively. Cells with uptake of fluorescent dextran were considered damaged from the formation of membrane pores that were greater in size than the dextran hydrodynamic radius. Interestingly, shear pulses caused a dramatic increase in damaged cells (over 6-fold in both SW480 and SW620 cells) as indicated by internalization of 3kD MW dextran (**Figure 4.4B**). Pulses also caused an increase in pore formation exceeding 2.3 nm in size, which was most pronounced in SW480 cells with a significant increase of 3-fold (**Figure 4.4C**). This membrane damage was unique to high magnitude shear pulses, as constant shear stress did not cause any appreciable change in dextran internalization. To measure cell membrane recovery and repair, cells were incubated with PI 20 min after FSS. Cells positive for PI were considered “unrecovered” as they were unable to sufficiently repair pores in the membrane and were therefore permeable to PI (**Figure 4.4A**). Despite the significant increase in cell membrane damage from shear pulses, over 80% of SW480 and SW620 cells were able to repair their membrane within minutes of FSS-induced damage (**Figure 4.4B, C**). This rapid membrane recovery is thought to explain why both SW480 and SW620 cells were relatively resistant to apoptosis from shear pulses.

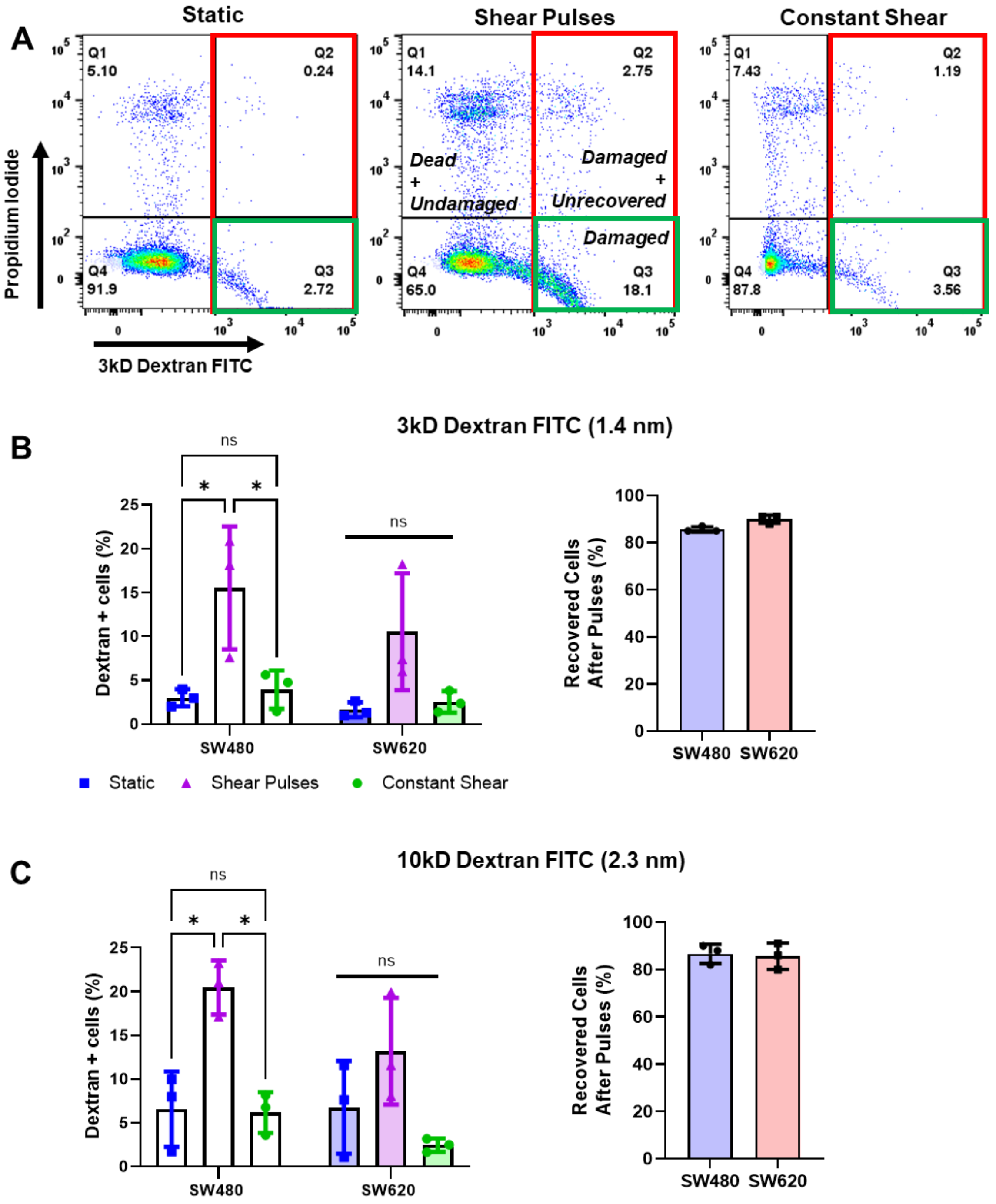

Figure 4.4. Shear pulses cause cell membrane damage, indicated by membrane pore formation, which is rapidly repaired. (A) Representative flow plots demonstrating enhanced dextran internalization after pulses of FSS. The percentage of damaged cells are shown in red and green (dextran+, Q3 and Q2), while the percentage of damaged cells that were unrecovered are shown in green (dextran+ and PI+, Q2 only). (**B-C**) Quantification of cell membrane damage and repair for 3k and 10k MW dextran, respectively. Percentage of recovered cells were calculated by dividing the population of damaged and recovered cells (Dextran+/PI+, Q3) by the total number of damaged cells (Dextran+, Q2 + Q3). N=3, ns = not significant, *p<0.05 (two-way ANOVA with multiple comparisons). Error bars represent mean ± SD.

4.3.4 FSS and resveratrol sensitize SW480 cells to TRAIL-mediated apoptosis

Despite significant decreases in cell viability in the SW480 cell line after FSS, both cell lines remained relatively resistant, and less than 30% of cells were apoptotic. Circulatory shear stress has been shown to sensitize cancer cells to chemotherapeutic agents and targeted therapies. We have demonstrated this previously in multiple cancer types with the use of TRAIL [272]. Shear pulses significantly sensitized SW480 cells to 50 ng/ml of TRAIL, while constant shear had minimal effects (**Figure 4.5A, B**). Interestingly, both forms of shear stress had no effect on TRAIL sensitization in SW620 cells (**Figure 4.5C**).

To investigate whether these cancer cells could be further sensitized to TRAIL via lipid raft alteration, we added a condition where cells were pre-treated with resveratrol before FSS. Resveratrol (RSV) is a polyphenol compound that has shown to have pleotropic effects on cancer cells, specially through its ability to form tightly packed liquid-ordered domains in the cell membrane [266]. Resveratrol has the ability to sensitize cancer cells to TRAIL under static conditions but hasn’t been investigated in the context of physiological FSS [65,254]. Additionally, resveratrol predominantly integrates into the plasma membrane within minutes of treating cells [308]. Taking this into account, cells were pretreated with 50 µM resveratrol for just 1 h, washed to remove trace amounts in solution, and then immediately exposed to FSS treatments to restrict the effects of resveratrol to the cell membrane. SW620 cells were significantly sensitized to TRAIL when pretreated with resveratrol under static conditions. However, cell viability remained similar between static and shear-treated cells regardless of treatment, further demonstrating the mechanoresistant phenotype of these cells (**Figure 4.5C**). In SW480 cells, shear pulses significantly reduced viability in the TRAIL+RSV treated condition, but this was not significantly different than FSS and TRAIL alone (**Figure 4.5B**). While FSS and resveratrol sensitize these cells to TRAIL individually, there were no appreciable synergistic effects when combined.

Our lab has determined that the mechanism for FSS-mediated TRAIL sensitization is through calcium influx [81]. To measure calcium influx in real time, cells were incubated with the acetoxymethyl (AM) ester calcium dyes Fluo-4 and FuraR, exposed to one pulse of shear stress, then immediately analyzed via flow cytometry (**Figure 4.5D**). Interestingly, there were minimal changes to intracellular calcium concentrations between static and shear conditions for both SW480 and SW620 cells (**Figure 4.5E, F).** Resveratrol caused slight increases, albeit insignificant, in calcium influx, potentially explaining the minimal changes in cell viability. While mechanical stimulation had minimal effects on intracellular calcium concentration and TRAIL-mediated apoptosis, more substantial calcium influxes were observed through treatment with chemical agonists of mechanosensitive ion channels [81].

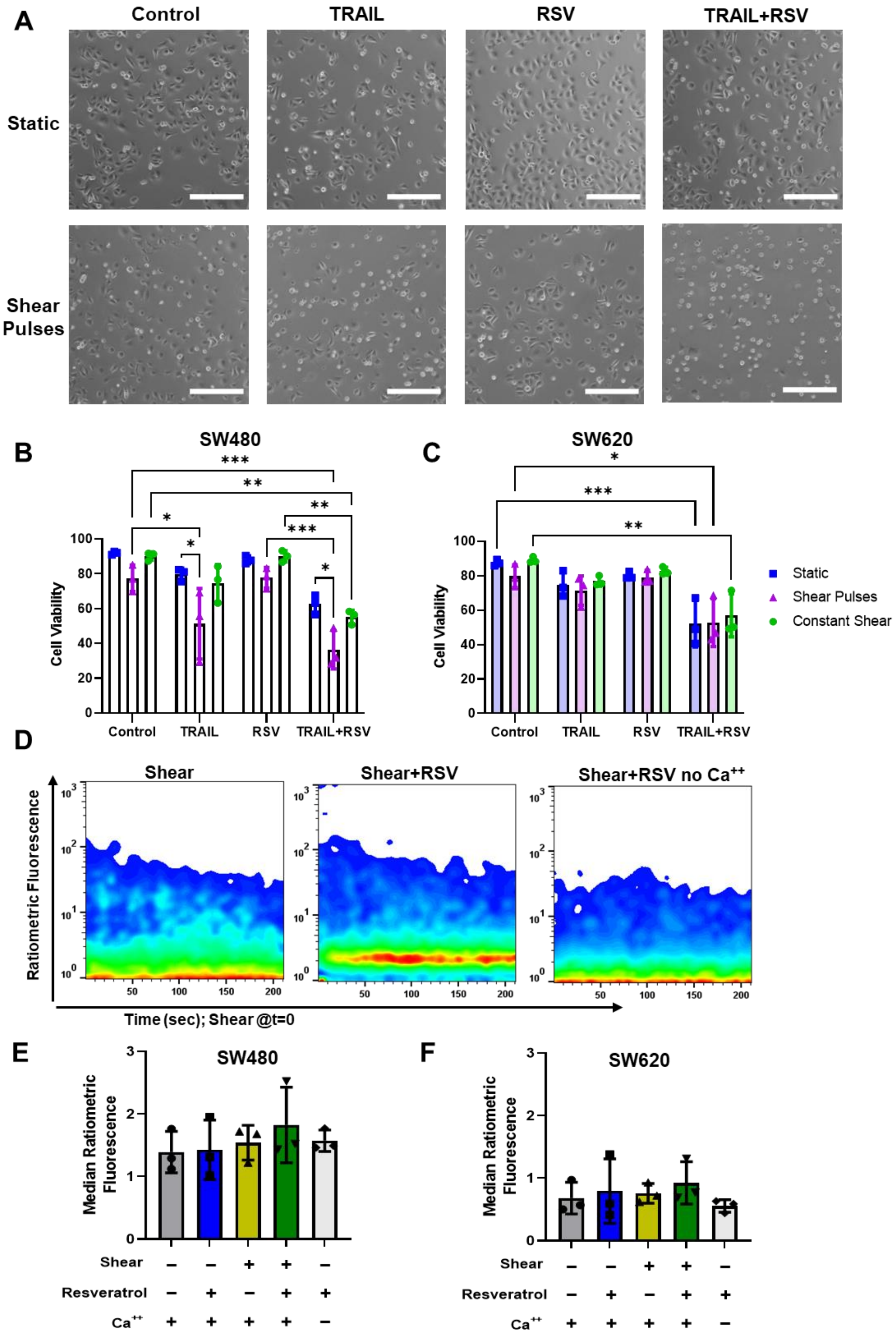
A
Control
TRAIL
RSV
TRAIL+RSV
Static
Shear Pulses
B
SW480
***
**
*
**
*
***
*
Cell Viability
0
20
40
60
80
100
Control
TRAIL
RSV
TRAIL+RSV
C
SW620
*
***
**
Cell Viability
0
20
40
60
80
100
Control
TRAIL
RSV
TRAIL+RSV
Static
Shear Pulses
Constant Shear
D
Shear
Shear+RSV
Shear+RSV no Ca++
Ratiometric Fluorescence
10^0
10^1
10^2
10^3
50
100
150
200
Time (sec); Shear @t=0
E
SW480
Median Ratiometric Fluorescence
0
1
2
3
Shear – – + + –
Resveratrol – + – + +
Ca++ + + + + –
F
SW620
Median Ratiometric Fluorescence
0
1
2
3
Shear – – + + –
Resveratrol – + – + +
Ca++ + + + + –

Figure 4.5. Shear pulses and resveratrol sensitize SW480 cells to TRAIL individually but have minimal synergistic effects. (A) Phase contrast images of SW480 cells 24 h after FSS treatment with 50 ng/ml TRAIL and 50 µM resveratrol. Samples exposed to shear pulses and treated with TRAIL+RSV displayed an increased number of apoptotic cells, as visualized by a rounded and shrunken morphology. Scale bar = 100 µm. **(B-C)** The viabilities of SW480 and SW620 cells measured via Annexin-V/PI staining following FSS treatments with or without 50 ng/ml TRAIL and 50 µM resveratrol. N=3 *$p<0.05$ **$p<0.01$ ***$p<0.001$ (two-way ANOVA with multiple comparisons). Error bars represent mean ± SD. **(D)** Ratiometric fluorescence of Fluo-4/FuraR as a metric of intracellular calcium concentration in real time. Cells were sheared with one pulse at t=0 then immediately analyzed via flow cytometry. **(E-F)** Insignificant changes in median fluorescence intensity of ratiometric calcium fluorescence for SW480 and SW620 cells, respectively. Median fluorescence was calculated over the course of the first 200 sec. N=3 (two-way ANOVA with multiple comparisons). Error bars represent mean ± SD.

4.3.5 Resveratrol increases calcium influx induced by Yoda1 chemical activation of Piezo1

To further examine the effects of mechanosensation in our isogenic CRC cell lines, we selectively activated Piezo1, a mechanosensitive ion channel that has been recently implicated in the mechanism of calcium entry and TRAIL sensitization [81]. Yoda1 is an agonist of the calcium-gated mechanosensitive ion channel Piezo1, acting as a molecular wedge within the transmembrane domain. While pretreatment with resveratrol had minimal effects on calcium influx from FSS, resveratrol did significantly increase calcium concentrations after 24 h of 10 µM Yoda1 treatment (**Figure 4.6A, B**). Interestingly, resveratrol treatment also caused cells to appear more mesenchymal in shape compared to Yoda1-only treated cells. Cell aspect ratio (a metric of spindle-shaped morphology and hallmark of EMT) was increased in resveratrol-treated cells and trended in a similar manner to calcium influx (**Figure 4.6F**). To measure instantaneous changes in cytosolic calcium, cells were treated as previously described, however with the pulse of FSS substituted with a bolus addition of Yoda1 immediately preceding analysis. Resveratrol-pretreated cells showed significantly increased activation of Piezo1, as indicated by increased concentrations of intracellular calcium (**Figure 4.6C, E**). Calcium influx increased by two-fold immediately following Yoda1 treatment and remained so for the 200 sec duration of measurement (**Figure 4.6D**).

4.3.6 SW480 cells are increasingly mechanosensitive compared to SW620 cells

While SW480 cells showed a significant increase in calcium influx from Yoda1-resveratrol combination treatment, there was no measurable difference for SW620 cells (**Supplementary Figure 4.1 A, B**). Additionally, total calcium influx remained significantly lower for SW620 cells compared to SW480 cells for all Yoda1-treated conditions (**Figure 4.6F**). This, in combination with our earlier data showing FSS-induced apoptosis and TRAIL sensitization, further supports the enhanced mechanosensation of SW480 cells compared to their metastatic counterparts. Notably, levels of calcium from Yoda1 treatment were approximately an order-of-magnitude higher than that observed after shear pulses. Considering that the level of cytosolic calcium remained relatively unchanged, and the fact that we previously showed that cell membrane damage is rapidly repaired, this could be explained by calcium-mediated mechanisms of lysosomal exocytosis, membrane patching, and cytosolic calcium buffering [309–312]. Membrane damage causes increased cytosolic calcium concentrations that remain local to the damaged site due to cytosolic buffering mechanisms which are able to decrease calcium changes by orders of magnitude in just milliseconds [309,313,314]. However, Yoda1 has been shown to initiate sustained activation of Piezo1 through stabilization of the open state for longer intervals [315].

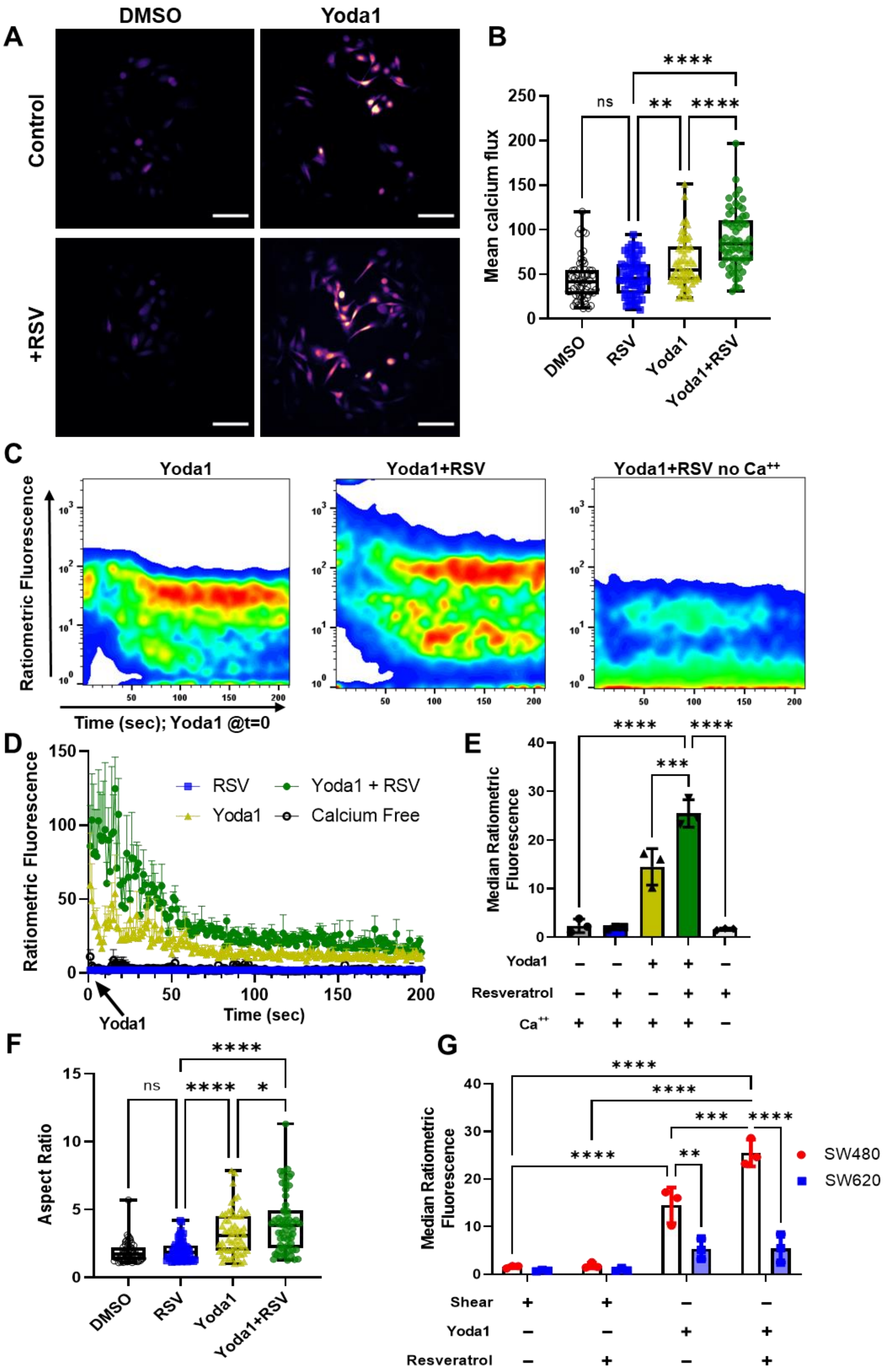
A
DMSO
Yoda1
Control
+RSV
B
Mean calcium flux
250
200
150
100
50
0
ns
**
****
****
DMSO
RSV
Yoda1
Yoda1+RSV
C
Yoda1
Yoda1+RSV
Yoda1+RSV no Ca++
Ratiometric Fluorescence
10^3
10^2
10^1
10^0
50
100
150
200
Time (sec); Yoda1 @t=0
D
Ratiometric Fluorescence
150
100
50
0
RSV
Yoda1
Yoda1 + RSV
Calcium Free
Time (sec)
Yoda1
E
Median Ratiometric Fluorescence
40
30
20
10
0
****
****
***
Yoda1 – – + + –
Resveratrol – + – + +
Ca++ + + + + –
F
Aspect Ratio
15
10
5
0
ns
****
****
*
DMSO
RSV
Yoda1
Yoda1+RSV
G
Median Ratiometric Fluorescence
40
30
20
10
0
****
****
***
****
****
**
SW480
SW620
Shear + + – –
Yoda1 – – + +
Resveratrol – + – +

Figure 4.6. Resveratrol increases calcium influx from Yoda1 in the more mechanosensitive SW480 cells. (A) Calcium imaging of Fluor-4 fluorescence after 24 h treatment of 10 µM Yoda1. Scale bar = 100 µm. **(B)** Quantification of mean calcium flux per cell after 24 h Yoda1 treatment. N=2 (60 cells per condition) **p<0.01 ****p<0.0001. **(C)** Representative time course flow cytometry plots showing instantaneous changes in SW480 calcium influx as measured by the ratiometric fluorescence of Fluo-4/FuraR. Yoda1 (10 µM) added at t=0. **(D)** Median ratiometric fluorescence as a function of time in SW480 cells. N=3. Error bars represent mean + SEM. **(E)** Average ratiometric calcium fluorescence over 200 sec after Yoda1 treatment. N=3 **p<0.01 ****p<0.0001 (one-way ANOVA with multiple comparisons). Error bars represent mean ± SD. (F) SW480 aspect ratio after 24 h treatment of Yoda1 (10 µM) and resveratrol (50 µM). N=2 (60 cells per condition) *p<0.05 ****p<0.0001. **(G)** Calcium influx comparing mechanical shear with Yoda1 activation of Piezo1 in SW480 and SW620 cells. N=3, ns = not significant, ***p<0.001 ****p<0.0001 (two-way ANOVA with multiple comparisons). Error bars represent mean ± SD.

4.3.7 Resveratrol increases colocalization of Piezo1 with lipid rafts

Numerous studies have shown that lipid rafts can amplify downstream signaling cascades through receptor oligomerization, supramolecular clustering, and scaffolding of membrane proteins [84,195]. However, little is known regarding lipid raft – mechanosensitive ion channel interplay, and how this affects channel activation. Staining for lipid rafts and Piezo1 before and after resveratrol treatment, we found that resveratrol not only increased lipid raft expression, but also increased the incidence of Piezo1 in these raft domains (**Figure 4.7A**). Resveratrol significantly increased the Pearson's correlation coefficient between Piezo1/LR in both SW480 and SW620 cells (**Figure 4.7B**). Further, resveratrol increased the FRET efficiency of Piezo1 (donor) and LR (acceptor) in both cell lines (**Supplementary Figure 4.2**). SW480 cells were found to have significantly increased expression of Piezo1 compared to SW620 cells (**Figure 4.7C, D**). This was supported by protein abundance data publicly available from the Broad Cancer Cell Line Encyclopedia [316]. Of all cell lines with proteomic data, there were two sets isolated from the same patient: SW480 and SW620 cells, and WM115 and WM2664 cells (melanoma cells isolated from the primary tumor and metastatic lymph node, respectively). Similar to our colon adenocarcinoma cell lines, the metastatic melanoma cell line exhibited decreased abundance of Piezo1 compared to cells from the primary tumor (**Figure 4.7E).** While this is only shown for two same-patient cell line models, this may support an obligatory mechanism of Piezo1 downregulation for successful survival in the circulation. FSS treatments had no effect on Piezo1 expression in either cell line (**Supplementary Figure 4.3**).

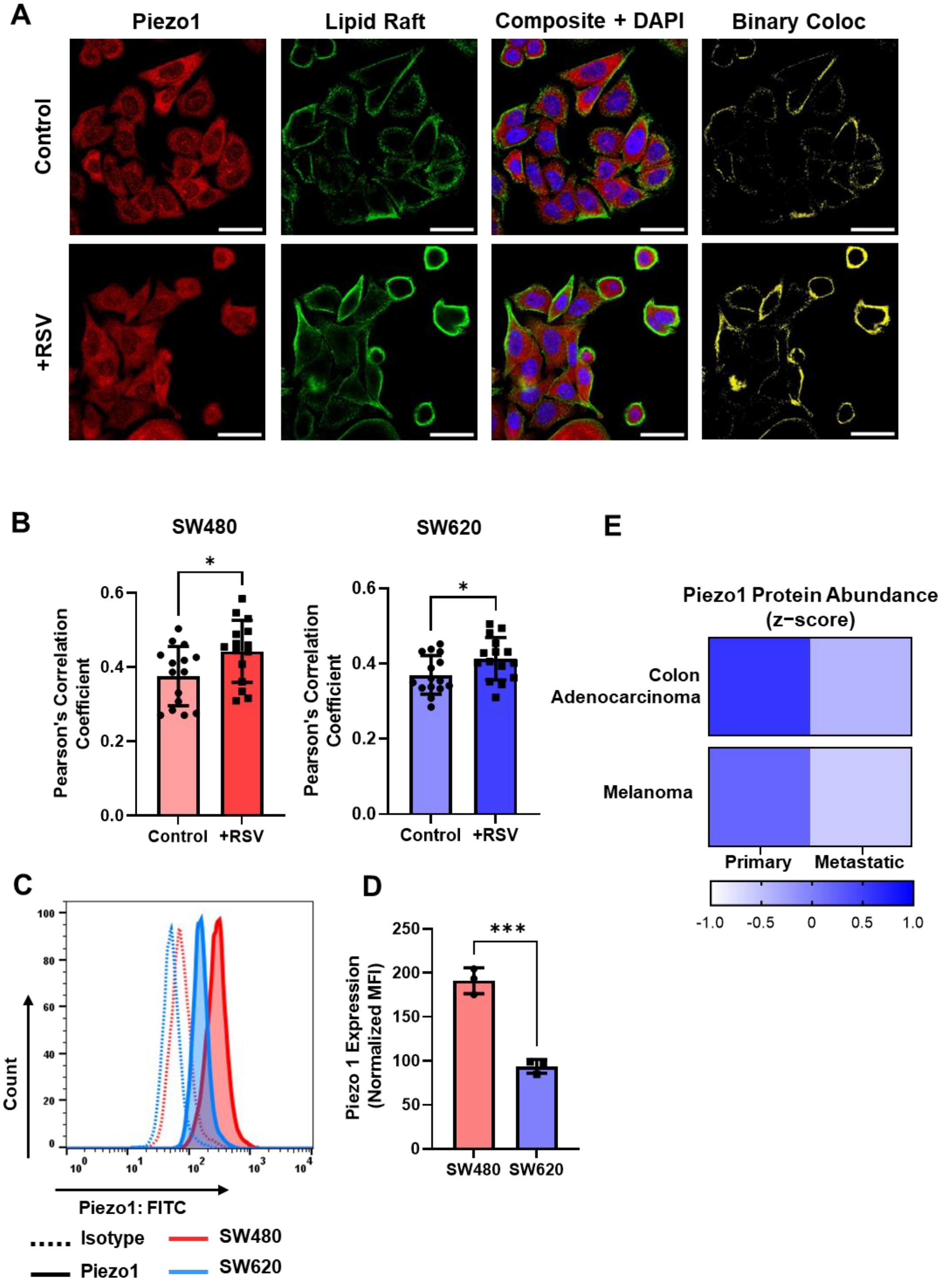

Figure 4.7. Resveratrol increases LR/Piezo1 colocalization, and SW480 cells have higher Piezo1 expression. (A) Confocal microscopy images of Piezo1 (red), lipid rafts (green), DAPI (blue) and colocalization events between Piezo1 and LR (yellow). Scale bar = 30 µm. **(B)** Pearson's correlation coefficient between LR/Piezo1 was calculated using the JACoP plugin in ImageJ. N=3 (n=15 images) *p<0.05 ***p<0.001 (two-tailed unpaired t-test). For all plots, error bars represent mean ± SD. **(C)** Expression of Piezo1 (solid line) and isotype controls (dashed lines) in SW480 (red) and SW620 (blue)

cells. **(D)** Median fluorescence intensity of Piezo1 normalized to the respective isotype control. N=3 ***p<0.001 (two-tailed unpaired t-test). **(E)** Protein abundance data (z-scores) from the Broad Cancer Cell Line Encyclopedia, downloaded from cBioPortal. Primary tumor and lymph node metastases from the same patient with colon adenocarcinoma (SW480 and SW620) and melanoma (WM115 and WM2664). Darker blue represents a higher z-score and higher Piezo1 abundance.

4.3.8 Resveratrol-induced increase in Piezo1 activation has a minimal effect on apoptosis due to calcium saturation

We hypothesized that the substantial changes in calcium influx from resveratrol+Yoda1 treated SW480 cells would have a significant effect on TRAIL-sensitivity. Surprisingly, the addition of resveratrol had no significant effect on viability following Yoda1 and TRAIL combination treatment (**Figure 4.8A**). Yoda1 sensitization, the percent decrease in viability from the addition of 10 µM Yoda1, remained unchanged between TRAIL and TRAIL+RSV treated conditions (**Figure 4.8B)**. To better understand this unexpected result, a computational model was adapted from our previous work to study how changes in calcium amplify the effects of TRAIL treatment and cause increased cellular apoptosis [81]. Apoptosis was simulated over a 24 h period by calculating the cleaved PARP (cPARP) concentration within the cells (**Supplementary Table 4.1**). A value over $5x10^5$ was considered the threshold indicative of apoptosis. Additionally, MOMP was calculated via the concentration of cytosolic Smac. The simulation was run across a range of different TRAIL concentrations, 0.5, 50, and 200 ng/ml, with 50 ng/ml matching the experiments performed *in vitro*. Calcium concentrations were taken from the flow cytometry median ratiometric fluorescence values (**Figure 4.6E**) and normalized to make the Yoda1 calcium concentration equal 1 µM. This yielded cytosolic free calcium concentrations just over 100 nM for control conditions (**Supplementary Table 4.2**), consistent with average concentrations at a resting state [317].

At the 50 ng/ml TRAIL concentration, the calcium free, control, and resveratrol treatment conditions showed that cPARP concentration did not reach a high enough level to be considered apoptotic (**Figure 4.8E**). Yoda1 calcium concentrations resulted in the cPARP concentration reaching the apoptotic threshold at t=15 h. Interestingly, at this TRAIL concentration, the increase in calcium caused by treatment with both Yoda1 and resveratrol did not result in a change in cPARP behavior in the computational model compared to just Yoda1 treatment. MOMP occurred at t=11 h in both the Yoda1 and the Yoda1+resveratrol treatment conditions (**Figure 4.8F**). The peak cytosolic Smac concentration on average was reached 4 h later in the simulations with lower intracellular calcium concentrations. Model results at the 0.5 ng/mL TRAIL condition were similar to those at the higher TRAIL dosage. In the Yoda1 and Yoda1-treatment conditions, no differences were calculated in cell apoptosis or MOMP times. The apoptotic threshold for cPARP was at the 19 h timepoint (**Figure 4.8C**). This is 4 h later than simulations corresponding to 50 ng/mL of TRAIL as an initial condition. The maximum concentration of cytosolic Smac for both groups occurred at the 17 h timepoint (**Figure 4.8D**). In the groups with lower initial calcium concentrations, the MOMP occurred 5 h later than the high calcium concentration conditions. Treatment with 200 ng/mL of TRAIL in the computational model showed minimal differences to the results using 50 ng/mL in both the cPARP and cytosolic Smac concentrations (**Figure 4.8G, H**). These results parallel the trends seen *in vitro*, where increasing TRAIL concentrations from 50 to 200 ng/mL had little effect on cell viability (**Supplementary Figure 4.4)**. According to these simulations, and in agreement with our experimental results, the extent of calcium needed to sensitize the cells to TRAIL was saturated at 1 µM by just Yoda1 treatment. Therefore, the additional influx of calcium (1.7 µM) by also treating with resveratrol had little effect on cell viability.

To better understand how variation in cancer cell populations can affect TRAIL sensitization via increased intracellular calcium concentrations, heterogeneous cell populations were simulated by running the model with randomly generated cytosolic Bcl-2 and XIAP concentrations. These proteins are inhibitors of apoptosis and were chosen based on their importance in regulating MOMP [81]. Simulated cancer cell populations were treated with each of the calcium concentrations described throughout the study to assess the changes in cell viability in each random cell population. Overall, model results showed consistency with the experimental results. **Figure 4.9A** shows the model output for cPARP over the course of 24 h in the calcium free condition treated with 50 ng/mL of TRAIL, where each individual line is the fate of one of the 1000 cells in the random population. Simulated cell viability in the calcium free condition was 71%. The viability was similar with TRAIL treatment in the control (**Figure 4.9B**) and the resveratrol only (**Figure 4.9C**) conditions, calculated to be 68% and 70%, respectively. In the groups with increased intracellular calcium concentration, the effect of TRAIL on cancer cell viability was more pronounced. Yoda1 and TRAIL treatment resulted in 47% cell viability after 24 h in the simulated experiments (**Figure 4.9D**). Adding resveratrol had a minimal effect on the sensitization of the cancer cells to TRAIL with a calculated cell viability of 46%. (**Figure 4.9E**). The *in vitro* and *in silico* models of calcium influx maintained a high degree of fidelity, confirming the saturating effect of calcium concentrations on cellular apoptosis above 1 µM (**Figure 4.9F**).

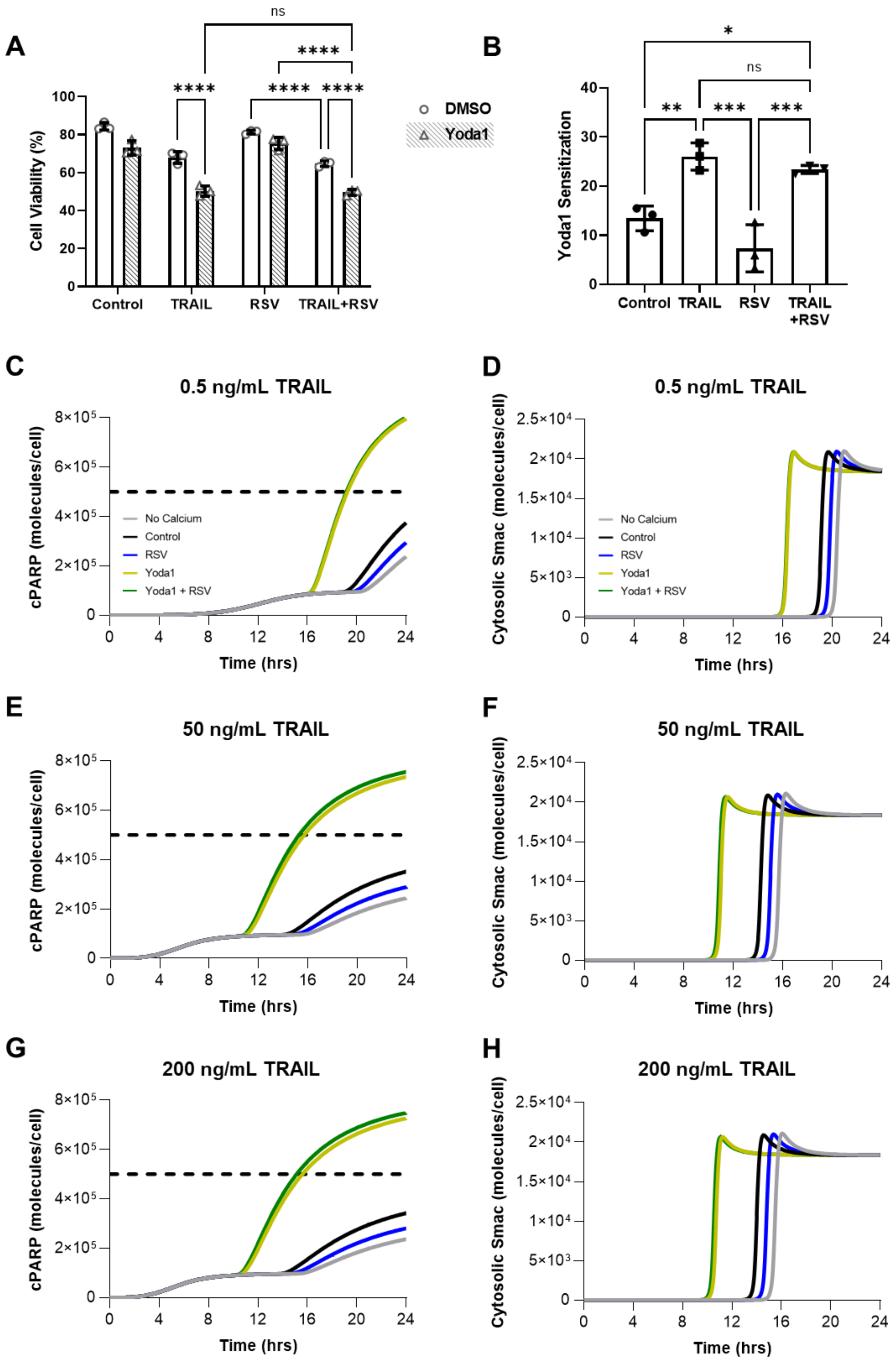
A
ns
****
****
****
****
100
80
60
40
20
0
Cell Viability (%)
Control
TRAIL
RSV
TRAIL+RSV
DMSO
Yoda1
B
*
ns
**
***
***
40
30
20
10
0
Yoda1 Sensitization
Control
TRAIL
RSV
TRAIL +RSV
C
0.5 ng/mL TRAIL
8×10^5
6×10^5
4×10^5
2×10^5
0
cPARP (molecules/cell)
No Calcium
Control
RSV
Yoda1
Yoda1 + RSV
0
4
8
12
16
20
24
Time (hrs)
D
0.5 ng/mL TRAIL
2.5×10^4
2×10^4
1.5×10^4
1×10^4
5×10^3
0
Cytosolic Smac (molecules/cell)
No Calcium
Control
RSV
Yoda1
Yoda1 + RSV
Time (hrs)
E
50 ng/mL TRAIL
cPARP (molecules/cell)
Time (hrs)
F
50 ng/mL TRAIL
Cytosolic Smac (molecules/cell)
Time (hrs)
G
200 ng/mL TRAIL
cPARP (molecules/cell)
Time (hrs)
H
200 ng/mL TRAIL
Cytosolic Smac (molecules/cell)
Time (hrs)

Figure 4.8. Resveratrol has a minimal effect on the TRAIL sensitizing ability of Yoda1. (A) SW480 cells treated for 24 h with 10 µM Yoda1 and 50 ng/ml TRAIL with or without 50 µM pretreatment with resveratrol. N=3 ****p<0.0001 (two-way ANOVA with multiple comparisons). Error bars represent mean ± SD. **(B)** Yoda1 sensitization from cell viabilities shown in (A). N=3, , ns = not significant, *p<0.05 **p<0.01 ***p<0.001 (one-way ANOVA with multiple comparisons). Error bars represent mean ± SD. **(C-H)** Computational model of apoptosis for 0.5 ng/ml, 50 ng/ml and 200 ng/ml TRAIL measuring concentrations of cleaved PARP and cytosolic Smac over time. *In vitro* calcium concentrations were used and normalized to Yoda1 (1 µM). Cells were considered apoptotic at cPARP concentrations exceeding $5x10^5$ molecules/cell.

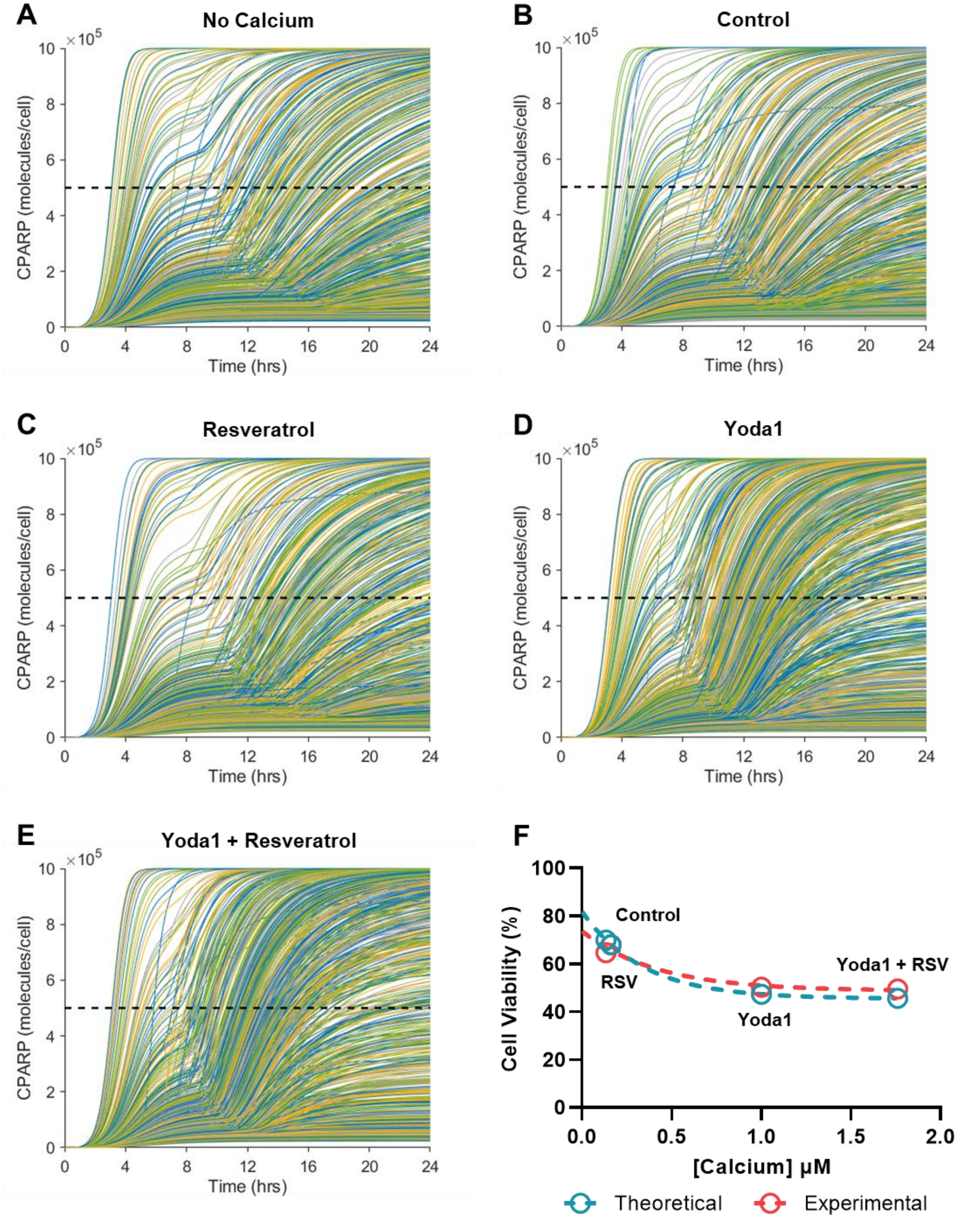

Figure 4.9. Computational modeling and experimental data demonstrate the saturating effects of increased calcium on cell apoptosis. (A-E) Simulation of heterogeneous cell populations with randomly generated, but normally distributed, cytosolic Bcl-2 and XIAP concentrations. Each line represents one cell with a randomized concentration of each protein, and each simulation was run for 1000 cells. A cPARP

concentration of 5×10^5 molecules/cell was used as the apoptotic threshold for each cell (cells above this line after 24 h were considered apoptotic). Cell viability was determined as the percentage of cells below this concentration after 24 h. **(F)** Theoretical (blue) and experimental (red) cell viabilities as a function of measured calcium influx (normalized to Yoda1) (nonlinear regression, one phase decay).

4.4 Discussion

Previous studies have shown that cancer cells are more resistant to fluid shear stress than cells from healthy epithelial origins [297,318,319]. Additionally, there is evidence that the propensity for FSS survival may predict metastatic organotropism in prostate cancer cell lines [294]. Similarly, our results demonstrate that CRC cells derived from a metastatic lymph node are more resistant to FSS than cells from the primary tumor. Given the isogenic nature of our cell lines, we can therefore draw conclusions on the phenotypic changes these cells undergo in order to survive and adapt to different fluid environments. While cells from the primary tumor showed the most significant increases in apoptosis, both cell lines remained relatively resistant to FSS death and displayed modest changes in mitochondrial depolarization. Moving forward, it is imperative that we work to understand the mechanisms of shear-resistance in metastatic cells. Similar to mechanisms of chemoresistance, which can be either intrinsic or acquired, future studies should examine whether FSS selects for subpopulations of cancer cells that are intrinsically insensitive to these physical forces, or if cells are primed by the circulation to make them more “mechanoresistant”.

Our results show that not all forms of fluid shear stress are alike. While both forms of FSS caused decreases in SW480 cell viability, cells responded in very distinct ways across these conditions. Shear pulses of high magnitudes acted in a manner dependent upon the biophysical properties of the cell membrane. Despite significant increases in cell membrane damage and the formation of pores at least 2.3 nm in size, cells were able to rapidly repair their membrane, likely explaining their ability to resist death. We have demonstrated that cell stiffness strongly correlates with FSS survival and softening agents that disrupt actin polymerization, such as cytochalasin D, can increase sensitivity to FSS [294]. However, SW480 cells have been shown to have a higher Young’s modulus and stiffer cytoskeleton than SW620 cells [320], suggesting that cell stiffness alone may not be an accurate predictor of FSS survival. For instance, endocytosis of plasma membrane wounds and subsequent repair mechanisms have been shown to occur in both a calcium-and lipid raft-dependent manner [309,321].

Meanwhile, shear stress treatments mimicking the conditions experienced by CTCs in the circulation caused decreased proliferation, most pronounced in SW480 cells. This is consistent with another study in CRC cells where FSS decreased proliferation though increased expression of β-catenin and c-myc [322]. Furthermore, c-myc has been implicated not only as a regulator of proliferation, but also in the expression of CSC markers such as CD133 in gliomas and other cancers [323]. This is consistent with the present results, as constant shear stress of 10 dyne/cm^2 caused significant upregulation of CD133 expression in surviving SW480 cells. This increase in CSC populations with EMT hallmarks and increased metastatic potential has also been observed in breast and lung cancer [295,296]. Additionally, decreased proliferation and increased invasiveness is a hallmark of the CSC phenotype [324]. Our results further support the role of FSS in metastatic priming.

These data also suggest that prolonged FSS may desensitize metastatic cancer cells to mechanisms of mechanotransduction. Metastatic SW620 cells were not only more resistant to apoptosis, but also resisted FSS-induced TRAIL sensitization and calcium influx upon Piezo1 activation. Furthermore, examining protein abundance data in primary and metastatic cells derived from the same CRC and melanoma patient, we highlighted that cells derived from lymph node metastases showed consistently downregulated expression of Piezo1. This is consistent with our *in vitro* results which showed that surface expression of Piezo1 was decreased in SW620 cells. This begs the question of whether downregulation of mechanosensitive ion channels such as Piezo1 is necessary for metastasis to occur. Another possibility is that FSS naturally selects for subpopulations of cancer cells that are impervious to the stress of shear due to lower innate levels of Piezo1. This is an interesting dichotomy, as numerous studies have implicated Piezo1 as a driver of cancer progression and many pro-metastatic processes [80]. Future studies should elucidate this role of Piezo1 in priming CTCs for survival in transit, for instance by using additional isogenic cell models of metastasis.

There is strong evidence that plasma membrane lipid composition has an effect on mechanosensitive ion channels such as Piezo1 [301,302]. In prior studies, depletion of cholesterol from the cell membrane using methyl-β-cyclodextrin decreased the chances of channel activation from mechanical stimuli and increased the force needed for opening. This highlights the biophysical requirements of the cell membrane for proper mechanosensitive ion channel activation, as cholesterol has been shown to increase membrane stiffness and rigidity [325]. Cholesterol is also an integral component of lipid rafts, however, surprisingly there are no studies investigating the role of lipid rafts in mechanosensitive ion channel function. Treatment with resveratrol, which has been well characterized to rapidly assimilate into the cell membrane to promote the formation of lipid-ordered domains [266,308], significantly increased Piezo1 colocalization with lipid rafts in both cell types. However, this increased raft colocalization corresponded to increased calcium influx and Piezo1 activation selectively in SW480 cells. This is hypothesized to be due to the aforementioned lower Piezo1 content in these cells. We postulate that like cholesterol, lipid rafts and resveratrol increase membrane rigidity locally, thereby stabilizing Piezo1 in an open state once activated via mechanical deformation or molecular wedging. Future studies should examine the molecular and biophysical mechanisms of this phenomenon.

Despite resveratrol's ability to facilitate the activation of Piezo1, we observed that ultimately there was little resulting enhancement to cell apoptosis. This was confirmed in our computational model of apoptosis, where cytosolic calcium concentrations exceeding 1 μM had minimal effects on cleaved PARP, release of cytosolic Smac, and eventual apoptosis. Despite a minimal change in apoptosis, it is possible that this increase in calcium could have consequential effects on other cellular processes not directly examined here. Calcium is a well-studied secondary messenger in many oncogenic and metastatic signaling processes, such as migration, invasion, proliferation and EMT [326]. In this study, we observed that increased calcium concentrations from Yoda1 and resveratrol correlated with increased aspect ratio, a hallmark of EMT. While there were insignificant changes in apoptosis within our *in vitro* and *in silico* models, future studies should examine these other calcium-related downstream effects related to cancer progression and metastasis.

In conclusion, SW480 cells from the primary tumor are more sensitive to FSS than SW620 cells that had successfully metastasized *in situ*. SW480 cells saw enhanced apoptosis, senescence, calcium influx, and TRAIL sensitization following FSS. High magnitude FSS pulses caused the formation of pores in the cell membrane which were rapidly repaired. Meanwhile, sustained levels of moderate FSS induced stem-like features, including increased CD133 expression and decreased cell proliferation. Metastatic SW620 cells had decreased Piezo1 expression, potentially demonstrating a necessity of Piezo1 downregulation for the survival of cancer cells in transit. Future studies should examine this clinically to see if non-apoptotic CTCs and cells from metastatic lesions are low Piezo1 expressors, or if this effect is unique to the circulation. This may inform treatment strategies for the small subpopulations of CTCs that are able to survive and colonize secondary sites. Additionally, the Piezo1 molecular agonist Yoda1 significantly increased intracellular calcium levels in SW480 cells, which was further increased through resveratrol-induced lipid raft colocalization of Piezo1. This presents a novel role for lipid rafts in the enhanced activation of Piezo1, which may also be present in other mechanosensitive ion channels. Moving forward, clinical utilization of lipid raft altering agents such as resveratrol or methyl-β-cyclodextrin should be explored to enhance or curb Piezo1 activation, respectively. Calcium is a secondary messenger that is involved in many premetastatic processes. Indirectly tailoring Piezo1 activation via pharmacological alteration of lipid rafts may be an elegant way to curb mechanotransduction events essential to metastasis. However, improved systemic delivery strategies will be crucial for translational adoption into the clinic.

4.5 Materials and Methods

4.5.1 Cell Culture

Colorectal cancer cell lines SW620 (ATCC, #CCL-227) and SW480 (ATCC, #CCL-228) were purchased from American Type Culture Collection. Cells were cultured in RPMI1640 cell culture medium (Gibco). Media was supplemented with 10% (v/v) fetal bovine serum and 1% (v/v) PenStrep, all purchased from Invitrogen. Cells were passaged at 70% confluency by washing with HBSS without calcium or magnesium (Gibco) and lifting with Trypsin-EDTA (0.25%) (Invitrogen). Both cell lines were maintained in a humidified incubation chamber at 37°C and 5% CO_2. SW480 cells are characterized as being epithelial in morphology with apical-basal polarity, while SW620 cells are increasingly mesenchymal with a loss in epithelial characteristics and polarity. Cells were screened for mycoplasma contamination and tested negative.

4.5.2 Fluid Shear Stress Treatments

To model different types of physiological shear stress, cells were exposed to three different shear conditions: static, shear pulses or constant shear. For shear pulses, 2 ml of media containing 200,000 cells/ml were loaded into a 5 ml syringe with a 30-gauge x ½ in needle. Syringes and needles were blocked for 30 min with 5% bovine serum albumin (BSA, Sigma) in HBSS before loading. Cells were sheared using a syringe pump (Harvard Apparatus) at a flow rate of 14 mL/min, as previously described [294]. Average shear stress was calculated to be 3950 dyne/cm^2 (395 Pa). Cells were exposed to 10 pulses with 2 min between each pulse, modeling the time it would take a cell to pass once through the entire circulatory system circuit [305]. To model constant fluid shear stress, 0.5 ml of cells in media were loaded into a cone-and-plate viscometer (Brookfield LVDVII) at a concentration of 1 million cells/ml (higher cell concentrations were used to increase viscosity and subsequently increase shear stress). Before loading cells, both the spindle and cup was blocked with 5% BSA for 30 min. Cells were sheared at 100RPM (740 s^{-1}) using the CP-40Z spindle for 2.5 hours with an approximate shear stress of 10 dyne/cm^2. Following treatment, cells were collected, and the cup and spindle were rinsed with 0.5 ml of fresh media to collect remaining cells. Static cells were left in a 1.5 mL conical tube at a concentration of 200,000 cells/ml while shear experiments were being performed. After FSS treatments, 1 ml of cell suspension was plated in a 12-well plate (CELLTREAT) and incubated overnight for subsequent analysis.

4.5.3 Annexin V/Propidium Iodide Apoptosis Assay

Cells were incubated for 24 h after shear treatments, then collected by recovering the supernatant and lifting the remaining adhered cells using 0.25% Trypsin-EDTA (Gibco). Cells were washed thoroughly with HBSS with calcium and magnesium and incubated for 15 min with FITC-conjugated Annexin-V and propidium iodide (PI) (BD Pharmingen) at room temperature (RT) in the absence of light. Cells were immediately analyzed using a Guava easyCyte 12HT benchtop flow cytometer (Millipore Sigma). Viable cells were identified as negative for both Annexin-V and PI, early apoptotic cells as positive for Annexin-V only, late apoptotic cells were positive for both Annexin-V and PI, and necrotic cells were positive for PI only. Flow cytometry plots were analyzed using FlowJo v10.8.0 software. Control samples included: unstained negative control with no Annexin-V/PI to adjust for background and autofluorescence, and Annexin V only and PI only samples for gating and compensation purposes.

4.5.4 JC-1 Mitochondrial Membrane Potential Assay

Following FSS treatments and overnight incubation, cells were lifted and collected as previously described. Cells were washed with HBSS without calcium or magnesium and incubated for 15 min with JC-1 dye (Abcam) in a humidified incubation chamber at 37°C. Cells were washed and JC-1 fluorescence was assessed via flow cytometry. Cells with healthy mitochondria were identified as having higher red fluorescence and lower green fluorescence, while those with depolarized mitochondria had lower red JC-1 fluorescence and higher green fluorescence.

4.5.5 Cell Cycle and Ki67 Proliferation Assay

Cells were incubated for 24 h after shear treatments, then collected by recovering the supernatant and lifting the remaining adhered cells using 0.25% Trypsin-EDTA (Gibco). Cells were washed twice with HBSS with calcium and magnesium, then resuspended in 50 µL of HBSS-/-. Then, 450 µL of chilled 70% ethanol in DI water was added to the cell suspension in a dropwise manner while vortexing to minimize cell aggregation. The cell suspension was incubated for 2 h at -20 ºC. Cells were washed twice with FACS buffer (HBSS with 1% BSA), then incubated with 5 µl PE anti-human Ki-67 (Biolegend, clone Ki-67) in 100 µl HBSS for 30 min at RT. Cells were washed twice, then incubated with 100 µl DAPI solution (3 µM in FACS buffer) for 15 min. Samples were then analyzed via flow cytometry using Blue-V (DAPI) and Yellow-B (PE-Ki67) channels. Cell cycle was determined using Watson Pragmatic modeling in FlowJo. Cell proliferation was determined by assessing Ki67+ cell population and gates were established from an unstained control sample.

4.5.6 Cell Membrane Damage and Repair

Cells were sheared as previously described in the presence of 10 µM FITC-conjugated dextran of 3,000 or 10,000 MW (Invitrogen). Cells were incubated for 5 min before shear and maintained in the dextran solution for the duration of the shear treatment. The cells were then allowed to recover for 20 min post-shear, washed with HBSS with calcium and magnesium, and incubated with PI (hydrodynamic radius ~0.8 nm) for 10 min to measure membrane repair. Samples were analyzed via flow cytometry using Green-B (FITC) and Red-B (PI) channels. Cells positive for FITC-dextran but negative for PI were considered damaged and repaired while FITC-dextran positive/PI positive cells were interpreted to be damaged and unrepaired.

4.5.7 Cancer Stem Cell Markers

After FSS treatments, cells were collected by recovering the supernatant and lifting the remaining adherent cells using 0.25% Trypsin-EDTA. Cells were fixed in 4% PFA in HBSS for 15 min at RT, washed twice with HBSS, then blocked in 100 µl FACS buffer for 30 min at 4°C. Samples were stained with 5 µl of both Brilliant Violet 421 anti-human CD133 (Biolegend, clone 7) and FITC anti-human CD44 (Biolegend, clone BJ18) for 30 min at 4°C. Samples were washed twice with HBSS and then incubated with PI to exclude dead cells from analysis. Samples were analyzed using a Guava easyCyte flow cytometer utilizing Blue-V (Brilliant Violet 421), Green-B (FITC) and Red-B (PI) channels.

4.5.8 *TRAIL and Resveratrol Treatments*

A 20 mM stock solution of resveratrol (Sigma-Aldrich) in DMSO was made fresh before each experiment. After cells were collected but prior to shear/Yoda1 treatments, cells were incubated with 50 µM resveratrol for 1 h at 37°C in serum-free media. To remove trace amounts of resveratrol remaining in solution that were not taken up by the cells, samples were centrifuged at 300xg for 5 min and the media was aspirated. Cells were resuspended in serum-containing media in the presence or absence of 50 ng/ml TRAIL. For FSS experiments, cells were then sheared as described previously and plated in 12-well cell culture plates for 24 h. For Yoda1 experiments, cells were treated with 10 µM Yoda1 (Tocris) and then incubated for 24 h. The next day, apoptosis was analyzed using Annexin V/PI staining and flow cytometry. Yoda1 sensitization was calculated using the following formula:

$$\text{Yoda1 Sensitization} \quad = \frac{(\%\text{DMSO viability}) - \ (\%\text{Yoda1 viability})}{(\%\text{DMSO viability})} * 100\%$$

for each treatment condition (Control, TRAIL, resveratrol, and TRAIL+resveratrol).

4.5.9 *Calcium Influx*

200,000 cells were collected in 1ml of serum free media and incubated for 30 min with 1 µM Fluo-4 and 2 µM Fura Red (Invitrogen) at 37 °C. For resveratrol-treated samples, cells were treated for 1 h with 50 µM resveratrol before incubating with calcium dyes. Cells were washed in calcium/magnesium-free HBSS, then resuspended in HBSS with calcium and magnesium for 30min at RT in the dark. For FSS samples, cells were sheared using the syringe pump system for 1 pulse, then immediately analyzed via flow cytometry. For Yoda1 studies, 10 µM Yoda1 was added to the cells and then immediately analyzed via flow cytometry. This allowed for a real-time analysis of calcium flux. Calcium flux was calculated as a measure of ratiometric fluorescence by dividing Fluo-4 fluorescence by Fura Red fluorescence (a higher ratiometric fluorescence would correspond with higher calcium influx).

To measure Yoda1-induced calcium influx over longer periods of time, 200,000 cells were plated in 12-well plates for 24 h. Resveratrol-treated samples were incubated with 50 µM resveratrol for 1 h at 37 °C before plating. Cells were then treated with 10 µM Yoda1 for 24 h, then incubated with 1 µM Fluo-4 for 30 min at 37 °C. Cells were washed in calcium/magnesium-free

HBSS, resuspended in HBSS with calcium and magnesium, then imaged using the green channel on an Olympus fluorescence microscope. Intracellular calcium was calculated by measuring the mean fluorescence intensity per cell and subtracting background fluorescence.

4.5.10 Confocal Microscopy

SW480 and SW620 cells were seeded onto polystyrene cell culture slides (Thermo Fisher Scientific). Cells were allowed to grow for 24 h at 37°C. Culture media was replaced with serum-free media in the presence or absence of 50 µM resveratrol for 1 h at 37 °C. Cells were then washed and lipid rafts stained using the Vybrant Alexa Fluor 488 Lipid Raft Labeling Kit (Invitrogen, V34403). Briefly, cells were incubated with Alexa488-conjugated cholera toxin subunit B (CT-B) followed by an anti-CT-B antibody to crosslink CT-B labeled rafts. Slides were fixed for 15 min with 4% paraformaldehyde (PFA) (Electron Microscopy Sciences) in PBS (Gibco) and then permeabilized using 0.1% Triton X-100 (Millipore Sigma) in PBS at RT. Slides were blocked for 2 h with 5% goat serum (Thermo Fisher Scientific) and 5% bovine serum albumin (BSA, Sigma) in HBSS. Primary staining was done overnight at 4°C with Piezo1 Monoclonal Antibody (Invitrogen clone 2-10) at a ratio of 1:100. Secondary staining was carried out with Alexa Fluor 555 goat anti-mouse IgG (H+L) (Invitrogen, A28180) for 45 min at RT (1:1000). Washes were done twice between each step for 5 min each using 0.02% Tween20 in PBS. Slides were assembled using 10 µl of Vectrashield antifade mounting media with DAPI (Vector Laboratories). Confocal imaging was performed using an LSM 880 (Carl Zeiss) with a 63×/1.40 Plan-Apochromat Oil, WD = 0.19 mm objective. At least five images were acquired per sample replicate. Pearson’s correlation coefficient was calculated for each image using the JACoP plugin in ImageJ [284].

4.5.11 Flow cytometry and FRET

Cells were cultured to 70% confluency upon collection and split into 250,000 cells per sample. Cells were fixed in 4% PFA in HBSS for 15 min at RT, then permeabilized with 0.1% Triton X-100 for 15 min with two HBSS washes between each step. Samples were blocked in 100 µl FACS buffer for 30 min at 4°C, then stained with 1 µl AlexaFluor488-conjugated Piezo1 antibody (Novus Biologicals, NBP1-78446AF488) for 30 min at 4°C. Samples were washed twice with HBSS and analyzed using a Guava easyCyte flow cytometer.

FRET analysis via flow cytometry was performed as described above, with the added step of staining for lipid rafts. After blocking in FACS buffer, cells were stained for LRs using the

Vybrant Alexa Fluor 555 Lipid Raft Labeling Kit (Invitrogen, V34404). Piezo staining was then carried out as previously described. Donor quenching FRET efficiency was calculated using the following formula:

$$\mathrm{E} = 1 - \frac{\mathrm{FI}_{\mathrm{LR+Piezo}} - \mathrm{FI}_{\mathrm{B}}}{\mathrm{FI}_{\mathrm{Piezo}} - \mathrm{FI}_{\mathrm{B}}}$$

where E is the FRET efficiency, $\mathrm{FI}_{\mathrm{LR+Piezo}}$ is the mean fluorescence intensity of the double-stained LR/Piezo1 sample (acceptor + donor), $\mathrm{FI}_{\mathrm{Piezo}}$ is the mean fluorescence intensity of the Piezo1-only stain (donor only), and FI_{B} is the fluorescence intensity of an unstained sample (background). Fluorescence intensity was recorded in the donor (Green-B) channel.

4.5.12 Computational Model of Cellular Apoptosis

The computational model was modified from the Hope et al. MATLAB-based model of Piezo1 sensitization of cancer cells to TRAIL-mediated apoptosis [81]. The simulations utilize ODEs to calculate changes in protein concentrations via mass action kinetics in the TRAIL-Piezo1-apoptosis pathway over time after treatment with TRAIL and various calcium flux stimulants. The main modification to the model was the addition of a random, normally distributed Bcl-2 and XIAP concentration generator for the random population analysis. Random-normal concentrations of cytosolic Bcl-2 (mean = 1.98×10^6; median = 1.98×10^6; standard deviation = 9.91×10^5) and XIAP (mean = 1.01×10^5; median = 1.01×10^5; standard deviation = 9.91×10^4) were generated and the model was run using 50 ng/ml as the TRAIL treatment. Simulated cells were considered apoptotic once their calculated cPARP exceeded a concentration of 5×10^5 molecules per cell. Cell viability was calculated as the percentage of cells which had not exceeded this apoptosis threshold. The biochemical reactions and their associated rate constants are listed in **Supplementary Table 4.1**. The non-zero initial conditions used in the model are displayed in **Supplementary Table 4.2**.

4.6 Supplementary Figures

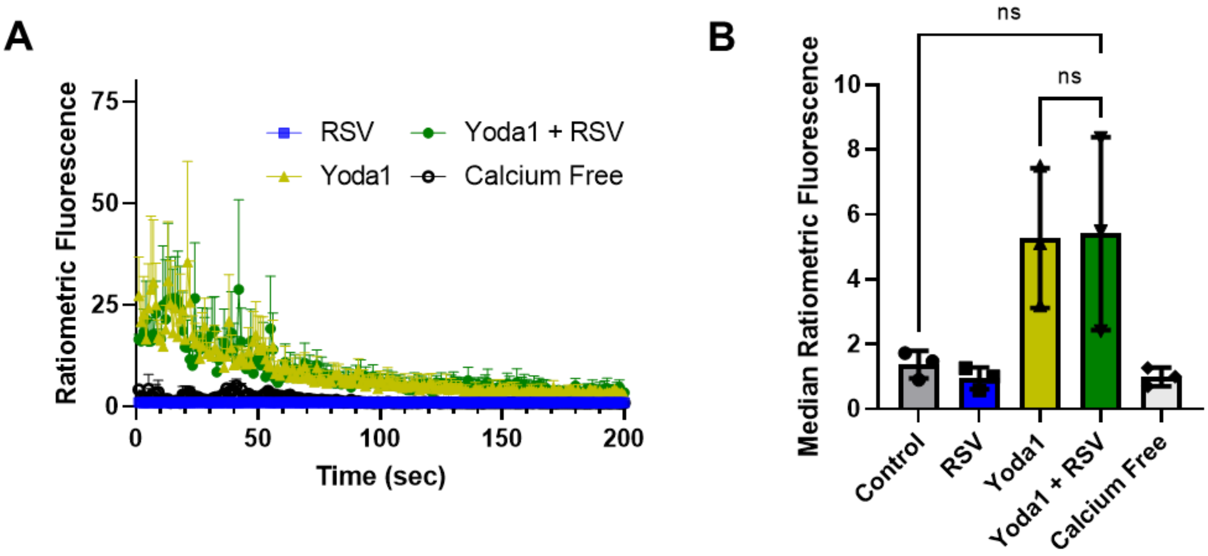

Supplementary Figure 4.1. Resveratrol has no effect on calcium influx following Yoda1 treatment in SW620 cells. (A) Median ratiometric fluorescence as a function of time in SW620 cells. N=3. Error bars represent mean + SEM. **(B)** Average ratiometric calcium fluorescence over 200 sec after Yoda1 treatment. N=3, *ns = not significant* (one-way ANOVA with multiple comparisons). Error bars represent mean ± SD.

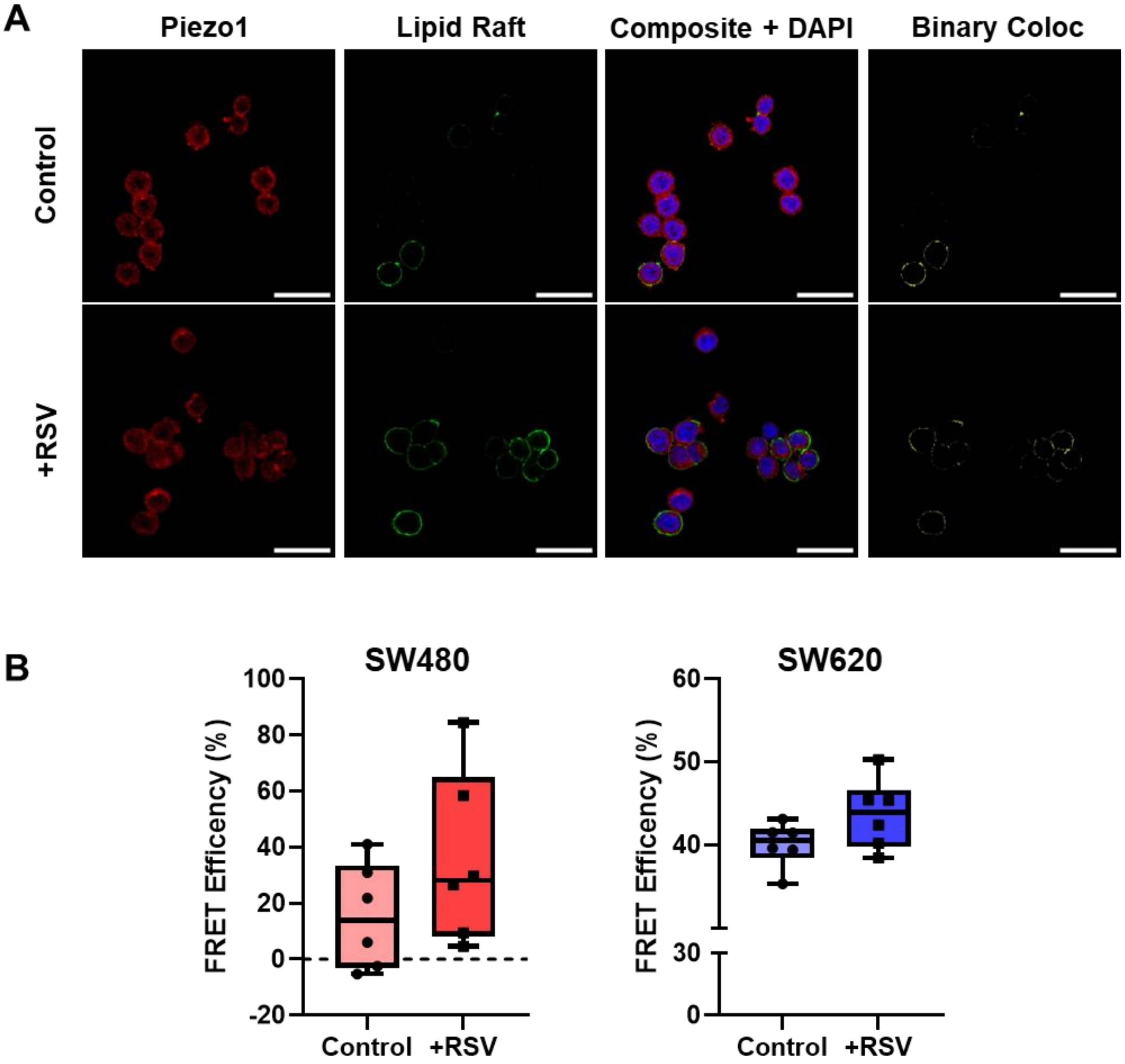

Supplementary Figure 4.2. Resveratrol increases Piezo1-lipid raft colocalization. (A) Confocal microscopy images of Piezo1 (red), lipid rafts (green), DAPI (blue) and colocalization events between Piezo1 and LR (yellow) in SW620 cells. Scale bar = 30 µm. **(B)** FRET efficiency measured via flow cytometry for SW480 and SW620 cells. N=3 (n=6).

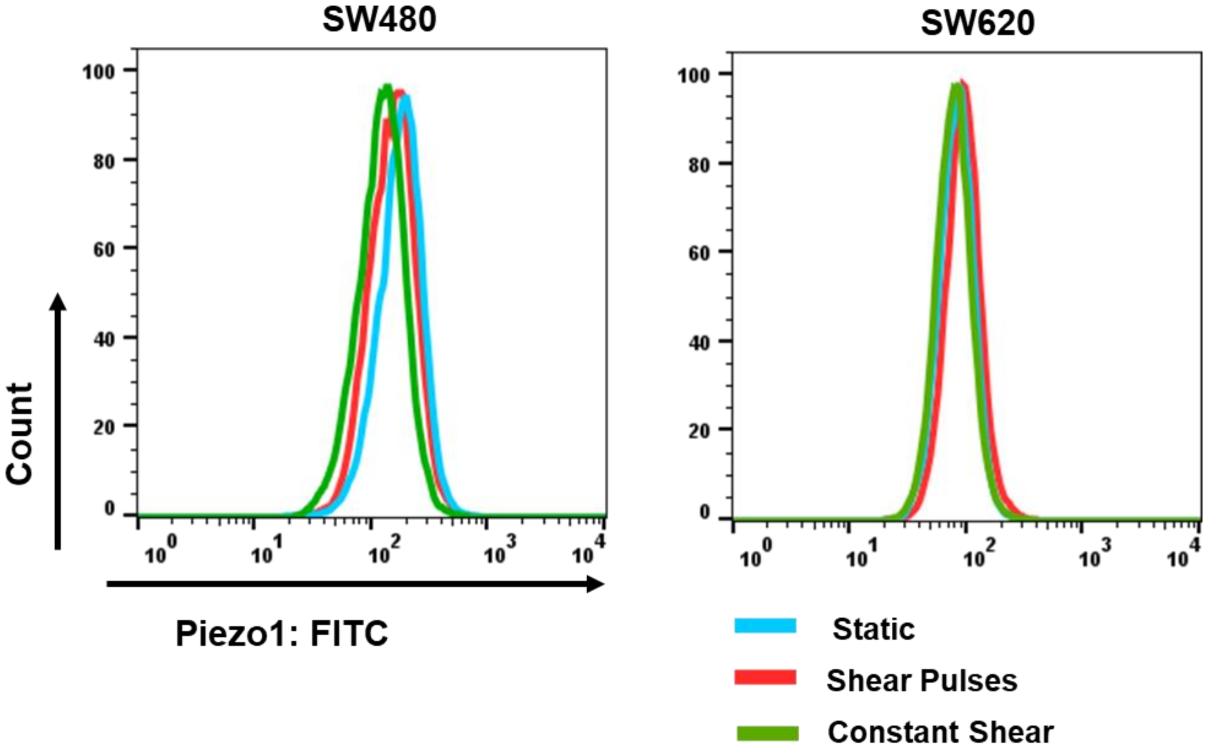

Supplementary Figure 4.3. Fluid shear stress shows no appreciable effect on Piezo1 expression.

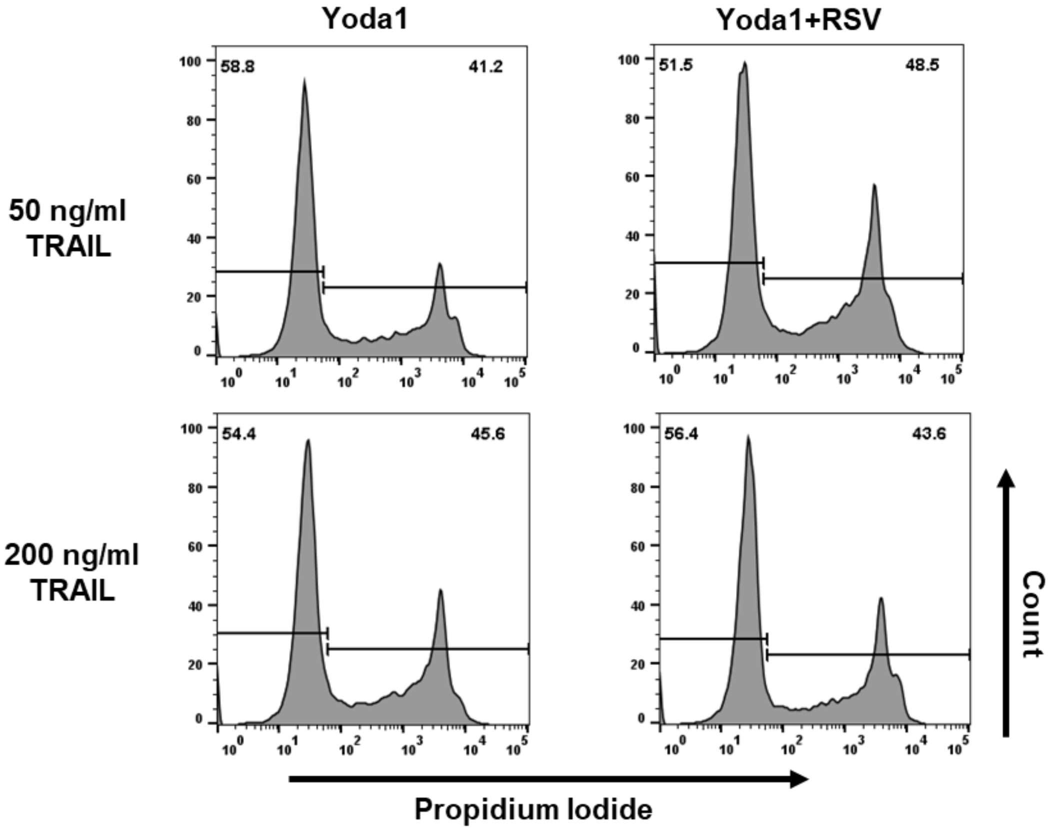

Supplementary Figure 4.4. Cell viability is similar for SW480 cells treated with Yoda1 and 50 ng/ml or 200 ng/ml of TRAIL.

Reaction	k_i	k_{-i}	k_c	Ref.
$L + R \leftrightarrow L{:}R \rightarrow R^*$	$4*10^{-6}$	$5*10^{-3}$	$1*10^{-5}$	[327]
$flip + DISC \leftrightarrow flip{:}Disc$	$5*10^{-7}$	$5*10^{-4}$	NA	[327]
$pC8 + DISC \leftrightarrow pC8{:}DISC \rightarrow C8 + DISC$	$5*10^{-7}$	$5*10^{-4}$	1	[327]
$C8 + BAR \leftrightarrow C8{:}BAR$	$5*10^{-8}$	$5*10^{-4}$	NA	[327]
$pC3 + C8 \leftrightarrow pC3{:}C8 \rightarrow C3 + C8$	$5*10^{-8}$	$5*10^{-4}$	1	[327]
$pC6 + C3 \leftrightarrow pC6{:}C3 \rightarrow C6 + C3$	$5*10^{-7}$	$5*10^{-4}$	1	[327]
$pC8 + C6 \leftrightarrow pC8{:}C6 \rightarrow C8 + C6$	$6*10^{-9}$	$5*10^{-4}$	1	[327]
$XIAP + C3 \leftrightarrow XIAP{:}C3 \rightarrow XIAP + C3_{ub}$	$2*10^{-7}$	$1*10^{-4}$	$1*10^{-4}$	[327]
$PARP + C3 \leftrightarrow PARP{:}C3 \rightarrow cPARP + C3$	$1*10^{-7}$	$1*10^{-3}$	1	[327]
$Bid + C8 \leftrightarrow Bid{:}C8 \rightarrow tBid + C8$	$5*10^{-7}$	$1*10^{-4}$	1	[327]
$tBid + Bcl2c \leftrightarrow tBid{:}Bcl2c$	$1*10^{-8}$	$1*10^{-4}$	NA	[327]
$Bax + tBid \leftrightarrow Bax{:}tBid \rightarrow aBax + tBid$	$1*10^{-9}$	$1*10^{-4}$	1	[327]
$aBax \leftrightarrow MBax$	0.01	0.01	NA	[327]
$MBax + Bcl2 \leftrightarrow MBax{:}Bcl2$	$1*10^{-7}$	$1*10^{-4}$	NA	[327]
$MBax + MBax \leftrightarrow Bax2$	$1*10^{-7}$	$1*10^{-4}$	NA	[327]
$Bax2 + Bax2 \leftrightarrow Bax4$	$1*10^{-7}$	$1*10^{-4}$	NA	[327]
$Bax4 + Bcl2 \leftrightarrow Bax4{:}Bcl2$	$1*10^{-7}$	$1*10^{-4}$	NA	[327]
$Bax4 + Mito \leftrightarrow Bax4{:}Mito \rightarrow AMito$	$1*10^{-7}$	$1*10^{-4}$	1	[327]
$AMito + mCytoc \leftrightarrow AMito{:}mCytoc \rightarrow AMito + ACytoc$	$2*10^{-7}$	$1*10^{-4}$	10	[327]
$AMito + mSmac \leftrightarrow AMito{:}mSmac \rightarrow AMito + ASmac$	$2*10^{-7}$	$1*10^{-4}$	10	[327]
$ACytoc \leftrightarrow cCytoc$	0.01	0.01	NA	[327]
$APAF + cCytoc \leftrightarrow APAF{:}cCytoc \rightarrow APAF^*$	$5*10^{-8}$	$1*10^{-4}$	1	[327]
$APAF^* + pC9 \leftrightarrow Apop$	$5*10^{-9}$	$1*10^{-4}$	NA	[327]
$Apop + pC3 \leftrightarrow Apop{:}pC3 \rightarrow Apop + C3$	$5*10^{-8}$	$1*10^{-4}$	1	[327]
$ASmac \leftrightarrow cSmac$	0.01	0.01	NA	[327]
$Apop + XIAP \leftrightarrow Apop{:}XIAP$	$2*10^{-7}$	$1*10^{-4}$	NA	[327]
$cSmac + XIAP \leftrightarrow cSmac{:}XIAP$	$7*10^{-7}$	$1*10^{-4}$	NA	[327]
$calcium + calpain \leftrightarrow calpain{:}ca$	$5*10^{-10}$	$1*10^{-4}$	NA	[328]
$calcium + calpastatin \leftrightarrow calpastatin^*$	$5*10^{-10}$	$1*10^{-4}$	NA	NA
$calpastatin^* + calpain{:}ca \leftrightarrow calpastatin^* \rightarrow calpain_{bl}$	$3*10^{-7}$	$1*10^{-4}$	1	NA
$C3 + calpain_{bl} \leftrightarrow C3{:}calpain_{bl} \rightarrow C3 + calpain^*$	$1*10^{-7}$	$1*10^{-4}$	1	NA
$calpain^* + Bid \leftrightarrow calpain^*{:}Bid \rightarrow tBid + calpain^*$	$5*10^{-7}$	$1*10^{-4}$	1	NA
$calpain^* + Bcl2c \leftrightarrow calpain^*{:}Bcl2c \rightarrow calpain^* + cBcl2c$	$2*10^{-7}$	$1*10^{-4}$	0.1	NA

Supplementary Table 4.1. List of reactions used in the computational model and their associated kinetic constants. Adapted from Hope, J.M.; Lopez-Cavestany, M.; Wang, W.; Reinhart-King, C.A.; King, M.R. Activation of Piezo1 Sensitizes Cells to TRAIL-Mediated Apoptosis through Mitochondrial Outer Membrane Permeability. *Cell Death Dis*. **2019**, *10*, 837. https://doi.org/10.1038/s41419-019-2063-6.)

Molecule	Basal initial condition (#/CC)	Ref.
$[\boldsymbol{Ligand}]$	$\mathbf{3000 = 50\frac{ng}{mL}}$ $\mathbf{0 = 0\frac{ng}{mL}}$ $\mathbf{30 = 0.05\frac{ng}{mL}}$ $\mathbf{12000 = 200\frac{ng}{mL}}$	[327]
$[\boldsymbol{Calcium}]$	$\boldsymbol{Calcium\ free\ buffer = 0.116}$ ($\mu\boldsymbol{M}$) $\boldsymbol{Control = 0.162}$ ($\mu\boldsymbol{M}$) $\boldsymbol{RSV = 0.134}$ ($\mu\boldsymbol{M}$) $\boldsymbol{Yoda1 = 1}$ ($\mu\boldsymbol{M}$) $\boldsymbol{Yoda1 + RSV = 1.76}$ ($\mu\boldsymbol{M}$)	*In vitro calcium values*
$[\boldsymbol{Receptor}]$	$\mathbf{200}$	[327]
$[\boldsymbol{FLIP}]$	$\mathbf{1 * 10^2}$	[327]
$[\boldsymbol{pC8}]$	$\mathbf{2 * 10^4}$	[327]
$[\boldsymbol{BAR}]$	$\mathbf{1 * 10^3}$	[327]
$[\boldsymbol{pC3}]$	$\mathbf{1 * 10^4}$	[327]
$[\boldsymbol{pC6}]$	$\mathbf{1 * 10^4}$	[327]
$[\boldsymbol{PARP}]$	$\mathbf{1 * 10^6}$	[327]
$[\boldsymbol{Bid}]$	$\mathbf{4 * 10^4}$	[327]
$[\boldsymbol{Bax}]$	$\mathbf{1 * 10^5}$	[327]
$[\boldsymbol{Mito}]$	$\mathbf{5 * 10^5}$	[327]
$[\boldsymbol{Cytochrome\ C}]$	$\mathbf{5 * 10^5}$	[327]
$[\boldsymbol{Smac}]$	$\mathbf{1 * 10^5}$	[327]
$[\boldsymbol{pC9}]$	$\mathbf{1 * 10^5}$	[327]
$[\boldsymbol{APAF}]$	$\mathbf{1 * 10^5}$	[327]
$[\boldsymbol{Calpain}]$	$\mathbf{1 * 10^5}$	[328]
$[\boldsymbol{Calpastatin}]$	$\mathbf{1 * 10^5}$	(NA)
$[\boldsymbol{cytosolic\ Bcl2}]$	$\mathbf{2 * 10^6}$	[327]
$[\boldsymbol{mitochondrial\ Bcl2}]$	$\mathbf{2 * 10^4}$	[327]
$[\boldsymbol{XIAP}]$	$\mathbf{1 * 10^5}$	[327]

Supplementary Table 4.2 Non-zero initial conditions utilized in the computational model. All species that are not listed have an initial condition equal to 1.

Chapter 5:

A Syngeneic MC38 Orthotopic Mouse Model of Colorectal Cancer Metastasis

Joshua D. Greenlee and Michael R. King

This chapter is adapted from *A syngeneic MC38 orthotopic mouse model of colorectal cancer metastasis* published in *Biology Methods and Protocols* and has been reproduced with permission of the publisher and co-author Michael King [329].

Greenlee, J.D.; King, M.R. A Syngeneic MC38 Orthotopic Mouse Model of Colorectal Cancer Metastasis. *Biology Methods and Protocols* 2022, *7*, bpac024, doi:10.1093/biomethods/bpac024.

5.1 Abstract

While subcutaneous tumor models remain the standard for studying drug efficacy *in vivo*, these tumors rarely metastasize and lack physiological relevance due to differences in the tumor microenvironment, vascularization, immune landscape and physiological cues associated with the organ of interest. Orthotopic tumors, grown from the organ corresponding with the cancer type, provide a more translational approach to study disease progression and drug efficacy. Utilization of a syngeneic mouse model allows for a complete immune landscape, key for adaptive immunotherapy studies. MC38 and CT26 cells are commonly used murine colorectal cancer cell lines with clinically relevant mutations. While CT26 cells have been orthotopically implanted with high fidelity, successful engraftment of orthotopic MC38 tumors varies greatly between studies. Thus, we have developed a detailed protocol for MC38 orthotopic tumor inoculation via intracecal injection. Nine C57BL/6 mice were injected with 2×10^6 cells into the cecal wall and sacrificed after 7-weeks. Survival after surgery was 100%, and one mouse died before the 7-week study endpoint from tumor burden and metastatic spread. We observed a successful tumor engraftment rate of 67%. Half of mice presenting with tumors were found to have macroscopic metastatic lesions in clinically relevant foci, including the mesenteric lymph nodes, liver, and peritoneum. These mice also presented with very large tumors and an enlarged spleen. The other half of the mice presented with small, localized tumors that did not metastasize. Herein, we describe tips specific for the intraceal injection of MC38 cells to improve the engraftment rate consistency in this model.

5.2 Introduction

Colorectal cancer (CRC) remains the second leading cause of cancer-related death amongst men and women in the United States [286]. Subcutaneous tumor models remain the standard for testing of drug efficacy *in vivo* [330]. However, these models are unable to recapitulate the physiological cues associated with the organ of interest and rarely metastasize, warranting study in more robust orthotopic platforms. Orthotopic mouse models have been shown to accurately model clinical patterns of metastasis and tumor progression experienced in humans, supporting their translational relevance [331]. Moreover, orthotopic tumors have been found to have varying sensitivities to chemotherapeutics and a distinct immune landscape compared to subcutaneous models [332,333]. Despite the increasing characterization of orthotopic mouse models of colorectal cancer, they remain rarely used in comparison to subcutaneous models due to their surgical difficulty, poor reproducibility and low rates of engraftment and metastasis [334]. Additionally, reports on the rate of engraftment are minimal, and successful tumor formation ranges greatly depending on the cell lines used, method of implantation and species of mouse [335,336]. Further, metastatic spread is rarely seen in all tumors that are successfully engrafted, likely attributed to surgical technique [334], immune rejection [337], or cellular heterogeneity.

Immunodeficient humanized mice, such as severe combined immunodeficient (scid), Rag1, or nude mice, are often used to allow for orthoptic implantation of human CRC cells, such as HT29, SW620, HCT116, and SW480 cells [283,336,338–340]. However, these models lack a full immune complement, limiting their usefulness for immuno-oncology research, specifically when examining the role of adaptive immunity, cytotoxic T cells, and checkpoint blockade therapies [339]. CT26 and MC38 cells are the most commonly used murine cell lines of colorectal cancer. These cells are hypermutated and have been validated as suitable preclinical models of human tumors [341]. While studies have reported on engrafting CT26 orthotopic tumors with high fidelity, successful inoculation of MC38 tumors remains contradictory [342]. For example, one study found that zero of eight mice that were orthotopically injected with MC38 cells developed tumors, while 23 of 26 mice developed CT26 tumors in under 4 weeks [332,343]. Similarly, another study showed just 25% tumor formation six weeks after microinjection of two million MC38 cells into the cecum subserosa [335]. CT26 cells have shown to metastasize to clinically relevant foci including the mesenteric lymph nodes in over half of mice [343], while metastatic occurrence in MC38 tumors remains inconsistent in published reports.

Common means of orthotopic implantation include: suturing of subcutaneously grown tumor sections to the exterior of the cecum [283,344], intraluminal injection of cells into the rectum via an endoscope [332,345–347], or subserosal microinjection of cells into the cecal wall [338,343,348]. From preliminary pilot studies, we have found microinjection of MC38 cells into the cecal wall to be the most reproducible method of inoculation. Herein, we provide a detailed protocol for orthotopic inoculation of MC38 as well as report on successful tumor engraftment and incidence of metastasis. Previous studies present conflicting evidence for orthotopic inoculation of MC38 tumors and subsequent metastatic dissemination, and often don't report on tumor rates. By providing a validated protocol of intracecal MC38 tumor inoculation we aim to elucidate these discrepancies.

5.3 Results and Discussion

Surgery was well tolerated by the mice; all mice survived from surgery and regained normal posture, eating, and grooming within 24 hours. In this study, we report a successful tumor inoculation of 67% (6/9), while half of the engrafted tumors metastasized (3/6) (**Table 1**).

Surgery Survival		**9/9**	**100%**
7-week Survival		**8/9**	**89%**
Successful Tumor Inoculation		6/9	67%
Tumors With Lymph Node Metastases		2/6	33%
Tumors With Organ Metastases		3/6	50%
	Peritoneum	3/6	50%
	Diaphragm	3/6	50%
	Liver	2/6	33%
	Pancreas	1/6	17%
	Kidney	1/6	17%

Table 5.1. Breakdown of tumor engraftments following intracecal injection of MC38 cells.

Tumors most frequently metastasized to clinically relevant foci, including the mesenteric lymph nodes, peritoneum, and liver (**Figure 5.1**). In one mouse, there was also evidence of macrometastasis in the pancreas and kidney. Metastasis corresponded with decreased survival, but no decrease in body weight (**Figure 5.2**), likely due to the associated weight gain from the tumors themselves.

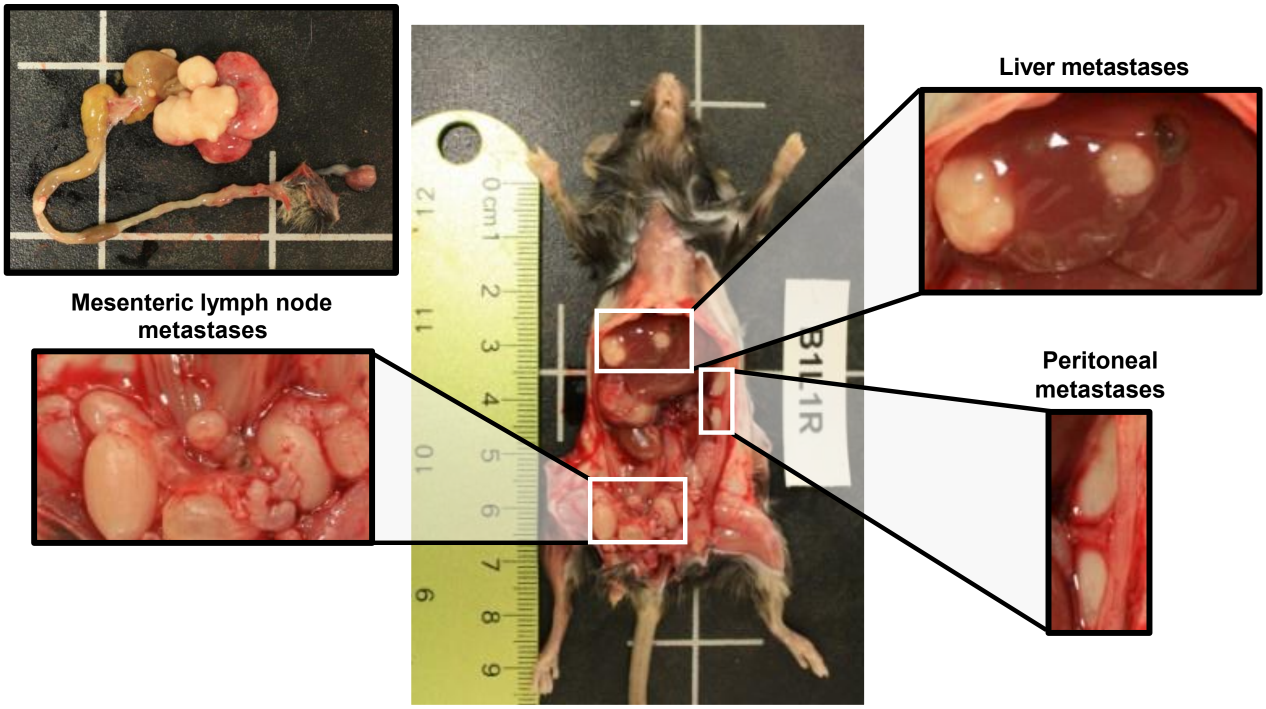

Figure 5.1. Macroscopic evidence of liver, lymph node, and peritoneal metastases (parietal).

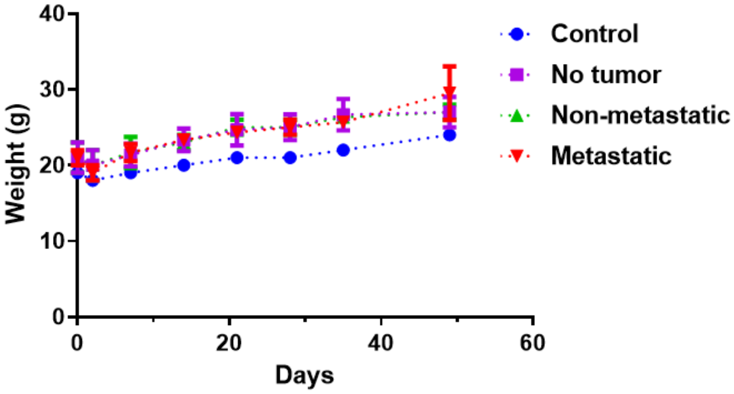

Figure 5.2. Body weights over seven weeks of orthotopic tumor growth.

Three mice displayed no evidence of a tumor, possibly due to injections that were too deep through the mucosal layer and into the lumen of the colon. Another contributing factor may be peristalsis or secretions of the colon during injection, described in troubleshooting of other orthotopic implantation methods [332]. To prevent colon movement and contraction during surgery, mice can be treated with atropine preoperatively. Of mice that did develop tumors, tumor size varied greatly, ranging from 8-1190 mm^3 in volume. When grouped by metastatic spread, mice with macroscopic evidence of metastasis showed an over 50-fold increase in primary tumor size compared to mice with only localized tumors (**Figure 5.3**).

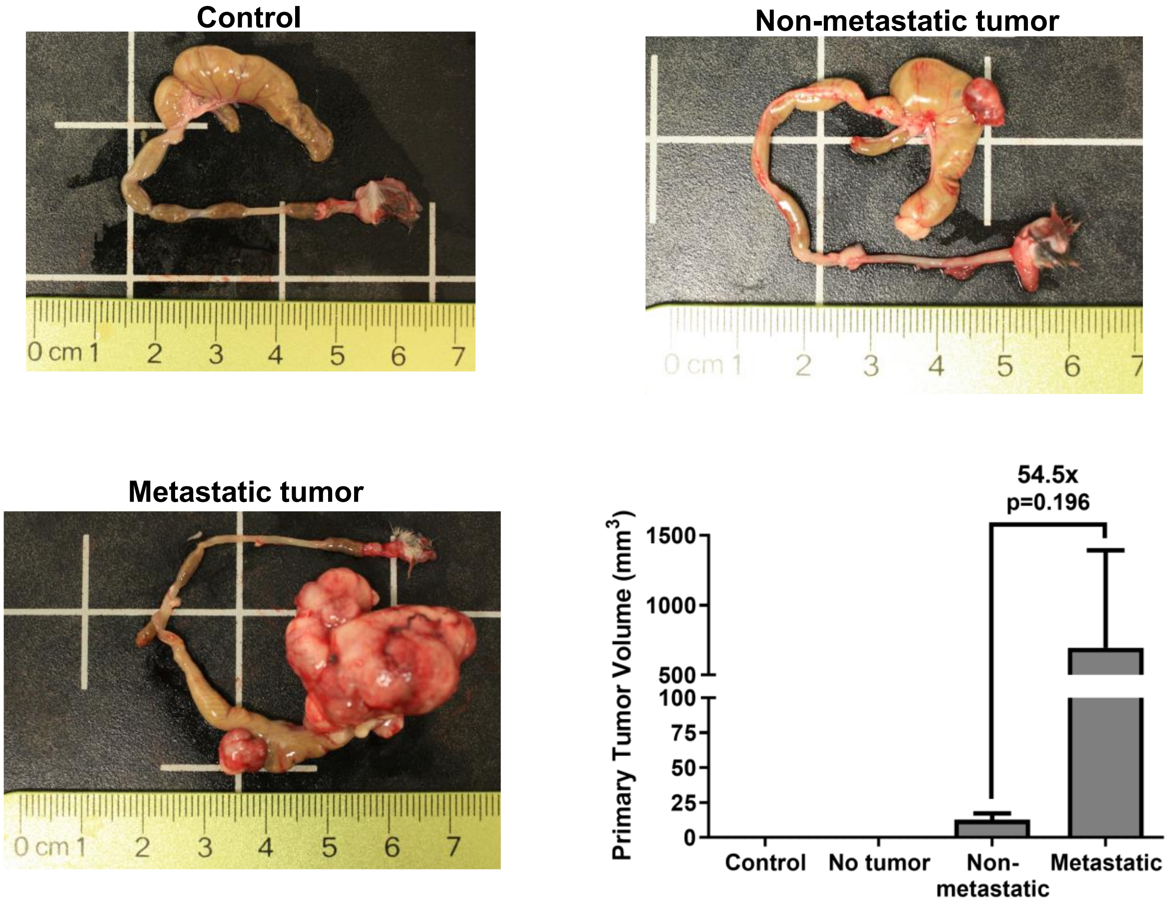

Figure 5.3. Primary tumor size varies greatly between mice. Control (n=1), no tumor (n=3), non-metastatic tumor (n=3) and metastatic tumor* (n=2); one-way ANOVA with multiple comparisons. *The metastatic tumor group is missing measurements from one mouse that died before the endpoint of the study.

Despite metastatic spread to the liver, liver mass remained unchanged between groups. However, mice with metastatic tumors presented with a significantly enlarged spleen despite no visual evidence of metastases, signifying increased inflammation in this subgroup (**Figure 5.4**).

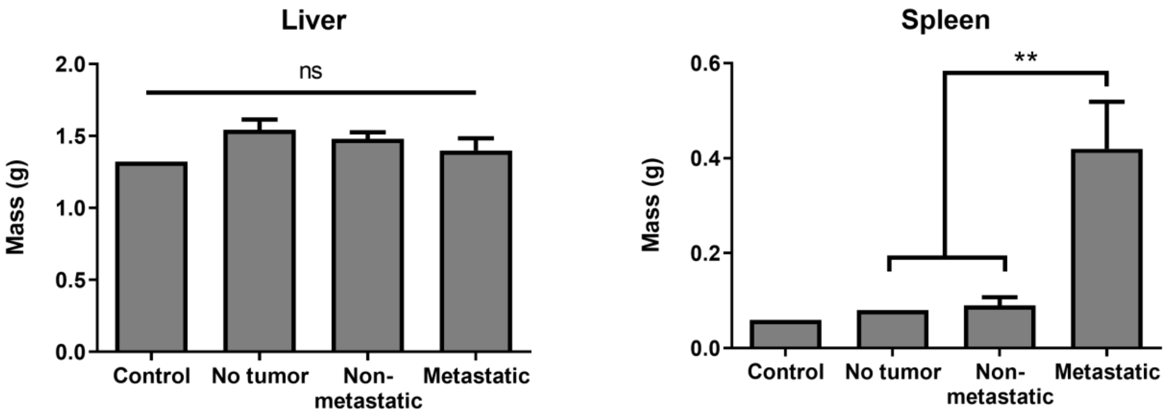

Figure 5.4. Organ weights of the liver and spleen. Control (n=1), no tumor (n=3), non-metastatic tumor (n=3) and metastatic tumor* (n=2); **p<0.01 (one-way ANOVA with multiple comparisons). *The metastatic tumor group is missing measurements from one mouse that died before the endpoint of the study.

The differences in tumor growth and metastasis between mice are interesting. One possibility is that there were unequal concentrations of cells injected due to inadequate mixing before loading the syringes or a lower viability of cells injected in later surgeries due to prolonged time in suspension. It is also possible that cells leaked from the submucosal space into the lumen during injection, likely the case in mice that did not present with tumors (n=3). However, there is evidence that a subset of mice will naturally form small, non-metastatic tumors in this model. Our results support findings from Trimaglio and colleagues which demonstrate two distinct subtypes of orthotopic tumor growth [337]. These authors report that only a minority of mice formed lethal tumors with a pro-tumor immune response that aided progression. Meanwhile, a large subgroup of tumors showed senescence or spontaneous rejection through an anti-tumor, CD8+ T cell-mediated immune response. Similarly, despite successful tumor engraftment in each group initially, a subset of mice developed small non-lethal tumors in our study.

While protocols for mucosal and serosal injection of some CRC cell lines exist, MC38 cells present an added challenge, exemplified by low orthotopic engraftment rates [332,335,343]. Implementing this mouse model in experimental cancer immunotherapies studies is key, as MC38 cells elicit a more modest immune response and have been shown to be resistant to adaptive immune cells and checkpoint blockade [349,350]. This makes the MC38 syngeneic model particularly intriguing to investigate treatments that target immune-refractory tumor subtypes.

In this study, we report an orthotopic engraftment of 67%, higher than multiple other studies of MC38 tumors, and even among CT26 tumors. [332,335,351]. We also demonstrate metastatic dissemination of tumors to clinically relevant foci in 50% of mice that developed tumors, higher than other studies which have characterized these tumors as weakly metastatic [335,352]. A benefit of serosal injection versus other techniques is an increased incidence of metastasis. While endoscopic tumor injections historically yield higher engraftment rates, these tumors rarely metastasize [332,342,345]. Likewise, the suturing of subcutaneous MC38 tumor fragments to the cecum has shown successful tumor growth, but no metastasis [344]. This highlights the value of the intracecal implantation method for future studies examining the efficacy of anti-metastatic immunotherapies. Furthermore, we have validated that orthotopic inoculation of MC38 tumors appears to yield two distinct tumor subtypes, with one being lethal and metastatic while the other senescent and nondisseminated. The following is a list of what we have found to be key in successfully engrafting orthotopic tumors from MC38 cells, specifically.

- Ensure MC38 cells are not overly confluent on the day of lifting for injections. Subpassage the cells no more than 3 days beforehand and prepare injections while cells are in the exponential growth phase.
- Inject cells in a Matrigel® suspension of at least 4 mg/ml to promote a tumor plug that limits extracecal leakage. Wait at least 10 seconds before removing the needle following injection. To practice this technique, sacrifice a mouse and inject a dye instead of cells for visual confirmation of a successful injection.
- Use a higher cell count of at least 2×10^6 cells per injection. Lower cell counts have shown to yield few or no tumors [332].
- Keep the injection volume small, ≤ 50 μl to prevent leakage. If a larger injection volume is needed, consider multiple injections of smaller volumes into different areas of the cecum.
- Inject cells with the cecum under magnification to ensure proper needle placement and the formation of a tumor plug.

5.4 Methods and Materials

Item	Supplier	Identifiers; *RRID*
MC38 Cell Line (CVCL_B288)	Kerafest	ENH204-FP; *RRID: CVCL_B288*
Dulbecco's Modified Eagle Medium with glucose, L-glutamine and Sodium Pyruvate	Gibco	11995-065
Fetal Bovine Serum (FBS)	American Type Culture Collection (ATCC)	30-2020
Penicillin-Streptomycin Solution	ATCC	30-2300
MEM Nonessential Amino Acids 100x	Corning	25-025-CI
HEPES Buffer	Corning	25-060-CI
0.05% Trypsin-EDTA	Gibco	25300054
HBSS, no calcium, no magnesium	Gibco	14175095
C57BL/6 mice	The Jackson Laboratory	*RRID:MGI:2159769*
BD Veo 31G Insulin Syringes	BD	324910
Heating Pad	Sunbeam	731-500-000R
Isoflurane USP	Piramal Critical Care	NDC 66794-017-25
Matrigel® Basement Membrane	Corning	354263
Autoclavable Sterilization Pouch	Fisherbrand	01-812-57
Purple Nitrile Sterile Gloves	Kimberly-Clark	55092
Nair Hair Remover		
Ketoprofen	University DAC	
Ethilon Monofilament Nylon 5-0 Suture	Ethicon	G698G
Vicryl Plus Synthetic Absorbable 5-0 Suture	Ethicon	022671
Purdue Products Betadine Swabsticks	Fisher Scientific	19-061617
Alcohol Prep Pad	Dukal Corporation	853
Sterile Cotton Tipped Applicators	Puritan	25-806 10WC
Sterile Gauze Pads	American White Cross	
Germinator 500 Glass Bead Sterilizer	Braintree Scientific	GER5287120V
Surgical magnification with light		
Needle holder		
Forceps		
Scalpel		
Scissors		

Table 5.2. List of materials used in Chapter 5.

5.4.1 Animal Ethics Statement

These animal studies were approved by Vanderbilt's Institutional Animal Care and Use Committee (IACUC) under protocol number M1700009-01. According to this protocol, all mice were given appropriate doses of anesthetics (2.5% isoflurane) and analgesics (5 mg/kg of ketoprofen). Heating pads were used during recovery to mitigate hypothermia risks. Mice were given unrestricted access to food and water during the study period and monitored closely for changes in weight, feeding or drinking habits, ambulation, and healing of the incision site.

5.4.2 Cell Culture

MC38 cells were purchased from Kerafest and cultured in Dulbecco's Modified Eagle Medium (DMEM) containing 4.5 g/L D-Glucose, L-glutamine, and 110 mg/L sodium pyruvate. Media was supplemented with 10% fetal bovine serum (FBS), 1% Penicillin-Streptomycin Solution (PenStrep) (100 I.U./mL penicillin, 100 µg/mL streptomycin), 1x MEM Nonessential Amino Acids and 1 mM HEPES. Cells were maintained in a humidified incubation chamber at 37ºC and 5% CO_2. Cells were passaged every 2-3 days, or at 50% - 70% confluency by lifting with 0.05% Trypsin-EDTA and subculturing at 1:5-1:10 ratios.

5.4.3 Orthotopic Surgery

Nine 6–8-week-old male C57BL/6 mice were anesthetized with 5% isoflurane, then placed on a sterile heating pad. For purposes of consistency and comparison between studies, male mice were used to prevent sex from being an added variable, since the majority of studies using this model use 6–8-week-old male mice. In humans, males have a higher incidence of colorectal cancer and higher mortality rates than women, further supporting the use of male mice [353]. A nose cone was used to deliver 2.5% isoflurane during surgery. The abdomen, which was removed of all hair the previous day using Nair, was prepared for sterile surgery by wiping with ethanol and then betadine three times. A small midline abdominal incision was made using a scalpel to cut through the skin, and scissors to carefully cut through the underlying musculature without nicking any organs. The cecum was exteriorized and supported on a piece of sterile gauze, then hydrated with sterile saline. A 50 µL suspension of $2×10^6$ MC38 cells in Matrigel® Basement Membrane (1:1 ratio) was carefully injected into the cecal wall from the serosal side under microscopic visualization. Observation of a visible bulla between the submucosal and subserosal tissues without leakage confirmed successful injection. The cecum was then returned to the peritoneum, and muscle and skin closures were completed using 5-0 biodegradable sutures and 5-0 monofilament nylon sutures, respectively.

5.4.4 Postoperative Care and Endpoints

Following surgery, mice were injected subcutaneously with 5 mg/kg of ketoprofen as an analgesic, and then placed in a fresh cage over the top of a heating pad. Mice were observed carefully during recovery, taking note of posture and ambulation. Twenty-four hours after surgery, mice were injected subcutaneously with a second dose of 5 mg/kg ketoprofen. Seven weeks after inoculation, all mice were euthanized, and necropsies were performed to visualize tumor progression and metastasis. Microscopic histological examination was not performed due to high costs and a history of not providing additional clinically useful information not already obtained from macroscopic observation [354,355].

5.4.5 Detailed Protocol

<u>Cell Preparation (30 – 45 minutes)</u>

Before starting:

- Supplement DMEM media with 10% fetal bovine serum (FBS), 1% Penicillin-Streptomycin Solution (PenStrep) (100 I.U./mL penicillin, 100 µg/mL streptomycin), 1 mM HEPES and 1x Non-Essential Amino Acids.
- Subculture cells every 2-3 days, or at 50% - 70% confluency, and passage at 1:5-1:10 ratios.
- Thaw Matrigel® solution overnight at 4ºC. Store any pipette tips, centrifuge tubes, or syringes that will come in contact with Matrigel® at 4 ºC. For detailed handling instructions, we recommend referring to Corning’s instructional resources.
- Aliquot Matrigel® into separate tubes. Store unused tubes at -20ºC.
- MC38 cells can be transfected with luciferase for noninvasive tumor monitoring using bioluminescence imaging techniques.

1. Plate MC38 cells (0.5-1×10^6) in a T75 flask with 10 ml of DMEM supplemented media.

*Do not allow cells to become overly confluent as this will drastically reduce viability before injection, limiting tumor engraftment. This is especially true for MC38 cells. On the day of surgery, cells should be between 50-70% confluent and in the exponential growth phase.

2. On the day of surgery, rinse flasks with HBSS (without calcium) and aspirate.
3. Lift cells using 0.05% Trypsin-EDTA for 5-10 min at 37ºC.
4. Rinse cells off flasks using culture media and place the cell suspension in a centrifuge tube.
5. Count cells using a hemocytometer or automated cell counter.
6. Centrifuge cells at 300×g for 5 min.

* Wait to begin collecting cells for as long as possible. Mice and surgical station should be prepped for surgery beforehand.

7. Resuspend pelleted cells in ice cold serum free media at a concentration of 2×10^6 cells/25 µl, at an appropriate volume depending on the number of mice for your study (each mouse will be injected with 2×10^6 cells).
8. Using pre-chilled pipette tips and tubes, pipette 25 µl of Matrigel® into the cell suspension for a 1:1 ratio. Working volume of Matrigel® should be ≥ 4mg/ml (Matrigel® is typically supplied at ~20 mg/ml, a 1:1 ratio yielding an injected solution of 10 mg/ml) . Keep cell/Matrigel® suspension on ice up until injection.

* For maximal consistency and reproducibility between injections, make a master mix of the cell suspension for all injections to ensure the same number of cells are being injected into each mouse. Mix the suspension well by pipetting up and down between injections.

Surgical Procedure (1 hour of prep; 30 – 45 minutes per mouse)

Before starting:

- The day before, remove hair from the abdomen of C57BL/6 mice using Nair. Be sure to thoroughly wipe up any excess Nair after using to prevent the risk of burning.

- Autoclave all surgical equipment (scissors, scalpel, forceps, needle holder) using a sterilization pouch.

1. Place mouse in an anesthesia chamber with 5% isoflurane.
2. Remove mouse and place on a sterile table over a heating pad. Place nose in a nose cone delivering 2.5% isoflurane. Tape extremities to the table to stabilize the mouse. Before beginning, ensure the mouse is anesthetized using a toe pinch.

*Wipe a small amount of petroleum jelly on the eyes of mice to prevent them from drying during surgery.

3. Drape the mouse and surgical site with sterile plastic wrapping, such as Glad Wrap. Cut a hole in the plastic around the abdomen/surgical site.
4. Prepare the incision area using an ethanol wipe. Wipe in a circular motion beginning in the center of the abdomen and radiating outward. Follow by wiping the abdomen with a betadine swab using the same technique. Repeat this process three times.
5. Perform a 2 cm midline abdominal incision using a scalpel, cutting through the skin.
6. Lift underlying muscle tissue with forceps, creating a small nick at the base of the incision and cut with scissors to make an equivalent cut in the muscle layer.

*It is important to lift the muscle tissue and use scissors instead of a scalpel to ensure you do not cut any intra-abdominal organs.

7. Gently exteriorize the cecum from the abdomen. Isolate by placing on sterile gauze pad and keep moist using sterile, warm saline. Flatten the cecum gently using forceps.

* The cecum will have blinding ending pouch.

8. Load 50 µl of the cell/Matrigel® suspension into a 31G insulin syringe.

* Keep syringes and cells on ice or at 4ºC at all times before injecting to prevent the Matrigel® from solidifying.

9. Inject the 50 µl cell suspension into the wall of the cecum from the serosal side, using magnification with light or a microscope for visualization. Wait at least 10 seconds after the injection before removing the syringe. Observation of a visible bulla formation between the submucosal and subserosal tissues without leakage confirms a successful injection (**Figure 5.5A**).

*Tip: To practice injection techniques, inject a 1:1 mixture of Matrigel® with a dye, such as Trypan Blue, using a previously sacrificed mouse (**Figure 5.5B**). The dye will allow for improved visual confirmation of bulla formation without leakage into the subserosal space.

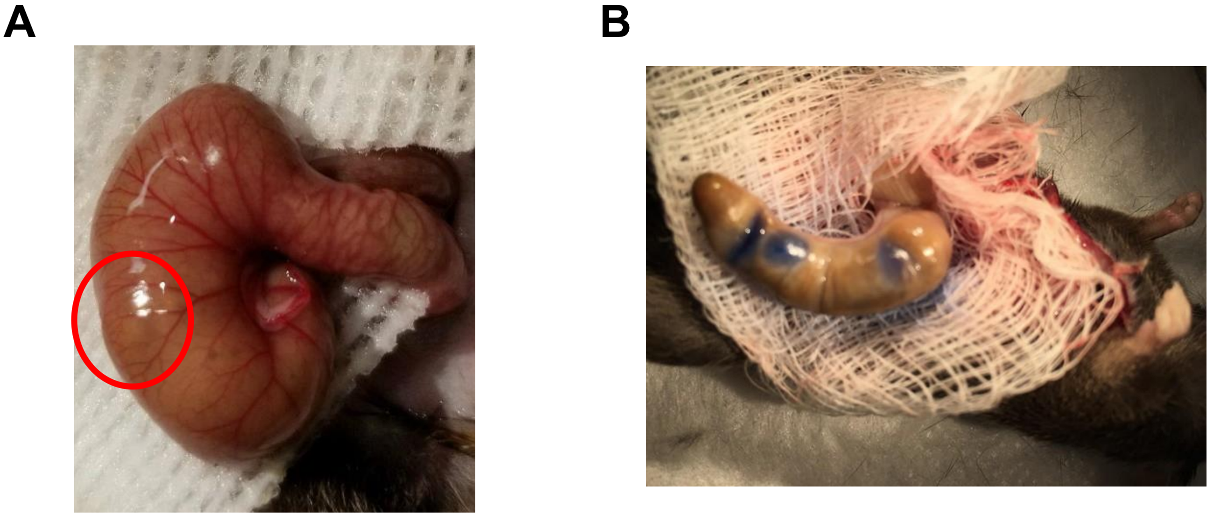

Figure 5.5. Bulla formation after intracecal injection. (A) Visible confirmation of successful injection of Matrigel® with MC38 cells (red circle). **(B)** Injection practice using a previously sacrificed mouse, substituting dye for cells to better visualize any sign of leakage.

10. Return the cecum back into the peritoneal cavity. Close the muscle layer using 3 interrupted 5-0 biodegradable sutures. Next, close the skin in the same manner using 3 interrupted 5-0 nylon sutures.

*Between mice, sterilize surgical instruments using a glass bead sterilizer such as the Germinator 500.

*Provide proper dosage of analgesics (subcutaneous injection of 5 mg/kg ketoprofen) and antibiotics (if required by protocol). Analgesics should be administered at a minimum of two times, directly after surgery and 24 hours post-op. Remove sutures approximately 1 week following surgery, or after the incisions have fully healed.

11. Place mouse in a fresh cage seated over the top of a heating pad to provide extra warmth during recovery.

*Monitor mice closely over the next 48 hours, taking special note of the condition of the incision, suture fidelity, and grooming/eating habits.

12. After 5-7 weeks, or humane endpoint, sacrifice mice and perform necropsies and any histological analysis. Humane endpoint should be defined as weight loss exceeding 20%, impaired ambulation, or visible tumor ulceration.

Chapter 6:

Conclusions and Future Work

6.1 Conclusions

TRAIL and TRAIL-conjugated nanoparticles are able to initiate apoptosis in chemoresistant colorectal cancer cell lines and CTCs in the blood of metastatic patients. The efficacy of TRAIL therapy can be improved through raft stabilization via resveratrol, and mechanosensitive ion channel activation via fluid shear stress or the Piezo1 agonist Yoda1. Additionally, the development of an orthotopic mouse model of CRC metastasis will allow for future investigation of TRAIL-conjugated nanoparticles in a preclinical animal model.

6.1.1 Oxaliplatin-resistant colorectal cancer is increasingly sensitive to TRAIL therapy

In Chapter 3, I discovered a novel mechanism explaining why oxaliplatin-resistant CRC cells displayed increased sensitivity to TRAIL-mediated apoptosis. Oxaliplatin-resistant derivatives of four colorectal cancer cell lines were generated by culturing with increasing doses of oxaliplatin until an IC50 increase of approximately 10-fold was achieved. HCT116 OxR and SW620 OxR cell lines displayed decreased expression of caspase-10, but this was found to be inconsequential in the observed apoptotic increase as determined through a stable CASP10 KO cell line. In OxR cells that were sensitized to TRAIL, there was a significant increase of DR4 on the cell surface. In support of this, the DR4-agonist monoclonal antibody mapatumumab significantly increased apoptosis in SW620 OxR cells compared to their parental counterparts. Additionally, DR4 was found to have enhanced colocalization in lipid rafts within OxR cell lines, confirmed using western blots of detergent-resistant raft fractions, colocalization algorithms from confocal microscopy images, and flow cytometry FRET efficiency. The increase in LR colocalization of DR4 strongly correlated with sensitization to TRAIL. I also demonstrated that altering lipid rafts in the cell membrane and colocalization of DR4 into these rafts had dramatic effects on TRAIL sensitivity. Resveratrol increased DR4 colocalization with LRs in HCT116 and SW620 cell lines and increased their apoptosis to TRAIL, resembling that of the OxR cell lines. Conversely, treating OxR cells with the cholesterol depleting agent nystatin reduced DR4-LR colocalization and inhibited TRAIL-mediated apoptosis.

I next determined that the mechanism of chronic oxaliplatin enhanced DR4 translocation into rafts was through increased palmitoylation of DR4. This post-translational modification of a palmitate to cystine residues allows for increased DR4 oligomerization and raft clustering. This was found to be a unique characteristic to the DR4 protein, as total palmitoylation remained similar between parental and OxR cells. I validated this mechanism by showing that inhibiting palmitoylation using 2-bromopalimate significantly decreased apoptosis in OxR cells, resembling that observed in the parental phenotype. This newly discovered link between oxaliplatin resistance, lipid rafts, and death receptor signaling is illustrated in **Figure 6.1**.

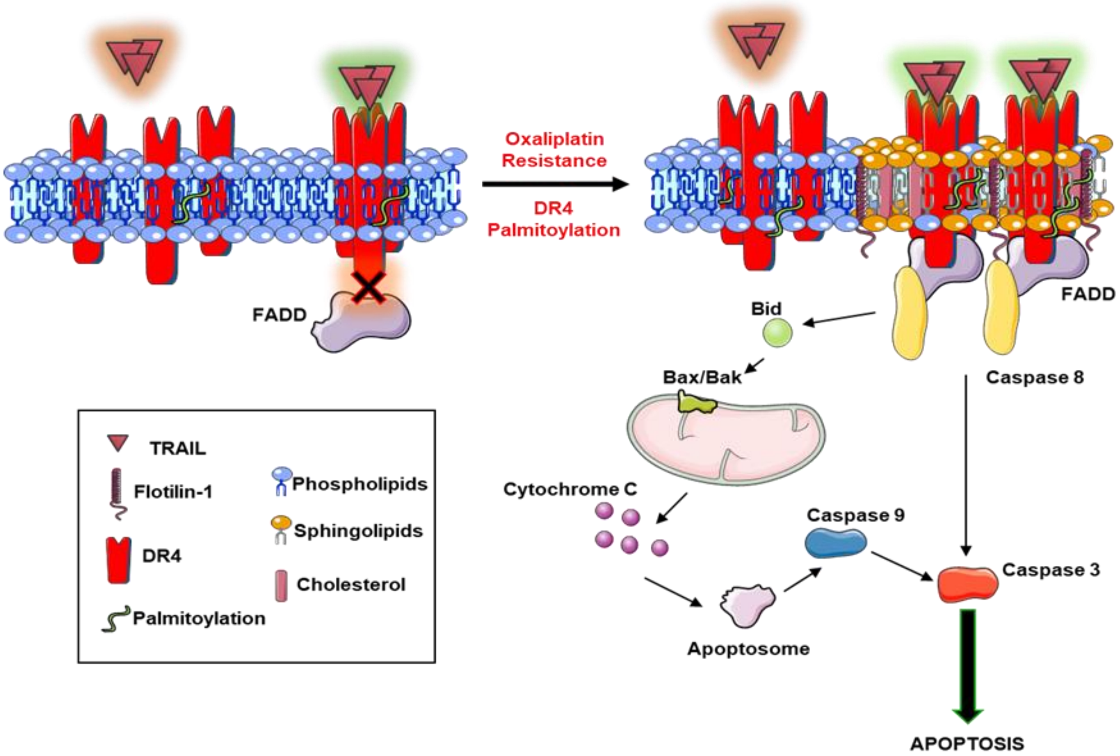

Figure 6.1. Oxaliplatin resistance increases palmitoylation of DR4, allowing for oligomerization, lipid raft colocalization, and supramolecular clustering of death receptors to potentiate apoptotic signaling.

Given the susceptibility of OxR cells to TRAIL, I engineered nanoscale liposomes conjugated with TRAIL and the adhesion protein E-selectin. Blood samples from 13 metastatic CRC patients who were currently undergoing or had failed oxaliplatin chemotherapy were treated with TRAIL liposomes in a cone-and-plate flow device to model circulatory shear stress. TRAIL liposomes reduced CTC viability by 57%, significantly more than oxaliplatin or soluble TRAIL. Incredibly, two patients had no detectable CTCs following TRAIL liposome treatment. In accordance with our *in vitro* data, patients with higher colocalization of DR4 with LRs saw increased therapeutic benefit of TRAIL liposomes and decreased response to oxaliplatin. This demonstrates the potential clinical benefit of liposomal TRAIL in chemorefractory CRC, and lipid raft DR4 as a predictive biomarker of treatment efficacy (**Figure 6.2**).

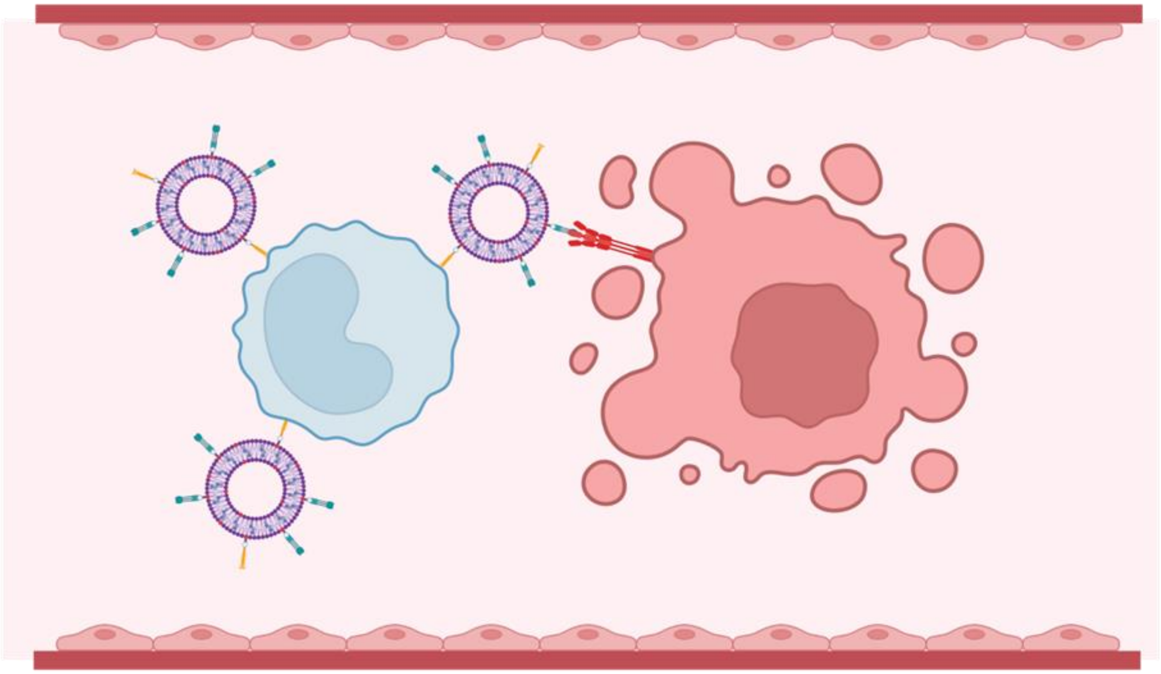

Figure 6.2. E-selectin/TRAIL liposomes hitchhike on the surface of immune cells in the blood and interact with CTCs to induce apoptosis via TRAIL.

6.1.2 Response to fluid shear stress and Piezo1 mechano-activation differs for metastatic and primary tumor CRC cells

Chapter 4 investigated the response of isogenic CRC cells lines to fluid hear stress and chemical activation of the mechanosensitive ion channel Piezo1. SW480 cells and SW620 were isolated from a primary colon adenocarcinoma and a metastatic tumor draining lymph node from the same patient one year later, respectively. I exposed cells to three different fluid environments: static, high magnitude shear pulses mimicking forces of passing through the heart, and constant shear stress of average magnitudes experienced in the circulation. Shear pulses were administered using a syringe pump and constant shear using a cone-and-plate viscometer. As hypothesized, SW480 cells from the primary tumor were more sensitive to cell death from both forms of FSS than metastatic SW620 cells. Different modes of FSS affected cells in unique ways. Constant FSS decreased proliferation and increased expression of CD133, a CSC hallmark in CRC. Meanwhile, shear pulses caused cell membrane damage, indicated by internalization of fluorescently labeled dextran. I found that both SW480 and SW620 cells were able to rapidly repair the cell membrane, possibly explaining the minimal decrease in cell viability from shear pulses. Additionally, shear pulses only caused slight increases in the influx of extracellular calcium, further supporting mechanisms of rapid repair and cytosolic calcium buffering.

To examine if FSS could sensitize these cell lines to therapeutic agents, cells were treated with resveratrol and TRAIL. In SW480 cells, shear pulses were able to sensitize cancer cells to the combination of TRAIL and resveratrol. SW620 cells remained unsensitized by FSS, further solidifying the mechanoresistant nature of these metastatic cells (**Figure 6.3**).

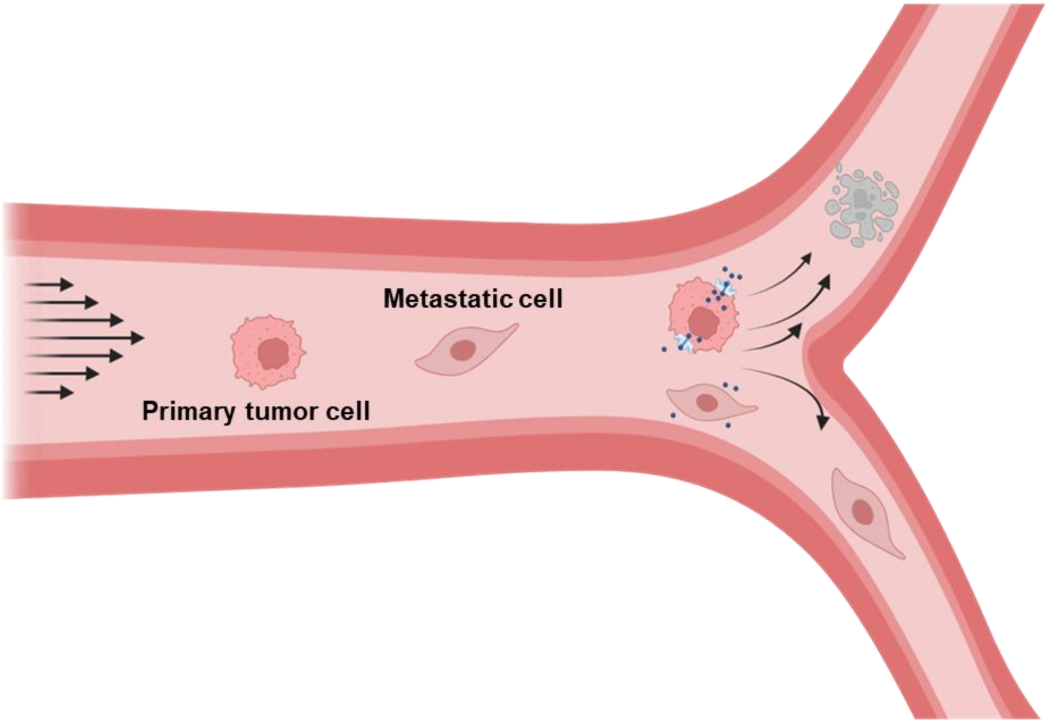

Figure 6.3. Cells from the primary tumor (SW480) and from a metastatic lymph node (SW620) have different sensitivities to fluid shear stress-mediated survival and mechanoactivation.

I also examined the activation of Piezo1 between these cell lines using the small molecule agonist Yoda1. Yoda1 caused significant increases in calcium influx compared to FSS. Additionally, resveratrol pretreatment significantly increased Piezo1 activation and calcium influx both instantaneously and over the span of 24 hours. Increased calcium influx from resveratrol pretreatment corresponded with increased lipid raft colocalization of Piezo1, demonstrating for the first time that mechanosensitive ion channel involvement with lipid rafts can enhance activation (**Figure 6.4)**. Piezo1 activation, and its consequential influx of calcium, was found to be significantly greater in SW480 cells than SW620 cells. This may be in part due to higher Piezo1 expression in SW480 cells than metastatic SW620 cells, a characteristic consistent with other isogenic cell line models of metastasis.

SW480 cells that were treated with Yoda1 in combination with TRAIL became significantly more apoptotic. Interestingly, the significant increases in calcium influx from the addition of resveratrol resulted in no increase in TRAIL-mediated apoptosis. To explain this, we used a computational model of death receptor-mediated apoptosis. Consistent with the *in vitro* data, this model predicted that while calcium sensitizes cancer cells to apoptosis, the effects become saturated past a cytosolic calcium concentration of 1 µM. While calcium effects became saturated for apoptotic signaling, preliminary results suggest calcium entry may affect other cellular processes such as EMT.

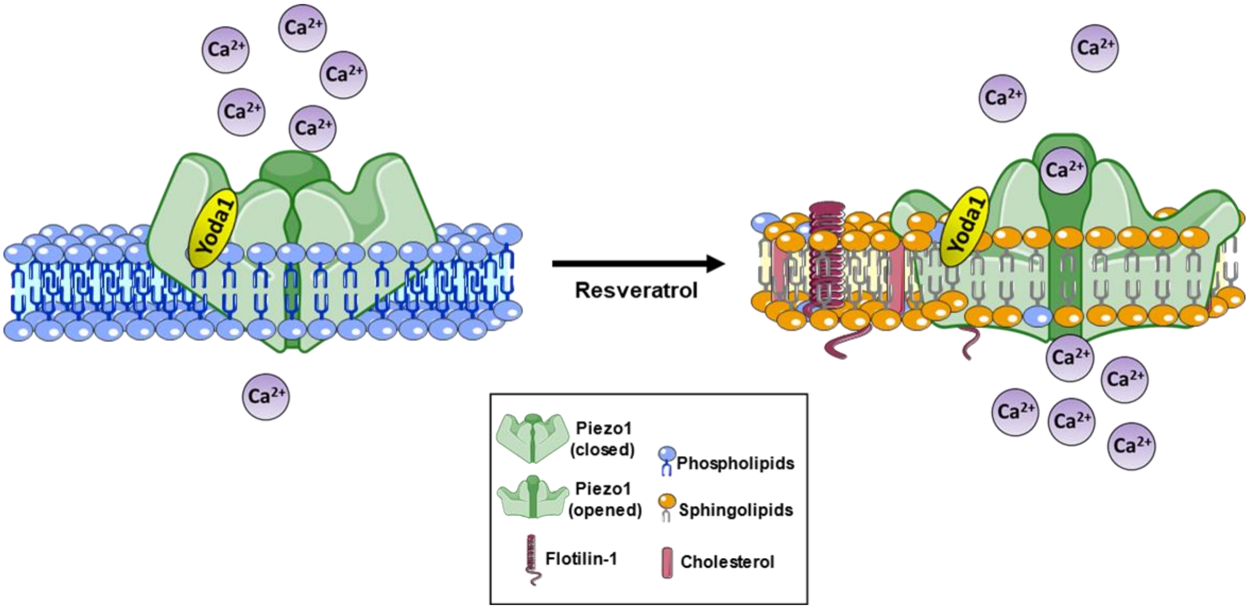

Figure 6.4. Resveratrol primes Piezo1 activation by changing the organization of the lipid bilayer.

6.1.3 An immunocompetent orthotopic mouse model of CRC produces metastases to clinically relevant foci

In Chapter 5, I established an immunocompetent mouse model of CRC metastasis. While subcutaneous tumor models remain the standard in determining treatment efficacy due to their simplicity, they lack clinical relevance due to their inability to metastasize [331]. However, orthotopic tumor models of colorectal cancer remain seldom used due to surgical difficulty, poor reproducibility, and inefficient metastasis to clinically relevant foci. To address this, I have developed a detailed protocol for orthotopic inoculation of MC38 cells using a microinjection technique into the cecal wall. This protocol generated tumors in two-thirds of mice, improving upon engraftment rates in multiple studies with MC38 and CT26 cells [332,335,351]. I also report a dissemination rate of 50%, contrary to other studies that have characterized MC38 cells as weakly metastatic *in vivo*. Importantly, macroscopic metastases were seen in clinically relevant organs, including the liver, peritoneum, mesenteric lymph nodes and pancreas. Interestingly, two tumor phenotypes were observed in this study: the first being large tumors that were highly metastatic, and the latter being small, non-disseminated tumors. This is consistent with other studies showing spontaneous immune rejection of MC38 tumors in some mice, while others developed lethal metastatic tumors [337]. Overall, this chapter improves upon existing protocols for orthotopic inoculation of CRC cells, specifically the elusive MC38 cell line. Since this is a syngeneic mouse model with a full immune complement, this lays the groundwork for preclinical studies to examine the efficacy of novel immunotherapies.

6.2 Future Work

6.2.1 TRAIL liposomes in an orthotopic mouse model

Given the success of TRAIL-conjugated liposomes *in vitro* and in blood samples of metastatic CRC patients, the next step would be to test the efficacy in an orthotopic mouse model. Our lab has shown success in using TRAIL nanoparticles to prevent metastasis in prostate and breast orthotopic models [271,356]. In Chapter 5, I laid the groundwork for a similar study in colorectal cancer by establishing an immunocompetent orthotopic mouse model though microinjection of MC38 cells into the cecal wall. Testing the efficacy of TRAIL liposomes versus soluble TRAIL will establish the necessity of drug delivery modalities for TRAIL. Additionally, intravenous (IV) versus intraperitoneal (IP) administration of liposomes should be explored, using biodistribution studies to examine differences in half-life, clearance, and unwanted accumulation within the liver. *In vivo* biodistribution studies can be completed noninvasively using a far-red fluorescent lipid tag within the liposomes, such as DiR, and an *in vivo* imaging system (IVIS). This can also be used to show liposome accumulation within tumors by using cell lines transfected with firefly luciferase.

Alternatively, human CRC cell lines, including OxR derivates discussed in Chapter 3, can be orthotopically implanted as previously described in a humanized mouse. Rag1 knockout mice have a full complement of innate immune cells and NK cells, but lack mature T and B cells, making them suitable for implantation of human cell lines. Examining differences in TRAIL liposome efficacy between parental and OxR cell lines will further solidify the apoptotic susceptibility of OxR cells to TRAIL that was proposed in Chapter 3.

6.2.2 Deeper mechanistic studies into oxaliplatin resistance induced DR4 changes

While Chapter 3 elucidated a novel mechanism with reasonable detail, there remain questions to be answered regarding how oxaliplatin resistance increases DR4 protein expression and selective palmitoylation. One explanation is epigenetic alterations between parental and OxR phenotypes since transcriptional analysis showed no significant differences in mRNA expression of DR4. Additionally, multiple studies using OxR CRC cell lines have shown dysregulation of specific miRNAs, such as miR-33a-5p, miR-200c, and miR-141, as predictive markers of sensitivity or resistance [257,357]. MicroRNAs have been heavily implicated in attenuating apoptotic signaling, including DR4 [358]. Death receptor palmitoylation can also be influenced by miRNA expression, as evidenced by a study showing miR-128 and miR-424 attenuation of Fas receptor palmitoylation and signaling [359]. Future studies should investigate these miRNAs, or ideally, utilize next generation sequencing or miRNA profilers to identify potential miRNA targets that explain differences in DR4 palmitoylation.

6.2.3 TRAIL liposome effects on macrophages

Studies have shown that macrophages are particularly susceptible to TRAIL compared to neutrophils and lymphocytes due to increased expression of functional death receptors [360]. Additionally, there’s evidence that tumor associated macrophages have increased susceptibility to TRAIL-mediated apoptosis compared to resident macrophages. The apoptotic effects of TRAIL liposomes should be explored in the mouse macrophage cell line RAW264.7, primary bone marrow derived monocytes, and human monocyte THP-1 cells. These cells can be polarized *in* *vitro* into M1 or M2 macrophage using lipopolysaccharides plus IFN-γ or IL-4, respectively. *In vitro* toxicity assays should explore differences in sensitivity between these polarized phenotypes to shed light into whether our liposomes can kill “two birds with one stone” (cancer cells and TAMs) while sparing proinflammatory macrophages. These studies should extend *in vivo* within the orthotopic models proposed previously.

While our E-selectin/TRAIL liposomes have shown to bind to multiple leukocyte populations in whole blood including monocytes, neutrophils, and NK cells [270], future studies should examine binding differences between M1 and M2 macrophages. Even if apoptosis in the M2 phenotype is minimal, liposomes may be able to hitchhike on the surface of these macrophages all the way into the tumor to deliver TRAIL. This could be investigated using a Boyden Chamber by treating macrophages with fluorescently conjugated liposomes and examining if successfully invaded cells express liposomes on their surface.

6.2.4 TRAIL liposomes in a CRC model of peritoneal metastasis

Cytoreductive surgery followed by HIPEC using “stone age” chemotherapies such as mitomycin c or oxaliplatin is the standard of care for patients with peritoneal carcinomatosis. A future direction of this dissertation is to investigate our TRAIL liposomes as a replacement of the standard HIPEC procedure. The peritoneal mesothelium, similar to the endothelium, has high expression of selectin ligands, and E-selectin adhesion is an essential mechanism of metastatic spread in ovarian, pancreatic and colorectal cancer [361,362]. This presents a promising opportunity for our E-selectin/TRAIL liposomes to bind selectin ligands within the peritoneum, arming the peritoneum with TRAIL for an extended period beyond surgery. Alternatively, liposomes could be modified to target peritoneal specific antigens such as carcinoembryonic antigen (CEA) instead of E-selectin [363]. Conjugation of anti-CEA Fab antibody fragments to the liposome surface would sequester free CEA while simultaneously delivering TRAIL to CEA expressing peritoneal metastases [364].

6.2.5 Evaluate FSS resistance in tumor spheroids and CTC clusters

Our lab has previously shown that clusters of cancer-associated fibroblasts (CAFs) with prostate cancer cells confer resistance to FSS [365]. Although rare in comparison to single CTCs, clusters have up to a 50-fold increase in metastatic potential, largely from to their ability to shield inner cells from inhospitable environments within the circulation [366,367]. Clusters often contain heterogenous cell populations, including cancer cells, fibroblasts, monocytes, neutrophils, and platelets. Future studies should expand on the FSS treatments used on single cancer cells in Chapter 4 to include heterogenous clusters of CRC cell lines with stromal cells. It will be intriguing to see what combinations of cells confer the greatest shear resistance, and if these protection mechanisms are conserved for both high magnitude shear pulses and constant shear stress conditions. Finally, it would be useful to study the presence of CTC clusters in the blood of metastatic colorectal cancer patients to identify which cell types are predominantly found within clusters, and how this correlates with treatment regimens and disease progression.

6.2.6 Evaluate Piezo1 expression in patient tumors and CTCs

In Chapter 4, I highlighted that protein abundance data from multiple isogenic cell line models of metastasis show that metastatic cell lines have decreased Piezo1 expression. To further evaluate this, isolated CTCs from metastatic patients could be stained for Piezo1 expression and compared with Piezo1 expression in metastatic tumor samples from the same patient. Counterstaining CTCs with viability markers such as propidium iodide would demonstrate whether Piezo1 downregulation is necessary for survival in the circulation. Comparing this with Piezo1 expression from the primary and metastatic tumors in the same patient could provide evidence for Piezo1 as a clinical biomarker to predict CTC survival and metastatic spread.

6.2.7 Further analysis of CSC phenotypes following FSS

In Chapter 4, I demonstrated that FSS decreased proliferation and increased expression of CD133, a CSC hallmark in CRC. CD133+ CRC populations have been characterized as increasingly migratory and refractory to chemotherapeutic agents [324,368]. Further analysis of cells surviving FSS treatments should include invasion assays, such as Transwell assays, to determine if FSS can prime cells for extravasation via CD133 upregulation. Additionally, wound healing assays could be utilized to assess changes in migratory potential following FSS.

It remains to be seen whether CD133+ cells are innately more resistant to FSS, or if FSS induces the observed increases in CD133 expression. To parse the cause-and-effect relationship between FSS and CD133, SW480 and SW620 cells could be FACS sorted based on CD133 expression. If $\text{CD133}_{\text{high}}$ cells are significantly more resistant to FSS, then the circulation may positively select for CD133+ subpopulations through a CD133-mediated protection mechanism. Conversely, if increases in CD133 expression are observed in $\text{CD133}_{\text{low}}$ cells after FSS, this would hint at a mechanotransduction effect, possibly through calcium signaling, that should be further explored.

6.2.8 Determine the role of lipid rafts in membrane damage following FSS

It would be interesting to understand the role of lipid rafts on membrane damage and repair following FSS. Chapter 4 showed that cells have adequate machinery to repair damaged parts of the cell membrane and prevent apoptosis. Future experiments should incubate cells with lipid raft destabilizers or cholesterol sequestering agents such as mβCD to understand the importance of LRs in membrane repair. It has been demonstrated that the pore-forming toxin streptolysin O (SLO) causes plasma membrane wounds that are repaired via lipid raft-mediated endocytosis at the injured site [321]. Since FSS pulses also caused membrane damage via the formation of pores, it would be intriguing to determine if lipid rafts are also responsible for FSS repair mechanisms.

It has been demonstrated that stiffer cells are more resistant to FSS, and cell softening agents such as cytochalasin D make cells more susceptible to FSS-mediated death [294]. While the cytoskeleton is known to play a dominant role in cell stiffness, cell membrane composition also has an important role. While cholesterol and LRs have been shown to decrease lateral fluidity in the membrane, they have paradoxically been shown to decrease cell stiffness through destabilization of linkages with the cortical cytoskeleton [369]. Since treatment with mβCD has been shown to increase cell stiffness through cholesterol depletion [370], it would be interesting to see these competing mechanisms at play. This would help answer the provocative question of whether lipid raft repair or cell stiffness is more crucial for survival from FSS damage.

6.2.9 Engineer E-selectin/TRAIL liposomes with resveratrol

Resveratrol has been used throughout this dissertation as a sensitizer to TRAIL-mediated apoptosis and Piezo1 activation. Despite its pleotropic effects in aging, inflammation, and cancer, resveratrol is rapidly metabolized following oral administration with C_{max} concentrations well below thresholds of therapeutic benefit. Even with high dose supplements of 500 mg, bioavailability is poor with peak plasma concentrations of 72 ng/ml (0.31 μM) [371], over 100-fold less than that used *in vitro* in my studies. This presents a need to engineer delivery systems for the sustained release of resveratrol at targeted tissues. Recognizing this, multiple studies have formulated nanoparticles to increase bioavailability [372–374]. Interestingly, resveratrol has been easily loaded into liposomes using standard film hydration methods discussed in previous chapters and used for the production of E-selectin/TRAIL liposomes [372]. Future studies should optimize liposome formulations to improve resveratrol delivery, either through leakage from the liposome membrane in the vicinity of targeted cells, or through liposome fusion to the cell membrane. This could increase concentrations of lipid rafts locally within the membrane at areas where TRAIL is bound to death receptors, enhancing apoptotic signaling through mechanisms discussed previously. Simultaneously, delivery of resveratrol to CTCs in the circulation may increase Piezo1 activation from fluid shear stress or chemical activation.

This leads into the next therapeutic iteration, which is to add Yoda1 delivery mechanisms within the current liposome design. Given Yoda1's hydrophobicity and natural affinity for the cell membrane, some model systems have explored this Piezo1 opening mechanism in artificial droplet lipid bilayers [315]. This provides encouraging evidence that, like resveratrol, Yoda1 may stably integrate into the lipid bilayer with a sustained release profile. Alternatively, Yoda1 may be encapsulated within micelles, a common approach for delivering hydrophobic drugs. These Yoda1 micelles can be encapsulated within E-selectin/TRAIL liposomes using a "Micelle-in-Liposome" approach for greater stability and sustained release [375]. Combining resveratrol, Yoda1 and TRAIL within one LNP platform could provide extreme TRAIL sensitization to treat even the most resistant metastatic cancers (**Figure 6.5)**. If Yoda1 delivery proves increasingly difficult, hydrophilic Piezo1 agonists such as Jedi1 can be encapsulated within the liposome core as an alternative approach.

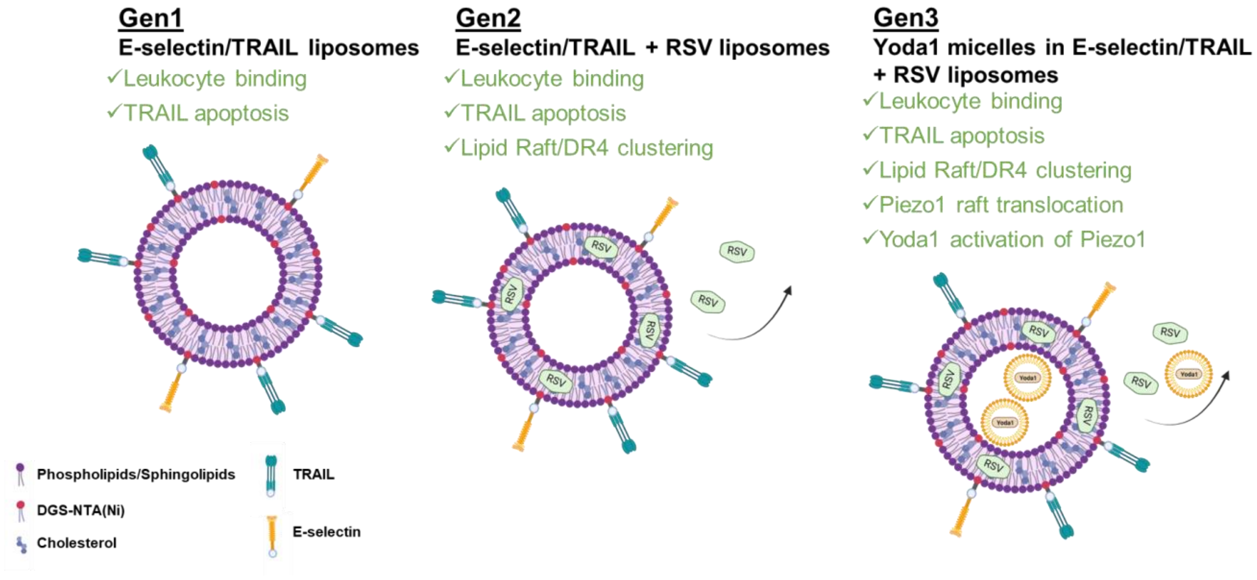

Figure 6.5. Next generation liposome approaches to increase TRAIL sensitization.

6.2.10 Determine the effects of hypercholesterolemia on lipid rafts and TRAIL signaling

Obesity is on pace to overtake smoking as the leading environmental cause of cancer. Hypercholesterolemia is a common metabolic condition in obese individuals and been has shown to increase the risk of developing CRC and the incidence of metastatic disease [376,377]. Exogenous and membrane cholesterol concentrations have been shown to alter lipid raft function, structure, and prevalence in immune cells, having consequential effects on surveillance and signaling [376,378,379]. Therefore, it is hypothesized pathological levels of cholesterol within colorectal cancer cells would have dramatic effects on lipid raft structure and death receptor signaling. Comparing the TRAIL-sensitizing effects of hypercholesterolemia in parental and chemoresistant CRC cells may provide translational value in CRC patients with obesity-related comorbidities. This can be studied *in vitro* through media supplementation with water-soluble cholesterol and free fatty acids. Further, *in vivo* studies could compare differences in lipid raft composition and TRAIL signaling between non-obese mice and obese mice that are fed a high fat diet.

Additionally, it would be interesting to analyze differences in treatment response between parental and OxR derivative cell lines to determine if hypercholesteremia is partial to oxaliplatin-resistant cell populations. Studies have shown that serum cholesterol levels and hyperlipidemia can drive stemness in colorectal cancer, promoting EMT and resistance to chemotherapy [380]. This makes examining hypercholesterolemia within OxR cell populations particularly intriguing.

6.2.11 Examine lipid raft protection mechanisms to promote immune evasion

Cytotoxic T lymphocytes (CTLs) elicit apoptosis in target cells through perforin secretion at the immunological synapse. Remarkably, this process is unidirectional in that CTLs remain spared from these perforin effects. A recent study showed that CTLs protect themselves through the arrangement of lipid rafts at the immune synapse which repel extracellular perforin [381]. This begs the question of whether cancer cells utilize similar mechanisms at the immune synapse to evade T cell killing. Future studies should closely examine the presence of lipid rafts on cancer cells at the immune synapse to determine if other cells possess this perforin repelling quality. Similar to cancer cell overexpression of checkpoint ligands like PD-L1 on the cell surface, lipid rafts may be another mechanism by which cancer cells have adapted to survive immune cell recognition.

6.2.12 Further elucidate the role of lipid rafts in mechanosensitive ion channel function

In Chapter 4, I present the first evidence for the role of lipid rafts in the activation of Piezo1. While this data remains far from causal, this will hopefully spark further enthusiasm into further understanding how lipid rafts affect the opening of mechanosensitive ion channels. This may include utilizing patch-clamp electrophysiology and real-time calcium imaging for a more mechanistic understanding of ion channel opening. Piezo1 and other MSCs can also be integrated into biomimetic synthetic lipid bilayers, such as liposomes [382]. This is advantageous as it provides a tunable platform for precisely adjusting membrane composition while removing unwanted complexities of the cell membrane.

6.2.13 Investigate other downstream effects from resveratrol + Yoda1 calcium influx

Calcium is a secondary messenger that is critical in numerous cellular processes. Chapter 4 demonstrated that resveratrol increases Yoda1 activation and calcium influx, possibly through Piezo1 colocalization with lipid rafts. While this increase in calcium had little effect on apoptotic signaling, there are many other downstream processes to explore. For example, augmented cytosolic calcium in cancer is associated with increased migration and EMT [383,384]. Invasion and migration assays should be explored while investigating EMT hallmarks, such as cell surface vimentin and loss of E-cadherin.

Appendix A:

TRAIL Liposomes Induce Apoptosis of MC38 Mouse Colorectal Cancer Cells but Not Macrophages

Joshua D. Greenlee, Zhenjiang Zhang, and Michael R. King

A.1 Abstract

CRC tumors have been characterized as having high infiltration of myeloid cells, specifically macrophages. MC38 cells have been used as a suitable model for hypermutated microsatellite instability high (MSI-H) CRC, while RAW264.7 cells are a macrophage cell line used extensively *in vitro*. The goal of this study was to examine the efficacy of TRAIL and TRAIL-conjugated liposomes within these commonly used mouse cell lines. Cells were plated overnight and treated with soluble TRAIL, DGS-NTA(Ni) liposomes conjugated with E-selectin/TRAIL (EST) proteins, or unconjugated EST liposomes for 24 hours. MC38 cells showed minimal sensitivity to TRAIL and unconjugated EST liposomes but were significantly sensitive to EST-conjugated liposomes. MC38 cells were characterized as having high expression of DR5, the only functional TRAIL receptor capable of inducing apoptosis in mouse cells. Interestingly, TRAIL and TRAIL-conjugated liposomes displayed minimal apoptotic effects on RAW264.7 macrophages. TRAIL-mediated apoptosis remained similar between unpolarized M0 macrophages and M1/M2 polarized cells, however M0 and M2 phenotypes had higher expression of DR5. To lay the groundwork for future 3D treatment studies, MC38 cells successfully formed 3D spheroids in monocultures and in cocultures with RAW264.7 cells using AggreWell™800 plates. Overall, E-selectin/TRAIL liposomes were found to be more effective than TRAIL to kill MC38 cells *in vitro*, prompting future studies to test liposome efficacy in 3D cultures and metastatic mouse models.

A.2 Introduction

Carcinogenic-induced mouse models of CRC have existed for nearly 80 years and have been crucial in the understanding of colon cancer biology [336]. More recently, genetically engineered mouse models (GEMMs), such as APC mutant models, have been developed to study both sporadic and hereditary CRC. While these inducible models are useful to study carcinogenesis, chemotoxicity, and immune cell infiltration in mice, they lack invasiveness and metastatic potential. To overcome these limitations, subcutaneous or orthotopic injection of stable CRC mouse cell lines have been utilized [329,334,351]. Orthotopic injection specifically has been shown to replicate metastatic spread seen in humans. Injection of human-derived cell lines requires transgenic "humanized" mice that lack a full immune complement to prevent host-immune rejection of tumors. Mouse-derived CRC cells, however, can be orthotopically or subcutaneously injected into wild-type mice to study tumor-immune cell interactions *in vivo*. For this reason, many current cancer immunotherapy studies use chemically-induced cell lines generated from a mouse, and transplant them subcutaneously or orthotopically [329,334,336,351].

The MC38 cell line was derived from a DMH (1,2-dimethylhydrazine dihydrochloride)-induced grade III colon adenocarcinoma in a female C57BL/6 mouse. Another commonly used syngeneic CRC model is the CT26 cell line, which was derived from a N-nitroso-N-methylrethane-induced colon carcinoma in a BALB/c mouse. Both of these carcinogen-induced models are characterized as having a high mutational burden and are suitable for the study of hypermutated human colon tumors [385]. However, MC38 cells are characterized as being more immunogenic with over six-fold greater immunoedited mutations compared to CT26 cells [386]. Additionally, MC38 cells have been characterized as MSI-H with mutations within MMR genes. MSI-H/MMR-deficient CRC accounts for approximately 15% of all cases, and these tumors are characterized as having increased neoantigens, higher infiltration of CD8+ T cells, and a more favorable response to checkpoint blockade therapy. MC38 tumors have shown greater resistant to chemotherapy *in vivo*, while both MC38 and CT26 tumors have demonstrated some response to anti-PD-1/PD-L1 and anti-CTLA-4 therapy [349,350].

Tumor associated macrophages (TAMs) have been shown to account for a large portion of cells within the tumor microenvironment (TME) and can undergo phenotypic polarization to support tumor progression [387]. M1 differentiated macrophages are characterized as proinflammatory and can kill tumor cells within the TME via phagocytosis. The presence of M1 macrophages in tumors is associated with favorable prognosis in patients [388]. Proinflammatory cytokines such as IFN-γ and TNF-α cause M1 differentiation, leading to the macrophage secretion of IL-6 to recruit other immune populations within the TME [387]. On the contrary, M2 macrophages are an anti-inflammatory subtype of cells that are activated from anti-inflammatory cytokines such as IL-4 and IL-10. CRC cells have been shown to convert TAMs within the TME into M2 phenotypes to promote tumorgenicity. Once differentiated, M2 macrophages can promote tumor survival though regulatory T cell (Treg) recruitment, suppression of $CD8^+$ T cells, and expression of checkpoint ligands PD-1 and CTLA-4 [387]. While these two macrophage subtypes are very distinct, their characterization is not binary, but rather exists on a spectrum between M1-like and M2-like [389]. This has motivated the discovery of therapeutics that can regulate macrophage plasticity within the TME to promote anti-tumor immunity.

The stromal landscape within MC38 tumors has been characterized by expansion of Tregs and TAMs during tumor development [350]. Accordingly, research suggests combining Treg or macrophage targeted agents in combination with checkpoint inhibitors may enhance treatment efficacy. Apart from the well characterized anti-cancer effects of TRAIL, recent studies have shown that TRAIL also induces apoptosis of TAMs while sparing other immune cell populations [360]. Additionally, there is some evidence that TRAIL may preferentially induce apoptosis in M2-like macrophages compared to M1 populations through upregulation of functional death receptor 5 (DR5). In this study, I investigate the apoptotic effects of TRAIL and TRAIL-conjugated liposomes in MC38 cells. Additionally, I elucidate death receptor expression and TRAIL response within the RAW264.7 macrophage-like cell line for the first time. Finally, I demonstrate successful 3D spheroid cocultures of MC38 and RAW264.7 cells for future studies to investigate treatment responses within a more complex tumor microenvironment.

A.3 Results

A.3.1 E-selectin/TRAIL are conjugated to liposomes via DGS-NTA(Ni) lipids

E-selectin/TRAIL liposomes (EST) were created using a thin film hydration method discussed in Chapter 3. Liposomes were stepwise extruded through 400nm, 200nm and 100nm filters, yielding liposomes approximately 100 nm in size. His-tagged TRAIL and E-selectin were conjugated to the liposome surface via DGS-NTA(Ni) lipids (**Figure A.1A**). Extrusion yielded monodispersed liposomes with a low polydispersity index (PDI) (**Figure A.1B, D**). To demonstrate successful conjugation via this click-chemistry mechanism, liposomes were synthesized with (+)

or without (-) DGS-NTA(Ni). Size measurements via dynamic light scattering (DLS) demonstrate EST(+) liposomes had an increase in average diameter compared to Naked Liposomes with no proteins and EST(-) liposomes, indicating successful conjugation (**Figure A.1B-C**). Cryo-transmission electron microscopy (CryoTEM) images allow for direct visualization of proteins on the liposome surface (**Figure A.1E**).

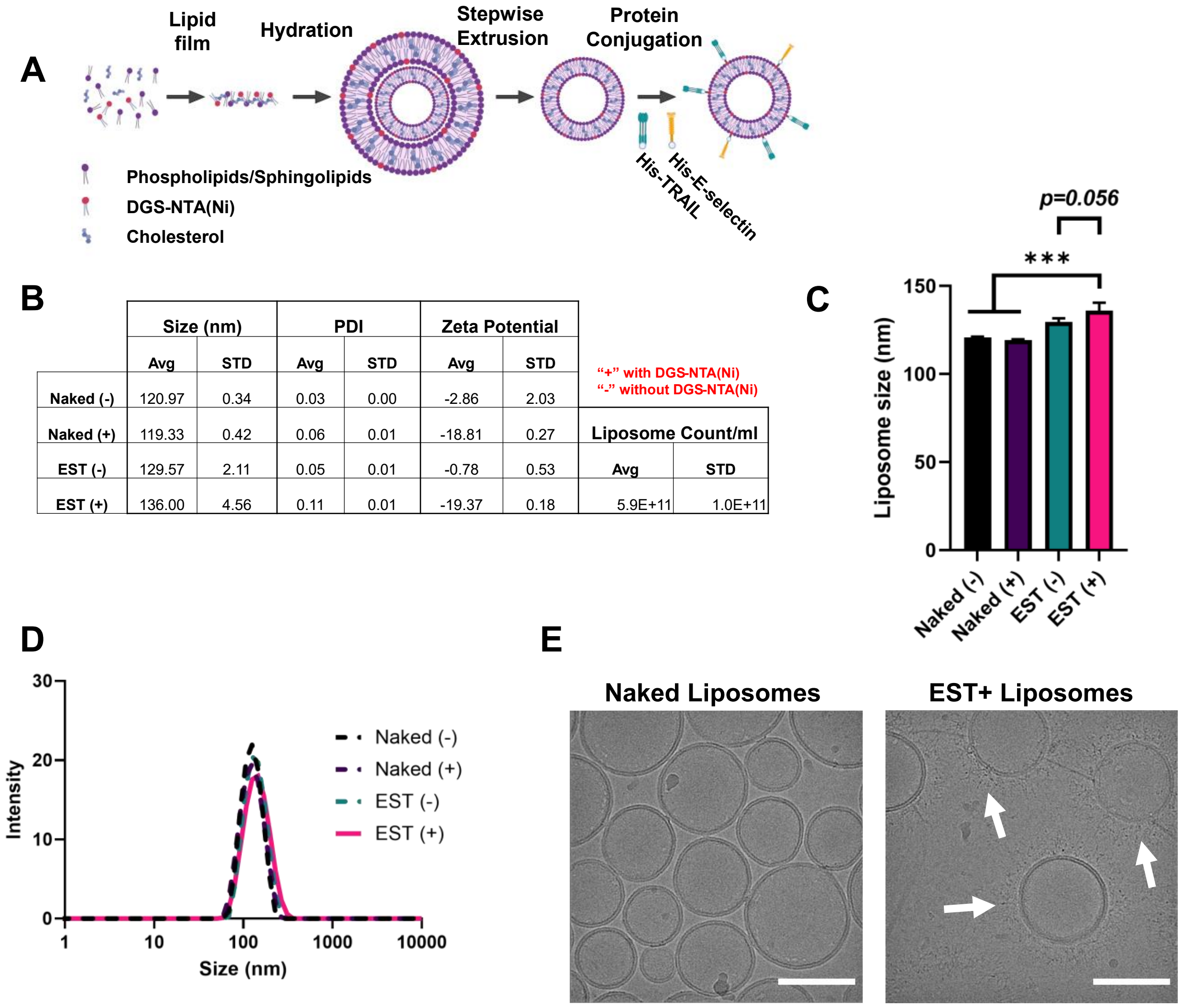

	Size (nm)		PDI		Zeta Potential		Liposome Count/ml	
	Avg	STD	Avg	STD	Avg	STD	Avg	STD
Naked (-)	120.97	0.34	0.03	0.00	-2.86	2.03		
Naked (+)	119.33	0.42	0.06	0.01	-18.81	0.27		
EST (-)	129.57	2.11	0.05	0.01	-0.78	0.53		
EST (+)	136.00	4.56	0.11	0.01	-19.37	0.18	5.9E+11	1.0E+11

"+" with DGS-NTA(Ni)
"-" without DGS-NTA(Ni)

Figure A.1. His-tagged E-selectin/TRAIL are successfully conjugated to the surface of nanoscale liposomes. (A) Liposomes are synthesized using a thin film hydration method, extrusion, and click-conjugation of his-tagged proteins. **(B)** Size, polydispersity, zeta potential and concentration measurements. **(C)** Average liposome size measurements. N=2; n=6; ***p<0.001. **(D)** Size distribution histograms in conjugated and unconjugated liposomes. **(E)** Cryo-TEM images of naked and EST liposomes. White arrows show proteins on the liposome surface. Scale bar = 100 nm.

A.3.2 Liposome-conjugated TRAIL is required to induce apoptosis in MC38 cells

MC38 cells were confirmed to have expression of the singular functional mouse TRAIL receptor, DR5, prompting investigation of treatment efficacy with our liposomes (**Figure A.2D**). MC38 cells were treated with soluble TRAIL (100 ng/ml), naked liposomes, or EST liposomes (at equivalent concentrations of TRAIL, 100 ng/ml). EST liposome treatment increased the percentage of apoptotic cells and decreased cell viability compared to soluble TRAIL (**Figure A.2A**). Images confirm shrunken morphology, membrane blebbing and floating cells, all indicative of apoptosis. Interestingly, liposomes conjugated with E-selectin and TRAIL had a significantly more pronounced effect on cell viability and apoptosis compared to unconjugated E-selectin/TRAIL liposomes or soluble TRAIL (**Figure A.2B-C**). This demonstrates that even in static *in vitro* cultures, liposomal TRAIL more effectively induces apoptosis in this mouse CRC cell line. From this point forward, all studies with EST liposomes are referring to EST+ conjugated liposomes containing DGS-NTA(Ni).

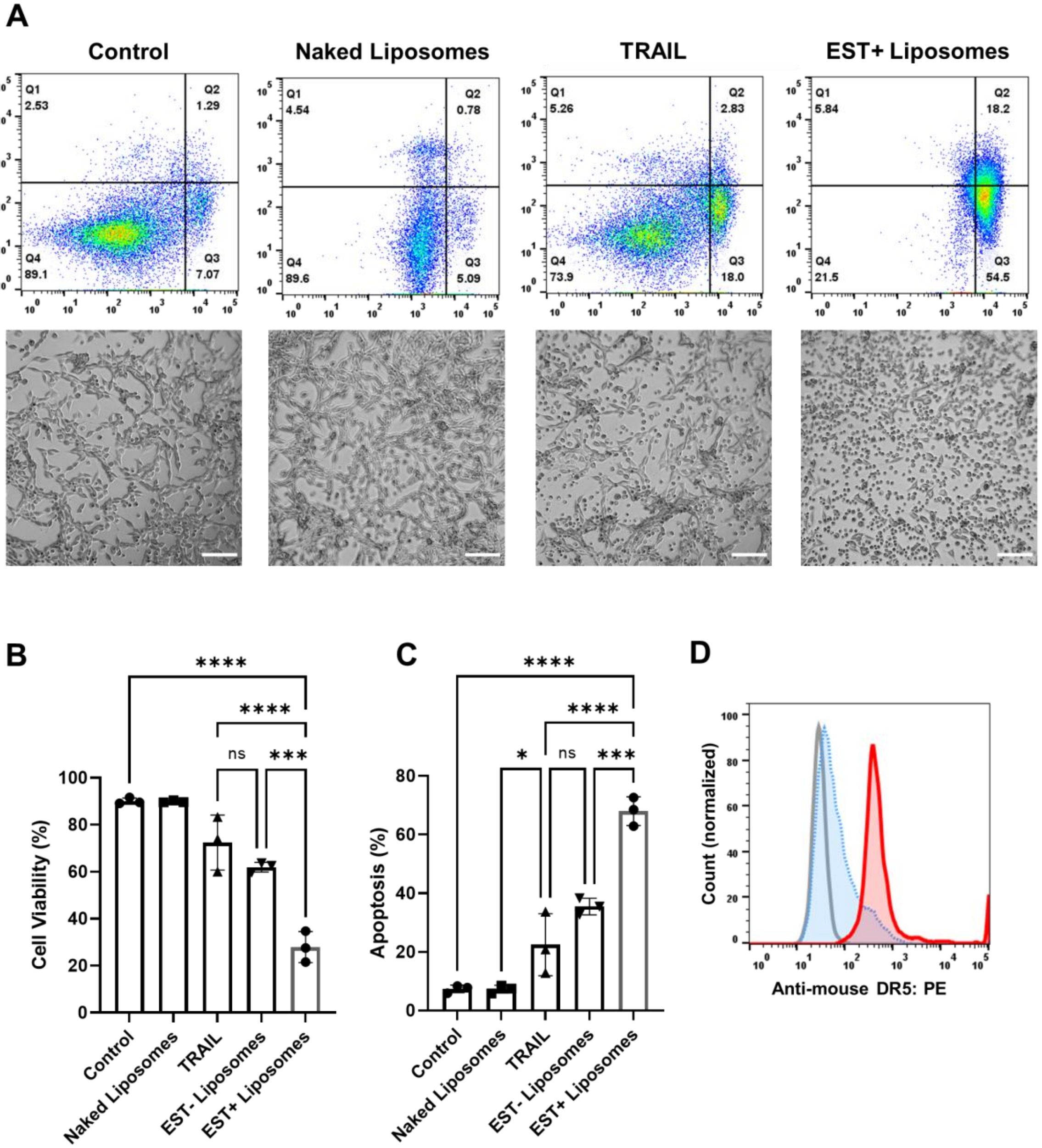

Figure A.2. EST-conjugated liposomes induce apoptosis in MC38 cells. (A) Annexin-V/PI plots showing necrotic (Q1), late apoptotic (Q2), early apoptotic (Q3), and viable cells (Q4) from liposome and TRAIL treatments. Corresponding brightfield images showing dramatic increases in apoptotic cells (rounded morphology) in EST+ Liposome treated samples. Scale bar = 200 µm **(B-C)** Cell viability and apoptosis quantified, respectively. N=3; ns=non-significant *p<0.05 **p<0.01 ***p<0.001 ****p<0.0001. **(D)** Expression of DR5 in MC38 cells. Gray = control, blue = isotype, red = anti-mouse DR5.

A.3.3 Naïve and M2 polarized RAW264.7 macrophages have higher expression of DR5 but remain resistant to EST liposomes.

RAW264.7 cells have been used as a suitable model of mouse macrophages for *in vitro* immunomodulation assays and cocultures [390]. Naïve M0 macrophages were polarized into M1 or M2 phenotypes using a previously described protocol [391]. Proinflammatory M1 macrophages were polarized by incubating with lipopolysaccharides (LPS) and INF-γ for 48 hours. Conversely, M2 tumor associated macrophages were polarized by treating with IL-4 for 48 hours. M1 cells have a starkly different appearance than M2 cells in culture, having a larger spindle shaped morphology (**Figure A.3A**). Immediately following the 48-hour polarization, macrophages were recovered and stained for expression of DR5. M0 macrophages were the highest expressors of DR5 while M1 cells had the lowest expression (**Figure A.3B-C**). All macrophages had lower expression of DR5 than MC38 cells. Polarized RAW264.7 cells were also treated with liposomes and soluble TRAIL. In accordance with the higher DR5 surface expression, naïve M0 cells were slightly sensitive to EST liposomes, and significantly more sensitive than polarized phenotypes (**Figure A.3B-C**). However, normalized viability remained greater than 80%, demonstrating the TRAIL-resistant nature of the RAW264.7 cell line.

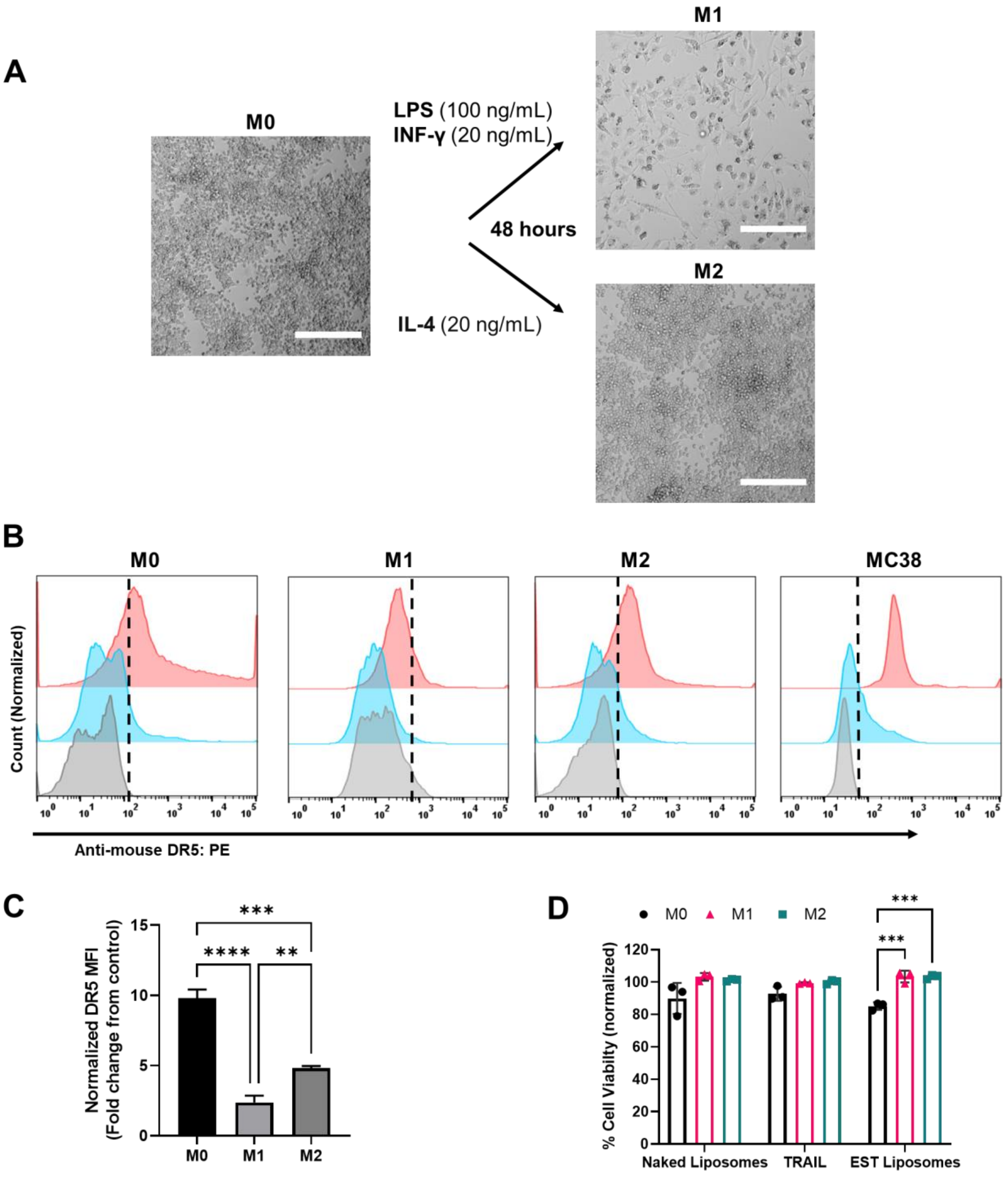

Figure A.3. Naïve and polarized RAW264.7 macrophages are resistant to TRAIL and EST liposomes. (A) Polarization protocol with images highlighting morphological differences between M0, M1 and M2 phenotypes. Scale bar = 200 µm. **(B)** Flow cytometry histograms of DR5 staining in naïve and polarized macrophages. Gray = control, blue = isotype, red = anti-mouse DR5. **(C)** Quantification of normalized median fluorescence intensity (MFI). Normalized MFI was calculated by dividing the median PE intensity of DR5 stained samples by the unstained control of each polarization condition. **(D)** Cell viability following 24 h treatments measured using Annexin-V/PI staining. N=3; $^{**}p<0.01$ $^{***}p<0.001$ $^{****}p<0.0001$.

A.3.4 MC38 cells form spheroids of tunable size in monocultures and cocultures with RAW264.7 cells

While 2D cultures are commonly used as a starting point to determine treatment efficacy, they lack physiological relevance and often are not predictive of *in vivo* response [392]. Three-dimensional spheroid cell cultures more closely mimic the architectures of tumors and represent an added challenge for treatment response. For example, our lab has previously shown that prostate cancer cells respond differently to chemotherapy in 3D spheroids compared to 2D cultures [393]. Taking this into account, I wanted to identify the spheroid forming characteristics of MC38 and RAW264.7 cells to lay the groundwork for future treatment studies.

Spheroids were formed using AggreWell™800 Microwell Culture Plates. Spheroid size was adjusted by changing initial seeding concentrations from 1,000 - 5,000 cells per spheroid. Naïve RAW264.7 cells alone did not form reproducible spheroids, but occasionally formed clusters of approximately 10-30 cells (**Figure A.4A**). MC38 cells formed spheroids with diameters that increased with seeding density, ranging from 0.4-0.5 mm (**Figure A.4B**). While RAW264.7 cells did not form spheroids by themselves, they did form spheroids in cocultures with MC38 cells. Higher ratios of RAW264.7:MC38 seeding corresponded with spheroids that were smaller in diameter (**Figure A.4C**). While this is likely due to RAW264.7 cells being much smaller, further studies should verify the presence of both cell lines within the formed spheroids to rule out the possibility of macrophage exclusion.

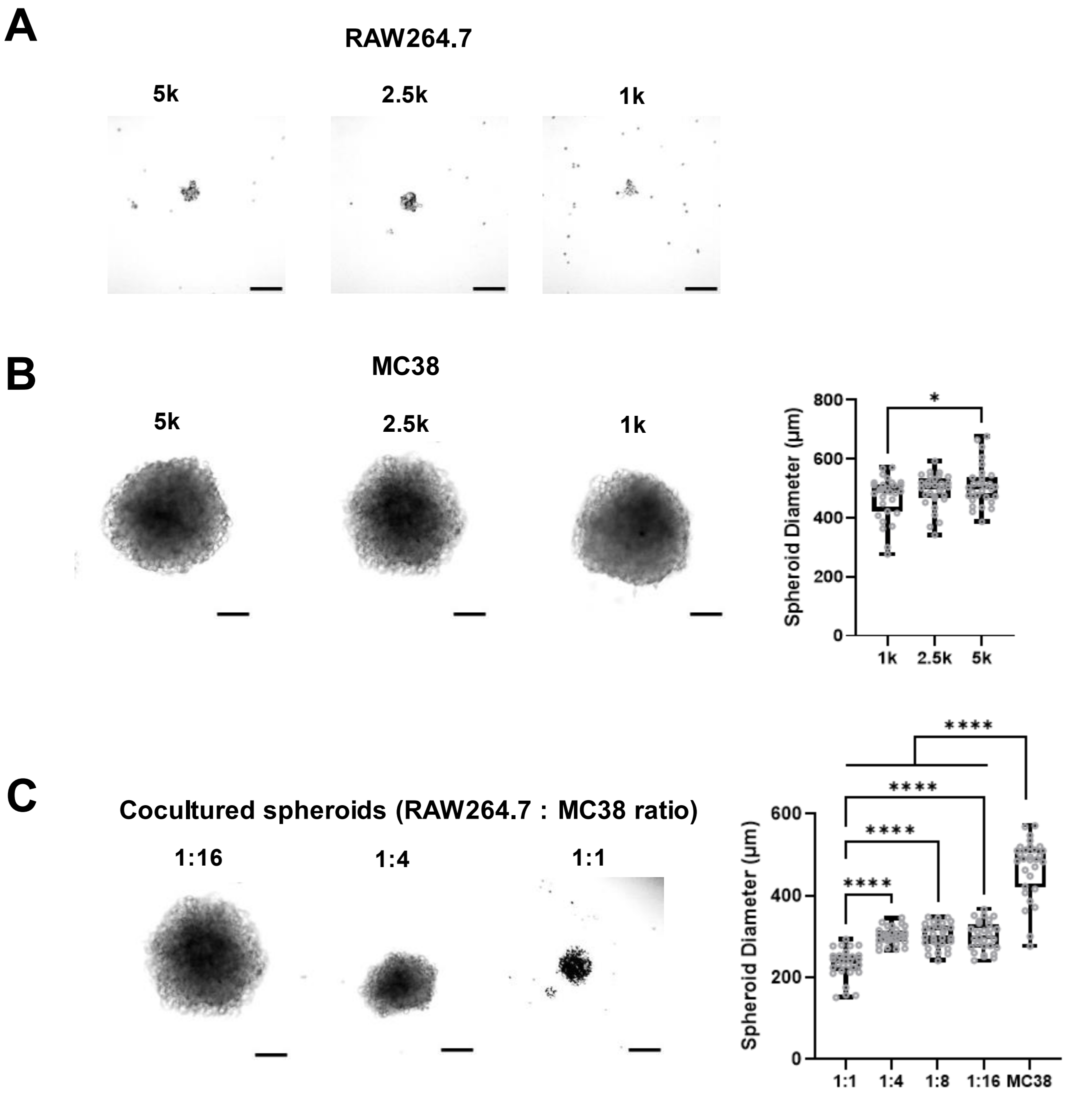

Figure A.4. MC38 cells form reproducible spheroids with tunable diameters depending on seeding density. (A) Representation of small RAW264.7 clusters. **(B)** MC38 spheroids of varying sizes dependent upon seeding density. **(C)** Cocultures of RAW264.7 and MC38 cells at varying ratios. 1k = 1,000 cells per spheroid, 2.5k = 2,500 cells per spheroid and 5k = 5,000 cells per spheroid seeding density. Scale bar = 200 µm for all images. n=30 spheroids analyzed per condition; *p<0.05 **p<0.01 ***p<0.001 ****p<0.0001.

A.4 Discussion

Our lab has demonstrated the utility of TRAIL-conjugated liposomes as an effective antimetastatic therapy through sensitization from fluid shear stress in the bloodstream [270,356]. E-selectin/TRAIL liposomes are advantageous compared to soluble TRAIL for *in vivo* applications as they have prolonged time in the circulation through immune cell hitchhiking. Interestingly, I have determined that TRAIL liposomes induce apoptosis to a significantly higher degree than soluble TRAIL in static 2D cultures with MC38 cells. Liposomes with unconjugated TRAIL had minimal apoptotic effects, likely pointing to an enhanced effect of TRAIL signaling due to conjugation with the liposome membrane. There is a highly regarded study from Wajant and colleagues that demonstrated TRAIL-R1 (DR4) is activated by both soluble and membrane TRAIL while TRAIL-R2 (DR5) is only activated by membrane TRAIL or TRAIL that is artificially cross-linked [394]. Studies in multiple other ligand-receptor interactions suggest that artificial cross-linking of soluble ligands mimics the biological activity of its membrane form [395]. This group also determined that soluble TRAIL can be converted to a TRAIL-R2 signaling ligand via artificial immobilization to the cell surface using a TRAIL-fusion protein [394]. Importantly, mouse cells only express one functional death receptor with homology closest to human TRAIL-R2/DR5. This would suggest that TRAIL signaling in mouse cells also requires membrane or cross-linked TRAIL. TRAIL conjugated to the surface of our liposomes may exhibit enhanced signaling via a similar mechanism to cross-linking, which is analogous to its membrane form. Additionally, E-selectin dependent immobilization on the cell surface may also contribute to increased ligand-receptor interaction. A more mechanistic understanding of the differences between soluble TRAIL and liposomal TRAIL on receptor binding and activation should be explored in future studies.

I also demonstrated that despite evidence for the apoptotic effects of TRAIL in primary derived macrophages, RAW264.7 cells were resistant to TRAIL and EST liposomes. Naïve M0 cells displayed slight decreases in viability from EST liposomes which may be explained by higher surface expression of DR5. EST liposomes had no effect on polarized M1 and M2 phenotypes. While RAW264.7 cells have proven to be a suitable macrophage model to study immunomodulators, they also differ substantially from bone marrow derived macrophages in biological processes including cell cycle control, cytoskeletal organization, and apoptosis [396]. Therefore, it is important to also test EST liposomes in primary derived cells before making conclusions on their macrophage targeting abilities.

In conclusion. E-selectin/TRAIL liposomes initiate apoptosis in MC38 cells which is dependent on successful conjugation of TRAIL to the liposome membrane. Demonstrating successful formation of MC38 spheroids is an initial important step for evaluating treatment efficacy in 3D models. Future studies should examine liposome treatments in these 3D spheroids and compare their efficacy with that in 2D. Determining macrophage polarization as a result of 3D spheroid cocultures with MC38 cells will also be key to understanding how the tumor microenvironment regulates immune function. These studies will be key before testing liposomes in an MC38 orthotopic mouse model, such as that described in Chapter 5.

A.5 Materials and Methods

A.5.1 Cell Culture

MC38 cells were purchased from Kerafest and cultured in Dulbecco's Modified Eagle Medium (DMEM) containing 4.5 g/L D-Glucose, L-glutamine, and 110 mg/L sodium pyruvate. Media was supplemented with 10% fetal bovine serum (FBS), 1% PenStrep, 1x MEM Nonessential Amino Acids and 1 mM HEPES. Cells were maintained in a humidified incubation chamber at 37ºC and 5% CO_2. Cells were passaged every 2-3 days, or at 50% - 70% confluency by lifting with 0.05% Trypsin-EDTA and subculturing at 1:5-1:10 ratios.

RAW264.7 cells were purchased from ATCC and cultured in (DMEM) containing 4.5 g/L D-Glucose, L-glutamine, and 110 mg/L sodium pyruvate. Media was supplemented with 10% FBS and 1% PenStrep. Cells were passaged ever 3-5 days by scraping and subculturing at 1:5 – 1:10 ratios.

A.5.2 Liposome Synthesis and Characterization

L-α-phosphatidylcholine (Egg PC), sphingomyelin (Egg SM), cholesterol, and 1,2-dioleoyl-sn-glycero-3-[(N-(5-amino-1-carboxypentyl)iminodiacetic acid)succinyl] (nickel salt) (18:1 DGS-NTA(Ni)) were purchased from Avanti Polar Lipids and reconstituted in chloroform and added at a 5:3:1:1 ratio by mass, respectively, for a total combined mass of 10 mg. Samples without DGS-NTA(Ni) were combined at a 6:3:1 ratio. The solution was dried overnight under vacuum in a desiccation chamber. The lipid film was hydrated the next day in 700 µl of liposome buffer (DI water with 150 mM NaCl, 10 mM HEPES, and 1 mM $MgCl_2$) and sonicated in a water bath at 50ºC for 1 h with interment vertexing. The resulting multilammelar vesicles were extruded through a 400 nm pore filter 10x, 200 nm filter 10x, and 100 nm 20x. His-tagged TRAIL (Enzo) and E-selectin (R&D Systems) were added to 200 µl of liposomes at 22.5 µg/ml and 15 µg/ml concentrations, respectively, and then incubated for 30 min at 37ºC. Liposomes were stored at 4ºC on a rotator for up to one week.

A.5.3 Annexin-V/PI Apoptosis Assays

MC38 cells were plated in a 12 well plate at 100,000 cells per well and naïve RAW264.7 cells were plated at 200,000 cells per well. Cells were treated with soluble TRAIL (100 ng/ml), EST liposomes with/without DGS:NTA(Ni) (0.1 mg of lipids or 100 ng/ml TRAIL), or naked liposomes with/without DGS:NTA(Ni) (0.1 mg lipids) for 24 h. After 24 h cells and the supernatant were recovered, washed 1x with HBSS and stained with 5 µl Annexin-V and 5 µl PI for 15 min at room temperature. Cells were immediately analyzed using a Guava easyCyte 12HT benchtop flow cytometer. Viable cells were identified as negative for both Annexin-V and PI, early apoptotic cells as positive for Annexin-V only, late apoptotic cells were positive for both Annexin-V and PI, and necrotic cells were positive for PI only. Flow cytometry plots were analyzed using FlowJo v10.8.0 software.

A.5.4 RAW264.7 Polarization

RAW264.7 cells were seeded at 200,000 cells per well in a 12 well plate for 24 hours. For M1 polarization, media was supplemented with 100 ng/ml LPS and 20 ng/ml INF-γ for 48 hours. For M2 polarization, media was supplemented with 20 ng/ml IL-4 for 48 hours. For liposome/TRAIL treatments, polarization factors were left in solution during overnight treatments.

A.5.4 Flow Cytometry DR5 Staining

Cells were collected from 12 well plates and washed with HBSS. Samples were fixed with 4% PFA for 15 min at RT, then washed and blocked in 1% BSA for 20 minutes. Cells were incubated with 1 µl mouse TruStain FcX for 10 minutes, then incubated with either 5 µl PE anti-mouse CD262 (DR5) or PE Anti-IgG Isotype Ctrl Armenian Hamster Monoclonal Antibody for 30 min on ice. Finally, cells were washed 2x with HBSS and analyzed via flow cytometry.

A.5.4 Spheroid Formation and Characterization

Spheroids were formed using the AggreWell™800 Microwell Culture Plates in accordance with the manufacturer's protocol. Briefly, wells were coated with 500 µl of anti-adherence solution and centrifuged, then rinsed 2x with media. Cells were plated at 1.5 million cells/well (for 5,000 cells per spheroid), 750,000 cells/well (for 2,500 cells per spheroid), or 300,000 cells/well (for 1,000 cells per spheroid). For cocultures, cells were mixed thoroughly at appropriate ratios to a final concentration of 750,000 cells/well before plating. Plates were centrifuged at 300xg for 5 minutes, and then incubated for 5 days (approximately 6 doubling times). Images were taken using an Olympus microscope and analyzed in ImageJ.

Appendix B:

TRAIL-Conjugated Liposomes That Bind Natural Killer Cells to Induce Colorectal Cancer Cell Apoptosis

Joshua D. Greenlee, Zhenjiang Zhang, and Michael R. King

B.1 Abstract

Natural Killer (NK) cell functionality is a strong indicator of favorable prognosis in cancer patients, making NK cells an appealing therapeutic target to prevent lymph node dissemination. I engineered liposomes that were conjugated with anti-CD335 antibodies for NK cell targeting, and the apoptotic ligand TRAIL to kill cancer cells. TRAIL/anti-CD335 liposomes successfully bound to isolated NK cells *in vitro*. Once piggybacked to the surface of NK cells, these “Super Natural Killer Cells” were able to more effectively kill oxaliplatin-resistant SW620 cells and COLO205 cells via TRAIL-mediated apoptosis compared to NK cells alone. Super NK cells were more effective under physiological levels of fluid shear stress found in the lymphatics. Liposome biodistribution after intravenous administration confirmed the sustained presence of liposomes within the spleen and tumor draining mesenteric lymph nodes for at least four days. These results provide the groundwork for *in vivo* treatment studies in an orthotopic mouse model of CRC metastasis.

B.2 Introduction

It is estimated that approximately 80% of cancers metastasize initially through lymphatics [397]. While the majority of all cancer related death is attributed to metastasis, there exist no effective anti-metastatic therapies to prevent lymphatic dissemination [398]. The tumor draining lymph nodes (TDLN) are often the first site of cancer metastasis and are indicative of tumor dissemination and poor prognosis due to the leaky and tortuous nature of lymphatic vessels [397]. Once in the TDLN, cancer cells have access to lymphatic and blood vessels that act as highways to distant organs.

An innate component of the lymph nodes are a subset of lymphocytes known as natural killer (NK) cells, which have been shown to exhibit an anti-tumor response but alone are ineffective in preventing metastasis [397]. NK cells have demonstrated anti-tumor effects through granzyme and perforin secretion as well as production of type II IFNs to recruit other immune cells [399]. NK cells have also been shown to mediate cancer cell cytotoxicity in part through the expression of membrane TRAIL on the cell surface [53,400]. Additionally, NK cells have been shown to detect and kill MHC mutant cancer cells that evade T cell detection. Many studies have shown that poor NK cell functionality is strongly correlated with recurrence and poor prognosis in patients, demonstrating their importance in anti-tumor surveillance [401–403].

Cancer cells residing within the TDLN can compromise immune functionality, thereby promoting distal dissemination. This demonstrates a need for a sentinel lymph node targeted therapy that provides a more robust anti-tumor response. In this study, I engineered and optimized liposomes conjugated with TRAIL and an NK cell targeted antibody. These liposomes bind effectively to NK cells to form a complex we termed “Super Natural Killer Cells”. The efficacy of Super NK cells was tested against clinically relevant chemoresistant and metastatic CRC cell lines under static conditions and physiological levels of fluid shear stress. Finally, liposome biodistribution was investigated in mice for different routes of administration to lay the groundwork for future *in vivo* studies.

B.3 Results

B.3.1 TRAIL/anti-CD335 liposomes bind NK cells in vitro

Our lab has previously shown the efficacy of TRAIL/anti-NK1.1 liposomes to prevent metastasis in a subcutaneous mouse model [404]. However, we have yet to investigate how different NK cell targeting antibodies improve liposome binding. To improve liposome binding, three antibodies were chosen targeting three different NK cell specific mouse antigens: NK1.1 (CD161), CD49b and CD335. While NK1.1 has previously been considered the most specific marker on murine NK cells in C57BL/6 mice, CD335 is also a highly specific marker that is expressed on human and mouse NK cells [405,406]. TRAIL and NK cell antibodies were thiolated using Traut's Reagent (2-iminothiolane) and conjugated to the surface of PEG-Maleimide liposomes via click chemistry (**Figure B.1A**). Dynamic light scattering (DLS) was used to quantify diameter size and confirm successful protein conjugation. Interestingly, TRAIL/anti-CD335 liposomes were the only group to have a significant increase in diameter, indicating successful conjugation. E-selectin/TRAIL liposomes discussed in Appendix A only saw modest increases in size after conjugation, likely due to the smaller hydrodynamic radii of these proteins. Meanwhile, IgG antibodies are much larger (150 kDa) with hydrodynamic radii of nearly 12 nm, making it easier to detect size differences from conjugation. A size increase from 109.3 ± 2.1 nm to 122.5 ± 2.9 nm with no changes in polydispersity confirmed successful conjugation of anti-CD335 and TRAIL (**Figure B.1B**).

To monitor binding to NK cells, liposomes were incorporated with the near-infrared fluorescent lipid dye DiR. NK cells were isolated from the spleen of C57BL/6 mice and incubated with liposomes for 30 min. Anti-CD335 liposomes saw the most specific binding with over a four-fold increase compared to anti-CD49b and a two-fold increase from anti-NK1.1 liposomes (**Figure B.1C**).

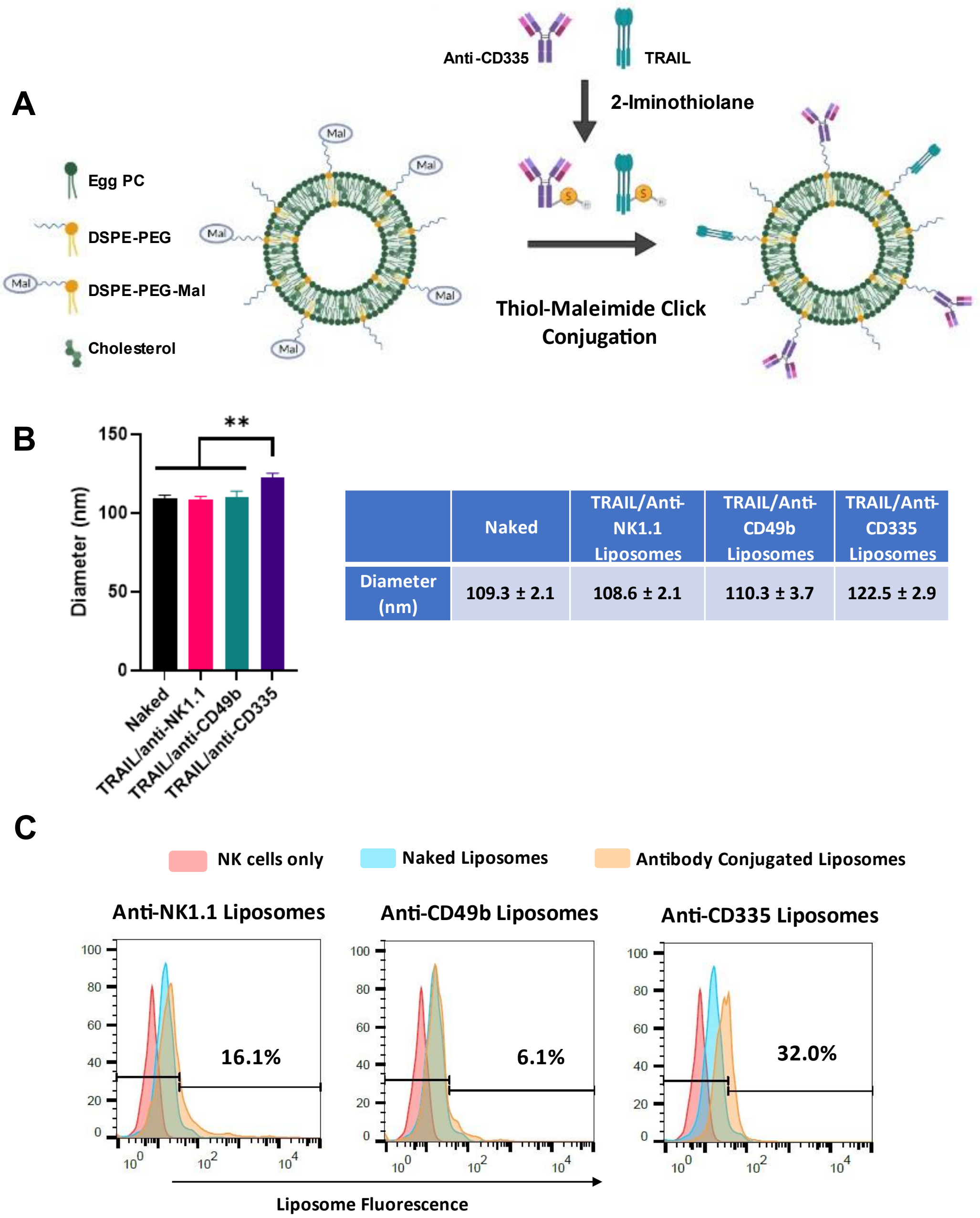

	Naked	TRAIL/Anti-NK1.1 Liposomes	TRAIL/Anti-CD49b Liposomes	TRAIL/Anti-CD335 Liposomes
Diameter (nm)	109.3 ± 2.1	108.6 ± 2.1	110.3 ± 3.7	122.5 ± 2.9

Figure B.1. TRAIL/anti-CD335 liposomes bind NK cells *in vitro*. (A) TRAIL and NK cell antibodies were thiolated using 2-imminothiolane and click conjugated to liposomes containing DSPE-PEG-Maleimide lipids. **(B)** Liposome size measurements from DLS. N=3 **p<0.01. **(C)** Fluorescent liposomes were incubated with NK cells for 30 min and fluorescence was measured using flow cytometry. Values represent binding specificity compared to naked (unconjugated) liposomes.

B.3.2 Super NK cells kill clinically relevant CRC cell lines under static and lymphatic flow conditions

To investigate the apoptotic effects of TRAIL/anti-CD335 liposomes, Super NK cells were formed by incubating liposomes with NK cells and then centrifuging to remove unbound liposomes. SW620 OxR and COLO205 CRC cells were treated with a 1:1 ratio of Super NK cells or controls, and apoptosis was measured using Annexin-V/PI staining (**Figure B.2A**). SW620 OxR is an oxaliplatin-resistant derived cell line isolated from the TDLN of a patient, described in detail in Chapter 3. COLO205 is a metastatic cell line derived from the ascites of a Stage IV CRC patient. Super NK cells significantly reduced cell viability in both cell lines compared to NK cells alone (**Figure B.2B**). COLO205 cells were more sensitive, with only 20% viable cells after 24 hours. Visualization via SEM confirms that Super NK cells were able to recognize CRC cells under static conditions, causing membrane blebbing and eventual apoptotic arrest (**Figure B.2C**).

Mouse lymphatic vessels have been characterized as having fluid forces between 0.4-12 dyne/cm^2 [407,408]. To study the effects of Super NK cells under these forces, Super NK cells were cocultured with SW620 OxR cells in a cone and plate viscometer and sheared at 2 dyne/cm^2 for 4 hours. This physiological FSS resulted in significant therapeutic sensitization, reinforcing the synergy between FSS and TRAIL that is observed comprehensively throughout this dissertation (**Figure B.3A-B**).

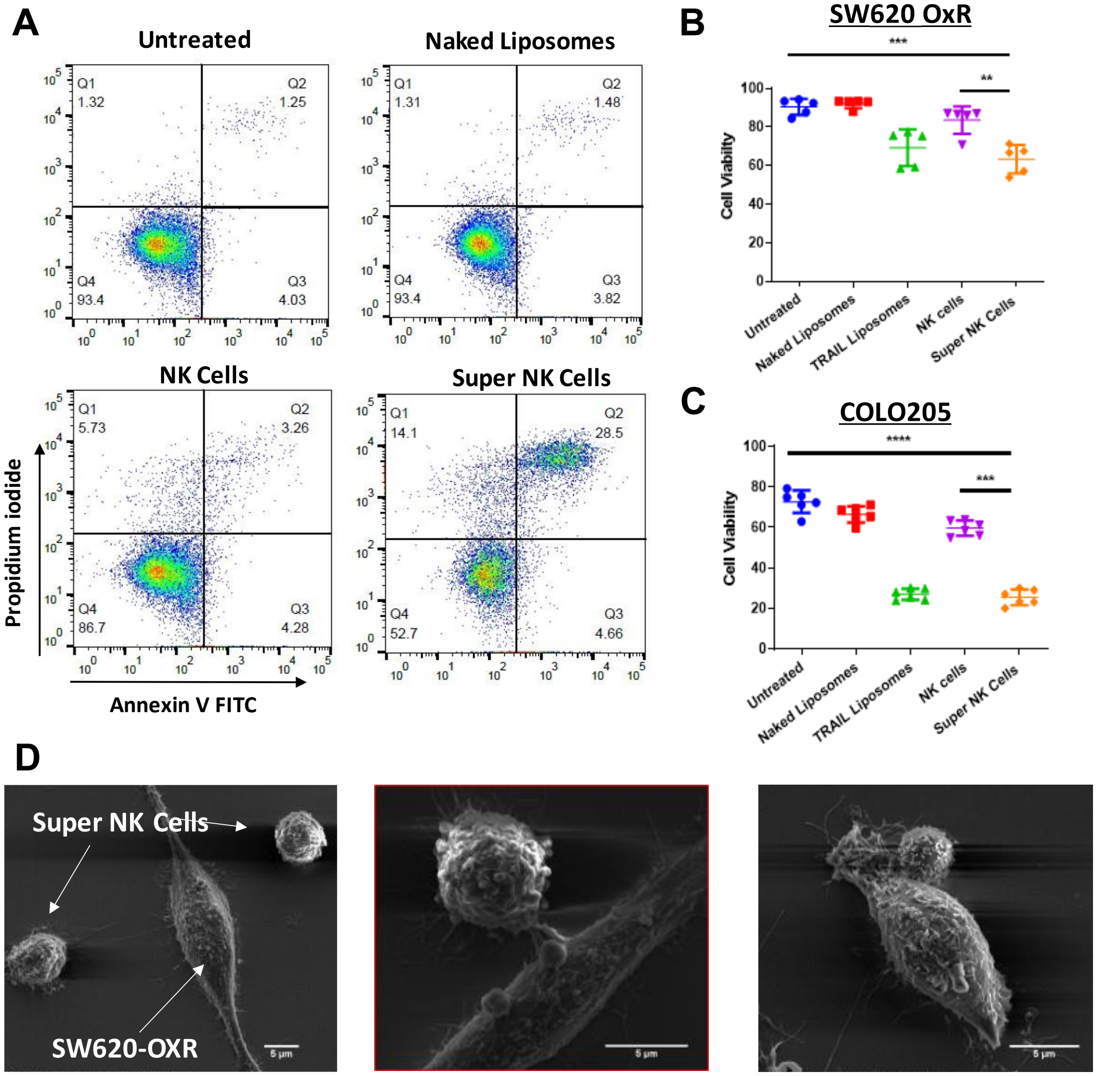

Figure B.2. Super NK cells kill CRC cell lines *in vitro*. (A) Representative Annexin-V/PI plots showing increases in apoptotic SW620 OxR cells from a 24 h coculture with Super NK cells. **(B-C)** Cell viability quantified after 24 h treatments in SW620 OxR and COLO205 cells, respectively. NK and Super NK cells were added at a 1:1 ratio with CRC cells. N=5, N=6, respectively. $^{**}p<0.01$ $^{***}p<0.001$ $^{****}p<0.0001$. **(D)** SEM images of Super NK cells inducing apoptosis in SW620 OxR cells. Super NK cells in proximity of a healthy SW220 OXR cell (left image), Super NK cell attaching to a SW620 OxR cell forming the immune synapse and initiating apoptosis (middle), large membrane blebbing and rounded morphology of an apoptotic SW620 OxR cell (right). Scale bar = 5 µm.

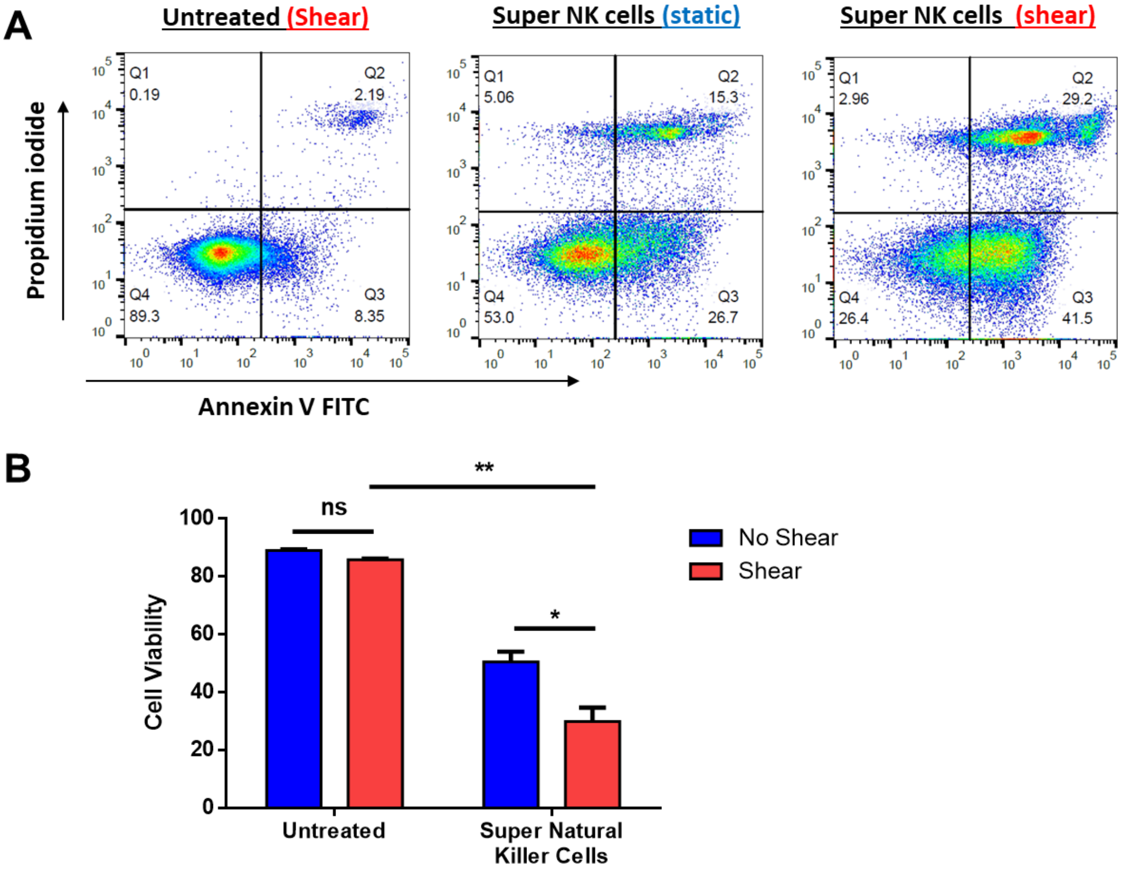

Figure B.3. Fluid shear stress sensitizes SW620 OxR cells to Super NK cells. (A) Representative Annexin-V/PI plots showing increases in Super NK cell-mediated apoptosis when combined with 2 dyne/cm^2 FSS for 4 h. **(B)** Cell viability quantified 24 h after Super NK cell treatment. N=3, *p<0.05 **p<0.01.

B.3.3 Intravenous administration of liposomes shows prolonged retention within the lymph nodes

To investigate liposome biodistribution *in vivo*, B6(Cg)-Tyr^{c-2J} (albino B6) mice were used. The lack of fur pigmentation in these albino mice allowed for noninvasive monitoring of liposome biodistribution using the DiR liposome dye. DiR was chosen since near-infrared fluorescence has greater penetrance though the skin. Mice were injected with either naked (unconjugated) or TRAIL/anti-CD335 liposomes and imaged periodically using an IVIS over the course of 3 days. Intravenous (IV) and intraperitoneal (IP) administration were compared to determine differences in organ and lymph node accumulation. Regardless of the administration route or conjugated moieties, liposomes were found to circulate for over 3 days and were found within the spleen, lymph nodes, liver, and colon after 4 days (**Figure B.4A-B**). IV injection was associated with increased liposome retention, specifically within the inguinal and mesenteric lymph nodes, compared to IP injection.

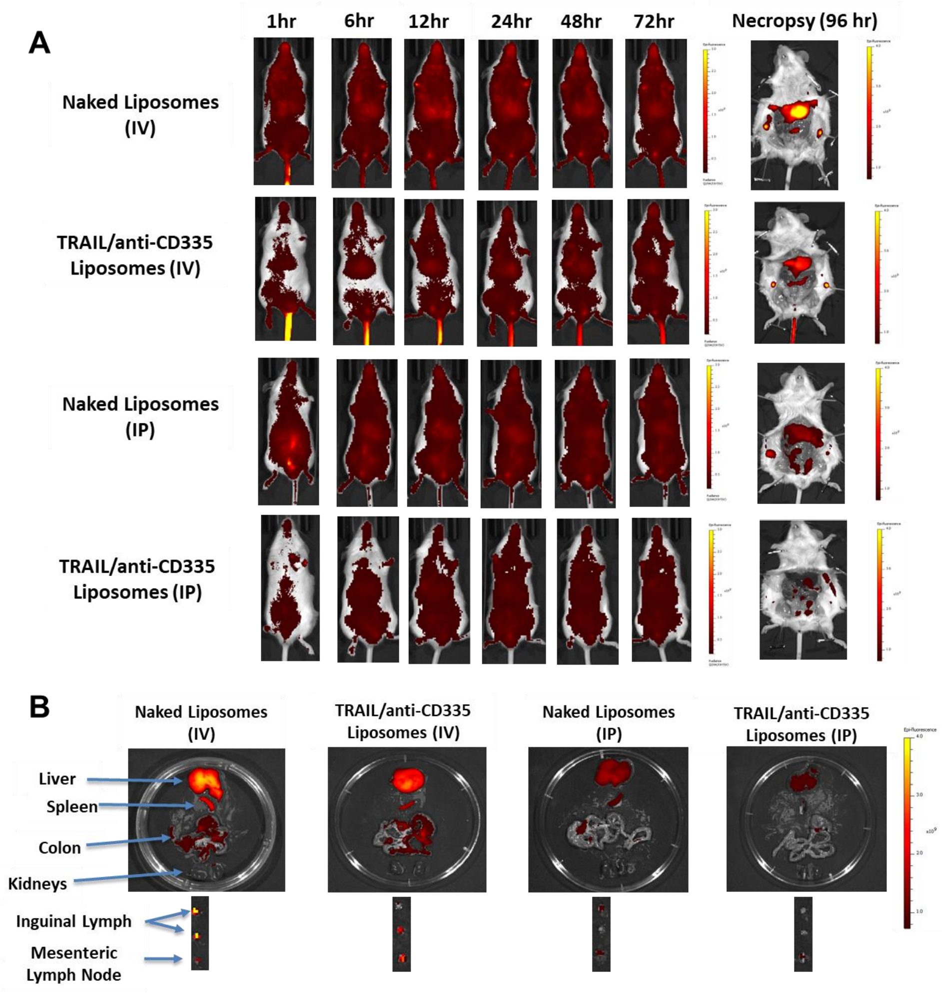

Figure B.4. Liposome biodistribution shows retention within the lymph nodes of B6(Cg)-Tyr^{c-2J} mice for more than 4 days. (A) Liposomes were tagged with the near-infrared lipid dye DiR and fluorescence biodistribution was imaged noninvasively using an IVIS. **(B)** Concentrations of liposomes within organs and lymph nodes following necropsies at the 96 h timepoint. IV: Intravenous administration, IP: Intraperitoneal administration.

B.4 Discussion

Our lab has previously shown the efficacy of TRAIL/anti-NK1.1 liposomes in a subcutaneous mouse model [404]. In the present study, I examined how different NK cell specific antibodies can improve liposome binding. Anti-CD335 liposomes not only demonstrated optimal conjugation, but also saw the highest specific binding to NK cells. CD335 is also an appealing target as it is an NK cell specific marker on both mouse and human NK cells [405]. Previous liposome iterations were targeted to NK1.1 which is solely expressed on mouse NK cells. This improves the translatability of our liposome design for future clinical use.

TRAIL/anti-CD335 liposomes attached to NK cells were able to successfully induce apoptosis and reduce viability in two different clinically relevant CRC cell lines. Applying physiological levels of FSS present in the lymph nodes significantly increased the apoptotic effects of Super NK cells, likely due to the activation of mechanosensitive ion channels and influx of calcium.

Biodistribution data encouragingly showed a sustained presence of liposomes within the lymph nodes for at least four days. Interestingly, IV injection showed greater distribution and increased circulation compared to IP injection. Further, IV injection saw greater presence of liposomes within the spleen and mesenteric and inguinal lymph nodes, where NK cells reside. This is important, as the previous TRAIL/anti-NK1.1 liposome study in subcutaneous tumors used an intertumoral injection of liposomes. In more advanced orthotopic models, like that discussed in Chapter 5, systemic administration via an IV or IP injection will be necessary. These results support that tail vein injection adequately circulates liposomes within the lymph nodes, specifically the mesenteric lymph nodes which act as the TDLN in CRC metastasis.

B.5 Materials and Methods

B.5.1 Cell Culture

SW620 OxR cells were obtained from Dr. Mika Hosokawa at Kobe Pharmaceutical University in Japan and were cultured in Leibovitz's L-15 cell culture medium. COLO205 cells were purchased from ATCC and cultured in RPMI media. Complete growth media was supplemented with 10% (v/v) fetal bovine serum and 1% (v/v) PenStrep. COLO205 cells are semiadherent, and as such were passaged by recovering cells in suspension and adherent cells using Trypsin. Cells were stored in a humidified incubation chamber at 37ºC and 5% CO_2.

B.5.2 NK cell isolation

Male C57BL/6 mice were sacrificed, and the spleen was resected. The spleen was ground into a pulp in a petri dish with 3-5 ml of media. The pulp was pipetted through a 40 µm nylon mesh filter to remove remaining chunks of tissue and the pass through was collected and centrifuged at 300xg for 5 minutes. The pellet was resuspended in 4 ml of 1x RBC lysis buffer for 5 minutes on ice. After RBCs were lysed, 10 ml of media was added and remaining mononuclear immune cells were centrifuged. Nk cells were isolated by immunomagnetic negative selection using the EasySep Mouse NK Cell Isolation Kit from StemCell. On average, one mouse spleen yields $1x10^6$ NK cells.

B.5.3 Liposome Synthesis and Characterization

Egg PC, cholesterol, DiR, 1,2-distearoyl-sn-glycero-3-phosphoethanolamine-N-[carboxy(polyethylene glycol)-2000] (DSPE-PEG), and DSPE-PEG-Maleimide were purchased from Avanti Polar Lipids, reconstituted in chloroform and combined at a 64:31:1:3:1 molar ratio, respectively, for a total combined mass of 5.15 mg. The solution was dried overnight under vacuum in a desiccation chamber. The lipid film was hydrated the next day in 700 µl of liposome buffer and sonicated in a water bath at 50ºC for 1 h with interment vertexing. The resulting multilamellar vesicles were extruded through a 200 nm filter 10x, and 100 nm 20x. NK cell antibodies and TRAIL were thiolated by incubating with 2-iminothiolane (Traut's Reagent) at a 1:12 molar ratio (Ab:Traut) for 2 h at RT in pH 8.0 PBS buffer with 6 mM EDTA. Excess Traut was removed using 10k spin columns, washing 2x with 100 mM potassium acetate. Thiolated antibodies/TRAIL were conjugated with liposomes overnight at 4°C.

B.5.4 Annexin-V/PI Assays

SW620 OxR and COLO205 cells were plated overnight at 100,000 cells/well in 24 well plates. The next day, the media was replaced with fresh media containing treatments: naked liposomes, TRAIL liposomes (no NK antibodies), 100,000 NK cells, or 100,000 Super NK cells. For Super NK cells, conjugated TRAIL/anti-CD335 liposomes were incubated with NK cells for 30 min and centrifuged to remove unbound liposomes. After 24 h cells were recovered using Trypsin, washed, and incubated with Annexin-V/PI. NK cells were differentiated from cancer cells by observing forward and side scatter; NK cells (and lymphocytes generally) are tightly clustered, smaller, and less granular than cancer cells.

For FSS experiments, Super NK cells were loaded into a cone-and-plate viscometer at a 1:1 ratio with SW620 OxR cells. Cells were sheared at 2 dyne/cm^2 for 4 hours and then incubated overnight in 24 well plates. Apoptosis was measured after 24 h in the same manner discussed above.

B.5.5 In Vivo Biodistribution

Eight-week-old B6(Cg)-Tyr^{c-2J} (albino B6) mice were purchased from Jackson Labs. Mice were injected with 150 µl of naked or TRAIL/anti-CD335 liposomes through the tail vein (IV) or intraperitoneally (IP). Biodistribution was monitored using an IVIS at 740 nm emission (far red) over the span of 96 hours. Mice were sacrificed after 4 days and necropsies were performed to look at biodistribution within individual organs.

Appendix C:

Engineered Fluidic Systems to Understand Lymphatic Cancer Metastasis

Joshua D. Greenlee and Michael R. King

This appendix is adapted from *Engineered Fluidic Systems to Understand Lymphatic Cancer Metastasis* published in *Biomicrofluidics* and has been reproduced with permission of the publisher and co-author Michael King [287].

Greenlee, J.D.; King, M.R. Engineered Fluidic Systems to Understand Lymphatic Cancer Metastasis. *Biomicrofluidics* 2020, *14*, 011502, doi:10.1063/1.5133970.

C.1 Abstract

The majority of all cancers metastasize initially through the lymphatic system. Despite this, the mechanisms of lymphogenous metastasis remain poorly understood and understudied compared to hematogenous metastasis. Over the past few decades, microfluidic devices have been used to model pathophysiological processes and drug interactions in numerous contexts. These devices carry many advantages over traditional 2D *in vitro* systems, allowing for better replication of *in vivo* microenvironments. This review will highlight prominent fluidic devices used to model the stages of cancer metastasis via the lymphatic system, specifically within lymphangiogenesis, vessel permeability, tumor cell chemotaxis, transendothelial migration, lymphatic circulation, and micrometastases within the lymph nodes. In addition, we present perspectives for the future roles that microfluidics might play within these settings and beyond.

C.2 Introduction: The Rise of Microfluidics

The discrepancies between scientific data gathered *in vitro* and *in vivo* versus clinical settings suggests new models are warranted to recapitulate human pathophysiological processes [409]. For years, there has existed a challenge in the field of bioengineering and drug discovery concerning the effectiveness of 2D cell cultures to model human physiology and drug interactions observed clinically [409–412]. Two-dimensional static cultures remain the standard for cellular biology, yet these models lack physiological relevance and have often proven ineffective as clinical predictors due to dilute and ineffective recapitulation of the cellular microenvironment [412,413]. While *in vivo* models remain necessary to assess drug interactions in the preclinical setting, the average success rate of translation from animal models to clinical cancer trials is less than 8% [414]. Aside from being “lost in translation”, animal models raise ethical concerns and are problematic when using human cells due to host-immune cell interactions [410,414].

The combination of these shortcomings has pushed research into the direction of using 3D and microfluidic platforms to recapitulate the physical and chemical microenvironments seen *in vivo*, while providing the means to precisely control and visualize cellular interactions in a high throughput manner. Microfluidics employ the use of small channels on the scale of tens to hundreds of microns in diameter to process minute fluid volumes [415]. Their small size allows for limited cell numbers or reagents, which are often expensive or low in quantity. Furthermore, these devices can more accurately model *in vivo* architectures through integration of 3D extracellular matrix (ECM) components [410,411,416]. The spatiotemporal control of these devices has allowed researchers to study specific cellular interactions in a more precise and controlled manner. Microfluidics are also advantageous as they can be fabricated to incorporate small working distances to allow for high-resolution, real-time imaging.

The usage of biologically compatible material substrates from molds allows for high throughput production of devices and subsequent analysis. A large majority of microfluidic devices for biological application use soft lithography techniques, which includes fabricating a master “stamp” from a photocurable polymer such as SU-8 [417]. This master can be used to imprint features into elastomeric materials, such as Polydimethylsiloxane (PDMS), with high resolution. PDMS is widely used in microfluidics since it is easy to handle, can be purposed in diverse applications, is economically viable, ideal for imaging due to its optical properties, and most importantly, is biologically inert [418]. While the field of microfluidics has advanced tremendously in terms of applications, the versatility of replication molding with PDMS has meant new fabrication techniques have lagged behind. Other means of fabrication often require advanced equipment and are not economically feasible at a small scale for research purposes, use materials which do not translate well with biological applications, or lack the high-resolution capabilities inherent with soft lithography [417]. However, certain applications may require more intricate fabrication techniques, such as micromachining, 3D printing or dry etching. **Table C.1** illustrates the ubiquity of PDMS and photolithography in the field of microfluidics for biomedical research.

Application	Device Summary	Substrate	Fabrication Method	Major Finding	Cell Lines	Year	References
Lymph-angiogenesis and LEC Barrier Function	Nine chamber radial flow device to model capillary morphogenesis under interstitial flow with applications in TME modeling	PDMS with fibrin gels	PMMA micromachining	Interstitial flow is vital for lymphatic morphogenesis, migration and proper molecular gradients *in vitro*	HMVEC (Human Dermal Microvascular Endothelial Cells) (lymphatic and blood), Human dermal fibroblasts, B16-F10 (murine melanoma)	2010	[419]
	Mimicking drainage function seen in lymphatic microvasculature	PDMS with fibrin gels	SU-8 photolithography	Drainage is required to preserve vascular stability and perfusion rates within fibrin scaffolds	HMVEC	2013	[420,421]
	Microcirculation model featuring both blood and lymphatic vessels for the purpose of examining vascular permeability	PDMS/PET membrane with fibronectin	SU-8 photolithography	Vascular permeability in a co-culture LEC and BEC system mimicked responses seen *in vivo*	HMVEC (lymphatic and blood)	2015	[422,423]
	Mimicking LEC sprouting seen *in vivo* using physical and biochemical cues	PDMS with fibrin gels	SU-8 photolithography	Interstitial flow-initiated outgrowth of lymphatic sprouts toward upstream of the flow while suppressing downstream-directed sprouting	HMVEC (lymphatic), NHLF (normal human lung fibroblasts)	2016	[424]
	Modeling lymph-angiogenesis and angiogenesis simultaneously within tumor microenvironment	PDMS with collagen-fibrin gels	SU-8 photolithography	Mimicked simultaneous angiogenesis and lymphangiogenesis of the TME using interactions of tumor cells with cellular and noncellular components	HUVEC (Human Umbilical Vein Endothelial Cells), HMVEC (lymphatic), Primary fibroblasts, SKOV3 (human ovarian adenocarcinoma), MKN-74 (human stomach adenocarcinoma), and SW620 (human colorectal adenocarcinoma)	2017	[425]
LEC/Tumor Cell Cross-Talk	Chemotaxis of tumor cells toward lymphatics via CCR7 signaling within a modified Boyden chamber	Modified Boyden Chamber with Matrigel	--	Physiological levels of IF can enhance tumor cell migration in the direction of flow via CCR7 autocrine signaling	HMVEC (lymphatic), MCF10A (human breast epithelial), MCF7 (human breast adenocarcinoma), ZR75-1 (human breast carcinoma), and MDA-MB-435 (human melanoma)	2007	[426]
	Modeling cross talk between LECs and cancer cells via VEGF-C and CCR7 signaling in a	Modified Boyden Chamber with collagen I	--	VEGF-C acts in an autocrine fashion to increase tumor invasiveness by increasing the proteolytic activity	HUVEC, HMVEC (lymphatic), MDA-MB-435S	2009	[427]

	modified Boyden chamber			and motility of tumor cells			
	Pressure gradient across collagen gels creates interstitial flow that influences tumor cell migration	PDMS with collagen I	SU-8 photolithography	Interstitial flow creates competing mechanisms of tumor migration downstream (CCR7 dependent) and upstream (CCR7 independent)	MDA-MB-231, MDA-MB-435	2011	[428,429]
	Modeling extravascular migration of tumor cells along lymphatics via 3D confined cell migration	PDMS with collagen IV	SU-8 photolithography	Subpopulations of cells showed sustained migratory potential despite treatment with Taxol chemotherapeutics	MDA-MB 231, H1650 (Lung adenocarcinoma), H446 Lung carcinoma, PC3 (Prostate adenocarcinoma), LnCaP (Prostate carcinoma), U-87MG (Glioblastoma), HT-29 (Colorectal adenocarcinoma)	2013	[430]
	IFN-DC-migration and interactions with cancer cells within 3D tumor environments	PDMS with collagen I	SU-8 photolithography	CXCR4/CCL12 axis guides IFN-DC toward apoptotic tumor cells for antigen uptake	Primary IFN-DCs (IFN-alpha Dendritic cells), SW620	2017	[431]
	First ex vivo cross talk system via secreted factors between lymph node and tumor samples	PDMS	SU-8 photolithography	Lymph node slices co-cultured with tumor slices appeared more immunosuppressed than those co-cultured with healthy tissue	Murine LN and tumor slices	2019	[432]
Transendothelial Migration	Micro-gaps force cell deformation to study effects on transmigration potential	PDMS with Matrigel	SU-8 photolithography	Extravasation potential was significantly affected by endothelial lining	HMVEC, HepG2 (hepatocellular carcinoma), HeLa (cervical adenocarcinoma), MDA-MB-435	2007	[433,434]
	Tumor cell interactions with endothelial cell barrier function	PDMS with hydrogel	SU-8 photolithography	Macrophage-secreted TNF-α induces endothelium permeability and tumor cell intravasation	HT1080, MDA-MB-231, RAW264.7 (macrophages)	2012	[435]
	Tumor cell interactions with artificial microvasculature under physiological shear	PDMS with collagen I	Aluminum replication molding	Cancer cells show biased growth toward vessels but do not contact the endothelium for transendothelial migration	MDA-MB-231, HT-1080, HUVEC, HMVEC	2014	[436]
	Perfusable metastasis chip with microposts allowing for endothelial cell monolayer formation for angiogenesis and intravasation	PDMS with fibrinogen	SU-8 photolithography	TNF-α treated EC monolayers demonstrated increased permeability and subsequent intravasation	MDA-MB-231	2014	[437]

	Cancer cell transmigration under transmural and interstitial flow across LEC monolayers	Somoss Watershed XC11122	High resolution stereolithography	Luminal and transmural flow upregulate tumor cell transmigration, partially through LEC CCL21 upregulation	HMVEC (lymphatic), MDA-MB-231	2015	[438]
	Simple transwell device to study mechanisms of tumor cell TEM in LECs	Transwell Plates	--	Lymphangiogenic peptide adrenomedullin facilitates TEM by promoting cancer cell binding to LECs and gap junction coupling	HMVEC (lymphatic), SK-MEL-2 (human melanoma), MCF7	2015	[439]
	Simple transwell device with interstitial flow to study leukocyte and cancer cell transmigration	Transwell Plates	--	Cancer cells prefer basal to apical transmigration in LECs compared to BECs	MCF7, MDA-MB-231, HMVEC, Mouse Primary Dermal Lymphatic Endothelial Cells, SVEC4-10 (mouse endothelial)	2017	[440]
	Microfluidic channels separated by porous membrane lined with primary endothelial cell monolayer	PDMS with collagen I	Replication molding	Cancer cells adhere to endothelium under flow, but transmigration was not observed	HMVEC, H838 (non-small cell lung cancer), SK-Mel-28 (human melanoma)	2018	[441]
Lymphatic Circulating Tumor Cells	Flow chamber to study tumor cell behaviors under lymphatic shear conditions	Parallel plate laminar flow chamber coated with collagen	--	Colorectal cancer cells remained attached, proliferative, and alive under lymphatic shear conditions	RKO (human colorectal carcinoma), HCT-8 (colorectal adenocarcinoma)	2007	[442]
	Cone and plate viscometer to apply hematogenous shear conditions to CTCs	Cone-and-plate viscometer	--	Cancer cells are sensitized to cytotoxic ligand TRAIL under hematogenous shear conditions	COLO205 (colorectal adenocarcinoma), PC3 (prostate adenocarcinoma)	2013	[270,272]
	Migration channels with choke points to mimic lymphatic capillary geometry and confinement	PDMS with collagen I	Soft lithography	(MAPK) family member, p38γ knock out cells show decreased motility through tighter choke point geometries	MDA-MB-231	2015	[443]
	Microcavities that model architecture of micrometastases in the lymph node	PDMS (Gas expansion molding)	Deep reactive ion etching	Engineered Natural Killer cells can eradicate LN micrometastases in 3D microcavities	LnCAP, COLO205 MDA-MB-231	2014	[444,445]

Table C.1. Microfluidic devices to model the stages of lymphogenous metastasis. Primary references are listed first, followed by supporting literature describing fabrication methodology where applicable.

Replication of tissue microenvironments within microfluidic devices has allowed the modeling of complex physiological processes systems in “organ on a chip” devices [446–451]. Meanwhile, incorporation of multiple organs on a chip in one integrated device can be used for the scaling of “microHumans” to study complex anatomical interactions and systemic drug toxicity [452,453]. Although initially intended to bridge the gaps between 2D *in vitro* studies and *in vivo* work, 3D fluidic models are evolving to study pathologies and drug interactions directly in patient-specific devices [410,454–458]. These technological advances have made it possible to study specific diseases, including cancer within a microfluidic device [409,410,416,447,459–461]. The applications for microfluidic devices are evolving and emerging in the field of cancer research, both from a biological perspective of understanding roles of immune and stromal cells to a translational perspective of investigating the efficacy of therapeutics in preclinical models.

C.3 The Role of Lymphatics in Cancer Metastasis

Approximately 90% of all cancer related death is attributed to metastasis [239]. Despite its high morbidity, cancer metastasis is a very inefficient process in which less than 0.01% of circulating tumor cells (CTCs) will actually go on to colonize and form macrometastases [462]. The metastatic cascade is composed of several sequential steps, each of which selects for a specific cellular phenotype that is able to overcome inhospitable environments. First, cancer and stromal cells in the primary tumor secrete pro-angiogenic factors such as VEGF to promote tumor microvasculature networks of both blood and lymphatic vessels. Tumor cells then undergo an epithelial to mesenchymal transition (EMT) which promotes cell motility through loss of cell-cell adhesion proteins such as E-cadherin and β-catenin [463]. Motile cells will then migrate and invade the basement membrane of nearby vasculature through both physical (high intratumoral pressures) and chemical (chemokine gradients) cues [462]. Cells may enter hematogenous or lymphatic circulation via transendothelial migration (TEM) from the tissue parenchyma into nearby blood or lymphatic vessels, respectively [239]. In the case of lymphatic intravasation, tumor cells will drain into collecting lymphatic vessels eventually emptying into the sentinel or “tumor draining lymph nodes” (TDLN) [397]. Successful migration to the sentinel lymph nodes provides cells with a direct route to systemic lymph nodes and the bloodstream via the thoracic duct and subclavian vein [464,465]. Once in circulation, cells can undergo extravasation, followed by a mesenchymal to epithelial transition (MET) and colonization of distant organs [239]. As suggested from Paget’s “seed and soil” hypothesis, tumor cells will have genetic and phenotypic advantages to promote seeding in specific organs over others [14,466]. Just as a seed needs proper nutrients to grow, tumor cell proliferation and survival is highly dependent upon the microenvironment where CTC extravasation occurs. This sequential model of metastasis is well studied, but has proven to be an oversimplification in many cancer models and in clinical observation [464,467].

It is estimated 80% of carcinomas and melanomas metastasize via lymphatics [397]. Despite the fact that the majority of all human cancers metastasize initially via the lymphatic system, the mechanisms of lymphogenous metastasis remain poorly understood and understudied compared to that of hematogenous metastasis [397,468]. There are many factors that help determine which metastatic route a cell will take [469]. Typically, metastatic subpopulations will develop mutational burdens which may be preferential for one mode over another. For instance, CCR7+ tumor cells will preferentially traffic toward CCL21 secreted by lymphatic endothelial cells (LECs), promoting initial metastasis through the lymphatic system. This signaling axis is typically used in CCR7+ dendritic cells (DC) trafficking into lymph nodes, while T-cells expressing CCR7 follow gradients toward increasing CCL19 secreted within the thymus and lymph nodes [470]. Additionally, CCL21 can be upregulated by VEGF-C/VEGFR-3 signaling, which has been shown to be highly expressed in primary tumors and tumor-derived lymphatic neovasculature [464]. By harnessing these signaling mechanisms employed by immune cells to traffic toward LECs for antigen presentation, cancer cells experience directed migration toward the lymphatic circulation [464,468]. Physical and mechanical forces have also been shown to play a role in lymphatic homing. High interstitial pressures within solid tumors promote interstitial flow (IF) toward the periphery of the tumor where lymphatic vessels are concentrated [288]. Interstitial flow has been shown to promote vascular remodeling and even promote tumor cell invasion via autologous chemotaxis toward lymphatic vessels along the tumor periphery. Furthermore, secretion of specific pro-lymphangiogenic factors can favor lymphatics versus blood [465]. For example, upregulated VEGF-C and VEGF-D secretion by cancer cells have been shown to induce preferential lymphatic metastasis via LEC VEGFR-2 and VEGFR-3, whereas blood endothelial cell (BEC) angiogenesis prefers VEGF-A/VEGFR-1 signaling.

Lymphatic capillaries lack pericytes and tight interendothelial junctions typically seen in blood vessels [464,471]. The leaky nature of lymphatic vessels facilitates tumor cell intravasation via transendothelial migration, promoting initial metastasis. Likewise, the lower fluid shear environment within lymphatic vessels (on the range of 0.4 dyne/cm^2 with surges between 4-12 dyne/cm^2) [407,408] compared to blood vasculature (upwards of 30 dyne/cm^2 in arteries) [290,472] increases the likelihood of cell survival in transit [469]. Mounting evidence exists suggesting that lymphatics may also play a role in curbing anti-tumor immune responses [473]. For example, initial lymphatic vessels formed as a result of tumor-induced lymphangiogenesis exhibit upregulated expression of the immune checkpoint ligand programmed cell death ligand 1 (PD-L1), which induces CD8+ T-cell anergy upon tumor associated antigen (TAA) presentation via MHC class 1 [464,468,474]. In addition, tumor-induced LECs have been shown to prevent dendritic cell maturation, increase T-cell tolerization, and inhibit proliferation of T-cells that have been stimulated by proinflammatory cytokines [468,475,476].

Despite the increasing evidence for the roles of lymphatics in promoting cancer progression and dissemination, there are innate characteristics of lymphatics that promote anti-tumor immunity. For instance, the presence of lymphatic networks at the primary tumor are important for TAA trafficking to immune cells to evoke a robust T-cell response [473]. In addition, lymphatic vessel density in solid tumors strongly correlates with the quantity of infiltrating cytotoxic CD8+ T-cells, promoting “hot” vs “cold” tumors in patients [477,478].

The involvement of lymphatics in cancer dissemination extends into the clinic. The presence of metastases in the sentinel lymph nodes of cancer patients is used as a basis for establishing tumor staging, predicting patient prognosis and formulating treatment strategies [479]. Axillary and sentinel lymph node biopsies in melanoma and breast cancer patients have proven to be fundamental for assessing the aggressiveness and extent of disease [480,481]. In fact, often times sentinel LN biopsies will reveal metastatic spread before detection by traditional imaging modalities such as positron emission tomography/computed tomography (PET-CT), or before the presence of bloodborne CTCs [479]. The clinical ramifications of this on the degree of lymphatic involvement in metastasis demonstrates the importance of the role of the lymphatic system in cancer.

The complex roles of lymphatics in metastatic progression are not yet fully understood. What is apparent, however, is that better understanding of the interplay between tumor cells, their microenvironment, and the lymphatic system during metastasis is vital to the discovery of new therapeutics to exploit tumor cell weaknesses. The tight control of physical and chemical stimuli, high-throughput nature, high-resolution capacity, and the physiologically relevant architecture of microfluidics, provide excellent means for better understanding these intricate interactions.

C.4 Microfluidic Models of Lymphogenous Metastasis

C.4.1 Lymphangiogenesis and LEC Barrier Function

Lymphatic vasculature is comprised of initial lymphatic vessels and collecting vessels, which function to prevent the accumulation of fluid, termed edema, in tissue [464,482]. Additionally, these vessels function to transport pathogens, antigens and antigen presenting cells from tissues toward immune cells residing within the lymph nodes. Initial lymphatic vessels, also known as lymphatic capillaries, range from 35-70 μm in diameter and absorb interstitial fluids, facilitated by pressure gradients between the interstitium and vessel lumen [483]. Lymph then drains into downstream collecting vessels that contain unidirectional valves and smooth muscle contractions to facilitate transport into the draining lymph nodes. Lymphangiogenesis is the analogue to angiogenesis, the process where lymphatic endothelial cells sprout to create new vasculature off existing vessels. Tumor induced lymphangiogenesis is characterized by VEGF-C or VEGF-D overexpression in tumors, which has been correlated with an increase in lymph node metastasis and high morbidity in patients [484–486]. Lymphatic vessels have a high permeability due to discontinuous interendothelial junctions and a sparse surrounding basement membrane [465]. While this facilitates immune cell intravasation and extravasation, it makes vessels susceptible to metastatic tumor cells as well.

Interstitial flow has been shown to be an important regulator of lymphangiogenesis *in vitro* and *in vivo* [487,488]. To model this, the Swartz Lab created a multichambered, high throughput flow device capable of replicating interstitial flow pressures through a 3D extracellular matrix [419]. This PDMS device allowed live imaging of morphogenesis of lymphatic and blood endothelial cells while incorporating tumor microenvironment (TME) components with co-cultures of tumor cells and fibroblasts. A related study by Kim et al. also investigated the roles of IF on lymphangiogenesis, discovering directionality of lymphatic sprouting was flow dependent [424]. Interstitial flow induced upstream lymphatic sprouting and suppressed downstream sprouting via LEC polarization. This PDMS device consisted of a center 3D fibrin channel containing LECs and microposts, surrounded by two flow channels and a 3D fibroblast culture. The same group later adapted the design to study the complex networks of lymphatic vessels in co-culture with BECs, fibroblasts and cancer cells in a 3D tumor microenvironment model, as shown in **Figure C.1A** [425]. This is the only known study to mimic angiogenesis and lymphangiogenesis simultaneously in one 3D microfluidic platform.

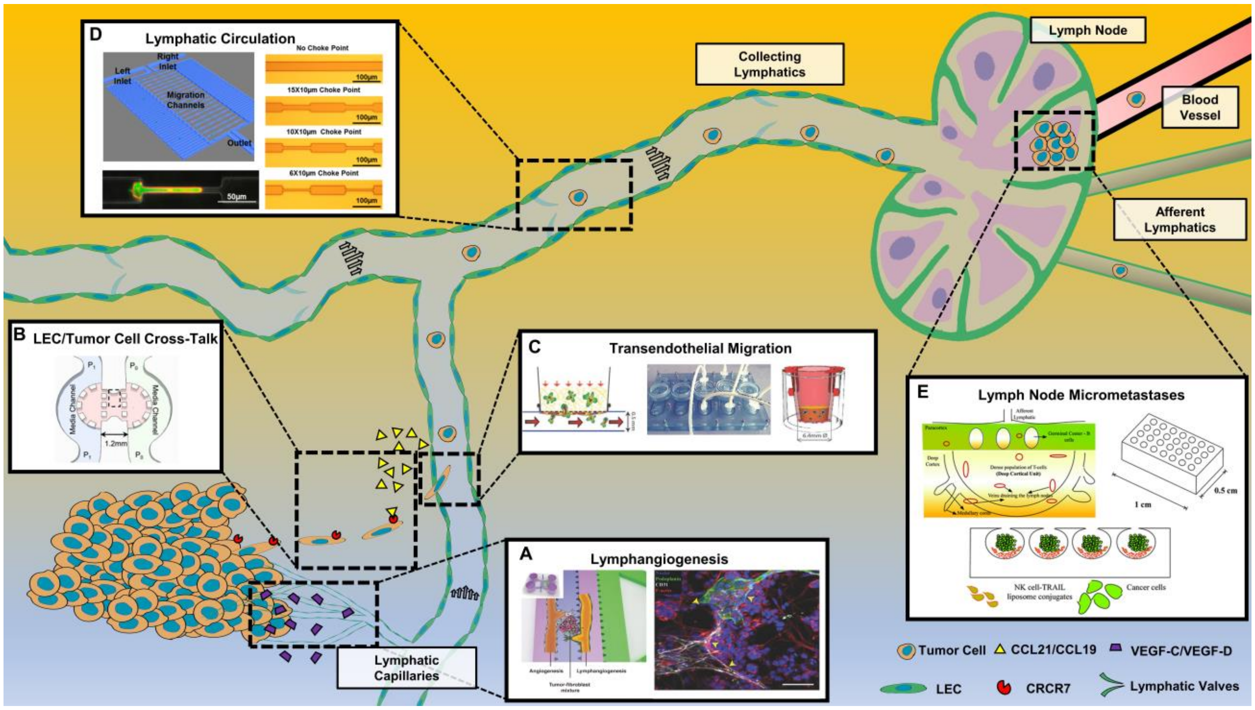

Figure C.1. Current microfluidic models to study the mechanisms of lymphatic cancer metastasis. Representative devices used to study (A) Lymphangiogenesis (reproduced with permission from Adv. Healthc. Mater. 6, 15 (2017). Copyright 2017, John Wiley and Sons.) [425], (B) Cross-talk between LECs and tumor cells (reproduced with permission from Proc. Natl. Acad. Sci. 108, 27 (2011). Copyright 2011, National Academy of Sciences.) [428], (C) Transendothelial migration, (reproduced with permission from Int. Bio. 5, 7 (2015). Copyright 2015, Oxford University Press.) [438], (D) CTCs in lymphatic circulation (reproduced with permission from Chen, Y.-C. *et al*, Sci. Rep., 5, 9980 (2015); licensed under a Creative Commons Attribution Springer Nature license.) [443], and (E) Formation of lymph node micrometastases (reproduced with permission from Lab Chip. 14, (2014). Copyright 2014, Royal Society of Chemistry.) [444].

Interstitial flow is also key in preserving endothelial barrier function in lymphatic neovasculature [288,488]. A study by Wong et al. used a new device to study endothelial cell perfusion to demonstrate the importance of lymphatic drainage in preserving vascular stability [420,421]. This device has the capability of being repurposed by introducing co-culture with cancer cells to study endothelial cell permeability and transendothelial migration under lymphatic drainage conditions. More recently, a device by Sato et al. investigated vascular permeability within co-cultures of LECs and BECs [422]. The PDMS device consisted of two microfluidic channels where LECs and BECs were cultured back-to-back, separated by a fibronectin coated polyethylene terephthalate (PET) membrane [423]. Their findings demonstrated that physiological flow conditions enhanced cell-cell junctions and recapitulated microvascular architecture seen *in vivo* [422].

While angiogenesis is a well characterized process that has been incorporated into many microfluidic devices [437,489–493], the process of lymphangiogenesis is less well understood. The described microfluidic devices have demonstrated incremental advances in understanding the roles of lymphatic vessel sprouting, morphogenesis and permeability in the context of the tumor microenvironment. Particularly within the last few years, there has been emphasis on the fabrication of more complex systems that model lymphangiogenesis in parallel with angiogenesis. While multiple devices have been employed to study lymphatic microvasculature function, few have incorporated components to model lymphangiogenesis in the context of the tumor microenvironment. Modifying or reapplying these devices to represent tumor-induced vascular remodeling will be instrumental in the future. The field is mature from a device design standpoint, but there remain many opportunities within existing devices for further studies, specifically within drug modulation of lymphangiogenesis and LEC barrier function. Currently, there are no FDA-approved compounds to prevent tumor-induced lymphangiogenesis, supporting the use of such microfluidic devices to study novel drug candidates before human trials [494].

C.4.2 Lymphatic-Induced Migration and Tumor Cross-Talk

The likelihood of successful metastatic dissemination is contingent upon a tumors cell's migratory potential [495]. Cancer cells in the primary tumor undergo EMT characterized by a loss of adhesion proteins like E-cadherin and the upregulation of vimentin [463]. These cancer cells resemble a cancer stem cell phenotype and morphology, including a decrease in proliferation and increase in migratory capacity. As previously alluded to, these cancer cells are able to harness the same chemotactic mechanisms typically employed by immune cells to migrate towards and into initial lymphatics [464,468]. Meanwhile, high intratumoral pressures direct interstitial flows toward the tumor periphery into peritumoral lymphatic vessels [288]. High interstitial flows can cause fibroblast contraction and collagen fiber alignment, along with tumor stiffening. This will increase tumor invasiveness, as cells will more easily migrate through aligned collagen fibers. When taken together, all these mechanisms promote tumor cell migration away from the primary tumor and toward peritumoral vasculature.

The Swartz Lab has pioneered microfluidic modeling of tumor cell chemotaxis toward lymphatics. In one study, Shields et al. used a modified 3D Boyden chamber, consisting of a tumor cell culture in 3D ECM with LECs cultured on the underside of the chamber [426]. By introducing interstitial flows of just 0.2 μm/s through the 3D ECM in the absence of LECs, cancer cell migration was enhanced via autologous CCR7 signaling. This novel finding first suggested that IF not only promoted directed migration through physical mechanisms, but also through autocrine signaling where a chemotactic gradient naturally forms at the leading edge of the cell. When cultured with LECs, paracrine CCL21 secretion enhanced CCR7 signaling and offered a complementary role for lymphatic directed chemotaxis. A separate study from the Swartz Lab built upon this observation in a similarly modified Boyden chamber device. Issa et al. demonstrated that tumor cell VEGF-C enhanced LEC CCL21 secretion through VEGFR-3 signaling, thereby enhancing tumor cell proteolysis and migration toward LECs [427].

Polacheck et al. created a two-channel PDMS device separated by a collagen interface in which a pressure difference between channels drove interstitial flow through the device, as shown in **Figure C.1B** [428,429]. This study further supported the previously demonstrated phenomena of autologous CCR7 chemotaxis downstream of interstitial flow. However, when blocking CCR7 signaling, migration was directed upstream of flow, hypothesized to be linked to flow-induced tension in integrins via phosphorylation of focal adhesion kinase (FAK).

Tumor cells under confinement show preferential migration in paths of least resistance through trajectories created by leader cells [496], collagen fiber alignment [497], or on the periphery of preexisting lymphatic and blood vessels [498]. Irimia et al. created a high throughput model of cancer cell migration under confinement using collagen-filled, cell-sized microchannels in a 96 well plate [430]. When treated with paclitaxel chemotherapy, overall cell migratory potential of MDA-MB-231 cells was significantly decreased. However, subpopulations of cells proved resistant to migratory inhibition and showed sustained migration in the presence of high concentrations of drug.

Tumor cells have been shown to create tolerization of immune cells prior to inhabiting the TDLN, creating a pre-metastatic niche that can be ideal for tumor cell seeding [397,499]. Moreover, technological advancement in the way of *ex vivo* tissue cultures has enabled more translational studies of drug-tumor interactions and personalized medicine [500,501]. Recently, Shim et al. created the first *ex vivo* cross talk system via secreted factors between lymph node and tumor slices. They designed a multi-layer PDMS device with integrated pumps to recirculate supernatant between tumor and LN tissue under physiological interstitial flow conditions [432]. Their findings demonstrated LN tissues cultured with tumor tissue contained immunosuppressed T-cell populations, as characterized by decreases in IFN-γ secretion, supporting established *in vivo* findings.

Since cancer cell and immune cell migration employ the use of the same chemokine signaling axes, it is important to understand how migration is modulated by the presence of drugs or immunotherapies. Parlato et al. created a PDMS device with an immune chamber and tumor chamber separated by confined connecting chambers to demonstrate the mechanisms behind IFN-α-conditioned DC migration toward tumor cells [431]. Their results demonstrated the CXCR4/CCL12 axis guides dendritic cells toward apoptotic cancer cells leading to TAA phagocytosis and cross-presentation to naïve T-cells. This study focused on immune cell migration upon treatment of tumor cells, but the device could straight forwardly be repurposed to examine simultaneous immune cell and cancer cell-directed migration in the presence or absence of a drug.

Overall, this has been the most studied stage in lymphatic metastasis using microfluidics. Precise control over device characteristics such as collagen density (and consequential stiffness), flow profiles, pressure gradients, chemotactic gradients and channel architectures make microfluidic devices well suited for modeling tumor migration and lymphatic crosstalk. However, to date no device yet exists to study LEC-induced chemotaxis of cancer cells simultaneously in the presence of immune cells. Most current systems are binary, only comprising of cancer cell lines in culture with LECs, or in the case of the previously described device, only address mechanisms of immune cell trafficking. Modeling the roles of LEC directed migration with lymphatics and cancer cells in tandem will be important for understanding drug interactions to prevent off target effects on immune cells. Moreover, the addition of immune cells will provide insights into symbiotic relationships between immune cells and cancer cells during lymphatic-directed migration. Furthermore, inclusion of other cell types such as cancer associated fibroblasts (CAFs) will be key in elucidating the complex roles these cell types have during migration [502]. More recent studies incorporating primary samples and *ex vivo* tissue samples are gaining traction due to their translational relevance [500,501]. It is expected that this trend will continue, specifically with applications in personalized medicine. One could imagine reapplication of the aforementioned Shim et al. *ex vivo* device [432], with patient derived slices of an excised tumor and LN samples to study patient immune tolerization and immunotherapy efficacy.

C.4.3 Transendothelial Migration Through Lymphatic Endothelium

A cancer cell's ability to disseminate to other organs is fully dependent upon its ability to enter the lymphatic or hematogenous circulation [462], Intravasation is the process in which cancer cells invade the basement membrane of the vasculature and then enter the circulation through a process known as transendothelial migration (TEM). There are two modes of TEM: paracellular (through endothelial cell-cell junctions) or transcellular (through endothelial cell bodies) [503]. TEM in the context of cancer intravasation or extravasation has been studied in a range of microfluidic devices [410,411,504,505]. However, until recently these studies were carried out predominantly with BECs in the context of blood vessel intravasation and extravasation.

The Kamm lab created a successful device that set a precedent the study of endothelial barrier function in the context of tumor metastasis [435]. Their PDMS device consisted of two independent channels where endothelial cells and tumor cells were seeded, separated by a 3D ECM hydrogel region. Permeability of BEC monolayers co-cultured with macrophages and subsequent transmigratory potential of HT1080 fibrosarcoma cells were quantified. This study was instrumental in elucidating the role of macrophage secreted TNF-α in endothelial monolayer permeability and tumor intravasation potential. Building on this, another group created artificial microvasculature from cylindrical channels lined with endothelial cells to study cancer cell migration and intravasation into perfusable vessels [436]. Another system was used to study extravasation, where a two-chamber PDMS device was split with a porous membrane containing an endothelial monolayer [441]. Cancer cells were perfused through the top chamber, while the bottom chamber contained a reservoir to collect any extravasated cancer cells. While the cancer cells adhered to the endothelium, no transendothelial migration was observed within the short time frame of cell rolling. These are just some of the many current microfluidic platforms used to study cancer cell migration through the blood endothelium [411,441,504–507]. Multiple devices have been created to study TEM through vascular endothelium in concert with other metastatic processes. Lee et al. created a “metastasis chip” that modeled both angiogenesis and subsequent intravasation of MDA-MB-231 cells together in one platform [437]. Likewise, Chaw et al. created a multi-step device where cells underwent deformation through 10μm trenches before passing through an endothelial monolayer [433,434]. The latter has applications in studying cell confinement through vessel contraction and subsequent lymphatic extravasation, an understudied phenomenon.

More recently, microfluidic devices have been fabricated for the purpose of investigating the role of lymphatic endothelium in TEM. Increasing emphasis on the role of lymphatics in initial metastasis along with the innate differences between blood and lymphatic endothelium have motivated such studies. For instance, unlike vascular endothelial monolayers, lymphatic monolayers are characterized by having increased permeability, an incomplete or absent basement membrane, and sparse, overlapping intercellular junctions [508]. The Swartz Lab pioneered one of the first devices of cancer cell transmigration in LECs. They fabricated a 5-channel microfluidic chamber which was designed to deliver both luminal and transmural flow to LEC monolayers, as shown in **Figure C.1C** [438]. Tumor cells in a 3D extracellular matrix were cultured above a membrane containing the monolayer. This device demonstrated that luminal, interstitial, and transmural flow promoted intravasation of MDA-MB-231 cells. The device was validated by demonstrating that luminal flow augmented LEC expressed CCL21 to drive cancer cell migration. Xiang et al. created a simplified version that used transwell inserts coated with an LEC monolayer to study vectorial migration and intravasation of immune cells and breast cancer cell lines [440]. This more recent model was designed to be more readily accessible and easier to use for other research labs to study TEM. A similar system using transwell inserts was used by Karpinich et al. to study tumor cell interaction with lymphatic endothelium [439]. Their study demonstrated that the peptide adrenomedullin promotes coupling of cancer cells to LEC gap junctions and facilitates heterocellular communications to induce transendothelial migration.

Microfluidic platforms are excellent tools for studying transendothelial migration of cancer cells, largely due to the ease of visualization via live cell imaging. In addition, precise control of endothelial monolayers more closely mimics endothelial barrier function observed *in vivo*. Due to known differences between lymphatic and blood endothelium, there exists a need to understand the different roles they play in relation to cancer cell intravasation. The majority of established hematogenous intravasation and extravasation devices could be readily modified to study LEC barrier function as well. Although straightforward in principle, inherent differences between blood and lymphatic endothelium will require these repurposed devices to be thoroughly screened and calibrated with LECs. If successfully implemented, future studies may examine differences in transmigratory potential of cancer cells between BECs and LECs within the same device, potentially revealing subpopulations of phenotypes that are prone to lymphatic versus hematogenous TEM. In addition, cancer cell extravasation through lymphatics is poorly understood and few *in vitro* or *in vivo* models exist to study this phenomenon. Modifying existing extravasation devices by culturing LECs instead of BECs will allow for modeling cancer cell rolling, arrest within the lymph node, and extravasation from lymphatics into nearby or distal tissues.

C.4.4 Lymphatic Circulating Tumor Cells

Once cancer cells transmigrate through the endothelium and enter the lymphatic circulation, they are subject to a unique physical and chemical environment [462,464,468,469,482]. There are many differences in the rheology and flow dynamics between lymphogenous and hematogenous circulation. With the absence of red blood cells and platelets, viscosity of lymph and interstitial fluid can be 2-4 fold less than that of blood [509,510]. Initial lymphatic vessels have low Reynolds number flow within the stokes flow regime, and in the largest vessels draining into the thoracic duct, flow remains laminar [482]. This deviates from arterial blood flow which is mostly laminar but can become turbulent in larger arteries. Overall, the higher shear rates within blood flow make CTC survival inauspicious compared to within lymphatics.

Early efforts to model shear effects of lymphatics on metastatic tumor cells included the use of parallel plate flow chambers, as demonstrated in a previous study with colorectal cancer cell lines [442]. In that study, a constant shear stress of 1.2 dyne/cm^2 was applied to cancer cells while cell proliferation, spreading, and apoptosis was quantified. In two separate studies, our lab modeled dynamic shear on CTC's in human blood using a cone-and-plate viscometer [270,272]. These studies demonstrated that physiological shear stress can sensitize cancer cells to TNF-α related apoptosis inducing ligand (TRAIL) via the activation of mechanosensitive ion channels [511]. Similar to parallel plate flow chambers, a cone-and-plate viscometer is widely available, easy to use, and readily adaptable to model a variety of different physiological shear processes, making it suitable for studying cancer cells in lymphatic transit.

The lymphatic system utilizes both extrinsic and intrinsic phasic pumping mechanisms from surrounding lymphatic muscle to produce the pulsatile flow of lymph from tissue [407,482]. The contractile properties of the lymphatics can create confined architectures for cancer cells, augmenting cell motility, proliferation and survival via the process of mechanotransduction [512]. Chen et al. created a migration device with choke points ranging from 6-30 μm to model metastasis through lymphatic capillaries [443]. This PDMS device, as shown in **Figure C.1D**, consisted of two separated serpentine channels, one loaded with cells and the other with chemotactic agents, separated by straight migration channels with constricted choke points of various diameters. Using MDA-MB-231 cells, cell migration through tight choke points was revealed to be dependent on Map Kinase family member p38γ.

Despite the high concentrations of immune cells surveilling the lymphatics, cancer cells are often able to seed within the sentinel lymph nodes and form micrometastases [397]. Often small and clinically undetectable without a lymph node biopsy, these cancer cells can reside and remain senescent for years while evading immune detection. To mimic this, our group created a PDMS microcavity device that recapitulated the architecture of the lymph node, as shown in **Figure C.1E** [444]. The device was fabricated using deep reactive ion etching in silicon, followed by gas expansion molding in PDMS to create spherical microbubbles [445]. Natural killer cells were co-cultured with cancer cells, modeling interactions between micrometastases, immune cells and therapeutics. Although this study was only conducted under static conditions, the same device was used in a separate study under continuously perfused flow to culture 3D spheroids [513].

Currently, there exist flow devices that can be applied to the study of lymphatic and hemodynamic shear on migratory cancer cells. Both parallel plate flow chambers and cone-and-plate viscometers are easily adaptable and widely available devices to study such phenomena. Despite this, surprisingly few studies exist to study cancer cell transit in lymphatic circulation. This represents an important research opportunity to make these devices more physiologically relevant. This may include culturing LEC monolayers on the inner walls of a device while perfusing intraluminal lymphatic flow to CTCs. Furthermore, creation of a device that allows for vessel dilation and constriction via smooth muscle, or artificially via transmural pressure, would better replicate lymphatic behavior *in vivo*. These physiological conditions may be modeled after similar devices that use whole artery or vein segments *ex vivo* [514,515]. Meanwhile, there is a need for more devices to model cancer cell seeding and senescence within the tumor draining lymph nodes, specifically devices that incorporate immune cell interactions with cancer cells. There currently are multiple “lymph node on a chip” devices existing outside of the applications of cancer [516–518]. Although outside of the scope of this review, incorporating cancer cells within lymph node on a chip microenvironments may elucidate mechanisms behind cancer cell seeding and survival.

C.5 Conclusions and Future Perspectives

Despite their great potential and versatility, microfluidic devices have not been fully harnessed to study the intricacies of lymphogenous metastasis. While there are an abundance of microfluidic devices studying metastasis in the context of the bloodstream, few devices exist that incorporate lymphatics as part of, or the focus of their model. This is surprising since the majority of all cancers metastasize via lymphatics and the mechanisms of lymphogenous metastasis are in many ways as poorly understood as that of hematogenous metastasis [397]. Given that the infrastructures of the aforementioned devices are widely adaptable, we propose progress within the field will mostly come from new applications of previously developed systems. A germane initial step would be to recreate previous studies, such as those modeling angiogenesis or TEM into blood vessels, but replacing blood microvasculature with lymphatic microvasculature. Even more ideal would be the incorporation of blood vessels and lymphatics within the same device, similar to that described by Sato et al. [422]. This could be instrumental in elucidating how cells decide between lymphogenous versus hematogenous metastasis, while characterizing subpopulations that are predisposed to one mode over another. Moreover, combining multiple stages within one device such as done by Lee et al., who studied both angiogenesis and intravasation [437], will be useful to determine how different metastatic steps affect one another. Fabrication of these all-in-one “lymphatic metastasis on a chip” devices will advance the field towards a device capable of modeling the entire metastatic cascade within one platform.

As previously mentioned, there may be difficulties with replacing BECs with LECs in existing devices. Although both are endothelial cells and carry out similar functions, they have distinct transcriptional profiles which make them unique in culture [519]. For example, BECs appear to be more reliant on ECM interactions for proper functionality, indicating that ECM components in existing devices with endothelial monolayers may need to be tailored to suit LEC culture. Additionally, lymphatic endothelium is known to have relatively looser interendothelial junctions, which could pose challenges for culturing uniform monolayers within devices [464,465]. Incorporating LECs into existing devices will require careful observation and calibration to ensure physiological relevance, especially when adapting features such as flow profiles, cell densities and ECM concentrations.

Immune cells play complex roles in relation to cancer development, and as such, numerous microfluidic devices exist to study these interactions [410,516,518,520–522]. Surprisingly, these devices tend to look exclusively at cancer-immune cell interactions strictly within the tumor microenvironment, not in relation to their roles during metastasis. Cancer cells trafficking toward and into the lymph nodes are certain to interact in some capacity with both adaptive and innate immune cells, further warranting their inclusion within these microfluidic systems. Investigating the roles of the immune system will be key to not only understanding how cancer cells can leverage these interactions, but also for exploiting cancer cell weaknesses with immunotherapies.

For more translational studies to exist, microfluidic devices must become more user-friendly and compatible for use in the clinical setting. This includes integration of automated image processing, routine sample processing, and minimalization of complex system components to allow for analysis to be done in completion within hospital laboratories. Meanwhile, reproducibility of such devices will be necessary for widespread implementation. The first step in the inclusion of clinical microfluidic devices would be validating drug toxicology and biological phenomena observed *in vivo* and in humans. This includes examining drug interactions of approved FDA compounds that have extensive clinical data and comparing those same interactions within relevant microfluidic devices for validation purposes. With regards to lymphatic devices, testing an FDA approved compound such as sorafenib, which has been shown to interfere with LEC expressed VEGFR-2 and VEGFR-3 and has been approved for the treatment of metastatic renal cell carcinoma [523], within a lymphangiogenesis device would be applicable for validating modeling capabilities. In addition, testing well characterized checkpoint inhibitors such as PD-L1 targeting antibody Atezolizumab to demonstrate blockage of checkpoint signaling by LECs would provide insight into mechanisms behind an LEC targeted therapy [524].

From a research perspective, new platforms to promote collaborations between biologists and engineers are warranted. This framework will in turn promote the fabrication of devices to answer pressing questions in the field of biology, rather than attempting to fit biological applications within preexisting, incompatible devices. A 2014 study by Sackmann et al. estimated that only 6% of all microfluidic devices are published in biology and medicine journals [525]. Interdisciplinary work within this field will be crucial for improved biological modeling and drug discovery.

References

**Select illustrations were created using Biorender.com and Servier Medical Art.*

1. Siegel, R.L.; Miller, K.D.; Fuchs, H.E.; Jemal, A. Cancer Statistics, 2022. *CA: A Cancer Journal for Clinicians* **2022**, *72*, 7–33, doi:10.3322/caac.21708.
2. Ma, Y.; Yang, Y.; Wang, F.; Zhang, P.; Shi, C.; Zou, Y.; Qin, H. Obesity and Risk of Colorectal Cancer: A Systematic Review of Prospective Studies. *PLOS ONE* **2013**, *8*, e53916, doi:10.1371/journal.pone.0053916.
3. Arima, K.; Zhong, R.; Ugai, T.; Zhao, M.; Haruki, K.; Akimoto, N.; Lau, M.C.; Okadome, K.; Mehta, R.S.; Väyrynen, J.P.; et al. Western-Style Diet, Pks Island-Carrying Escherichia Coli, and Colorectal Cancer: Analyses From Two Large Prospective Cohort Studies. *Gastroenterology* **2022**, *163*, 862–874, doi:10.1053/j.gastro.2022.06.054.
4. Carter, A.J.R.; Nguyen, C.N. A Comparison of Cancer Burden and Research Spending Reveals Discrepancies in the Distribution of Research Funding. *BMC Public Health* **2012**, *12*, 526, doi:10.1186/1471-2458-12-526.
5. Weber, G.F. Why Does Cancer Therapy Lack Effective Anti-Metastasis Drugs? *Cancer Lett.* **2013**, *328*, 207–211, doi:10.1016/j.canlet.2012.09.025.
6. Stock, A.-M.; Troost, G.; Niggemann, B.; Zänker, K.S.; Entschladen, F. Targets for Anti-Metastatic Drug Development. *Curr. Pharm. Des.* **2013**, *19*, 5127–5134.
7. Vogelstein, B.; Fearon, E.R.; Hamilton, S.R.; Kern, S.E.; Preisinger, A.C.; Leppert, M.; Nakamura, Y.; White, R.; Smits, A.M.; Bos, J.L. Genetic Alterations during Colorectal-Tumor Development. *N Engl J Med* **1988**, *319*, 525–532, doi:10.1056/NEJM198809013190901.
8. Nguyen, H.T.; Duong, H.-Q. The Molecular Characteristics of Colorectal Cancer: Implications for Diagnosis and Therapy (Review). *Oncology Letters* **2018**, *16*, 9–18, doi:10.3892/ol.2018.8679.
9. Leslie, A.; Carey, F.A.; Pratt, N.R.; Steele, R.J.C. The Colorectal Adenoma–Carcinoma Sequence. *British Journal of Surgery* **2002**, *89*, 845–860, doi:10.1046/j.1365-2168.2002.02120.x.
10. Hanahan, D.; Weinberg, R.A. The Hallmarks of Cancer. *Cell* **2000**, *100*, 57–70, doi:10.1016/S0092-8674(00)81683-9.
11. Welch, D.R.; Hurst, D.R. Defining the Hallmarks of Metastasis. *Cancer Res* **2019**, *79*, 3011–3027, doi:10.1158/0008-5472.CAN-19-0458.
12. Chaffer, C.L.; Weinberg, R.A. A Perspective on Cancer Cell Metastasis. *Science* **2011**, *331*, 1559–1564, doi:10.1126/science.1203543.
13. Valastyan, S.; Weinberg, R.A. Tumor Metastasis: Molecular Insights and Evolving Paradigms. *Cell* **2011**, *147*, 275–292, doi:10.1016/j.cell.2011.09.024.
14. Fidler, I.J. The Pathogenesis of Cancer Metastasis: The “seed and Soil” Hypothesis Revisited. *Nat Rev Cancer* **2003**, *3*, 453–458, doi:10.1038/nrc1098.
15. Riihimäki, M.; Hemminki, A.; Sundquist, J.; Hemminki, K. Patterns of Metastasis in Colon and Rectal Cancer. *Sci Rep* **2016**, *6*, 29765, doi:10.1038/srep29765.
16. Vatandoust, S.; Price, T.J.; Karapetis, C.S. Colorectal Cancer: Metastases to a Single Organ. *World J Gastroenterol* **2015**, *21*, 11767–11776, doi:10.3748/wjg.v21.i41.11767.
17. Pretzsch, E.; Bösch, F.; Neumann, J.; Ganschow, P.; Bazhin, A.; Guba, M.; Werner, J.; Angele, M. Mechanisms of Metastasis in Colorectal Cancer and Metastatic Organotropism:

Hematogenous versus Peritoneal Spread Available online: https://www.hindawi.com/journals/jo/2019/7407190/ (accessed on 29 January 2020).

18. Colon Cancer Surgery | Types of Colon Cancer Surgery Available online: https://www.cancer.org/cancer/colon-rectal-cancer/treating/colon-surgery.html (accessed on 10 November 2022).
19. Stintzing, S. Management of Colorectal Cancer. *F1000Prime Rep* **2014**, *6*, 108, doi:10.12703/P6-108.
20. Mirnezami, R.; Chang, G.J.; Das, P.; Chandrakumaran, K.; Tekkis, P.; Darzi, A.; Mirnezami, A.H. Intraoperative Radiotherapy in Colorectal Cancer: Systematic Review and Meta-Analysis of Techniques, Long-Term Outcomes, and Complications. *Surg Oncol* **2013**, *22*, 22–35, doi:10.1016/j.suronc.2012.11.001.
21. Tam, S.Y.; Wu, V.W.C. A Review on the Special Radiotherapy Techniques of Colorectal Cancer. *Front Oncol* **2019**, *9*, 208, doi:10.3389/fonc.2019.00208.
22. Hu, J.-B.; Sun, X.-N.; Yang, Q.-C.; Xu, J.; Wang, Q.; He, C. Three-Dimensional Conformal Radiotherapy Combined with FOLFOX4 Chemotherapy for Unresectable Recurrent Rectal Cancer. *World J Gastroenterol* **2006**, *12*, 2610–2614, doi:10.3748/wjg.v12.i16.2610.
23. He, Z.; Chen, G.; Ouyang, B.; Zhang, H.; Chen, H.; Wang, Y.; Yan, S.; Pan, W. Conformal Radiation Therapy or Stereotactic Body Radiation Therapy: Institutional Experience in the Management of Colorectal Liver Metastases by Radiation Therapy. *Technol Cancer Res Treat* **2018**, *17*, 1533033818816080, doi:10.1177/1533033818816080.
24. Arhin, N.D.; Shen, C.; Bailey, C.E.; Matsuoka, L.K.; Hawkins, A.T.; Holowatyj, A.N.; Ciombor, K.K.; Hopkins, M.B.; Geiger, T.M.; Kam, A.E.; et al. Surgical Resection and Survival Outcomes in Metastatic Young Adult Colorectal Cancer Patients. *Cancer Med* **2021**, *10*, 4269–4281, doi:10.1002/cam4.3940.
25. Kanemitsu, Y.; Shitara, K.; Mizusawa, J.; Hamaguchi, T.; Shida, D.; Komori, K.; Ikeda, S.; Ojima, H.; Ike, H.; Shiomi, A.; et al. Primary Tumor Resection Plus Chemotherapy Versus Chemotherapy Alone for Colorectal Cancer Patients With Asymptomatic, Synchronous Unresectable Metastases (JCOG1007; IPACS): A Randomized Clinical Trial. *JCO* **2021**, *39*, 1098–1107, doi:10.1200/JCO.20.02447.
26. Kim, C.W.; Baek, J.-H.; Choi, G.-S.; Yu, C.S.; Kang, S.B.; Park, W.C.; Lee, B.H.; Kim, H.R.; Oh, J.H.; Kim, J.-H.; et al. The Role of Primary Tumor Resection in Colorectal Cancer Patients with Asymptomatic, Synchronous Unresectable Metastasis: Study Protocol for a Randomized Controlled Trial. *Trials* **2016**, *17*, 34, doi:10.1186/s13063-016-1164-0.
27. Feo, L.; Polcino, M.; Nash, G.M. Resection of the Primary Tumor in Stage IV Colorectal Cancer: When Is It Necessary? *Surg Clin North Am* **2017**, *97*, 657–669, doi:10.1016/j.suc.2017.01.012.
28. Holch, J.; Stintzing, S.; Heinemann, V. Treatment of Metastatic Colorectal Cancer: Standard of Care and Future Perspectives. *Visc Med* **2016**, *32*, 178–183, doi:10.1159/000446052.
29. Rodriguez-Bigas, M.A.; Lin, E.H.; Crane, C.H. Stage IV Colorectal Cancer. *Holland-Frei Cancer Medicine. 6th edition* **2003**.
30. Devanabanda, B.; Kasi, A. Oxaliplatin. In *StatPearls*; StatPearls Publishing: Treasure Island (FL), 2022.
31. de Gramont, A.; Figer, A.; Seymour, M.; Homerin, M.; Hmissi, A.; Cassidy, J.; Boni, C.; Cortes-Funes, H.; Cervantes, A.; Freyer, G.; et al. Leucovorin and Fluorouracil with or without Oxaliplatin as First-Line Treatment in Advanced Colorectal Cancer. *J Clin Oncol* **2000**, *18*, 2938–2947, doi:10.1200/JCO.2000.18.16.2938.
32. Reyhanoglu, G.; Smith, T. Irinotecan. In *StatPearls*; StatPearls Publishing: Treasure Island (FL), 2022.
33. Douillard, J.; Cunningham, D.; Roth, A.; Navarro, M.; James, R.; Karasek, P.; Jandik, P.; Iveson, T.; Carmichael, J.; Alakl, M.; et al. Irinotecan Combined with Fluorouracil Compared

with Fluorouracil Alone as First-Line Treatment for Metastatic Colorectal Cancer: A Multicentre Randomised Trial. *The Lancet* **2000**, *355*, 1041–1047, doi:10.1016/S0140-6736(00)02034-1.

34. Neugut, A.I.; Lin, A.; Raab, G.T.; Hillyer, G.C.; Keller, D.; O'Neil, D.S.; Accordino, M.K.; Kiran, R.P.; Wright, J.; Hershman, D.L. FOLFOX and FOLFIRI Use in Stage IV Colon Cancer: Analysis of SEER-Medicare Data. *Clin Colorectal Cancer* **2019**, *18*, 133–140, doi:10.1016/j.clcc.2019.01.005.
35. Tournigand, C.; André, T.; Achille, E.; Lledo, G.; Flesh, M.; Mery-Mignard, D.; Quinaux, E.; Couteau, C.; Buyse, M.; Ganem, G.; et al. FOLFIRI Followed by FOLFOX6 or the Reverse Sequence in Advanced Colorectal Cancer: A Randomized GERCOR Study. *JCO* **2004**, *22*, 229–237, doi:10.1200/JCO.2004.05.113.
36. Falcone, A.; Ricci, S.; Brunetti, I.; Pfanner, E.; Allegrini, G.; Barbara, C.; Crinò, L.; Benedetti, G.; Evangelista, W.; Fanchini, L.; et al. Phase III Trial of Infusional Fluorouracil, Leucovorin, Oxaliplatin, and Irinotecan (FOLFOXIRI) Compared with Infusional Fluorouracil, Leucovorin, and Irinotecan (FOLFIRI) as First-Line Treatment for Metastatic Colorectal Cancer: The Gruppo Oncologico Nord Ovest. *J Clin Oncol* **2007**, *25*, 1670–1676, doi:10.1200/JCO.2006.09.0928.
37. Datta, J.; Narayan, R.R.; Kemeny, N.E.; D'Angelica, M.I. Role of Hepatic Artery Infusion Chemotherapy in Treatment of Initially Unresectable Colorectal Liver Metastases: A Review. *JAMA Surg* **2019**, *154*, 768–776, doi:10.1001/jamasurg.2019.1694.
38. Elias, D.; Lefevre, J.H.; Chevalier, J.; Brouquet, A.; Marchal, F.; Classe, J.-M.; Ferron, G.; Guilloit, J.-M.; Meeus, P.; Goéré, D.; et al. Complete Cytoreductive Surgery Plus Intraperitoneal Chemohyperthermia With Oxaliplatin for Peritoneal Carcinomatosis of Colorectal Origin. *JCO* **2008**, *27*, 681–685, doi:10.1200/JCO.2008.19.7160.
39. Grothey, A.; Van Cutsem, E.; Sobrero, A.; Siena, S.; Falcone, A.; Ychou, M.; Humblet, Y.; Bouché, O.; Mineur, L.; Barone, C.; et al. Regorafenib Monotherapy for Previously Treated Metastatic Colorectal Cancer (CORRECT): An International, Multicentre, Randomised, Placebo-Controlled, Phase 3 Trial. *Lancet* **2013**, *381*, 303–312, doi:10.1016/S0140-6736(12)61900-X.
40. Syed, Y.Y.; McKeage, K. Aflibercept: A Review in Metastatic Colorectal Cancer. *Drugs* **2015**, *75*, 1435–1445, doi:10.1007/s40265-015-0444-4.
41. Rawla, P.; Barsouk, A.; Hadjinicolaou, A.V.; Barsouk, A. Immunotherapies and Targeted Therapies in the Treatment of Metastatic Colorectal Cancer. *Med Sci (Basel)* **2019**, *7*, 83, doi:10.3390/medsci7080083.
42. Le, D.T.; Uram, J.N.; Wang, H.; Bartlett, B.R.; Kemberling, H.; Eyring, A.D.; Skora, A.D.; Luber, B.S.; Azad, N.S.; Laheru, D.; et al. PD-1 Blockade in Tumors with Mismatch-Repair Deficiency. *N Engl J Med* **2015**, *372*, 2509–2520, doi:10.1056/NEJMoa1500596.
43. Briffa, R.; Langdon, S.P.; Grech, G.; J.Harrison, D. Acquired and Intrinsic Resistance to Colorectal Cancer Treatment. *Colorectal Cancer - Diagnosis, Screening and Management* **2017**, doi:10.5772/intechopen.70781.
44. Tsutani, Y.; Yoshida, K.; Sanada, Y.; Wada, Y.; Konishi, K.; Fukushima, M.; Okada, M. Decreased Orotate Phosphoribosyltransferase Activity Produces 5-Fluorouracil Resistance in a Human Gastric Cancer Cell Line. *Oncol Rep* **2008**, *20*, 1545–1551.
45. Pratt, S.; Shepard, R.L.; Kandasamy, R.A.; Johnston, P.A.; Perry, W.; Dantzig, A.H. The Multidrug Resistance Protein 5 (ABCC5) Confers Resistance to 5-Fluorouracil and Transports Its Monophosphorylated Metabolites. *Mol Cancer Ther* **2005**, *4*, 855–863, doi:10.1158/1535-7163.MCT-04-0291.
46. Misale, S.; Yaeger, R.; Hobor, S.; Scala, E.; Janakiraman, M.; Liska, D.; Valtorta, E.; Schiavo, R.; Buscarino, M.; Siravegna, G.; et al. Emergence of KRAS Mutations and Acquired Resistance to Anti-EGFR Therapy in Colorectal Cancer. *Nature* **2012**, *486*, 532–536, doi:10.1038/nature11156.

47. Russo, A.; Bazan, V.; Iacopetta, B.; Kerr, D.; Soussi, T.; Gebbia, N.; TP53-CRC Collaborative Study Group The TP53 Colorectal Cancer International Collaborative Study on the Prognostic and Predictive Significance of P53 Mutation: Influence of Tumor Site, Type of Mutation, and Adjuvant Treatment. *J Clin Oncol* **2005**, *23*, 7518–7528, doi:10.1200/JCO.2005.00.471.
48. Gourdier, I.; Del Rio, M.; Crabbé, L.; Candeil, L.; Copois, V.; Ychou, M.; Auffray, C.; Martineau, P.; Mechti, N.; Pommier, Y.; et al. Drug Specific Resistance to Oxaliplatin Is Associated with Apoptosis Defect in a Cellular Model of Colon Carcinoma. *FEBS Lett* **2002**, *529*, 232–236, doi:10.1016/s0014-5793(02)03347-1.
49. Liu, C.; Jin, Y.; Fan, Z. The Mechanism of Warburg Effect-Induced Chemoresistance in Cancer. *Frontiers in Oncology* **2021**, *11*.
50. Lee, A.J.X.; Endesfelder, D.; Rowan, A.J.; Walther, A.; Birkbak, N.J.; Futreal, P.A.; Downward, J.; Szallasi, Z.; Tomlinson, I.P.M.; Howell, M.; et al. Chromosomal Instability Confers Intrinsic Multidrug Resistance. *Cancer Res* **2011**, *71*, 1858–1870, doi:10.1158/0008-5472.CAN-10-3604.
51. Holohan, C.; Van Schaeybroeck, S.; Longley, D.B.; Johnston, P.G. Cancer Drug Resistance: An Evolving Paradigm. *Nat Rev Cancer* **2013**, *13*, 714–726, doi:10.1038/nrc3599.
52. LeBlanc, H.N.; Ashkenazi, A. Apo2L/TRAIL and Its Death and Decoy Receptors. *Cell Death Differ* **2003**, *10*, 66–75, doi:10.1038/sj.cdd.4401187.
53. Sheard, M.A.; Asgharzadeh, S.; Liu, Y.; Lin, T.-Y.; Wu, H.-W.; Ji, L.; Groshen, S.; Lee, D.A.; Seeger, R.C. Membrane-Bound TRAIL Supplements Natural Killer Cell Cytotoxicity Against Neuroblastoma Cells. *J Immunother* **2013**, *36*, 319–329, doi:10.1097/CJI.0b013e31829b4493.
54. Garrido, C.; Galluzzi, L.; Brunet, M.; Puig, P.E.; Didelot, C.; Kroemer, G. Mechanisms of Cytochrome c Release from Mitochondria. *Cell Death & Differentiation* **2006**, *13*, 1423–1433, doi:10.1038/sj.cdd.4401950.
55. Elmore, S. Apoptosis: A Review of Programmed Cell Death. *Toxicol Pathol* **2007**, *35*, 495–516, doi:10.1080/01926230701320337.
56. Thorburn, A.; Behbakht, K.; Ford, H. TRAIL Receptor-Targeted Therapeutics: Resistance Mechanisms and Strategies to Avoid Them. *Drug Resist Updat* **2008**, *11*, 17–24, doi:10.1016/j.drup.2008.02.001.
57. Micheau, O.; Shirley, S.; Dufour, F. Death Receptors as Targets in Cancer. *Br J Pharmacol* **2013**, *169*, 1723–1744, doi:10.1111/bph.12238.
58. Wang, S. The Promise of Cancer Therapeutics Targeting the TNF-Related Apoptosis-Inducing Ligand and TRAIL Receptor Pathway. *Oncogene* **2008**, *27*, 6207–6215, doi:10.1038/onc.2008.298.
59. Galligan, L.; Longley, D.B.; McEwan, M.; Wilson, T.R.; McLaughlin, K.; Johnston, P.G. Chemotherapy and TRAIL-Mediated Colon Cancer Cell Death: The Roles of P53, TRAIL Receptors, and c-FLIP. *Mol Cancer Ther* **2005**, *4*, 2026–2036, doi:10.1158/1535-7163.MCT-05-0262.
60. El Fajoui, Z.; Toscano, F.; Jacquemin, G.; Abello, J.; Scoazec, J.-Y.; Micheau, O.; Saurin, J.-C. Oxaliplatin Sensitizes Human Colon Cancer Cells to TRAIL through JNK-Dependent Phosphorylation of Bcl-XL. *Gastroenterology* **2011**, *141*, 663–673, doi:10.1053/j.gastro.2011.04.055.
61. Xu, L.; Qu, X.; Zhang, Y.; Hu, X.; Yang, X.; Hou, K.; Teng, Y.; Zhang, J.; Sada, K.; Liu, Y. Oxaliplatin Enhances TRAIL-Induced Apoptosis in Gastric Cancer Cells by CBL-Regulated Death Receptor Redistribution in Lipid Rafts. *FEBS Lett.* **2009**, *583*, 943–948, doi:10.1016/j.febslet.2009.02.014.
62. Voelkel-Johnson, C.; Hannun, Y.A.; El-Zawahry, A. Resistance to TRAIL Is Associated with Defects in Ceramide Signaling That Can Be Overcome by Exogenous C6-Ceramide

without Requiring down-Regulation of Cellular FLICE Inhibitory Protein. *Mol. Cancer Ther.* **2005**, *4*, 1320–1327, doi:10.1158/1535-7163.MCT-05-0086.

63. Toscano, F.; Fajoui, Z.E.; Gay, F.; Lalaoui, N.; Parmentier, B.; Chayvialle, J.-A.; Scoazec, J.-Y.; Micheau, O.; Abello, J.; Saurin, J.-C. P53-Mediated Upregulation of DcR1 Impairs Oxaliplatin/TRAIL-Induced Synergistic Anti-Tumour Potential in Colon Cancer Cells. *Oncogene* **2008**, *27*, 4161–4171, doi:10.1038/onc.2008.52.
64. Sussman, R.T.; Ricci, M.S.; Hart, L.S.; Sun, S.Y.; El-Deiry, W.S. Chemotherapy-Resistant Side-Population of Colon Cancer Cells Has a Higher Sensitivity to TRAIL than the Non-SP, a Higher Expression of c-Myc and TRAIL-Receptor DR4. *Cancer Biology & Therapy* **2007**, *6*, 1486–1491, doi:10.4161/cbt.6.9.4905.
65. Greenlee, J.D.; Lopez-Cavestany, M.; Ortiz-Otero, N.; Liu, K.; Subramanian, T.; Cagir, B.; King, M.R. Oxaliplatin Resistance in Colorectal Cancer Enhances TRAIL Sensitivity via Death Receptor 4 Upregulation and Lipid Raft Localization. *eLife* **2021**, *10*, e67750, doi:10.7554/eLife.67750.
66. Jin, Z.; McDonald, E.R.; Dicker, D.T.; El-Deiry, W.S. Deficient Tumor Necrosis Factor-Related Apoptosis-Inducing Ligand (TRAIL) Death Receptor Transport to the Cell Surface in Human Colon Cancer Cells Selected for Resistance to TRAIL-Induced Apoptosis. *Journal of Biological Chemistry* **2004**, *279*, 35829–35839, doi:10.1074/jbc.M405538200.
67. Snajdauf, M.; Havlova, K.; Vachtenheim, J.; Ozaniak, A.; Lischke, R.; Bartunkova, J.; Smrz, D.; Strizova, Z. The TRAIL in the Treatment of Human Cancer: An Update on Clinical Trials. *Frontiers in Molecular Biosciences* **2021**, *8*.
68. Stuckey, D.W.; Shah, K. TRAIL on Trial: Preclinical Advances for Cancer Therapy. *Trends in molecular medicine* **2013**, *19*, doi:10.1016/j.molmed.2013.08.007.
69. Trarbach, T.; Moehler, M.; Heinemann, V.; Köhne, C.-H.; Przyborek, M.; Schulz, C.; Sneller, V.; Gallant, G.; Kanzler, S. Phase II Trial of Mapatumumab, a Fully Human Agonistic Monoclonal Antibody That Targets and Activates the Tumour Necrosis Factor Apoptosis-Inducing Ligand Receptor-1 (TRAIL-R1), in Patients with Refractory Colorectal Cancer. *Br J Cancer* **2010**, *102*, 506–512, doi:10.1038/sj.bjc.6605507.
70. Tenchov, R.; Bird, R.; Curtze, A.E.; Zhou, Q. Lipid Nanoparticles─From Liposomes to MRNA Vaccine Delivery, a Landscape of Research Diversity and Advancement. *ACS Nano* **2021**, *15*, 16982–17015, doi:10.1021/acsnano.1c04996.
71. Zhang, H. Thin-Film Hydration Followed by Extrusion Method for Liposome Preparation. In *Liposomes: Methods and Protocols*; D’Souza, G.G.M., Ed.; Methods in Molecular Biology; Springer: New York, NY, 2017; pp. 17–22 ISBN 978-1-4939-6591-5.
72. Milla, P.; Dosio, F.; Cattel, L. PEGylation of Proteins and Liposomes: A Powerful and Flexible Strategy to Improve the Drug Delivery. *Curr Drug Metab* **2012**, *13*, 105–119, doi:10.2174/138920012798356934.
73. Lee, Y.; Thompson, D.H. Stimuli-Responsive Liposomes for Drug Delivery. *Wiley Interdiscip Rev Nanomed Nanobiotechnol* **2017**, *9*, 10.1002/wnan.1450, doi:10.1002/wnan.1450.
74. Riley, R.S.; June, C.H.; Langer, R.; Mitchell, M.J. Delivery Technologies for Cancer Immunotherapy. *Nature reviews Drug discovery* **2019**, *18*, 175–196.
75. Yao, Y.; Zhou, Y.; Liu, L.; Xu, Y.; Chen, Q.; Wang, Y.; Wu, S.; Deng, Y.; Zhang, J.; Shao, A. Nanoparticle-Based Drug Delivery in Cancer Therapy and Its Role in Overcoming Drug Resistance. *Frontiers in Molecular Biosciences* **2020**, *7*.
76. Current Nanomedicines for the Treatment of Cancer | Biopharma PEG Available online: https://www.biochempeg.com/article/188.html (accessed on 15 November 2022).
77. Thi, T.T.H.; Suys, E.J.A.; Lee, J.S.; Nguyen, D.H.; Park, K.D.; Truong, N.P. Lipid-Based Nanoparticles in the Clinic and Clinical Trials: From Cancer Nanomedicine to COVID-19 Vaccines. *Vaccines (Basel)* **2021**, *9*, 359, doi:10.3390/vaccines9040359.

78. Paluch, E.K.; Nelson, C.M.; Biais, N.; Fabry, B.; Moeller, J.; Pruitt, B.L.; Wollnik, C.; Kudryasheva, G.; Rehfeldt, F.; Federle, W. Mechanotransduction: Use the Force(s). *BMC Biol* **2015**, *13*, 47, doi:10.1186/s12915-015-0150-4.
79. Hope, J.; Greenlee, J.; King, M. Mechanosensitive Ion Channels: TRPV4 and P2X7 in Disseminating Cancer Cells. *The Cancer Journal* **2018**, *24*, 84–92, doi:10.1097/PPO.0000000000000312.
80. Dombroski, J.A.; Hope, J.M.; Sarna, N.S.; King, M.R. Channeling the Force: Piezo1 Mechanotransduction in Cancer Metastasis. *Cells* **2021**, *10*, 2815, doi:10.3390/cells10112815.
81. Hope, J.M.; Lopez-Cavestany, M.; Wang, W.; Reinhart-King, C.A.; King, M.R. Activation of Piezo1 Sensitizes Cells to TRAIL-Mediated Apoptosis through Mitochondrial Outer Membrane Permeability. *Cell Death & Disease* **2019**, *10*, 1–15, doi:10.1038/s41419-019-2063-6.
82. Botello-Smith, W.M.; Jiang, W.; Zhang, H.; Ozkan, A.D.; Lin, Y.-C.; Pham, C.N.; Lacroix, J.J.; Luo, Y. A Mechanism for the Activation of the Mechanosensitive Piezo1 Channel by the Small Molecule Yoda1. *Nat Commun* **2019**, *10*, 4503, doi:10.1038/s41467-019-12501-1.
83. Wang, Y.; Chi, S.; Guo, H.; Li, G.; Wang, L.; Zhao, Q.; Rao, Y.; Zu, L.; He, W.; Xiao, B. A Lever-like Transduction Pathway for Long-Distance Chemical- and Mechano-Gating of the Mechanosensitive Piezo1 Channel. *Nat Commun* **2018**, *9*, 1300, doi:10.1038/s41467-018-03570-9.
84. Greenlee, J.D.; Subramanian, T.; Liu, K.; King, M.R. Rafting Down the Metastatic Cascade: The Role of Lipid Rafts in Cancer Metastasis, Cell Death, and Clinical Outcomes. *Cancer Res* **2021**, *81*, 5–17, doi:10.1158/0008-5472.CAN-20-2199.
85. Simons, K.; Ikonen, E. Functional Rafts in Cell Membranes. *Nature* **1997**, *387*, 569–572, doi:10.1038/42408.
86. Singer, S.J.; Nicolson, G.L. THE FLUID MOSAIC MODEL OF THE STRUCTURE OF CELL MEMBRANES Reprinted with Permission from Science, Copyright AAA, 18 February 1972, Volume 175, Pp. 720–731. In *Membranes and Viruses in Immunopathology*; Day, S.B., Good, R.A., Eds.; Academic Press, 1972; pp. 7–47 ISBN 978-0-12-207250-5.
87. Sezgin, E.; Levental, I.; Mayor, S.; Eggeling, C. The Mystery of Membrane Organization: Composition, Regulation and Roles of Lipid Rafts. *Nat Rev Mol Cell Biol* **2017**, *18*, 361–374, doi:10.1038/nrm.2017.16.
88. Simons, K.; Ehehalt, R. Cholesterol, Lipid Rafts, and Disease. *J Clin Invest* **2002**, *110*, 597–603, doi:10.1172/JCI16390.
89. Hanzal-Bayer, M.F.; Hancock, J.F. Lipid Rafts and Membrane Traffic. *FEBS Letters* **2007**, *581*, 2098–2104, doi:10.1016/j.febslet.2007.03.019.
90. Karnovsky, M.J.; Kleinfeld, A.M.; Hoover, R.L.; Klausner, R.D. The Concept of Lipid Domains in Membranes. *J. Cell Biol.* **1982**, *94*, 1–6, doi:10.1083/jcb.94.1.1.
91. Chamberlain, L.H. Detergents as Tools for the Purification and Classification of Lipid Rafts. *FEBS Letters* **2004**, *559*, 1–5, doi:10.1016/S0014-5793(04)00050-X.
92. Brown, D.A.; London, E. Functions of Lipid Rafts in Biological Membranes. *Annual Review of Cell and Developmental Biology* **1998**, *14*, 111–136, doi:10.1146/annurev.cellbio.14.1.111.
93. Klymchenko, A.S.; Kreder, R. Fluorescent Probes for Lipid Rafts: From Model Membranes to Living Cells. *Chemistry & Biology* **2014**, *21*, 97–113, doi:10.1016/j.chembiol.2013.11.009.
94. Martinez-Outschoorn, U.E.; Sotgia, F.; Lisanti, M.P. Caveolae and Signalling in Cancer. *Nature Reviews Cancer* **2015**, *15*, 225–237, doi:10.1038/nrc3915.
95. Galbiati, F.; Razani, B.; Lisanti, M.P. Emerging Themes in Lipid Rafts and Caveolae. *Cell* **2001**, *106*, 403–411, doi:10.1016/S0092-8674(01)00472-X.

96. de Laurentiis, A.; Donovan, L.; Arcaro, A. Lipid Rafts and Caveolae in Signaling by Growth Factor Receptors. *Open Biochem J* **2007**, *1*, 12–32, doi:10.2174/1874091X00701010012.
97. Otto, G.P.; Nichols, B.J. The Roles of Flotillin Microdomains – Endocytosis and Beyond. *J Cell Sci* **2011**, *124*, 3933–3940, doi:10.1242/jcs.092015.
98. Simons, K.; Toomre, D. Lipid Rafts and Signal Transduction. *Nature Reviews Molecular Cell Biology* **2000**, *1*, 31–39, doi:10.1038/35036052.
99. Shi, D.; Lv, X.; Zhang, Z.; Yang, X.; Zhou, Z.; Zhang, L.; Zhao, Y. Smoothened Oligomerization/Higher Order Clustering in Lipid Rafts Is Essential for High Hedgehog Activity Transduction. *J. Biol. Chem.* **2013**, *288*, 12605–12614, doi:10.1074/jbc.M112.399477.
100. Staubach, S.; Hanisch, F.-G. Lipid Rafts: Signaling and Sorting Platforms of Cells and Their Roles in Cancer. *Expert Review of Proteomics* **2011**, *8*, 263–277, doi:10.1586/epr.11.2.
101. Mehlen, P.; Puisieux, A. Metastasis: A Question of Life or Death. *Nature Reviews Cancer* **2006**, *6*, 449–458, doi:10.1038/nrc1886.
102. Vincent, L.; Chen, W.; Hong, L.; Mirshahi, F.; Mishal, Z.; Mirshahi-Khorassani, T.; Vannier, J.-P.; Soria, J.; Soria, C. Inhibition of Endothelial Cell Migration by Cerivastatin, an HMG-CoA Reductase Inhibitor: Contribution to Its Anti-Angiogenic Effect. *FEBS Letters* **2001**, *495*, 159–166, doi:10.1016/S0014-5793(01)02337-7.
103. Badana, A.; Chintala, M.; Varikuti, G.; Pudi, N.; Kumari, S.; Kappala, V.R.; Malla, R.R. Lipid Raft Integrity Is Required for Survival of Triple Negative Breast Cancer Cells. *J Breast Cancer* **2016**, *19*, 372–384, doi:10.4048/jbc.2016.19.4.372.
104. Raghu, H.; Sodadasu, P.K.; Malla, R.R.; Gondi, C.S.; Estes, N.; Rao, J.S. Localization of UPAR and MMP-9 in Lipid Rafts Is Critical for Migration, Invasion and Angiogenesis in Human Breast Cancer Cells. *BMC Cancer* **2010**, *10*, 647, doi:10.1186/1471-2407-10-647.
105. Tahir, S.A.; Park, S.; Thompson, T.C. Caveolin-1 Regulates VEGF-Stimulated Angiogenic Activities in Prostate Cancer and Endothelial Cells. *Cancer Biol Ther* **2009**, *8*, 2286–2296.
106. Noghero, A.; Perino, A.; Seano, G.; Saglio, E.; Lo Sasso, G.; Veglio, F.; Primo, L.; Hirsch, E.; Bussolino, F.; Morello, F. Liver X Receptor Activation Reduces Angiogenesis by Impairing Lipid Raft Localization and Signaling of Vascular Endothelial Growth Factor Receptor-2. *Arterioscler. Thromb. Vasc. Biol.* **2012**, *32*, 2280–2288, doi:10.1161/ATVBAHA.112.250621.
107. Nomura, S.; Iwata, S.; Hatano, R.; Komiya, E.; Dang, N.H.; Iwao, N.; Ohnuma, K.; Morimoto, C. Inhibition of VEGF-Dependent Angiogenesis by the Anti-CD82 Monoclonal Antibody 4F9 through Regulation of Lipid Raft Microdomains. *Biochemical and Biophysical Research Communications* **2016**, *474*, 111–117, doi:10.1016/j.bbrc.2016.04.081.
108. Wang, X.; Zhang, Y.; Zhao, Y.; Liang, Y.; Xiang, C.; Zhou, H.; Zhang, H.; Zhang, Q.; Qing, H.; Jiang, B.; et al. CD24 Promoted Cancer Cell Angiogenesis via Hsp90-Mediated STAT3/VEGF Signaling Pathway in Colorectal Cancer. *Oncotarget* **2016**, *7*, 55663–55676, doi:10.18632/oncotarget.10971.
109. He, L.; Zhu, W.; Chen, Q.; Yuan, Y.; Wang, Y.; Wang, J.; Wu, X. Ovarian Cancer Cell-Secreted Exosomal MiR-205 Promotes Metastasis by Inducing Angiogenesis. *Theranostics* **2019**, *9*, 8206–8220, doi:10.7150/thno.37455.
110. Zuo, W.; Chen, Y.-G. Specific Activation of Mitogen-Activated Protein Kinase by Transforming Growth Factor-β Receptors in Lipid Rafts Is Required for Epithelial Cell Plasticity. *Mol Biol Cell* **2009**, *20*, 1020–1029, doi:10.1091/mbc.E08-09-0898.
111. Jin, H.; He, Y.; Zhao, P.; Hu, Y.; Tao, J.; Chen, J.; Huang, Y. Targeting Lipid Metabolism to Overcome EMT-Associated Drug Resistance via Integrin Β3/FAK Pathway and Tumor-Associated Macrophage Repolarization Using Legumain-Activatable Delivery. *Theranostics* **2019**, *9*, 265–278, doi:10.7150/thno.27246.
112. Hung, C.-M.; Kuo, D.-H.; Chou, C.-H.; Su, Y.-C.; Ho, C.-T.; Way, T.-D. Osthole Suppresses Hepatocyte Growth Factor (HGF)-Induced Epithelial-Mesenchymal Transition via

Repression of the c-Met/Akt/MTOR Pathway in Human Breast Cancer Cells. *J. Agric. Food Chem.* **2011**, *59*, 9683–9690, doi:10.1021/jf2021489.

113. Fernández-Muñoz, B.; Yurrita, M.M.; Martín-Villar, E.; Carrasco-Ramírez, P.; Megías, D.; Renart, J.; Quintanilla, M. The Transmembrane Domain of Podoplanin Is Required for Its Association with Lipid Rafts and the Induction of Epithelial-Mesenchymal Transition. *The International Journal of Biochemistry & Cell Biology* **2011**, *43*, 886–896, doi:10.1016/j.biocel.2011.02.010.
114. Liang, W.; Hao, Z.; Han, J.-L.; Zhu, D.-J.; Jin, Z.-F.; Xie, W.-L. CAV-1 Contributes to Bladder Cancer Progression by Inducing Epithelial-to-Mesenchymal Transition. *Urologic Oncology: Seminars and Original Investigations* **2014**, *32*, 855–863, doi:10.1016/j.urolonc.2014.01.005.
115. Cheng, Y.; Song, Y.; Qu, J.; Che, X.; Song, N.; Fan, Y.; Wen, T.; Xu, L.; Gong, J.; Wang, X.; et al. The Chemokine Receptor CXCR4 and C-MET Cooperatively Promote Epithelial-Mesenchymal Transition in Gastric Cancer Cells. *Transl Oncol* **2018**, *11*, 487–497, doi:10.1016/j.tranon.2018.02.002.
116. Li, Q.; Peng, J.; Li, X.; Leng, A.; Liu, T. MiR-449a Targets Flot2 and Inhibits Gastric Cancer Invasion by Inhibiting TGF-β-Mediated EMT. *Diagn Pathol* **2015**, *10*, doi:10.1186/s13000-015-0435-5.
117. Tisza, M.J.; Zhao, W.; Fuentes, J.S.R.; Prijic, S.; Chen, X.; Levental, I.; Chang, J.T. Motility and Stem Cell Properties Induced by the Epithelial-Mesenchymal Transition Require Destabilization of Lipid Rafts. *Oncotarget* **2016**, *7*, 51553–51568, doi:10.18632/oncotarget.9928.
118. Zhang, Q.; Furukawa, K.; Chen, H.-H.; Sakakibara, T.; Urano, T.; Furukawa, K. Metastatic Potential of Mouse Lewis Lung Cancer Cells Is Regulated via Ganglioside GM1 by Modulating the Matrix Metalloprotease-9 Localization in Lipid Rafts. *J. Biol. Chem.* **2006**, *281*, 18145–18155, doi:10.1074/jbc.M512566200.
119. Liu, Y.; Sun, R.; Wan, W.; Wang, J.; Oppenheim, J.J.; Chen, L.; Zhang, N. The Involvement of Lipid Rafts in Epidermal Growth Factor-Induced Chemotaxis of Breast Cancer Cells. *Molecular Membrane Biology* **2007**, *24*, 91–101, doi:10.1080/10929080600990500.
120. Gupta, V.K.; Sharma, N.S.; Kesh, K.; Dauer, P.; Nomura, A.; Giri, B.; Dudeja, V.; Banerjee, S.; Bhattacharya, S.; Saluja, A.; et al. Metastasis and Chemoresistance in CD133 Expressing Pancreatic Cancer Cells Are Dependent on Their Lipid Raft Integrity. *Cancer Lett.* **2018**, *439*, 101–112, doi:10.1016/j.canlet.2018.09.028.
121. Berger, T.; Ueda, T.; Arpaia, E.; Chio, I.I.C.; Shirdel, E.A.; Jurisica, I.; Hamada, K.; You-Ten, A.; Haight, J.; Wakeham, A.; et al. Flotillin-2 Deficiency Leads to Reduced Lung Metastases in a Mouse Breast Cancer Model. *Oncogene* **2013**, *32*, 4989–4994, doi:10.1038/onc.2012.499.
122. Xie, G.; Li, J.; Chen, J.; Tang, X.; Wu, S.; Liao, C. Knockdown of Flotillin-2 Impairs the Proliferation of Breast Cancer Cells through Modulation of Akt/FOXO Signaling. *Oncol. Rep.* **2015**, *33*, 2285–2290, doi:10.3892/or.2015.3826.
123. Chantôme, A.; Potier-Cartereau, M.; Clarysse, L.; Fromont, G.; Marionneau-Lambot, S.; Guéguinou, M.; Pagès, J.-C.; Collin, C.; Oullier, T.; Girault, A.; et al. Pivotal Role of the Lipid Raft SK3–Orai1 Complex in Human Cancer Cell Migration and Bone Metastases. *Cancer Res* **2013**, *73*, 4852–4861, doi:10.1158/0008-5472.CAN-12-4572.
124. Yang, Y.-F.; Jan, Y.-H.; Liu, Y.-P.; Yang, C.-J.; Su, C.-Y.; Chang, Y.-C.; Lai, T.-C.; Chiou, J.; Tsai, H.-Y.; Lu, J.; et al. Squalene Synthase Induces Tumor Necrosis Factor Receptor 1 Enrichment in Lipid Rafts to Promote Lung Cancer Metastasis. *Am J Respir Crit Care Med* **2014**, *190*, 675–687, doi:10.1164/rccm.201404-0714OC.
125. Conley-LaComb, M.K.; Semaan, L.; Singareddy, R.; Li, Y.; Heath, E.I.; Kim, S.; Cher, M.L.; Chinni, S.R. Pharmacological Targeting of CXCL12/CXCR4 Signaling in Prostate Cancer Bone Metastasis. *Molecular Cancer* **2016**, *15*, 68, doi:10.1186/s12943-016-0552-0.

126. Sbrissa, D.; Semaan, L.; Govindarajan, B.; Li, Y.; Caruthers, N.J.; Stemmer, P.M.; Cher, M.L.; Sethi, S.; Vaishampayan, U.; Shisheva, A.; et al. A Novel Cross-Talk between CXCR4 and PI4KIIIα in Prostate Cancer Cells. *Oncogene* **2019**, *38*, 332–344, doi:10.1038/s41388-018-0448-0.
127. Li, G.; Sasaki, T.; Asahina, S.; Roy, M.C.; Mochizuki, T.; Koizumi, K.; Zhang, Y. Patching of Lipid Rafts by Molecular Self-Assembled Nanofibrils Suppresses Cancer Cell Migration. *Chem* **2017**, *2*, 283–298, doi:10.1016/j.chempr.2017.01.002.
128. Grolez, G.P.; Gordiendko, D.V.; Clarisse, M.; Hammadi, M.; Desruelles, E.; Fromont, G.; Prevarskaya, N.; Slomianny, C.; Gkika, D. TRPM8-Androgen Receptor Association within Lipid Rafts Promotes Prostate Cancer Cell Migration. *Cell Death & Disease* **2019**, *10*, 1–17, doi:10.1038/s41419-019-1891-8.
129. Shi, H.; Fang, W.; Liu, M.; Fu, D. Complement Component 1, q Subcomponent Binding Protein (C1QBP) in Lipid Rafts Mediates Hepatic Metastasis of Pancreatic Cancer by Regulating IGF-1/IGF-1R Signaling. *International Journal of Cancer* **2017**, *141*, 1389–1401, doi:10.1002/ijc.30831.
130. Yamaguchi, H.; Takeo, Y.; Yoshida, S.; Kouchi, Z.; Nakamura, Y.; Fukami, K. Lipid Rafts and Caveolin-1 Are Required for Invadopodia Formation and Extracellular Matrix Degradation by Human Breast Cancer Cells. *Cancer Res* **2009**, *69*, 8594–8602, doi:10.1158/0008-5472.CAN-09-2305.
131. Yang, H.; Guan, L.; Li, S.; Jiang, Y.; Xiong, N.; Li, L.; Wu, C.; Zeng, H.; Liu, Y. Mechanosensitive Caveolin-1 Activation-Induced PI3K/Akt/MTOR Signaling Pathway Promotes Breast Cancer Motility, Invadopodia Formation and Metastasis in Vivo. *Oncotarget* **2016**, *7*, 16227–16247, doi:10.18632/oncotarget.7583.
132. Knopf, J.D.; Tholen, S.; Koczorowska, M.M.; De Wever, O.; Biniossek, M.L.; Schilling, O. The Stromal Cell-Surface Protease Fibroblast Activation Protein-α Localizes to Lipid Rafts and Is Recruited to Invadopodia. *Biochim. Biophys. Acta* **2015**, *1853*, 2515–2525, doi:10.1016/j.bbamcr.2015.07.013.
133. Martín-Villar, E.; Borda-d’Agua, B.; Carrasco-Ramirez, P.; Renart, J.; Parsons, M.; Quintanilla, M.; Jones, G.E. Podoplanin Mediates ECM Degradation by Squamous Carcinoma Cells through Control of Invadopodia Stability. *Oncogene* **2015**, *34*, 4531–4544, doi:10.1038/onc.2014.388.
134. Wang, R.; Bi, J.; Ampah, K.K.; Ba, X.; Liu, W.; Zeng, X. Lipid Rafts Control Human Melanoma Cell Migration by Regulating Focal Adhesion Disassembly. *Biochimica et Biophysica Acta (BBA) - Molecular Cell Research* **2013**, *1833*, 3195–3205, doi:10.1016/j.bbamcr.2013.09.007.
135. Huang, Q.; Shen, H.-M.; Shui, G.; Wenk, M.R.; Ong, C.-N. Emodin Inhibits Tumor Cell Adhesion through Disruption of the Membrane Lipid Raft-Associated Integrin Signaling Pathway. *Cancer Res.* **2006**, *66*, 5807–5815, doi:10.1158/0008-5472.CAN-06-0077.
136. Li, C.; Lu, N.; Qi, Q.; Li, F.; Ling, Y.; Chen, Y.; Qin, Y.; Li, Z.; Zhang, H.; You, Q.; et al. Gambogic Acid Inhibits Tumor Cell Adhesion by Suppressing Integrin Β1 and Membrane Lipid Rafts-Associated Integrin Signaling Pathway. *Biochem. Pharmacol.* **2011**, *82*, 1873–1883, doi:10.1016/j.bcp.2011.09.013.
137. Lee, J.-L.; Wang, M.-J.; Sudhir, P.-R.; Chen, J.-Y. CD44 Engagement Promotes Matrix-Derived Survival through the CD44-SRC-Integrin Axis in Lipid Rafts. *Mol Cell Biol* **2008**, *28*, 5710–5723, doi:10.1128/MCB.00186-08.
138. Baumann, P.; Thiele, W.; Cremers, N.; Muppala, S.; Krachulec, J.; Diefenbacher, M.; Kassel, O.; Mudduluru, G.; Allgayer, H.; Frame, M.; et al. CD24 Interacts with and Promotes the Activity of C-Src within Lipid Rafts in Breast Cancer Cells, Thereby Increasing Integrin-Dependent Adhesion. *Cell. Mol. Life Sci.* **2012**, *69*, 435–448, doi:10.1007/s00018-011-0756-9.

139. Murai, T.; Maruyama, Y.; Mio, K.; Nishiyama, H.; Suga, M.; Sato, C. Low Cholesterol Triggers Membrane Microdomain-Dependent CD44 Shedding and Suppresses Tumor Cell Migration. *J Biol Chem* **2011**, *286*, 1999–2007, doi:10.1074/jbc.M110.184010.
140. Mohammadalipour, A.; Showalter, C.; Muturi, H.T.; Sharma, V.; Farnoud, A.M.; Puri, V.; Najjar, S.M.; Burdick, M.M. Abstract 98: Cell Membrane Cholesterol Modulates Lung Cancer Cell Adhesion and Rolling on E-Selectin. *Cancer Res* **2018**, *78*, 98–98, doi:10.1158/1538-7445.AM2018-98.
141. Babina, I.S.; McSherry, E.A.; Donatello, S.; Hill, A.D.; Hopkins, A.M. A Novel Mechanism of Regulating Breast Cancer Cell Migration via Palmitoylation-Dependent Alterations in the Lipid Raft Affiliation of CD44. *Breast Cancer Research* **2014**, *16*, R19, doi:10.1186/bcr3614.
142. Hitosugi, T.; Sato, M.; Sasaki, K.; Umezawa, Y. Lipid Raft Specific Knockdown of SRC Family Kinase Activity Inhibits Cell Adhesion and Cell Cycle Progression of Breast Cancer Cells. *Cancer Res.* **2007**, *67*, 8139–8148, doi:10.1158/0008-5472.CAN-06-4539.
143. Gopalakrishna, P.; Rangaraj, N.; Pande, G. Cholesterol Alters the Interaction of Glycosphingolipid GM3 with Alpha5beta1 Integrin and Increases Integrin-Mediated Cell Adhesion to Fibronectin. *Exp. Cell Res.* **2004**, *300*, 43–53, doi:10.1016/j.yexcr.2004.06.012.
144. Okada, Y.; Nishikawa, J.; Semma, M.; Ichikawa, A. Role of Lipid Raft Components and Actin Cytoskeleton in Fibronectin-Binding, Surface Expression, and de Novo Synthesis of Integrin Subunits in PGE2- or 8-Br-CAMP-Stimulated Mastocytoma P-815 Cells. *Biochem. Pharmacol.* **2014**, *88*, 364–371, doi:10.1016/j.bcp.2014.01.039.
145. Leitinger, B.; Hogg, N. The Involvement of Lipid Rafts in the Regulation of Integrin Function. *Journal of Cell Science* **2002**, *115*, 963–972.
146. Chen, X.; Li, W.; Ren, J.; Huang, D.; He, W.; Song, Y.; Yang, C.; Li, W.; Zheng, X.; Chen, P.; et al. Translocation of Mixed Lineage Kinase Domain-like Protein to Plasma Membrane Leads to Necrotic Cell Death. *Cell Research* **2014**, *24*, 105–121, doi:10.1038/cr.2013.171.
147. Dondelinger, Y.; Declercq, W.; Montessuit, S.; Roelandt, R.; Goncalves, A.; Bruggeman, I.; Hulpiau, P.; Weber, K.; Sehon, C.A.; Marquis, R.W.; et al. MLKL Compromises Plasma Membrane Integrity by Binding to Phosphatidylinositol Phosphates. *Cell Rep* **2014**, *7*, 971–981, doi:10.1016/j.celrep.2014.04.026.
148. Zhang, X.; Kitatani, K.; Toyoshima, M.; Ishibashi, M.; Usui, T.; Minato, J.; Egiz, M.; Shigeta, S.; Fox, T.; Deering, T.; et al. Ceramide Nanoliposomes as a MLKL-Dependent, Necroptosis-Inducing, Chemotherapeutic Reagent in Ovarian Cancer. *Mol Cancer Ther* **2018**, *17*, 50–59, doi:10.1158/1535-7163.MCT-17-0173.
149. Li, Y.C.; Park, M.J.; Ye, S.-K.; Kim, C.-W.; Kim, Y.-N. Elevated Levels of Cholesterol-Rich Lipid Rafts in Cancer Cells Are Correlated with Apoptosis Sensitivity Induced by Cholesterol-Depleting Agents. *Am. J. Pathol.* **2006**, *168*, 1107–1118; quiz 1404–1405, doi:10.2353/ajpath.2006.050959.
150. Park, E.-K.; Park, M.J.; Lee, S.-H.; Li, Y.C.; Kim, J.; Lee, J.-S.; Lee, J.W.; Ye, S.-K.; Park, J.-W.; Kim, C.-W.; et al. Cholesterol Depletion Induces Anoikis-like Apoptosis via FAK down-Regulation and Caveolae Internalization. *J. Pathol.* **2009**, *218*, 337–349, doi:10.1002/path.2531.
151. Lee, S.-H.; Koo, K.H.; Park, J.-W.; Kim, H.-J.; Ye, S.-K.; Park, J.B.; Park, B.-K.; Kim, Y.-N. HIF-1 Is Induced via EGFR Activation and Mediates Resistance to Anoikis-like Cell Death under Lipid Rafts/Caveolae-Disrupting Stress. *Carcinogenesis* **2009**, *30*, 1997–2004, doi:10.1093/carcin/bgp233.
152. Xiao, W.; Ishdorj, G.; Sun, J.; Johnston, J.B.; Gibson, S.B. Death Receptor 4 Is Preferentially Recruited to Lipid Rafts in Chronic Lymphocytic Leukemia Cells Contributing to Tumor Necrosis Related Apoptosis Inducing Ligand-Induced Synergistic Apoptotic Responses. *Leuk. Lymphoma* **2011**, *52*, 1290–1301, doi:10.3109/10428194.2011.567317.

153. Marconi, M.; Ascione, B.; Ciarlo, L.; Vona, R.; Garofalo, T.; Sorice, M.; Gianni, A.M.; Locatelli, S.L.; Carlo-Stella, C.; Malorni, W.; et al. Constitutive Localization of DR4 in Lipid Rafts Is Mandatory for TRAIL-Induced Apoptosis in B-Cell Hematologic Malignancies. *Cell Death Dis* **2013**, *4*, e863, doi:10.1038/cddis.2013.389.
154. Ouyang, W.; Yang, C.; Liu, Y.; Xiong, J.; Zhang, J.; Zhong, Y.; Zhang, G.; Zhou, F.; Zhou, Y.; Xie, C. Redistribution of DR4 and DR5 in Lipid Rafts Accounts for the Sensitivity to TRAIL in NSCLC Cells. *International Journal of Oncology* **2011**, *39*, 1577–1586, doi:10.3892/ijo.2011.1129.
155. Song, J.H.; Tse, M.C.L.; Bellail, A.; Phuphanich, S.; Khuri, F.; Kneteman, N.M.; Hao, C. Lipid Rafts and Nonrafts Mediate Tumor Necrosis Factor–Related Apoptosis-Inducing Ligand–Induced Apoptotic and Nonapoptotic Signals in Non–Small Cell Lung Carcinoma Cells. *Cancer Res* **2007**, *67*, 6946–6955, doi:10.1158/0008-5472.CAN-06-3896.
156. Delmas, D.; Rébé, C.; Micheau, O.; Athias, A.; Gambert, P.; Grazide, S.; Laurent, G.; Latruffe, N.; Solary, E. Redistribution of CD95, DR4 and DR5 in Rafts Accounts for the Synergistic Toxicity of Resveratrol and Death Receptor Ligands in Colon Carcinoma Cells. *Oncogene* **2004**, *23*, 8979–8986, doi:10.1038/sj.onc.1208086.
157. Gajate, C.; Mollinedo, F. The Antitumor Ether Lipid ET-18-OCH(3) Induces Apoptosis through Translocation and Capping of Fas/CD95 into Membrane Rafts in Human Leukemic Cells. *Blood* **2001**, *98*, 3860–3863, doi:10.1182/blood.v98.13.3860.
158. Reis-Sobreiro, M.; Gajate, C.; Mollinedo, F. Involvement of Mitochondria and Recruitment of Fas/CD95 Signaling in Lipid Rafts in Resveratrol-Mediated Antimyeloma and Antileukemia Actions. *Oncogene* **2009**, *28*, 3221–3234, doi:10.1038/onc.2009.183.
159. Gao, X.; Zhang, J. Spatiotemporal Analysis of Differential Akt Regulation in Plasma Membrane Microdomains. *Mol Biol Cell* **2008**, *19*, 4366–4373, doi:10.1091/mbc.E08-05-0449.
160. Gilmore, A.P. Anoikis. *Cell Death & Differentiation* **2005**, *12*, 1473–1477, doi:10.1038/sj.cdd.4401723.
161. Ben-Zaken, O.; Gingis-Velitski, S.; Vlodavsky, I.; Ilan, N. Heparanase Induces Akt Phosphorylation via a Lipid Raft Receptor. *Biochem Biophys Res Commun* **2007**, *361*, 829–834, doi:10.1016/j.bbrc.2007.06.188.
162. Chatterjee, S.; Heukamp, L.C.; Siobal, M.; Schöttle, J.; Wieczorek, C.; Peifer, M.; Frasca, D.; Koker, M.; König, K.; Meder, L.; et al. Tumor VEGF:VEGFR2 Autocrine Feed-Forward Loop Triggers Angiogenesis in Lung Cancer. *J Clin Invest* **2013**, *123*, 1732–1740, doi:10.1172/JCI65385.
163. Hoshino, A.; Costa-Silva, B.; Shen, T.-L.; Rodrigues, G.; Hashimoto, A.; Tesic Mark, M.; Molina, H.; Kohsaka, S.; Di Giannatale, A.; Ceder, S.; et al. Tumour Exosome Integrins Determine Organotropic Metastasis. *Nature* **2015**, *527*, 329–335, doi:10.1038/nature15756.
164. Xu, J.; Lamouille, S.; Derynck, R. TGF-β-Induced Epithelial to Mesenchymal Transition. *Cell Research* **2009**, *19*, 156–172, doi:10.1038/cr.2009.5.
165. Head, B.P.; Patel, H.H.; Insel, P.A. Interaction of Membrane/Lipid Rafts with the Cytoskeleton: Impact on Signaling and Function: Membrane/Lipid Rafts, Mediators of Cytoskeletal Arrangement and Cell Signaling. *Biochim. Biophys. Acta* **2014**, *1838*, 532–545, doi:10.1016/j.bbamem.2013.07.018.
166. Gialeli, C.; Theocharis, A.D.; Karamanos, N.K. Roles of Matrix Metalloproteinases in Cancer Progression and Their Pharmacological Targeting. *The FEBS Journal* **2011**, *278*, 16–27, doi:10.1111/j.1742-4658.2010.07919.x@10.1002/(ISSN)1742-4658(CAT)FreeReviewContent(VI)Reviews1011.
167. Brand, S.; Dambacher, J.; Beigel, F.; Olszak, T.; Diebold, J.; Otte, J.-M.; Göke, B.; Eichhorst, S.T. CXCR4 and CXCL12 Are Inversely Expressed in Colorectal Cancer Cells

and Modulate Cancer Cell Migration, Invasion and MMP-9 Activation. *Experimental Cell Research* **2005**, *310*, 117–130, doi:10.1016/j.yexcr.2005.07.006.

168. Arya, M.; Ahmed, H.; Silhi, N.; Williamson, M.; Patel, H.R.H. Clinical Importance and Therapeutic Implications of the Pivotal CXCL12-CXCR4 (Chemokine Ligand-Receptor) Interaction in Cancer Cell Migration. *TBI* **2007**, *28*, 123–131, doi:10.1159/000102979.
169. Reymond, N.; d'Água, B.B.; Ridley, A.J. Crossing the Endothelial Barrier during Metastasis. *Nature Reviews Cancer* **2013**, *13*, 858–870, doi:10.1038/nrc3628.
170. Roland, C.L.; Harken, A.H.; Sarr, M.G.; Barnett, C.C. ICAM-1 Expression Determines Malignant Potential of Cancer. *Surgery* **2007**, *141*, 705–707, doi:10.1016/j.surg.2007.01.016.
171. Rahn, J.J.; Chow, J.W.; Horne, G.J.; Mah, B.K.; Emerman, J.T.; Hoffman, P.; Hugh, J.C. MUC1 Mediates Transendothelial Migration in Vitro by Ligating Endothelial Cell ICAM-1. *Clin. Exp. Metastasis* **2005**, *22*, 475–483, doi:10.1007/s10585-005-3098-x.
172. Tokui, N.; Yoneyama, M.S.; Hatakeyama, S.; Yamamoto, H.; Koie, T.; Saitoh, H.; Yamaya, K.; Funyu, T.; Nakamura, T.; Ohyama, C.; et al. Extravasation during Bladder Cancer Metastasis Requires Cortactin-mediated Invadopodia Formation. *Mol Med Rep* **2014**, *9*, 1142–1146, doi:10.3892/mmr.2014.1965.
173. Williams, K.C.; Cepeda, M.A.; Javed, S.; Searle, K.; Parkins, K.M.; Makela, A.V.; Hamilton, A.M.; Soukhtehzari, S.; Kim, Y.; Tuck, A.B.; et al. Invadopodia Are Chemosensing Protrusions That Guide Cancer Cell Extravasation to Promote Brain Tropism in Metastasis. *Oncogene* **2019**, *38*, 3598–3615, doi:10.1038/s41388-018-0667-4.
174. Gligorijevic, B.; Wyckoff, J.; Yamaguchi, H.; Wang, Y.; Roussos, E.T.; Condeelis, J. N-WASP-Mediated Invadopodium Formation Is Involved in Intravasation and Lung Metastasis of Mammary Tumors. *J. Cell. Sci.* **2012**, *125*, 724–734, doi:10.1242/jcs.092726.
175. Leong, H.S.; Robertson, A.E.; Stoletov, K.; Leith, S.J.; Chin, C.A.; Chien, A.E.; Hague, M.N.; Ablack, A.; Carmine-Simmen, K.; McPherson, V.A.; et al. Invadopodia Are Required for Cancer Cell Extravasation and Are a Therapeutic Target for Metastasis. *Cell Reports* **2014**, *8*, 1558–1570, doi:10.1016/j.celrep.2014.07.050.
176. Bendas, G.; Borsig, L. Cancer Cell Adhesion and Metastasis: Selectins, Integrins, and the Inhibitory Potential of Heparins Available online: https://www.hindawi.com/journals/ijcb/2012/676731/ (accessed on 11 May 2020).
177. Sun, M.; Northup, N.; Marga, F.; Huber, T.; Byfield, F.J.; Levitan, I.; Forgacs, G. The Effect of Cellular Cholesterol on Membrane-Cytoskeleton Adhesion. *Journal of Cell Science* **2007**, *120*, 2223–2231, doi:10.1242/jcs.001370.
178. Eich, C.; Manzo, C.; Keijzer, S. de; Bakker, G.-J.; Reinieren-Beeren, I.; García-Parajo, M.F.; Cambi, A. Changes in Membrane Sphingolipid Composition Modulate Dynamics and Adhesion of Integrin Nanoclusters. *Scientific Reports* **2016**, *6*, 20693, doi:10.1038/srep20693.
179. Yates, A.J.; Rampersaud, A. Sphingolipids as Receptor Modulators: An Overview. *Annals of the New York Academy of Sciences* **1998**, *845*, 57–71, doi:10.1111/j.1749-6632.1998.tb09662.x.
180. Marhaba, R.; Zöller, M. CD44 in Cancer Progression: Adhesion, Migration and Growth Regulation. *Histochem J* **2004**, *35*, 211–231, doi:10.1023/B:HIJO.0000032354.94213.69.
181. Draffin, J.E.; McFarlane, S.; Hill, A.; Johnston, P.G.; Waugh, D.J.J. CD44 Potentiates the Adherence of Metastatic Prostate and Breast Cancer Cells to Bone Marrow Endothelial Cells. *Cancer Res* **2004**, *64*, 5702–5711, doi:10.1158/0008-5472.CAN-04-0389.
182. Herrera-Gayol, A.; Jothy, S. CD44 Modulates Hs578T Human Breast Cancer Cell Adhesion, Migration, and Invasiveness. *Experimental and Molecular Pathology* **1999**, *66*, 99–108, doi:10.1006/exmp.1999.2236.
183. Wang, H.; Zhu, Y.; Zhao, M.; Wu, C.; Zhang, P.; Tang, L.; Zhang, H.; Chen, X.; Yang, Y.; Liu, G. MiRNA-29c Suppresses Lung Cancer Cell Adhesion to Extracellular Matrix and

Metastasis by Targeting Integrin B1 and Matrix Metalloproteinase2 (MMP2). *PLoS One* **2013**, *8*, doi:10.1371/journal.pone.0070192.

184. Albelda, S.M. Role of Integrins and Other Cell Adhesion Molecules in Tumor Progression and Metastasis. *Lab. Invest.* **1993**, *68*, 4–17.
185. Felding-Habermann, B.; O'Toole, T.E.; Smith, J.W.; Fransvea, E.; Ruggeri, Z.M.; Ginsberg, M.H.; Hughes, P.E.; Pampori, N.; Shattil, S.J.; Saven, A.; et al. Integrin Activation Controls Metastasis in Human Breast Cancer. *PNAS* **2001**, *98*, 1853–1858, doi:10.1073/pnas.98.4.1853.
186. Sun, F.; Schroer, C.F.E.; Palacios, C.R.; Xu, L.; Luo, S.-Z.; Marrink, S.J. Molecular Mechanism for Bidirectional Regulation of CD44 for Lipid Raft Affiliation by Palmitoylations and PIP2. *PLOS Computational Biology* **2020**, *16*, e1007777, doi:10.1371/journal.pcbi.1007777.
187. Renehan, A.G.; Booth, C.; Potten, C.S. What Is Apoptosis, and Why Is It Important? *BMJ* **2001**, *322*, 1536–1538.
188. Borges, H.L.; Linden, R.; Wang, J.Y. DNA Damage-Induced Cell Death. *Cell Res* **2008**, *18*, 17–26, doi:10.1038/cr.2007.110.
189. Fernald, K.; Kurokawa, M. Evading Apoptosis in Cancer. *Trends Cell Biol* **2013**, *23*, 620–633, doi:10.1016/j.tcb.2013.07.006.
190. Syntichaki, P.; Tavernarakis, N. Death by Necrosis. *EMBO Rep* **2002**, *3*, 604–609, doi:10.1093/embo-reports/kvf138.
191. Proskuryakov, S.Ya.; Gabai, V.L.; Konoplyannikov, A.G. Necrosis Is an Active and Controlled Form of Programmed Cell Death. *Biochemistry (Moscow)* **2002**, *67*, 387–408, doi:10.1023/A:1015289521275.
192. Weber, K.; Roelandt, R.; Bruggeman, I.; Estornes, Y.; Vandenabeele, P. Nuclear RIPK3 and MLKL Contribute to Cytosolic Necrosome Formation and Necroptosis. *Communications Biology* **2018**, *1*, 1–13, doi:10.1038/s42003-017-0007-1.
193. Larsen, B.D.; Sørensen, C.S. The Caspase-Activated DNase: Apoptosis and Beyond. *The FEBS Journal* **2017**, *284*, 1160–1170, doi:10.1111/febs.13970.
194. Mollinedo, F.; Gajate, C. Lipid Rafts as Major Platforms for Signaling Regulation in Cancer. *Advances in Biological Regulation* **2015**, *57*, 130–146, doi:10.1016/j.jbior.2014.10.003.
195. Mollinedo, F.; Gajate, C. Lipid Rafts, Death Receptors and CASMERs: New Insights for Cancer Therapy. *Future Oncology* **2010**, *6*, 491–494, doi:10.2217/fon.10.22.
196. Kim, Y.-N.; Koo, K.H.; Sung, J.Y.; Yun, U.-J.; Kim, H. Anoikis Resistance: An Essential Prerequisite for Tumor Metastasis. *Int J Cell Biol* **2012**, *2012*, doi:10.1155/2012/306879.
197. Wang, X.; Yang, Q.; Guo, L.; Li, X.-H.; Zhao, X.-H.; Song, L.-B.; Lin, H.-X. Flotillin-2 Is Associated with Breast Cancer Progression and Poor Survival Outcomes. *J Transl Med* **2013**, *11*, 190, doi:10.1186/1479-5876-11-190.
198. Li, Z.; Yang, Y.; Gao, Y.; Wu, X.; Yang, X.; Zhu, Y.; Yang, H.; Wu, L.; Yang, C.; Song, L. Elevated Expression of Flotillin-1 Is Associated with Lymph Node Metastasis and Poor Prognosis in Early-Stage Cervical Cancer. *Am J Cancer Res* **2015**, *6*, 38–50.
199. Liu, Y.; Lin, L.; Huang, Z.; Ji, B.; Mei, S.; Lin, Y.; Shen, Z. High Expression of Flotillin-2 Is Associated with Poor Clinical Survival in Cervical Carcinoma. *Int J Clin Exp Pathol* **2015**, *8*, 622–628.
200. Baig, N.; Li, Z.; Lu, J.; Chen, H.; Yu, S.; Li, T.; Niu, Z.; Niu, J. Clinical Significance and Comparison of Flotillin 1 Expression in Left and Right Colon Cancer. *Oncol Lett* **2019**, *18*, 997–1004, doi:10.3892/ol.2019.10401.
201. Li, T.; Cao, C.; Xiong, Q.; Liu, D. FLOT2 Overexpression Is Associated with the Progression and Prognosis of Human Colorectal Cancer. *Oncol Lett* **2019**, *17*, 2802–2808, doi:10.3892/ol.2019.9882.

202. Zhang, S.-H.; Wang, C.-J.; Shi, L.; Li, X.-H.; Zhou, J.; Song, L.-B.; Liao, W.-T. High Expression of FLOT1 Is Associated with Progression and Poor Prognosis in Hepatocellular Carcinoma. *PLoS ONE* **2013**, *8*, e64709, doi:10.1371/journal.pone.0064709.
203. Xu, Z.; Wang, T.; Song, H.; Jiang, X. Flotillin-2 Predicts Poor Prognosis and Promotes Tumor Invasion in Intrahepatic Cholangiocarcinoma. *Oncol Lett* **2020**, *19*, 2243–2250, doi:10.3892/ol.2020.11349.
204. Liu, J.; Huang, W.; Ren, C.; Wen, Q.; Liu, W.; Yang, X.; Wang, L.; Zhu, B.; Zeng, L.; Feng, X.; et al. Flotillin-2 Promotes Metastasis of Nasopharyngeal Carcinoma by Activating NF-KB and PI3K/Akt3 Signaling Pathways. *Sci Rep* **2015**, *5*, 11614, doi:10.1038/srep11614.
205. Zhao, L.; Shi, M.; Duan, J.; Ma, H.; Wu, Z.; Chen, X.; Yang, T.; Liao, W. Flotillin-2 Role in Nasopharyngeal Carcinoma Metastasis and Correlation with Poor Survival Outcomes. *JCO* **2014**, *32*, e17050–e17050, doi:10.1200/jco.2014.32.15_suppl.e17050.
206. Tomiyama, A.; Uekita, T.; Kamata, R.; Sasaki, K.; Takita, J.; Ohira, M.; Nakagawara, A.; Kitanaka, C.; Mori, K.; Yamaguchi, H.; et al. Flotillin-1 Regulates Oncogenic Signaling in Neuroblastoma Cells by Regulating ALK Membrane Association. *Cancer Res.* **2014**, *74*, 3790–3801, doi:10.1158/0008-5472.CAN-14-0241.
207. Zhao, L.; Li, J.; Liu, Y.; Zhou, W.; Shan, Y.; Fan, X.; Zhou, X.; Shan, B.; Song, Y.; Zhan, Q. Flotillin1 Promotes EMT of Human Small Cell Lung Cancer via TGF-β Signaling Pathway. *Cancer Biology & Medicine* **2018**, *15*, 400-414–414.
208. Deng, Y.; Ge, P.; Tian, T.; Dai, C.; Wang, M.; Lin, S.; Liu, K.; Zheng, Y.; Xu, P.; Zhou, L.; et al. Prognostic Value of Flotillins (Flotillin-1 and Flotillin-2) in Human Cancers: A Meta-Analysis. *Clin. Chim. Acta* **2018**, *481*, 90–98, doi:10.1016/j.cca.2018.02.036.
209. Ou, Y.; Liu, F.; Chen, F.; Zhu, Z. Prognostic Value of Flotillin-1 Expression in Patients with Solid Tumors. *Oncotarget* **2017**, *8*, 52665–52677, doi:10.18632/oncotarget.17075.
210. Hong-ying; Zhang; Zhu; Zheng; Wu; Gaó; Ruan; Yang; Ying-jie; Xiaoliu; et al. High Expression of Flotillin-1 Is Associated with Lymph Node Metastasis and Poor Prognosis in Vulvar Squamous Cell Carcinoma.; 2016.
211. Raja, S.A.; Shah, S.T.A.; Tariq, A.; Bibi, N.; Sughra, K.; Yousuf, A.; Khawaja, A.; Nawaz, M.; Mehmood, A.; Khan, M.J.; et al. Caveolin-1 and Dynamin-2 Overexpression Is Associated with the Progression of Bladder Cancer. *Oncol Lett* **2019**, *18*, 219–226, doi:10.3892/ol.2019.10310.
212. Rajjayabun, P.H.; Garg, S.; Durkan, G.C.; Charlton, R.; Robinson, M.C.; Mellon, J.K. Caveolin-1 Expression Is Associated with High-Grade Bladder Cancer. *Urology* **2001**, *58*, 811–814, doi:10.1016/s0090-4295(01)01337-1.
213. Wang, S.-W.; Xu, K.-L.; Ruan, S.-Q.; Zhao, L.-L.; Chen, L.-R. Overexpression of Caveolin-1 in Cancer-Associated Fibroblasts Predicts Good Outcome in Breast Cancer. *BRC* **2012**, *7*, 477–483, doi:10.1159/000345464.
214. Witkiewicz, A.K.; Dasgupta, A.; Nguyen, K.H.; Liu, C.; Kovatich, A.J.; Schwartz, G.F.; Pestell, R.G.; Sotgia, F.; Rui, H.; Lisanti, M.P. Stromal Caveolin-1 Levels Predict Early DCIS Progression to Invasive Breast Cancer. *Cancer Biol. Ther.* **2009**, *8*, 1071–1079, doi:10.4161/cbt.8.11.8874.
215. Eliyatkin, N.; Aktas, S.; Diniz, G.; Ozgur, H.H.; Ekin, Z.Y.; Kupelioglu, A. Expression of Stromal Caveolin- 1 May Be a Predictor for Aggressive Behaviour of Breast Cancer. *Pathol. Oncol. Res.* **2018**, *24*, 59–65, doi:10.1007/s12253-017-0212-8.
216. Qian, N.; Ueno, T.; Kawaguchi-Sakita, N.; Kawashima, M.; Yoshida, N.; Mikami, Y.; Wakasa, T.; Shintaku, M.; Tsuyuki, S.; Inamoto, T.; et al. Prognostic Significance of Tumor/Stromal Caveolin-1 Expression in Breast Cancer Patients. *Cancer Sci.* **2011**, *102*, 1590–1596, doi:10.1111/j.1349-7006.2011.01985.x.
217. Chiu, W.-T.; Lee, H.-T.; Huang, F.-J.; Aldape, K.D.; Yao, J.; Steeg, P.S.; Chou, C.-Y.; Lu, Z.; Xie, K.; Huang, S. Caveolin-1 Upregulation Mediates Suppression of Primary Breast

Tumor Growth and Brain Metastases by Stat3 Inhibition. *Cancer Res.* **2011**, *71*, 4932–4943, doi:10.1158/0008-5472.CAN-10-4249.

218. Neofytou, K.; Pikoulis, E.; Petrou, A.; Agrogiannis, G.; Petrides, C.; Papakonstandinou, I.; Papalambros, A.; Aggelou, A.; Kavatzas, N.; Liakakos, T.; et al. Weak Stromal Caveolin-1 Expression in Colorectal Liver Metastases Predicts Poor Prognosis after Hepatectomy for Liver-Only Colorectal Metastases. *Sci Rep* **2017**, *7*, 2058, doi:10.1038/s41598-017-02251-9.
219. Sun, D.S.; Hong, S.A.; Won, H.S.; Yoo, S.H.; Lee, H.H.; Kim, O.; Ko, Y.H. Prognostic Value of Metastatic Tumoral Caveolin-1 Expression in Patients with Resected Gastric Cancer Available online: https://www.hindawi.com/journals/grp/2017/5905173/ (accessed on 11 May 2020).
220. Seker, M.; Aydin, D.; Bilici, A.; Yavuzer, D.; Ozgun, M.G.; Ozcelik, M.; Aydin, O.; Aliustaoglu, M. Correlation of Caveolin-1 Expression with Prognosis in Patients with Gastric Cancer after Gastrectomy. *ORT* **2017**, *40*, 185–190, doi:10.1159/000456620.
221. Yoo, S.-H.; Park, Y.S.; Kim, H.-R.; Sung, S.W.; Kim, J.H.; Shim, Y.S.; Lee, S.D.; Choi, Y.-L.; Kim, M.-K.; Chung, D.H. Expression of Caveolin-1 Is Associated with Poor Prognosis of Patients with Squamous Cell Carcinoma of the Lung. *Lung Cancer* **2003**, *42*, 195–202, doi:10.1016/s0169-5002(03)00287-3.
222. Ho, C.-C.; Kuo, S.-H.; Huang, P.-H.; Huang, H.-Y.; Yang, C.-H.; Yang, P.-C. Caveolin-1 Expression Is Significantly Associated with Drug Resistance and Poor Prognosis in Advanced Non-Small Cell Lung Cancer Patients Treated with Gemcitabine-Based Chemotherapy. *Lung Cancer* **2008**, *59*, 105–110, doi:10.1016/j.lungcan.2007.07.024.
223. Hammarsten, P.; Dahl Scherdin, T.; Hägglöf, C.; Andersson, P.; Wikström, P.; Stattin, P.; Egevad, L.; Granfors, T.; Bergh, A. High Caveolin-1 Expression in Tumor Stroma Is Associated with a Favourable Outcome in Prostate Cancer Patients Managed by Watchful Waiting. *PLoS ONE* **2016**, *11*, e0164016, doi:10.1371/journal.pone.0164016.
224. Kim, D.; Kim, H.; Koo, J.S. Expression of Caveolin-1, Caveolin-2 and Caveolin-3 in Thyroid Cancer and Stroma. *Pathobiology* **2012**, *79*, 1–10, doi:10.1159/000329472.
225. Liu, X.; Liu, W.; Wang, L.; Zhu, B.; Shi, X.; Peng, Z.; Zhu, H.; Liu, X.; Zhong, M.; Xie, D.; et al. Roles of Flotillins in Tumors. *J Zhejiang Univ Sci B* **2018**, *19*, 171–182, doi:10.1631/jzus.B1700102.
226. Umapathy, G.; Mendoza-Garcia, P.; Hallberg, B.; Palmer, R.H. Targeting Anaplastic Lymphoma Kinase in Neuroblastoma. *APMIS* **2019**, *127*, 288–302, doi:10.1111/apm.12940.
227. Qian, X.-L.; Pan, Y.-H.; Huang, Q.-Y.; Shi, Y.-B.; Huang, Q.-Y.; Hu, Z.-Z.; Xiong, L.-X. Caveolin-1: A Multifaceted Driver of Breast Cancer Progression and Its Application in Clinical Treatment. *Onco Targets Ther* **2019**, *12*, 1539–1552, doi:10.2147/OTT.S191317.
228. Shi, Y.; Tan, S.-H.; Ng, S.; Zhou, J.; Yang, N.-D.; Koo, G.-B.; McMahon, K.-A.; Parton, R.G.; Hill, M.M.; Pozo, M.A. del; et al. Critical Role of CAV1/Caveolin-1 in Cell Stress Responses in Human Breast Cancer Cells via Modulation of Lysosomal Function and Autophagy. *Autophagy* **2015**, *11*, 769–784, doi:10.1080/15548627.2015.1034411.
229. Plaks, V.; Koopman, C.D.; Werb, Z. Circulating Tumor Cells. *Science* **2013**, *341*, 1186–1188, doi:10.1126/science.1235226.
230. Beloribi-Djefaflia, S.; Vasseur, S.; Guillaumond, F. Lipid Metabolic Reprogramming in Cancer Cells. *Oncogenesis* **2016**, *5*, e189–e189, doi:10.1038/oncsis.2015.49.
231. Gupta, V.K.; Banerjee, S. Isolation of Lipid Raft Proteins from CD133+ Cancer Stem Cells. *Methods Mol. Biol.* **2017**, *1609*, 25–31, doi:10.1007/978-1-4939-6996-8_3.
232. Schworer, S.A.; Smirnova, I.I.; Kurbatova, I.; Bagina, U.; Churova, M.; Fowler, T.; Roy, A.L.; Degterev, A.; Poltorak, A. Toll-like Receptor-Mediated Down-Regulation of the Deubiquitinase Cylindromatosis (CYLD) Protects Macrophages from Necroptosis in Wild-Derived Mice. *J. Biol. Chem.* **2014**, *289*, 14422–14433, doi:10.1074/jbc.M114.547547.

233. He, S.; Liang, Y.; Shao, F.; Wang, X. Toll-like Receptors Activate Programmed Necrosis in Macrophages through a Receptor-Interacting Kinase-3–Mediated Pathway. *PNAS* **2011**, *108*, 20054–20059, doi:10.1073/pnas.1116302108.
234. Yang, D.; Liang, Y.; Zhao, S.; Ding, Y.; Zhuang, Q.; Shi, Q.; Ai, T.; Wu, S.-Q.; Han, J. ZBP1 Mediates Interferon-Induced Necroptosis. *Cellular & Molecular Immunology* **2020**, *17*, 356–368, doi:10.1038/s41423-019-0237-x.
235. Gu, L.; Saha, S.T.; Thomas, J.; Kaur, M. Targeting Cellular Cholesterol for Anticancer Therapy. *The FEBS Journal* **2019**, *286*, 4192–4208, doi:10.1111/febs.15018.
236. Lee, S.Y.; Ko, S.-H.; Shim, J.-S.; Kim, D.-D.; Cho, H.-J. Tumor Targeting and Lipid Rafts Disrupting Hyaluronic Acid-Cyclodextrin-Based Nanoassembled Structure for Cancer Therapy. *ACS Appl Mater Interfaces* **2018**, *10*, 36628–36640, doi:10.1021/acsami.8b08243.
237. Siegel, R.L.; Miller, K.D.; Jemal, A. Cancer Statistics, 2019. *CA: A Cancer Journal for Clinicians* **2019**, *69*, 7–34, doi:10.3322/caac.21551.
238. Survival Rates for Colorectal Cancer Available online: https://www.cancer.org/cancer/colon-rectal-cancer/detection-diagnosis-staging/survival-rates.html (accessed on 3 April 2020).
239. Mehlen, P.; Puisieux, A. Metastasis: A Question of Life or Death. *Nat Rev Cancer* **2006**, *6*, 449–458, doi:10.1038/nrc1886.
240. Werner, J.; Heinemann, V. Standards and Challenges of Care for Colorectal Cancer Today. *Visc Med* **2016**, *32*, 156–157, doi:10.1159/000447070.
241. Martinez-Balibrea, E.; Martínez-Cardús, A.; Ginés, A.; Porras, V.R. de; Moutinho, C.; Layos, L.; Manzano, J.L.; Bugés, C.; Bystrup, S.; Esteller, M.; et al. Tumor-Related Molecular Mechanisms of Oxaliplatin Resistance. *Mol Cancer Ther* **2015**, *14*, 1767–1776, doi:10.1158/1535-7163.MCT-14-0636.
242. Van der Jeught, K.; Xu, H.-C.; Li, Y.-J.; Lu, X.-B.; Ji, G. Drug Resistance and New Therapies in Colorectal Cancer. *World J Gastroenterol* **2018**, *24*, 3834–3848, doi:10.3748/wjg.v24.i34.3834.
243. Combès, E.; Andrade, A.F.; Tosi, D.; Michaud, H.-A.; Coquel, F.; Garambois, V.; Desigaud, D.; Jarlier, M.; Coquelle, A.; Pasero, P.; et al. Inhibition of Ataxia-Telangiectasia Mutated and RAD3-Related (ATR) Overcomes Oxaliplatin Resistance and Promotes Antitumor Immunity in Colorectal Cancer. *Cancer Res.* **2019**, *79*, 2933–2946, doi:10.1158/0008-5472.CAN-18-2807.
244. Ruiz de Porras, V.; Bystrup, S.; Martínez-Cardús, A.; Pluvinet, R.; Sumoy, L.; Howells, L.; James, M.I.; Iwuji, C.; Manzano, J.L.; Layos, L.; et al. Curcumin Mediates Oxaliplatin-Acquired Resistance Reversion in Colorectal Cancer Cell Lines through Modulation of CXC-Chemokine/NF-KB Signalling Pathway. *Sci Rep* **2016**, *6*, doi:10.1038/srep24675.
245. Cuello, M.; Ettenberg, S.A.; Nau, M.M.; Lipkowitz, S. Synergistic Induction of Apoptosis by the Combination of Trail and Chemotherapy in Chemoresistant Ovarian Cancer Cells. *Gynecol. Oncol.* **2001**, *81*, 380–390, doi:10.1006/gyno.2001.6194.
246. von Karstedt, S.; Montinaro, A.; Walczak, H. Exploring the TRAILs Less Travelled: TRAIL in Cancer Biology and Therapy. *Nature Reviews Cancer* **2017**, *17*, 352–366, doi:10.1038/nrc.2017.28.
247. Marconi, M.; Ascione, B.; Ciarlo, L.; Vona, R.; Garofalo, T.; Sorice, M.; Gianni, A.M.; Locatelli, S.L.; Carlo-Stella, C.; Malorni, W.; et al. Constitutive Localization of DR4 in Lipid Rafts Is Mandatory for TRAIL-Induced Apoptosis in B-Cell Hematologic Malignancies. *Cell Death & Disease* **2013**, *4*, e863–e863, doi:10.1038/cddis.2013.389.
248. Mollinedo, F.; Gajate, C. Lipid Rafts as Signaling Hubs in Cancer Cell Survival/Death and Invasion: Implications in Tumor Progression and Therapy. *J. Lipid Res.* **2020**, jlr.TR119000439, doi:10.1194/jlr.TR119000439.

249. George, K.S.; Wu, S. Lipid Raft: A Floating Island Of Death or Survival. *Toxicol Appl Pharmacol* **2012**, *259*, 311–319, doi:10.1016/j.taap.2012.01.007.
250. Naval, J.; de Miguel, D.; Gallego-Lleyda, A.; Anel, A.; Martinez-Lostao, L. Importance of TRAIL Molecular Anatomy in Receptor Oligomerization and Signaling. Implications for Cancer Therapy. *Cancers (Basel)* **2019**, *11*, doi:10.3390/cancers11040444.
251. Nagane, M.; Pan, G.; Weddle, J.J.; Dixit, V.M.; Cavenee, W.K.; Huang, H.J. Increased Death Receptor 5 Expression by Chemotherapeutic Agents in Human Gliomas Causes Synergistic Cytotoxicity with Tumor Necrosis Factor-Related Apoptosis-Inducing Ligand in Vitro and in Vivo. *Cancer Res.* **2000**, *60*, 847–853.
252. Gibson, S.B.; Oyer, R.; Spalding, A.C.; Anderson, S.M.; Johnson, G.L. Increased Expression of Death Receptors 4 and 5 Synergizes the Apoptosis Response to Combined Treatment with Etoposide and TRAIL. *Mol Cell Biol* **2000**, *20*, 205–212.
253. Baritaki, S.; Huerta-Yepez, S.; Sakai, T.; Spandidos, D.A.; Bonavida, B. Chemotherapeutic Drugs Sensitize Cancer Cells to TRAIL-Mediated Apoptosis: Up-Regulation of DR5 and Inhibition of Yin Yang 1. *Mol Cancer Ther* **2007**, *6*, 1387–1399, doi:10.1158/1535-7163.MCT-06-0521.
254. Xu, L.; Qu, X.; Zhang, Y.; Hu, X.; Yang, X.; Hou, K.; Teng, Y.; Zhang, J.; Sada, K.; Liu, Y. Oxaliplatin Enhances TRAIL-Induced Apoptosis in Gastric Cancer Cells by CBL-Regulated Death Receptor Redistribution in Lipid Rafts. *FEBS Lett.* **2009**, *583*, 943–948, doi:10.1016/j.febslet.2009.02.014.
255. Dallas, N.A.; Xia, L.; Fan, F.; Gray, M.J.; Gaur, P.; van Buren, G.; Samuel, S.; Kim, M.P.; Lim, S.J.; Ellis, L.M. Chemoresistant Colorectal Cancer Cells, the Cancer Stem Cell Phenotype and Increased Sensitivity to Insulin-like Growth Factor Receptor-1 Inhibition. *Cancer Res* **2009**, *69*, 1951–1957, doi:10.1158/0008-5472.CAN-08-2023.
256. Yang, A.D.; Fan, F.; Camp, E.R.; Buren, G. van; Liu, W.; Somcio, R.; Gray, M.J.; Cheng, H.; Hoff, P.M.; Ellis, L.M. Chronic Oxaliplatin Resistance Induces Epithelial-to-Mesenchymal Transition in Colorectal Cancer Cell Lines. *Clin Cancer Res* **2006**, *12*, 4147–4153, doi:10.1158/1078-0432.CCR-06-0038.
257. Tanaka, S.; Hosokawa, M.; Yonezawa, T.; Hayashi, W.; Ueda, K.; Iwakawa, S. Induction of Epithelial-Mesenchymal Transition and down-Regulation of MiR-200c and MiR-141 in Oxaliplatin-Resistant Colorectal Cancer Cells. *Biol. Pharm. Bull.* **2015**, *38*, 435–440, doi:10.1248/bpb.b14-00695.
258. Hitomi, J.; Katayama, T.; Eguchi, Y.; Kudo, T.; Taniguchi, M.; Koyama, Y.; Manabe, T.; Yamagishi, S.; Bando, Y.; Imaizumi, K.; et al. Involvement of Caspase-4 in Endoplasmic Reticulum Stress-Induced Apoptosis and Abeta-Induced Cell Death. *J. Cell Biol.* **2004**, *165*, 347–356, doi:10.1083/jcb.200310015.
259. Ozören, N.; El-Deiry, W.S. Cell Surface Death Receptor Signaling in Normal and Cancer Cells. *Semin. Cancer Biol.* **2003**, *13*, 135–147, doi:10.1016/s1044-579x(02)00131-1.
260. Sandra, F.; Hendarmin, L.; Nakamura, S. Osteoprotegerin (OPG) Binds with Tumor Necrosis Factor-Related Apoptosis-Inducing Ligand (TRAIL): Suppression of TRAIL-Induced Apoptosis in Ameloblastomas. *Oral Oncol.* **2006**, *42*, 415–420, doi:10.1016/j.oraloncology.2005.09.009.
261. Si, W.; Shen, J.; Zheng, H.; Fan, W. The Role and Mechanisms of Action of MicroRNAs in Cancer Drug Resistance. *Clinical Epigenetics* **2019**, *11*, 25, doi:10.1186/s13148-018-0587-8.
262. Just, C.; Knief, J.; Lazar-Karsten, P.; Petrova, E.; Hummel, R.; Röcken, C.; Wellner, U.; Thorns, C. MicroRNAs as Potential Biomarkers for Chemoresistance in Adenocarcinomas of the Esophagogastric Junction Available online: https://www.hindawi.com/journals/jo/2019/4903152/ (accessed on 17 April 2020).
263. Suprynowicz, F.A.; Disbrow, G.L.; Krawczyk, E.; Simic, V.; Lantzky, K.; Schlegel, R. HPV-16 E5 Oncoprotein Upregulates Lipid Raft Components Caveolin-1 and Ganglioside GM1

at the Plasma Membrane of Cervical Cells. *Oncogene* **2008**, *27*, 1071–1078, doi:10.1038/sj.onc.1210725.

264. Xiao, W.; Ishdorj, G.; Sun, J.; Johnston, J.B.; Gibson, S.B. Death Receptor 4 Is Preferentially Recruited to Lipid Rafts in Chronic Lymphocytic Leukemia Cells Contributing to Tumor Necrosis Related Apoptosis Inducing Ligand-Induced Synergistic Apoptotic Responses. *Leukemia & Lymphoma* **2011**, *52*, 1290–1301, doi:10.3109/10428194.2011.567317.
265. Ujlaky-Nagy, L.; Nagy, P.; Szöllősi, J.; Vereb, G. Flow Cytometric FRET Analysis of Protein Interactions. *Methods Mol Biol* **2018**, *1678*, 393–419, doi:10.1007/978-1-4939-7346-0_17.
266. Neves, A.R.; Nunes, C.; Reis, S. Resveratrol Induces Ordered Domains Formation in Biomembranes: Implication for Its Pleiotropic Action. *Biochimica et Biophysica Acta (BBA) - Biomembranes* **2016**, *1858*, 12–18, doi:10.1016/j.bbamem.2015.10.005.
267. Rossin, A.; Derouet, M.; Abdel-Sater, F.; Hueber, A.-O. Palmitoylation of the TRAIL Receptor DR4 Confers an Efficient TRAIL-Induced Cell Death Signalling. *Biochem. J.* **2009**, *419*, 185–192, 2 p following 192, doi:10.1042/BJ20081212.
268. Draper, J.M.; Smith, C.D. Palmitoyl Acyltransferase Assays and Inhibitors (Review). *Mol Membr Biol* **2009**, *26*, 5–13, doi:10.1080/09687680802683839.
269. Ortiz-Otero, N.; Marshall, J.R.; Lash, B.; King, M.R. Chemotherapy-Induced Release of Circulating-Tumor Cells into the Bloodstream in Collective Migration Units with Cancer-Associated Fibroblasts in Metastatic Cancer Patients. *BMC Cancer* **2020**, *20*, 873, doi:10.1186/s12885-020-07376-1.
270. Mitchell, M.J.; Wayne, E.; Rana, K.; Schaffer, C.B.; King, M.R. TRAIL-Coated Leukocytes That Kill Cancer Cells in the Circulation. *PNAS* **2014**, *111*, 930–935, doi:10.1073/pnas.1316312111.
271. Jyotsana, N.; Zhang, Z.; Himmel, L.E.; Yu, F.; King, M.R. Minimal Dosing of Leukocyte Targeting TRAIL Decreases Triple-Negative Breast Cancer Metastasis Following Tumor Resection. *Science Advances* **2019**, *5*, eaaw4197, doi:10.1126/sciadv.aaw4197.
272. Mitchell, M.J.; King, M.R. Fluid Shear Stress Sensitizes Cancer Cells to Receptor-Mediated Apoptosis via Trimeric Death Receptors. *New J. Phys.* **2013**, *15*, 015008, doi:10.1088/1367-2630/15/1/015008.
273. Mühlethaler-Mottet, A.; Flahaut, M.; Bourloud, K.B.; Nardou, K.; Coulon, A.; Liberman, J.; Thome, M.; Gross, N. Individual Caspase-10 Isoforms Play Distinct and Opposing Roles in the Initiation of Death Receptor-Mediated Tumour Cell Apoptosis. *Cell Death & Disease* **2011**, *2*, e125–e125, doi:10.1038/cddis.2011.8.
274. Sprick, M.R.; Rieser, E.; Stahl, H.; Grosse-Wilde, A.; Weigand, M.A.; Walczak, H. Caspase-10 Is Recruited to and Activated at the Native TRAIL and CD95 Death-Inducing Signalling Complexes in a FADD-Dependent Manner but Can Not Functionally Substitute Caspase-8. *EMBO J* **2002**, *21*, 4520–4530, doi:10.1093/emboj/cdf441.
275. Horn, S.; Hughes, M.A.; Schilling, R.; Sticht, C.; Tenev, T.; Ploesser, M.; Meier, P.; Sprick, M.R.; MacFarlane, M.; Leverkus, M. Caspase-10 Negatively Regulates Caspase-8-Mediated Cell Death, Switching the Response to CD95L in Favor of NF-KB Activation and Cell Survival. *Cell Rep* **2017**, *19*, 785–797, doi:10.1016/j.celrep.2017.04.010.
276. Gasiulė, S.; Dreize, N.; Kaupinis, A.; Ražanskas, R.; Čiupas, L.; Stankevičius, V.; Kapustina, Ž.; Laurinavičius, A.; Valius, M.; Vilkaitis, G. Molecular Insights into MiRNA-Driven Resistance to 5-Fluorouracil and Oxaliplatin Chemotherapy: MiR-23b Modulates the Epithelial–Mesenchymal Transition of Colorectal Cancer Cells. *J Clin Med* **2019**, *8*, doi:10.3390/jcm8122115.
277. Evert, J.; Pathak, S.; Sun, X.-F.; Zhang, H. A Study on Effect of Oxaliplatin in MicroRNA Expression in Human Colon Cancer. *J Cancer* **2018**, *9*, 2046–2053, doi:10.7150/jca.24474.
278. Delmas, D.; Rébé, C.; Micheau, O.; Athias, A.; Gambert, P.; Grazide, S.; Laurent, G.; Latruffe, N.; Solary, E. Redistribution of CD95, DR4 and DR5 in Rafts Accounts for the

Synergistic Toxicity of Resveratrol and Death Receptor Ligands in Colon Carcinoma Cells. *Oncogene* **2004**, *23*, 8979–8986, doi:10.1038/sj.onc.1208086.

279. Ouyang, W.; Yang, C.; Zhang, S.; Liu, Y.; Yang, B.; Zhang, J.; Zhou, F.; Zhou, Y.; Xie, C. Absence of Death Receptor Translocation into Lipid Rafts in Acquired TRAIL-Resistant NSCLC Cells. *International Journal of Oncology* **2013**, *42*, 699–711, doi:10.3892/ijo.2012.1748.
280. Song, J.H.; Tse, M.C.L.; Bellail, A.; Phuphanich, S.; Khuri, F.; Kneteman, N.M.; Hao, C. Lipid Rafts and Nonrafts Mediate Tumor Necrosis Factor–Related Apoptosis-Inducing Ligand–Induced Apoptotic and Nonapoptotic Signals in Non–Small Cell Lung Carcinoma Cells. *Cancer Res* **2007**, *67*, 6946–6955, doi:10.1158/0008-5472.CAN-06-3896.
281. Chakrabandhu, K.; Hérincs, Z.; Huault, S.; Dost, B.; Peng, L.; Conchonaud, F.; Marguet, D.; He, H.-T.; Hueber, A.-O. Palmitoylation Is Required for Efficient Fas Cell Death Signaling. *EMBO J* **2007**, *26*, 209–220, doi:10.1038/sj.emboj.7601456.
282. Zhang, X.-L.; Ding, H.-H.; Xu, T.; Liu, M.; Ma, C.; Wu, S.-L.; Wei, J.-Y.; Liu, C.-C.; Zhang, S.-B.; Xin, W.-J. Palmitoylation of δ-Catenin Promotes Kinesin-Mediated Membrane Trafficking of Nav1.6 in Sensory Neurons to Promote Neuropathic Pain. *Sci. Signal.* **2018**, *11*, doi:10.1126/scisignal.aar4394.
283. Tseng, W.; Leong, X.; Engleman, E. Orthotopic Mouse Model of Colorectal Cancer. *J Vis Exp* **2007**, doi:10.3791/484.
284. Bolte, S.; Cordelières, F.P. A Guided Tour into Subcellular Colocalization Analysis in Light Microscopy. *J Microsc* **2006**, *224*, 213–232, doi:10.1111/j.1365-2818.2006.01706.x.
285. Greenlee, J.D.; Liu, K.; Lopez-Cavestany, M.; King, M.R. Piezo1 Mechano-Activation Is Augmented by Resveratrol and Differs between Colorectal Cancer Cells of Primary and Metastatic Origin. *Molecules* **2022**, *27*, 5430, doi:10.3390/molecules27175430.
286. Siegel, R.L.; Miller, K.D.; Fuchs, H.E.; Jemal, A. Cancer Statistics, 2021. *CA: A Cancer Journal for Clinicians* **2021**, *71*, 7–33, doi:10.3322/caac.21654.
287. Greenlee, J.D.; King, M.R. Engineered Fluidic Systems to Understand Lymphatic Cancer Metastasis. *Biomicrofluidics* **2020**, *14*, 011502, doi:10.1063/1.5133970.
288. Swartz, M.A.; Lund, A.W. Lymphatic and Interstitial Flow in the Tumour Microenvironment: Linking Mechanobiology with Immunity. *Nature Reviews Cancer* **2012**, *12*, 210–219, doi:10.1038/nrc3186.
289. Mitchell, M.J.; King, M.R. Computational and Experimental Models of Cancer Cell Response to Fluid Shear Stress. *Front Oncol* **2013**, *3*, 44, doi:10.3389/fonc.2013.00044.
290. Huang, Q.; Hu, X.; He, W.; Zhao, Y.; Hao, S.; Wu, Q.; Li, S.; Zhang, S.; Shi, M. Fluid Shear Stress and Tumor Metastasis. *Am J Cancer Res* **2018**, *8*, 763–777.
291. Fidler, I.J. Metastasis: Quantitative Analysis of Distribution and Fate of Tumor Emboli Labeled with 125 I-5-Iodo-2’-Deoxyuridine. *J Natl Cancer Inst* **1970**, *45*, 773–782.
292. Tsai, W.-S.; Chen, J.-S.; Shao, H.-J.; Wu, J.-C.; Lai, J.-M.; Lu, S.-H.; Hung, T.-F.; Chiu, Y.-C.; You, J.-F.; Hsieh, P.-S.; et al. Circulating Tumor Cell Count Correlates with Colorectal Neoplasm Progression and Is a Prognostic Marker for Distant Metastasis in Non-Metastatic Patients. *Sci Rep* **2016**, *6*, 24517, doi:10.1038/srep24517.
293. Kapeleris, J.; Kulasinghe, A.; Warkiani, M.E.; Vela, I.; Kenny, L.; O’Byrne, K.; Punyadeera, C. The Prognostic Role of Circulating Tumor Cells (CTCs) in Lung Cancer. *Frontiers in Oncology* **2018**, *8*.
294. Hope, J.M.; Bersi, M.R.; Dombroski, J.A.; Clinch, A.B.; Pereles, R.S.; Merryman, W.D.; King, M.R. Circulating Prostate Cancer Cells Have Differential Resistance to Fluid Shear Stress-Induced Cell Death. *J Cell Sci* **2021**, doi:10.1242/jcs.251470.
295. Xin, Y.; Li, K.; Yang, M.; Tan, Y. Fluid Shear Stress Induces EMT of Circulating Tumor Cells via JNK Signaling in Favor of Their Survival during Hematogenous Dissemination. *Int J Mol Sci* **2020**, *21*, 8115, doi:10.3390/ijms21218115.

296. Choi, H.Y.; Yang, G.-M.; Dayem, A.A.; Saha, S.K.; Kim, K.; Yoo, Y.; Hong, K.; Kim, J.-H.; Yee, C.; Lee, K.-M.; et al. Hydrodynamic Shear Stress Promotes Epithelial-Mesenchymal Transition by Downregulating ERK and GSK3β Activities. *Breast Cancer Research* **2019**, *21*, 6, doi:10.1186/s13058-018-1071-2.
297. Moose, D.L.; Krog, B.L.; Kim, T.-H.; Zhao, L.; Williams-Perez, S.; Burke, G.; Rhodes, L.; Vanneste, M.; Breheny, P.; Milhem, M.; et al. Cancer Cells Resist Mechanical Destruction in Circulation via RhoA/Actomyosin-Dependent Mechano-Adaptation. *Cell Reports* **2020**, *30*, 3864-3874.e6, doi:10.1016/j.celrep.2020.02.080.
298. Alvarado-Estrada, K.; Marenco-Hillembrand, L.; Maharjan, S.; Mainardi, V.L.; Zhang, Y.S.; Zarco, N.; Schiapparelli, P.; Guerrero-Cazares, H.; Sarabia-Estrada, R.; Quinones-Hinojosa, A.; et al. Circulatory Shear Stress Induces Molecular Changes and Side Population Enrichment in Primary Tumor-Derived Lung Cancer Cells with Higher Metastatic Potential. *Sci Rep* **2021**, *11*, doi:10.1038/s41598-021-82634-1.
299. Yoshimura, K.; Sokabe, M. Mechanosensitivity of Ion Channels Based on Protein–Lipid Interactions. *J R Soc Interface* **2010**, *7*, S307–S320, doi:10.1098/rsif.2010.0095.focus.
300. Cox, C.D.; Bavi, N.; Martinac, B. Biophysical Principles of Ion-Channel-Mediated Mechanosensory Transduction. *Cell Rep* **2019**, *29*, 1–12, doi:10.1016/j.celrep.2019.08.075.
301. Chubinskiy-Nadezhdin, V.I.; Negulyaev, Y.A.; Morachevskaya, E.A. Cholesterol Depletion-Induced Inhibition of Stretch-Activated Channels Is Mediated via Actin Rearrangement. *Biochem Biophys Res Commun* **2011**, *412*, 80–85, doi:10.1016/j.bbrc.2011.07.046.
302. Ridone, P.; Pandzic, E.; Vassalli, M.; Cox, C.D.; Macmillan, A.; Gottlieb, P.A.; Martinac, B. Disruption of Membrane Cholesterol Organization Impairs the Activity of PIEZO1 Channel Clusters. *J Gen Physiol* **2020**, *152*, e201912515, doi:10.1085/jgp.201912515.
303. Simons, K.; Ikonen, E. Functional Rafts in Cell Membranes. *Nature* **1997**, *387*, 569–572, doi:10.1038/42408.
304. Hewitt, R.E.; McMarlin, A.; Kleiner, D.; Wersto, R.; Martin, P.; Tsoskas, M.; Stamp, G.W.H.; Stetler-Stevenson, W.G. Validation of a Model of Colon Cancer Progression. *The Journal of Pathology* **2000**, *192*, 446–454, doi:10.1002/1096-9896(2000)9999:9999<::AID-PATH775>3.0.CO;2-K.
305. Krog, B.L.; Henry, M.D. Biomechanics of the Circulating Tumor Cell Microenvironment. *Adv Exp Med Biol* **2018**, *1092*, 209–233, doi:10.1007/978-3-319-95294-9_11.
306. Meng, S.; Tripathy, D.; Frenkel, E.P.; Shete, S.; Naftalis, E.Z.; Huth, J.F.; Beitsch, P.D.; Leitch, M.; Hoover, S.; Euhus, D.; et al. Circulating Tumor Cells in Patients with Breast Cancer Dormancy. *Clinical Cancer Research* **2004**, *10*, 8152–8162, doi:10.1158/1078-0432.CCR-04-1110.
307. Ren, F.; Sheng, W.-Q.; Du, X. CD133: A Cancer Stem Cells Marker, Is Used in Colorectal Cancers. *World J Gastroenterol* **2013**, *19*, 2603–2611, doi:10.3748/wjg.v19.i17.2603.
308. Milardi, G.L.; Stringaro, A.; Colone, M.; Bonincontro, A.; Risuleo, G. The Cell Membrane Is the Main Target of Resveratrol as Shown by Interdisciplinary Biomolecular/Cellular and Biophysical Approaches. *J Membr Biol* **2014**, *247*, 1–8, doi:10.1007/s00232-013-9604-1.
309. Cheng, X.; Zhang, X.; Yu, L.; Xu, H. Calcium Signaling in Membrane Repair. *Semin Cell Dev Biol* **2015**, *45*, 24–31, doi:10.1016/j.semcdb.2015.10.031.
310. Idone, V.; Tam, C.; Goss, J.W.; Toomre, D.; Pypaert, M.; Andrews, N.W. Repair of Injured Plasma Membrane by Rapid Ca2+-Dependent Endocytosis. *J Cell Biol* **2008**, *180*, 905–914, doi:10.1083/jcb.200708010.
311. Reddy, A.; Caler, E.V.; Andrews, N.W. Plasma Membrane Repair Is Mediated by Ca2+-Regulated Exocytosis of Lysosomes. *Cell* **2001**, *106*, 157–169, doi:10.1016/S0092-8674(01)00421-4.
312. McNeil, P. Membrane Repair Redux: Redox of MG53. *Nat Cell Biol* **2009**, *11*, 7–9, doi:10.1038/ncb0109-7.

313. Xu, T.; Naraghi, M.; Kang, H.; Neher, E. Kinetic Studies of Ca2+ Binding and Ca2+ Clearance in the Cytosol of Adrenal Chromaffin Cells. *Biophys J* **1997**, *73*, 532–545.
314. Naraghi, M.; Neher, E. Linearized Buffered Ca2+ Diffusion in Microdomains and Its Implications for Calculation of [Ca2+] at the Mouth of a Calcium Channel. *J Neurosci* **1997**, *17*, 6961–6973, doi:10.1523/JNEUROSCI.17-18-06961.1997.
315. Syeda, R.; Xu, J.; Dubin, A.E.; Coste, B.; Mathur, J.; Huynh, T.; Matzen, J.; Lao, J.; Tully, D.C.; Engels, I.H.; et al. Chemical Activation of the Mechanotransduction Channel Piezo1. *eLife* **2015**, *4*, e07369, doi:10.7554/eLife.07369.
316. Nusinow, D.P.; Szpyt, J.; Ghandi, M.; Rose, C.M.; McDonald, E.R.; Kalocsay, M.; Jané-Valbuena, J.; Gelfand, E.; Schweppe, D.K.; Jedrychowski, M.; et al. Quantitative Proteomics of the Cancer Cell Line Encyclopedia. *Cell* **2020**, *180*, 387-402.e16, doi:10.1016/j.cell.2019.12.023.
317. Bagur, R.; Hajnóczky, G. Intracellular Ca2+ Sensing: Role in Calcium Homeostasis and Signaling. *Mol Cell* **2017**, *66*, 780–788, doi:10.1016/j.molcel.2017.05.028.
318. Barnes, J.M.; Nauseef, J.T.; Henry, M.D. Resistance to Fluid Shear Stress Is a Conserved Biophysical Property of Malignant Cells. *PLOS ONE* **2012**, *7*, e50973, doi:10.1371/journal.pone.0050973.
319. Mitchell, M.J.; Denais, C.; Chan, M.F.; Wang, Z.; Lammerding, J.; King, M.R. Lamin A/C Deficiency Reduces Circulating Tumor Cell Resistance to Fluid Shear Stress. *American Journal of Physiology-Cell Physiology* **2015**, *309*, C736–C746, doi:10.1152/ajpcell.00050.2015.
320. Palmieri, V.; Lucchetti, D.; Maiorana, A.; Papi, M.; Maulucci, G.; Calapà, F.; Ciasca, G.; Giordano, R.; Sgambato, A.; Spirito, M.D. Mechanical and Structural Comparison between Primary Tumor and Lymph Node Metastasis Cells in Colorectal Cancer. *Soft Matter* **2015**, *11*, 5719–5726, doi:10.1039/C5SM01089F.
321. Miller, H.; Castro-Gomes, T.; Corrotte, M.; Tam, C.; Maugel, T.K.; Andrews, N.W.; Song, W. Lipid Raft–Dependent Plasma Membrane Repair Interferes with the Activation of B Lymphocytes. *J Cell Biol* **2015**, *211*, 1193–1205, doi:10.1083/jcb.201505030.
322. Fan, R.; Emery, T.; Zhang, Y.; Xia, Y.; Sun, J.; Wan, J. Circulatory Shear Flow Alters the Viability and Proliferation of Circulating Colon Cancer Cells. *Sci Rep* **2016**, *6*, 27073, doi:10.1038/srep27073.
323. Wang, J.; Wang, H.; Li, Z.; Wu, Q.; Lathia, J.D.; McLendon, R.E.; Hjelmeland, A.B.; Rich, J.N. C-Myc Is Required for Maintenance of Glioma Cancer Stem Cells. *PLOS ONE* **2008**, *3*, e3769, doi:10.1371/journal.pone.0003769.
324. Ayob, A.Z.; Ramasamy, T.S. Cancer Stem Cells as Key Drivers of Tumour Progression. *Journal of Biomedical Science* **2018**, *25*, 20, doi:10.1186/s12929-018-0426-4.
325. Chakraborty, S.; Doktorova, M.; Molugu, T.R.; Heberle, F.A.; Scott, H.L.; Dzikovski, B.; Nagao, M.; Stingaciu, L.-R.; Standaert, R.F.; Barrera, F.N.; et al. How Cholesterol Stiffens Unsaturated Lipid Membranes. *Proceedings of the National Academy of Sciences* **2020**, *117*, 21896–21905, doi:10.1073/pnas.2004807117.
326. Alharbi, A.; Zhang, Y.; Parrington, J. Deciphering the Role of Ca2+ Signalling in Cancer Metastasis: From the Bench to the Bedside. *Cancers (Basel)* **2021**, *13*, 179, doi:10.3390/cancers13020179.
327. Albeck, J.G.; Burke, J.M.; Spencer, S.L.; Lauffenburger, D.A.; Sorger, P.K. Modeling a Snap-Action, Variable-Delay Switch Controlling Extrinsic Cell Death. *PLOS Biology* **2008**, *6*, e299, doi:10.1371/journal.pbio.0060299.
328. Hong, J.-Y.; Kim, G.-H.; Kim, J.-W.; Kwon, S.-S.; Sato, E.F.; Cho, K.-H.; Shim, E.B. Computational Modeling of Apoptotic Signaling Pathways Induced by Cisplatin. *BMC Systems Biology* **2012**, *6*, 122, doi:10.1186/1752-0509-6-122.

329. Greenlee, J.D.; King, M.R. A Syngeneic MC38 Orthotopic Mouse Model of Colorectal Cancer Metastasis. *Biology Methods and Protocols* **2022**, *7*, bpac024, doi:10.1093/biomethods/bpac024.
330. Teicher, B.A. Tumor Models for Efficacy Determination. *Mol. Cancer Ther.* **2006**, *5*, 2435–2443, doi:10.1158/1535-7163.MCT-06-0391.
331. Hoffman, R.M. Orthotopic Metastatic Mouse Models for Anticancer Drug Discovery and Evaluation: A Bridge to the Clinic. *Invest New Drugs* **1999**, *17*, 343–360, doi:10.1023/A:1006326203858.
332. Zhao, X.; Li, L.; Starr, T.K.; Subramanian, S. Tumor Location Impacts Immune Response in Mouse Models of Colon Cancer. *Oncotarget* **2017**, *8*, 54775–54787, doi:10.18632/oncotarget.18423.
333. Wilmanns, C.; Fan, D.; O'Brian, C.A.; Bucana, C.D.; Fidler, I.J. Orthotopic and Ectopic Organ Environments Differentially Influence the Sensitivity of Murine Colon Carcinoma Cells to Doxorubicin and 5-Fluorouracil. *Int. J. Cancer* **1992**, *52*, 98–104, doi:10.1002/ijc.2910520118.
334. Oliveira, R.C.; Abrantes, A.M.; Tralhão, J.G.; Botelho, M.F. The Role of Mouse Models in Colorectal Cancer Research—The Need and the Importance of the Orthotopic Models. *Animal Models and Experimental Medicine* **2020**, *3*, 1–8, doi:10.1002/ame2.12102.
335. Xu, H.; Zhang, Y.; Peña, M.M.; Pirisi, L.; Creek, K.E. Six1 Promotes Colorectal Cancer Growth and Metastasis by Stimulating Angiogenesis and Recruiting Tumor-Associated Macrophages. *Carcinogenesis* **2017**, *38*, 281–292, doi:10.1093/carcin/bgw121.
336. Bürtin, F.; Mullins, C.S.; Linnebacher, M. Mouse Models of Colorectal Cancer: Past, Present and Future Perspectives. *World Journal of Gastroenterology* **2020**, *26*, 1394–1426, doi:10.3748/wjg.v26.i13.1394.
337. Trimaglio, G.; Tilkin-Mariamé, A.-F.; Feliu, V.; Lauzéral-Vizcaino, F.; Tosolini, M.; Valle, C.; Ayyoub, M.; Neyrolles, O.; Vergnolle, N.; Rombouts, Y.; et al. Colon-Specific Immune Microenvironment Regulates Cancer Progression versus Rejection. *OncoImmunology* **2020**, *9*, 1790125, doi:10.1080/2162402X.2020.1790125.
338. Céspedes, M.V.; Espina, C.; García-Cabezas, M.A.; Trias, M.; Boluda, A.; Gómez del Pulgar, M.T.; Sancho, F.J.; Nistal, M.; Lacal, J.C.; Mangues, R. Orthotopic Microinjection of Human Colon Cancer Cells in Nude Mice Induces Tumor Foci in All Clinically Relevant Metastatic Sites. *Am. J. Pathol.* **2007**, *170*, 1077–1085, doi:10.2353/ajpath.2007.060773.
339. Tian, H.; Lyu, Y.; Yang, Y.-G.; Hu, Z. Humanized Rodent Models for Cancer Research. *Front Oncol* **2020**, *10*, 1696, doi:10.3389/fonc.2020.01696.
340. Bettenworth, D.; Mücke, M.M.; Schwegmann, K.; Faust, A.; Poremba, C.; Schäfers, M.; Domagk, D.; Lenz, P. Endoscopy-Guided Orthotopic Implantation of Colorectal Cancer Cells Results in Metastatic Colorectal Cancer in Mice. *Clin Exp Metastasis* **2016**, *33*, 551–562, doi:10.1007/s10585-016-9797-7.
341. Zhong, W.; Myers, J.S.; Wang, F.; Wang, K.; Lucas, J.; Rosfjord, E.; Lucas, J.; Hooper, A.T.; Yang, S.; Lemon, L.A.; et al. Comparison of the Molecular and Cellular Phenotypes of Common Mouse Syngeneic Models with Human Tumors. *BMC Genomics* **2020**, *21*, 2, doi:10.1186/s12864-019-6344-3.
342. Chen, C.; Neumann, J.; Kühn, F.; Lee, S.M.L.; Drefs, M.; Andrassy, J.; Werner, J.; Bazhin, A.V.; Schiergens, T.S. Establishment of an Endoscopy-Guided Minimally Invasive Orthotopic Mouse Model of Colorectal Cancer. *Cancers (Basel)* **2020**, *12*, 3007, doi:10.3390/cancers12103007.
343. Terracina, K.P.; Aoyagi, T.; Huang, W.-C.; Nagahashi, M.; Yamada, A.; Aoki, K.; Takabe, K. Development of a Metastatic Murine Colon Cancer Model. *J Surg Res* **2015**, *199*, 106–114, doi:10.1016/j.jss.2015.04.030.
344. Hamada, K.; Kubota, Y.; Aoki, Y.; Sugisawa, N.; Yamamoto, J.; Tashiro, Y.; Bouvet, M.; Tsunoda, T.; Hoffman, R.M. Obesity Strongly Promotes Growth of Mouse MC38 Colon

Cancer in an Orthotopic-Syngeneic C57BL/6 Mouse Model. *In Vivo* **2022**, *36*, 1643–1646, doi:10.21873/invivo.12875.

345. Zigmond, E.; Halpern, Z.; Elinav, E.; Brazowski, E.; Jung, S.; Varol, C. Utilization of Murine Colonoscopy for Orthotopic Implantation of Colorectal Cancer. *PLoS One* **2011**, *6*, e28858, doi:10.1371/journal.pone.0028858.
346. Uccello, T.P.; Kintzel, S.A.; Mills, B.N.; Murphy, J.D.; Garrett-Larsen, J.; Battaglia, N.G.; Rodriguez, C.J.; Drage, M.G.; Ye, J.; Love, T.M.T.; et al. Development of an Orthotopic Murine Model of Rectal Cancer in Conjunction With Targeted Short-Course Radiation Therapy. *Advances in Radiation Oncology* **2022**, *7*, 100867, doi:10.1016/j.adro.2021.100867.
347. Kashtan, H.; Rabau, M.; Mullen, J.B.M.; Wong, A.H.C.; Roder, J.C.; Shpitz, B.; Stern, H.S.; Gallinger, S. Intra-Rectal Injection of Tumour Cells: A Novel Animal Model of Rectal Cancer. *Surgical Oncology* **1992**, *1*, 251–256, doi:10.1016/0960-7404(92)90072-S.
348. Kasashima, H.; Duran, A.; Cid-Diaz, T.; Muta, Y.; Kinoshita, H.; Batlle, E.; Diaz-Meco, M.T.; Moscat, J. Mouse Model of Colorectal Cancer: Orthotopic Co-Implantation of Tumor and Stroma Cells in Cecum and Rectum. *STAR Protocols* **2021**, *2*, 100297, doi:10.1016/j.xpro.2021.100297.
349. Taniura, T.; Iida, Y.; Kotani, H.; Ishitobi, K.; Tajima, Y.; Harada, M. Immunogenic Chemotherapy in Two Mouse Colon Cancer Models. *Cancer Science* **2020**, *111*, 3527–3539, doi:10.1111/cas.14624.
350. Taylor, M.A.; Hughes, A.M.; Walton, J.; Coenen-Stass, A.M.L.; Magiera, L.; Mooney, L.; Bell, S.; Staniszewska, A.D.; Sandin, L.C.; Barry, S.T.; et al. Longitudinal Immune Characterization of Syngeneic Tumor Models to Enable Model Selection for Immune Oncology Drug Discovery. *J Immunother Cancer* **2019**, *7*, 328, doi:10.1186/s40425-019-0794-7.
351. Evans, J.P.; Winiarski, B.K.; Sutton, P.A.; Ressel, L.; Duckworth, C.A.; Pritchard, D.M.; Palmer, D.H.; Goldring, C.E.; Kitteringham, N.R. Development of an Orthotopic Syngeneic Murine Model of Colorectal Cancer for Use in Translational Research. *Lab Anim* **2019**, *53*, 598–609, doi:10.1177/0023677219826165.
352. SMITH, J.J.; DEANE, N.G.; WU, F.; MERCHANT, N.B.; ZHANG, B.; JIANG, A.; LU, P.; JOHNSON, J.C.; SCHMIDT, C.; BAILEY, C.E.; et al. Experimentally Derived Metastasis Gene Expression Profile Predicts Recurrence and Death in Patients With Colon Cancer. *Gastroenterology* **2010**, *138*, 958–968, doi:10.1053/j.gastro.2009.11.005.
353. Abancens, M.; Bustos, V.; Harvey, H.; McBryan, J.; Harvey, B.J. Sexual Dimorphism in Colon Cancer. *Frontiers in Oncology* **2020**, *10*.
354. Reid, W.A. Cost Effectiveness of Routine Postmortem Histology. *Journal of Clinical Pathology* **1987**, *40*, 459–461, doi:10.1136/jcp.40.4.459.
355. Williams, J.O.; Goddard, M.J.; Gresham, G.A.; Wyatt, B.A. The Use of Histopathology in the Practice of Necropsy. *Journal of Clinical Pathology* **1997**, *50*, 695–698, doi:10.1136/jcp.50.8.695.
356. Wayne, E.C.; Chandrasekaran, S.; Mitchell, M.J.; Chan, M.F.; Lee, R.E.; Schaffer, C.B.; King, M.R. TRAIL-Coated Leukocytes That Prevent the Bloodborne Metastasis of Prostate Cancer. *J Control Release* **2016**, *223*, 215–223, doi:10.1016/j.jconrel.2015.12.048.
357. Tanaka, S.; Hosokawa, M.; Miyamoto, T.; Nakagawa, A.; Haruna, M.; Ueda, K.; Iwakawa, S.; Ogawara, K. MiR-33a-5p in Small Extracellular Vesicles as Non-Invasive Biomarker for Oxaliplatin Sensitivity in Human Colorectal Cancer Cells. *Biochem Biophys Rep* **2021**, *26*, 100996, doi:10.1016/j.bbrep.2021.100996.
358. Garofalo, M.; Condorelli, G.L.; Croce, C.M.; Condorelli, G. MicroRNAs as Regulators of Death Receptors Signaling. *Cell Death Differ* **2010**, *17*, 200–208, doi:10.1038/cdd.2009.105.

359. Berg, V.; Rusch, M.; Vartak, N.; Jüngst, C.; Schauss, A.; Waldmann, H.; Hedberg, C.; Pallasch, C.P.; Bastiaens, P.I.H.; Hallek, M.; et al. MiRs-138 and -424 Control Palmitoylation-Dependent CD95-Mediated Cell Death by Targeting Acyl Protein Thioesterases 1 and 2 in CLL. *Blood* **2015**, *125*, 2948–2957, doi:10.1182/blood-2014-07-586511.
360. Liguori, M.; Buracchi, C.; Pasqualini, F.; Bergomas, F.; Pesce, S.; Sironi, M.; Grizzi, F.; Mantovani, A.; Belgiovine, C.; Allavena, P. Functional TRAIL Receptors in Monocytes and Tumor-Associated Macrophages: A Possible Targeting Pathway in the Tumor Microenvironment. *Oncotarget* **2016**, *7*, 41662–41676, doi:10.18632/oncotarget.9340.
361. Hassan, A.A.; Artemenko, M.; Tang, M.K.S.; Wong, A.S.T. Selectins: An Important Family of Glycan-Binding Cell Adhesion Molecules in Ovarian Cancer. *Cancers (Basel)* **2020**, *12*, 2238, doi:10.3390/cancers12082238.
362. Gebauer, F.; Wicklein, D.; Stübke, K.; Nehmann, N.; Schmidt, A.; Salamon, J.; Peldschus, K.; Nentwich, M.F.; Adam, G.; Tolstonog, G.; et al. Selectin Binding Is Essential for Peritoneal Carcinomatosis in a Xenograft Model of Human Pancreatic Adenocarcinoma in Pfp−−/Rag2−− Mice. *Gut* **2013**, *62*, 741–750, doi:10.1136/gutjnl-2011-300629.
363. Hasbahceci, M.; Malya, F.; Kunduz, E.; Guler, M.; Unver, N.; Akcakaya, A. Use of Serum and Peritoneal CEA and CA19-9 in Prediction of Peritoneal Dissemination and Survival of Gastric Adenocarcinoma Patients: Are They Prognostic Factors? *Ann R Coll Surg Engl* **2018**, *100*, 257–266, doi:10.1308/rcsann.2018.0011.
364. Hyams, D.M.; Esteban, J.M.; Lollo, C.P.; Beatty, B.G.; Beatty, J.D. Therapy of Peritoneal Carcinomatosis of Human Colon Cancer Xenografts With Yttrium 90—Labeled Anti—Carcinoembryonic Antigen Antibody ZCE025. *Archives of Surgery* **1987**, *122*, 1333–1337, doi:10.1001/archsurg.1987.01400230121021.
365. Ortiz-Otero, N.; Clinch, A.B.; Hope, J.; Wang, W.; Reinhart-King, C.A.; King, M.R. Cancer Associated Fibroblasts Confer Shear Resistance to Circulating Tumor Cells during Prostate Cancer Metastatic Progression. *Oncotarget* **2020**, *11*, 1037–1050, doi:10.18632/oncotarget.27510.
366. Aceto, N.; Bardia, A.; Miyamoto, D.T.; Donaldson, M.C.; Wittner, B.S.; Spencer, J.A.; Yu, M.; Pely, A.; Engstrom, A.; Zhu, H.; et al. Circulating Tumor Cell Clusters Are Oligoclonal Precursors of Breast Cancer Metastasis. *Cell* **2014**, *158*, 1110–1122, doi:10.1016/j.cell.2014.07.013.
367. Amintas, S.; Bedel, A.; Moreau-Gaudry, F.; Boutin, J.; Buscail, L.; Merlio, J.-P.; Vendrely, V.; Dabernat, S.; Buscail, E. Circulating Tumor Cell Clusters: United We Stand Divided We Fall. *Int J Mol Sci* **2020**, *21*, 2653, doi:10.3390/ijms21072653.
368. Akbari, M.; Shanehbandi, D.; Asadi, M.; Shomali, N.; Faraji, A.; Khaze, V.; Pakdel, A.; Mokhtarzadeh, A.; Ebrahimi, A.A.; Shabani, A.; et al. Effects of CD133 Silencing on Survival and Migration of HT-29 Colorectal Cancer Cells. *Iran J Immunol* **2019**, *16*, 246–257, doi:10.22034/IJI.2019.80275.
369. Ayee, M.A.; Levitan, I. Paradoxical Impact of Cholesterol on Lipid Packing and Cell Stiffness. *Frontiers in Bioscience-Landmark* **2016**, *21*, 1245–1259, doi:10.2741/4454.
370. Biswas, A.; Kashyap, P.; Datta, S.; Sengupta, T.; Sinha, B. Cholesterol Depletion by MβCD Enhances Cell Membrane Tension and Its Variations-Reducing Integrity. *Biophys J* **2019**, *116*, 1456–1468, doi:10.1016/j.bpj.2019.03.016.
371. SERGIDES, C.; CHIRILĂ, M.; SILVESTRO, L.; PITTA, D.; PITTAS, A. Bioavailability and Safety Study of Resveratrol 500 Mg Tablets in Healthy Male and Female Volunteers. *Exp Ther Med* **2016**, *11*, 164–170, doi:10.3892/etm.2015.2895.
372. Isailović, B.D.; Kostić, I.T.; Zvonar, A.; Đorđević, V.B.; Gašperlin, M.; Nedović, V.A.; Bugarski, B.M. Resveratrol Loaded Liposomes Produced by Different Techniques. *Innovative Food Science & Emerging Technologies* **2013**, *19*, 181–189, doi:10.1016/j.ifset.2013.03.006.

373. Peñalva, R.; Morales, J.; González-Navarro, C.J.; Larrañeta, E.; Quincoces, G.; Peñuelas, I.; Irache, J.M. Increased Oral Bioavailability of Resveratrol by Its Encapsulation in Casein Nanoparticles. *Int J Mol Sci* **2018**, *19*, 2816, doi:10.3390/ijms19092816.
374. Zu, Y.; Overby, H.; Ren, G.; Fan, Z.; Zhao, L.; Wang, S. Resveratrol Liposomes and Lipid Nanocarriers: Comparison of Characteristics and Inducing Browning of White Adipocytes. *Colloids Surf B Biointerfaces* **2018**, *164*, 414–423, doi:10.1016/j.colsurfb.2017.12.044.
375. Zhang, Z.; Patel, S.B.; King, M.R. Micelle-in-Liposomes for Sustained Delivery of Anticancer Agents That Promote Potent TRAIL-Induced Cancer Cell Apoptosis. *Molecules* **2020**, *26*, 157, doi:10.3390/molecules26010157.
376. Tie, G.; Yan, J.; Khair, L.; Messina, J.A.; Deng, A.; Kang, J.; Fazzio, T.; Messina, L.M. Hypercholesterolemia Increases Colorectal Cancer Incidence by Reducing Production of NKT and Γδ T Cells from Hematopoietic Stem Cells. *Cancer Res* **2017**, *77*, 2351–2362, doi:10.1158/0008-5472.CAN-16-1916.
377. Notarnicola, M.; Altomare, D.F.; Correale, M.; Ruggieri, E.; D'Attoma, B.; Mastrosimini, A.; Guerra, V.; Caruso, M.G. Serum Lipid Profile in Colorectal Cancer Patients with and without Synchronous Distant Metastases. *Oncology* **2005**, *68*, 371–374, doi:10.1159/000086977.
378. Kannan, K.B.; Barlos, D.; Hauser, C.J. Free Cholesterol Alters Lipid Raft Structure and Function Regulating Neutrophil Ca2+ Entry and Respiratory Burst: Correlations with Calcium Channel Raft Trafficking. *J. Immunol.* **2007**, *178*, 5253–5261, doi:10.4049/jimmunol.178.8.5253.
379. Marwali, M.R.; Rey-Ladino, J.; Dreolini, L.; Shaw, D.; Takei, F. Membrane Cholesterol Regulates LFA-1 Function and Lipid Raft Heterogeneity. *Blood* **2003**, *102*, 215–222, doi:10.1182/blood-2002-10-3195.
380. Shen, Y.; Wang, C.; Ren, Y.; Ye, J. A Comprehensive Look at the Role of Hyperlipidemia in Promoting Colorectal Cancer Liver Metastasis. *J Cancer* **2018**, *9*, 2981–2986, doi:10.7150/jca.25640.
381. Rudd-Schmidt, J.A.; Hodel, A.W.; Noori, T.; Lopez, J.A.; Cho, H.-J.; Verschoor, S.; Ciccone, A.; Trapani, J.A.; Hoogenboom, B.W.; Voskoboinik, I. Lipid Order and Charge Protect Killer T Cells from Accidental Death. *Nat Commun* **2019**, *10*, 5396, doi:10.1038/s41467-019-13385-x.
382. Islam, Md.S.; Gaston, J.P.; Baker, M.A.B. Fluorescence Approaches for Characterizing Ion Channels in Synthetic Bilayers. *Membranes (Basel)* **2021**, *11*, 857, doi:10.3390/membranes11110857.
383. Jones, C.A.; Hazlehurst, L.A. Role of Calcium Homeostasis in Modulating EMT in Cancer. *Biomedicines* **2021**, *9*, 1200, doi:10.3390/biomedicines9091200.
384. Davis, F.M.; Azimi, I.; Faville, R.A.; Peters, A.A.; Jalink, K.; Putney, J.W.; Goodhill, G.J.; Thompson, E.W.; Roberts-Thomson, S.J.; Monteith, G.R. Induction of Epithelial-Mesenchymal Transition (EMT) in Breast Cancer Cells Is Calcium Signal Dependent. *Oncogene* **2014**, *33*, 2307–2316, doi:10.1038/onc.2013.187.
385. Zhong, W.; Myers, J.S.; Wang, F.; Wang, K.; Lucas, J.; Rosfjord, E.; Lucas, J.; Hooper, A.T.; Yang, S.; Lemon, L.A.; et al. Comparison of the Molecular and Cellular Phenotypes of Common Mouse Syngeneic Models with Human Tumors. *BMC Genomics* **2020**, *21*, 2, doi:10.1186/s12864-019-6344-3.
386. Efremova, M.; Rieder, D.; Klepsch, V.; Charoentong, P.; Finotello, F.; Hackl, H.; Hermann-Kleiter, N.; Löwer, M.; Baier, G.; Krogsdam, A.; et al. Targeting Immune Checkpoints Potentiates Immunoediting and Changes the Dynamics of Tumor Evolution. *Nat Commun* **2018**, *9*, 32, doi:10.1038/s41467-017-02424-0.
387. Wang, H.; Tian, T.; Zhang, J. Tumor-Associated Macrophages (TAMs) in Colorectal Cancer (CRC): From Mechanism to Therapy and Prognosis. *Int J Mol Sci* **2021**, *22*, 8470, doi:10.3390/ijms22168470.

388. Edin, S.; Wikberg, M.L.; Dahlin, A.M.; Rutegård, J.; Öberg, Å.; Oldenborg, P.-A.; Palmqvist, R. The Distribution of Macrophages with a M1 or M2 Phenotype in Relation to Prognosis and the Molecular Characteristics of Colorectal Cancer. *PLoS One* **2012**, *7*, e47045, doi:10.1371/journal.pone.0047045.
389. Boutilier, A.J.; Elsawa, S.F. Macrophage Polarization States in the Tumor Microenvironment. *Int J Mol Sci* **2021**, *22*, 6995, doi:10.3390/ijms22136995.
390. Elisia, I.; Pae, H.B.; Lam, V.; Cederberg, R.; Hofs, E.; Krystal, G. Comparison of RAW264.7, Human Whole Blood and PBMC Assays to Screen for Immunomodulators. *J Immunol Methods* **2018**, *452*, 26–31, doi:10.1016/j.jim.2017.10.004.
391. Li, H.; Huang, N.; Zhu, W.; Wu, J.; Yang, X.; Teng, W.; Tian, J.; Fang, Z.; Luo, Y.; Chen, M.; et al. Modulation the Crosstalk between Tumor-Associated Macrophages and Non-Small Cell Lung Cancer to Inhibit Tumor Migration and Invasion by Ginsenoside Rh2. *BMC Cancer* **2018**, *18*, 579, doi:10.1186/s12885-018-4299-4.
392. Kapałczyńska, M.; Kolenda, T.; Przybyła, W.; Zajączkowska, M.; Teresiak, A.; Filas, V.; Ibbs, M.; Bliźniak, R.; Łuczewski, Ł.; Lamperska, K. 2D and 3D Cell Cultures – a Comparison of Different Types of Cancer Cell Cultures. *Arch Med Sci* **2018**, *14*, 910–919, doi:10.5114/aoms.2016.63743.
393. Grayson, K.A.; Jyotsana, N.; Ortiz-Otero, N.; King, M.R. Overcoming TRAIL-Resistance by Sensitizing Prostate Cancer 3D Spheroids with Taxanes. *PLoS One* **2021**, *16*, e0246733, doi:10.1371/journal.pone.0246733.
394. Wajant, H.; Moosmayer, D.; Wüest, T.; Bartke, T.; Gerlach, E.; Schönherr, U.; Peters, N.; Scheurich, P.; Pfizenmaier, K. Differential Activation of TRAIL-R1 and -2 by Soluble and Membrane TRAIL Allows Selective Surface Antigen-Directed Activation of TRAIL-R2 by a Soluble TRAIL Derivative. *Oncogene* **2001**, *20*, 4101–4106, doi:10.1038/sj.onc.1204558.
395. Mühlenbeck, F.; Schneider, P.; Bodmer, J.-L.; Schwenzer, R.; Hauser, A.; Schubert, G.; Scheurich, P.; Moosmayer, D.; Tschopp, J.; Wajant, H. The Tumor Necrosis Factor-Related Apoptosis-Inducing Ligand Receptors TRAIL-R1 and TRAIL-R2 Have Distinct Cross-Linking Requirements for Initiation of Apoptosis and Are Non-Redundant in JNK Activation *. *Journal of Biological Chemistry* **2000**, *275*, 32208–32213, doi:10.1074/jbc.M000482200.
396. Ng, A.Y.; Tu, C.; Shen, S.; Xu, D.; Oursler, M.J.; Qu, J.; Yang, S. Comparative Characterization of Osteoclasts Derived From Murine Bone Marrow Macrophages and RAW 264.7 Cells Using Quantitative Proteomics. *JBMR Plus* **2018**, *2*, 328–340, doi:10.1002/jbm4.10058.
397. Chandrasekaran, S.; King, M.R. Microenvironment of Tumor-Draining Lymph Nodes: Opportunities for Liposome-Based Targeted Therapy. *Int J Mol Sci* **2014**, *15*, 20209–20239, doi:10.3390/ijms151120209.
398. Stock, A.-M.; Troost, G.; Niggemann, B.; Zänker, K.S.; Entschladen, F. Targets for Anti-Metastatic Drug Development. *Curr. Pharm. Des.* **2013**, *19*, 5127–5134.
399. Paul, S.; Lal, G. The Molecular Mechanism of Natural Killer Cells Function and Its Importance in Cancer Immunotherapy. *Front Immunol* **2017**, *8*, 1124, doi:10.3389/fimmu.2017.01124.
400. Hamilton, C.A.; Mahan, S.; Bell, C.R.; Villarreal-Ramos, B.; Charleston, B.; Entrican, G.; Hope, J.C. Frequency and Phenotype of Natural Killer Cells and Natural Killer Cell Subsets in Bovine Lymphoid Compartments and Blood. *Immunology* **2017**, *151*, 89–97, doi:10.1111/imm.12708.
401. Tartter, P.I.; Steinberg, B.; Barron, D.M.; Martinelli, G. The Prognostic Significance of Natural Killer Cytotoxicity in Patients With Colorectal Cancer. *Archives of Surgery* **1987**, *122*, 1264–1268, doi:10.1001/archsurg.1987.01400230050009.
402. Pasero, C.; Gravis, G.; Granjeaud, S.; Guerin, M.; Thomassin-Piana, J.; Rocchi, P.; Salem, N.; Walz, J.; Moretta, A.; Olive, D. Highly Effective NK Cells Are Associated with Good

Prognosis in Patients with Metastatic Prostate Cancer. *Oncotarget* **2015**, *6*, 14360–14373, doi:10.18632/oncotarget.3965.

403. Liljefors, M.; Nilsson, B.; Hjelm Skog, A.-L.; Ragnhammar, P.; Mellstedt, H.; Frödin, J.-E. Natural Killer (NK) Cell Function Is a Strong Prognostic Factor in Colorectal Carcinoma Patients Treated with the Monoclonal Antibody 17-1A. *Int J Cancer* **2003**, *105*, 717–723, doi:10.1002/ijc.11139.
404. Chandrasekaran, S.; Chan, M.F.; Li, J.; King, M.R. Super Natural Killer Cells That Target Metastases in the Tumor Draining Lymph Nodes. *Biomaterials* **2016**, *77*, 66–76, doi:10.1016/j.biomaterials.2015.11.001.
405. Freud, A.G.; Zhao, S.; Wei, S.; Gitana, G.M.; Molina-Kirsch, H.F.; Atwater, S.K.; Natkunam, Y. Expression of the Activating Receptor, NKp46 (CD335), in Human Natural Killer and T-Cell Neoplasia. *American Journal of Clinical Pathology* **2013**, *140*, 853–866, doi:10.1309/AJCPWGG69MCZOWMM.
406. Reichlin, A.; Yokoyama, W.M. Natural Killer Cell Proliferation Induced by Anti-NK1.1 and IL-2. *Immunol. Cell Biol.* **1998**, *76*, 143–152, doi:10.1046/j.1440-1711.1998.00726.x.
407. Zawieja, D.C. Contractile Physiology of Lymphatics. *Lymphat Res Biol* **2009**, *7*, 87–96, doi:10.1089/lrb.2009.0007.
408. Dixon, J.B.; Greiner, S.T.; Gashev, A.A.; Cote, G.L.; Moore, J.E.; Zawieja, D.C. Lymph Flow, Shear Stress, and Lymphocyte Velocity in Rat Mesenteric Prenodal Lymphatics. *Microcirculation* **2006**, *13*, 597–610, doi:10.1080/10739680600893909.
409. Shang, M.; Soon, R.H.; Lim, C.T.; Khoo, B.L.; Han, J. Microfluidic Modelling of the Tumor Microenvironment for Anti-Cancer Drug Development. *Lab Chip* **2019**, *19*, 369–386, doi:10.1039/C8LC00970H.
410. Boussommier-Calleja, A.; Li, R.; Chen, M.B.; Wong, S.C.; Kamm, R.D. Microfluidics: A New Tool for Modeling Cancer-Immune Interactions. *Trends Cancer* **2016**, *2*, 6–19, doi:10.1016/j.trecan.2015.12.003.
411. Ma, Y.-H.V.; Middleton, K.; You, L.; Sun, Y. A Review of Microfluidic Approaches for Investigating Cancer Extravasation during Metastasis. *Microsystems & Nanoengineering* **2018**, *4*, 17104, doi:10.1038/micronano.2017.104.
412. Hoarau-Véchot, J.; Rafii, A.; Touboul, C.; Pasquier, J. Halfway between 2D and Animal Models: Are 3D Cultures the Ideal Tool to Study Cancer-Microenvironment Interactions? *Int J Mol Sci* **2018**, *19*, doi:10.3390/ijms19010181.
413. Candini, O.; Grisendi, G.; Foppiani, E.M.; Brogli, M.; Aramini, B.; Masciale, V.; Spano, C.; Petrachi, T.; Veronesi, E.; Conte, P.; et al. A Novel 3D In Vitro Platform for Pre-Clinical Investigations in Drug Testing, Gene Therapy, and Immuno-Oncology. *Sci Rep* **2019**, *9*, 1–12, doi:10.1038/s41598-019-43613-9.
414. Mak, I.W.; Evaniew, N.; Ghert, M. Lost in Translation: Animal Models and Clinical Trials in Cancer Treatment. *Am J Transl Res* **2014**, *6*, 114–118.
415. Whitesides, G.M. The Origins and the Future of Microfluidics. *Nature* **2006**, *442*, 368–373, doi:10.1038/nature05058.
416. Sleeboom, J.J.F.; Eslami Amirabadi, H.; Nair, P.; Sahlgren, C.M.; den Toonder, J.M.J. Metastasis in Context: Modeling the Tumor Microenvironment with Cancer-on-a-Chip Approaches. *Dis Model Mech* **2018**, *11*, doi:10.1242/dmm.033100.
417. Gale, B.K.; Jafek, A.R.; Lambert, C.J.; Goenner, B.L.; Moghimifam, H.; Nze, U.C.; Kamarapu, S.K. A Review of Current Methods in Microfluidic Device Fabrication and Future Commercialization Prospects. *Inventions* **2018**, *3*, 60, doi:10.3390/inventions3030060.
418. Friend, J.; Yeo, L. Fabrication of Microfluidic Devices Using Polydimethylsiloxane. *Biomicrofluidics* **2010**, *4*, doi:10.1063/1.3259624.
419. Bonvin, C.; Overney, J.; Shieh, A.C.; Dixon, J.B.; Swartz, M.A. A Multichamber Fluidic Device for 3D Cultures under Interstitial Flow with Live Imaging: Development,

Characterization, and Applications. *Biotechnology and Bioengineering* **2010**, *105*, 982–991, doi:10.1002/bit.22608.

420. Wong, K.H.K.; Truslow, J.G.; Khankhel, A.H.; Chan, K.L.S.; Tien, J. Artificial Lymphatic Drainage Systems for Vascularized Microfluidic Scaffolds. *J Biomed Mater Res A* **2013**, *0*, 2181–2190, doi:10.1002/jbm.a.34524.
421. Price, G.M.; Tien, J. *Subtractive Methods for Forming Microfluidic Gels of Extracellular Matrix Proteins*;
422. Sato, M.; Sasaki, N.; Ato, M.; Hirakawa, S.; Sato, K.; Sato, K. Microcirculation-on-a-Chip: A Microfluidic Platform for Assaying Blood- and Lymphatic-Vessel Permeability. *PLoS One* **2015**, *10*, doi:10.1371/journal.pone.0137301.
423. Chueh, B.; Huh, D.; Kyrtsos, C.R.; Houssin, T.; Futai, N.; Takayama, S. Leakage-Free Bonding of Porous Membranes into Layered Microfluidic Array Systems. *Anal Chem* **2007**, *79*, 3504–3508, doi:10.1021/ac062118p.
424. Kim, S.; Chung, M.; Jeon, N.L. Three-Dimensional Biomimetic Model to Reconstitute Sprouting Lymphangiogenesis in Vitro. *Biomaterials* **2016**, *78*, 115–128, doi:10.1016/j.biomaterials.2015.11.019.
425. Chung, M.; Ahn, J.; Son, K.; Kim, S.; Jeon, N.L. Biomimetic Model of Tumor Microenvironment on Microfluidic Platform. *Advanced Healthcare Materials* **2017**, *6*, 1700196, doi:10.1002/adhm.201700196.
426. Shields, J.D.; Fleury, M.E.; Yong, C.; Tomei, A.A.; Randolph, G.J.; Swartz, M.A. Autologous Chemotaxis as a Mechanism of Tumor Cell Homing to Lymphatics via Interstitial Flow and Autocrine CCR7 Signaling. *Cancer Cell* **2007**, *11*, 526–538, doi:10.1016/j.ccr.2007.04.020.
427. Issa, A.; Le, T.X.; Shoushtari, A.N.; Shields, J.D.; Swartz, M.A. Vascular Endothelial Growth Factor-C and C-C Chemokine Receptor 7 in Tumor Cell–Lymphatic Cross-Talk Promote Invasive Phenotype. *Cancer Res* **2009**, *69*, 349–357, doi:10.1158/0008-5472.CAN-08-1875.
428. Polacheck, W.J.; Charest, J.L.; Kamm, R.D. Interstitial Flow Influences Direction of Tumor Cell Migration through Competing Mechanisms. *Proc Natl Acad Sci U S A* **2011**, *108*, 11115–11120, doi:10.1073/pnas.1103581108.
429. Vickerman, V.; Blundo, J.; Chung, S.; Kamm, R.D. Design, Fabrication and Implementation of a Novel Multi Parameter Control Microfluidic Platform for Three-Dimensional Cell Culture and Real-Time Imaging. *Lab Chip* **2008**, *8*, 1468–1477, doi:10.1039/b802395f.
430. Irimia, D.; Toner, M. Spontaneous Migration of Cancer Cells under Conditions of Mechanical Confinement. *Integr Biol (Camb)* **2009**, *1*, 506–512, doi:10.1039/b908595e.
431. Parlato, S.; Ninno, A.D.; Molfetta, R.; Toschi, E.; Salerno, D.; Mencattini, A.; Romagnoli, G.; Fragale, A.; Roccazzello, L.; Buoncervello, M.; et al. 3D Microfluidic Model for Evaluating Immunotherapy Efficacy by Tracking Dendritic Cell Behaviour toward Tumor Cells. *Scientific Reports* **2017**, *7*, 1093, doi:10.1038/s41598-017-01013-x.
432. Shim, S.; Belanger, M.C.; Harris, A.R.; Munson, J.M.; Pompano, R.R. Two-Way Communication between Ex Vivo Tissues on a Microfluidic Chip: Application to Tumor–Lymph Node Interaction. *Lab Chip* **2019**, *19*, 1013–1026, doi:10.1039/C8LC00957K.
433. Chaw, K.C.; Manimaran, M.; Tay, E.H.; Swaminathan, S. Multi-Step Microfluidic Device for Studying Cancer Metastasis. *Lab Chip* **2007**, *7*, 1041–1047, doi:10.1039/B707399M.
434. Sudo, R.; Chung, S.; Zervantonakis, I.K.; Vickerman, V.; Toshimitsu, Y.; Griffith, L.G.; Kamm, R.D. Transport-Mediated Angiogenesis in 3D Epithelial Coculture. *FASEB J.* **2009**, *23*, 2155–2164, doi:10.1096/fj.08-122820.
435. Zervantonakis, I.K.; Hughes-Alford, S.K.; Charest, J.L.; Condeelis, J.S.; Gertler, F.B.; Kamm, R.D. Three-Dimensional Microfluidic Model for Tumor Cell Intravasation and Endothelial Barrier Function. *PNAS* **2012**, *109*, 13515–13520, doi:10.1073/pnas.1210182109.

436. Wong, A.D.; Searson, P.C. Live-Cell Imaging of Invasion and Intravasation in an Artificial Microvessel Platform. *Cancer Res* **2014**, *74*, 4937–4945, doi:10.1158/0008-5472.CAN-14-1042.
437. Lee, H.; Park, W.; Ryu, H.; Jeon, N.L. A Microfluidic Platform for Quantitative Analysis of Cancer Angiogenesis and Intravasation. *Biomicrofluidics* **2014**, *8*, doi:10.1063/1.4894595.
438. Pisano, M.; Triacca, V.; Barbee, K.A.; Swartz, M.A. An in Vitro Model of the Tumor-Lymphatic Microenvironment with Simultaneous Transendothelial and Luminal Flows Reveals Mechanisms of Flow Enhanced Invasion. *Integr Biol (Camb)* **2015**, *7*, 525–533, doi:10.1039/c5ib00085h.
439. Karpinich, N.O.; Caron, K.M. Gap Junction Coupling Is Required for Tumor Cell Migration through Lymphatic Endothelium. *Arterioscler Thromb Vasc Biol* **2015**, *35*, 1147–1155, doi:10.1161/ATVBAHA.114.304752.
440. Xiong, Y.; Brinkman, C.C.; Famulski, K.S.; Mongodin, E.F.; Lord, C.J.; Hippen, K.L.; Blazar, B.R.; Bromberg, J.S. A Robust in Vitro Model for Trans-Lymphatic Endothelial Migration. *Sci Rep* **2017**, *7*, doi:10.1038/s41598-017-01575-w.
441. Kühlbach, C.; da Luz, S.; Baganz, F.; Hass, V.C.; Mueller, M.M. A Microfluidic System for the Investigation of Tumor Cell Extravasation. *Bioengineering (Basel)* **2018**, *5*, doi:10.3390/bioengineering5020040.
442. Yoo, P.S.; Mulkeen, A.L.; Dardik, A.; Cha, C.H. A Novel In Vitro Model of Lymphatic Metastasis from Colorectal Cancer. *Journal of Surgical Research* **2007**, *143*, 94–98, doi:10.1016/j.jss.2007.03.042.
443. Chen, Y.-C.; Allen, S.G.; Ingram, P.N.; Buckanovich, R.; Merajver, S.D.; Yoon, E. Single-Cell Migration Chip for Chemotaxis-Based Microfluidic Selection of Heterogeneous Cell Populations. *Scientific Reports* **2015**, *5*, 9980, doi:10.1038/srep09980.
444. Chandrasekaran, S.; McGuire, M.J.; King, M.R. Sweeping Lymph Node Micrometastases off Their Feet: An Engineered Model to Evaluate Natural Killer Cell Mediated Therapeutic Intervention of Circulating Tumor Cells That Disseminate to the Lymph Nodes. *Lab Chip* **2014**, *14*, 118–127, doi:10.1039/c3lc50584g.
445. Giang, U.-B.T.; Lee, D.; King, M.R.; DeLouise, L.A. Microfabrication of Cavities in Polydimethylsiloxane Using DRIE Silicon Molds. *Lab Chip* **2007**, *7*, 1660–1662, doi:10.1039/b714742b.
446. Hassell, B.A.; Goyal, G.; Lee, E.; Sontheimer-Phelps, A.; Levy, O.; Chen, C.S.; Ingber, D.E. Human Organ Chip Models Recapitulate Orthotopic Lung Cancer Growth, Therapeutic Responses, and Tumor Dormancy In Vitro. *Cell Rep* **2017**, *21*, 508–516, doi:10.1016/j.celrep.2017.09.043.
447. Bhatia, S.N.; Ingber, D.E. Microfluidic Organs-on-Chips. *Nature Biotechnology* **2014**, *32*, 760–772, doi:10.1038/nbt.2989.
448. Booth, R.; Kim, H. Characterization of a Microfluidic in Vitro Model of the Blood-Brain Barrier (MBBB). *Lab Chip* **2012**, *12*, 1784–1792, doi:10.1039/C2LC40094D.
449. Novik, E.; Maguire, T.J.; Chao, P.; Cheng, K.C.; Yarmush, M.L. A Microfluidic Hepatic Coculture Platform for Cell-Based Drug Metabolism Studies. *Biochemical Pharmacology* **2010**, *79*, 1036–1044, doi:10.1016/j.bcp.2009.11.010.
450. Esch, M.B.; Sung, J.H.; Yang, J.; Yu, C.; Yu, J.; March, J.C.; Shuler, M.L. On Chip Porous Polymer Membranes for Integration of Gastrointestinal Tract Epithelium with Microfluidic “body-on-a-Chip” Devices. *Biomed Microdevices* **2012**, *14*, 895–906, doi:10.1007/s10544-012-9669-0.
451. Jang, K.-J.; Mehr, A.P.; Hamilton, G.A.; McPartlin, L.A.; Chung, S.; Suh, K.-Y.; Ingber, D.E. Human Kidney Proximal Tubule-on-a-Chip for Drug Transport and Nephrotoxicity Assessment. *Integr Biol (Camb)* **2013**, *5*, 1119–1129, doi:10.1039/c3ib40049b.

452. P. Wikswo, J.; L. Curtis, E.; E. Eagleton, Z.; C. Evans, B.; Kole, A.; H. Hofmeister, L.; J. Matloff, W. Scaling and Systems Biology for Integrating Multiple Organs-on-a-Chip. *Lab on a Chip* **2013**, *13*, 3496–3511, doi:10.1039/C3LC50243K.
453. Kimura, H.; Sakai, Y.; Fujii, T. Organ/Body-on-a-Chip Based on Microfluidic Technology for Drug Discovery. *Drug Metabolism and Pharmacokinetics* **2018**, *33*, 43–48, doi:10.1016/j.dmpk.2017.11.003.
454. Zhang, W.; Lee, W.Y.; Siegel, D.S.; Tolias, P.; Zilberberg, J. Patient-Specific 3D Microfluidic Tissue Model for Multiple Myeloma. *Tissue Eng Part C Methods* **2014**, *20*, 663–670, doi:10.1089/ten.TEC.2013.0490.
455. Song, P.; Hu, R.; Tng, D.J.H.; Yong, K.-T. Moving towards Individualized Medicine with Microfluidics Technology. *RSC Adv.* **2014**, *4*, 11499–11511, doi:10.1039/C3RA45629C.
456. Jodat, Y.A.; Kang, M.G.; Kiaee, K.; Kim, G.J.; Martinez, A.F.H.; Rosenkranz, A.; Bae, H.; Shin, S.R. Human-Derived Organ-on-a-Chip for Personalized Drug Development. *Curr Pharm Des* **2018**, *24*, 5471–5486, doi:10.2174/1381612825666190308150055.
457. Williamson, A.; Singh, S.; Fernekorn, U.; Schober, A. The Future of the Patient-Specific Body-on-a-Chip. *Lab Chip* **2013**, *13*, 3471–3480, doi:10.1039/c3lc50237f.
458. Caballero, D.; Kaushik, S.; Correlo, V.M.; Oliveira, J.M.; Reis, R.L.; Kundu, S.C. Organ-on-Chip Models of Cancer Metastasis for Future Personalized Medicine: From Chip to the Patient. *Biomaterials* **2017**, *149*, 98–115, doi:10.1016/j.biomaterials.2017.10.005.
459. Sontheimer-Phelps, A.; Hassell, B.A.; Ingber, D.E. Modelling Cancer in Microfluidic Human Organs-on-Chips. *Nat Rev Cancer* **2019**, *19*, 65–81, doi:10.1038/s41568-018-0104-6.
460. Tsai, H.-F.; Trubelja, A.; Shen, A.Q.; Bao, G. Tumour-on-a-Chip: Microfluidic Models of Tumour Morphology, Growth and Microenvironment. *J R Soc Interface* **2017**, *14*, doi:10.1098/rsif.2017.0137.
461. Chen, Y.; Gao, D.; Wang, Y.; Lin, S.; Jiang, Y. A Novel 3D Breast-Cancer-on-Chip Platform for Therapeutic Evaluation of Drug Delivery Systems. *Analytica Chimica Acta* **2018**, *1036*, 97–106, doi:10.1016/j.aca.2018.06.038.
462. Valastyan, S.; Weinberg, R.A. Tumor Metastasis: Molecular Insights and Evolving Paradigms. *Cell* **2011**, *147*, 275–292, doi:10.1016/j.cell.2011.09.024.
463. Brabletz, T.; Kalluri, R.; Nieto, M.A.; Weinberg, R.A. EMT in Cancer. *Nat Rev Cancer* **2018**, *18*, 128–134, doi:10.1038/nrc.2017.118.
464. Farnsworth, R.H.; Achen, M.G.; Stacker, S.A. The Evolving Role of Lymphatics in Cancer Metastasis. *Current Opinion in Immunology* **2018**, *53*, 64–73, doi:10.1016/j.coi.2018.04.008.
465. Paduch, R. The Role of Lymphangiogenesis and Angiogenesis in Tumor Metastasis. *Cell Oncol (Dordr)* **2016**, *39*, 397–410, doi:10.1007/s13402-016-0281-9.
466. Paget, S. THE DISTRIBUTION OF SECONDARY GROWTHS IN CANCER OF THE BREAST. *The Lancet* **1889**, *133*, 571–573, doi:10.1016/S0140-6736(00)49915-0.
467. Nathanson, S.D. Insights into the Mechanisms of Lymph Node Metastasis. *Cancer* **2003**, *98*, 413–423, doi:10.1002/cncr.11464.
468. Podgrabinska, S.; Skobe, M. Role of Lymphatic Vasculature in Regional and Distant Metastasis. *Microvasc Res* **2014**, *95*, 46–52, doi:10.1016/j.mvr.2014.07.004.
469. Wong, S.Y.; Hynes, R.O. Lymphatic or Hematogenous Dissemination: How Does a Metastatic Tumor Cell Decide? *Cell Cycle* **2006**, *5*, 812–817.
470. Stein, J.V.; Nombela-Arrieta, C. Chemokine Control of Lymphocyte Trafficking: A General Overview. *Immunology* **2005**, *116*, 1–12, doi:10.1111/j.1365-2567.2005.02183.x.
471. Scavelli, C.; Weber, E.; Aglianò, M.; Cirulli, T.; Nico, B.; Vacca, A.; Ribatti, D. Lymphatics at the Crossroads of Angiogenesis and Lymphangiogenesis. *J Anat* **2004**, *204*, 433–449, doi:10.1111/j.0021-8782.2004.00293.x.
472. Papaioannou, T.G.; Stefanadis, C. Vascular Wall Shear Stress: Basic Principles and Methods. *Hellenic J Cardiol* **2005**, *46*, 9–15.

473. Garnier, L.; Gkountidi, A.-O.; Hugues, S. Tumor-Associated Lymphatic Vessel Features and Immunomodulatory Functions. *Front Immunol* **2019**, *10*, doi:10.3389/fimmu.2019.00720.
474. Tewalt, E.F.; Cohen, J.N.; Rouhani, S.J.; Guidi, C.J.; Qiao, H.; Fahl, S.P.; Conaway, M.R.; Bender, T.P.; Tung, K.S.; Vella, A.T.; et al. Lymphatic Endothelial Cells Induce Tolerance via PD-L1 and Lack of Costimulation Leading to High-Level PD-1 Expression on CD8 T Cells. *Blood* **2012**, *120*, 4772–4782, doi:10.1182/blood-2012-04-427013.
475. Tewalt, E.F.; Cohen, J.N.; Rouhani, S.J.; Engelhard, V.H. Lymphatic Endothelial Cells - Key Players in Regulation of Tolerance and Immunity. *Front Immunol* **2012**, *3*, doi:10.3389/fimmu.2012.00305.
476. Podgrabinska, S.; Kamalu, O.; Mayer, L.; Shimaoka, M.; Snoeck, H.; Randolph, G.J.; Skobe, M. Inflamed Lymphatic Endothelium Suppresses Dendritic Cell Maturation and Function via Mac–/ICAM-1-Dependent Mechanism. *J Immunol* **2009**, *183*, 1767–1779, doi:10.4049/jimmunol.0802167.
477. Bordry, N.; Broggi, M.A.S.; de Jonge, K.; Schaeuble, K.; Gannon, P.O.; Foukas, P.G.; Danenberg, E.; Romano, E.; Baumgaertner, P.; Fankhauser, M.; et al. Lymphatic Vessel Density Is Associated with CD8+ T Cell Infiltration and Immunosuppressive Factors in Human Melanoma. *Oncoimmunology* **2018**, *7*, e1462878, doi:10.1080/2162402X.2018.1462878.
478. Fankhauser, M.; Broggi, M.A.S.; Potin, L.; Bordry, N.; Jeanbart, L.; Lund, A.W.; Da Costa, E.; Hauert, S.; Rincon-Restrepo, M.; Tremblay, C.; et al. Tumor Lymphangiogenesis Promotes T Cell Infiltration and Potentiates Immunotherapy in Melanoma. *Sci Transl Med* **2017**, *9*, doi:10.1126/scitranslmed.aal4712.
479. Zahoor, S.; Haji, A.; Battoo, A.; Qurieshi, M.; Mir, W.; Shah, M. Sentinel Lymph Node Biopsy in Breast Cancer: A Clinical Review and Update. *J Breast Cancer* **2017**, *20*, 217–227, doi:10.4048/jbc.2017.20.3.217.
480. Veronesi, U.; Paganelli, G.; Viale, G.; Luini, A.; Zurrida, S.; Galimberti, V.; Intra, M.; Veronesi, P.; Maisonneuve, P.; Gatti, G.; et al. Sentinel-Lymph-Node Biopsy as a Staging Procedure in Breast Cancer: Update of a Randomised Controlled Study. *Lancet Oncol.* **2006**, *7*, 983–990, doi:10.1016/S1470-2045(06)70947-0.
481. Gonzalez, A. Sentinel Lymph Node Biopsy: Past and Present Implications for the Management of Cutaneous Melanoma with Nodal Metastasis. *Am J Clin Dermatol* **2018**, *19*, 24–30, doi:10.1007/s40257-018-0379-0.
482. Moore, J.E.; Bertram, C.D. Lymphatic System Flows. *Annu Rev Fluid Mech* **2018**, *50*, 459–482, doi:10.1146/annurev-fluid-122316-045259.
483. Breslin, J.W. Mechanical Forces and Lymphatic Transport. *Microvasc Res* **2014**, *0*, 46–54, doi:10.1016/j.mvr.2014.07.013.
484. Christiansen, A.; Detmar, M. Lymphangiogenesis and Cancer. *Genes Cancer* **2011**, *2*, 1146–1158, doi:10.1177/1947601911423028.
485. Stacker, S.A.; Caesar, C.; Baldwin, M.E.; Thornton, G.E.; Williams, R.A.; Prevo, R.; Jackson, D.G.; Nishikawa, S.; Kubo, H.; Achen, M.G. VEGF-D Promotes the Metastatic Spread of Tumor Cells via the Lymphatics. *Nat. Med.* **2001**, *7*, 186–191, doi:10.1038/84635.
486. Mandriota, S.J.; Jussila, L.; Jeltsch, M.; Compagni, A.; Baetens, D.; Prevo, R.; Banerji, S.; Huarte, J.; Montesano, R.; Jackson, D.G.; et al. Vascular Endothelial Growth Factor-C-Mediated Lymphangiogenesis Promotes Tumour Metastasis. *EMBO J* **2001**, *20*, 672–682, doi:10.1093/emboj/20.4.672.
487. Goldman, J.; Conley, K.A.; Raehl, A.; Bondy, D.M.; Pytowski, B.; Swartz, M.A.; Rutkowski, J.M.; Jaroch, D.B.; Ongstad, E.L. Regulation of Lymphatic Capillary Regeneration by Interstitial Flow in Skin. *American Journal of Physiology-Heart and Circulatory Physiology* **2007**, *292*, H2176–H2183, doi:10.1152/ajpheart.01011.2006.

488. Boardman, K.C.; Swartz, M.A. Interstitial Flow as a Guide for Lymphangiogenesis. *Circ. Res.* **2003**, *92*, 801–808, doi:10.1161/01.RES.0000065621.69843.49.
489. Jeong, G.S.; Han, S.; Shin, Y.; Kwon, G.H.; Kamm, R.D.; Lee, S.-H.; Chung, S. Sprouting Angiogenesis under a Chemical Gradient Regulated by Interactions with an Endothelial Monolayer in a Microfluidic Platform. *Anal. Chem.* **2011**, *83*, 8454–8459, doi:10.1021/ac202170e.
490. Xiaozhen, D.; Shaoxi, C.; Qunfang, Y.; Jiahuan, J.; Xiaoqing, Y.; Xin, X.; Qifeng, J.; Albert Chih-Lueh, W.; Yi, T. A Novel in Vitro Angiogenesis Model Based on a Microfluidic Device. *Chin. Sci. Bull.* **2011**, *56*, 3301–3309, doi:10.1007/s11434-011-4717-3.
491. Wang, X.; Sun, Q.; Pei, J. Microfluidic-Based 3D Engineered Microvascular Networks and Their Applications in Vascularized Microtumor Models. *Micromachines (Basel)* **2018**, *9*, doi:10.3390/mi9100493.
492. Kuzmic, N.; Moore, T.; Devadas, D.; Young, E.W.K. Modelling of Endothelial Cell Migration and Angiogenesis in Microfluidic Cell Culture Systems. *Biomech Model Mechanobiol* **2019**, *18*, 717–731, doi:10.1007/s10237-018-01111-3.
493. Nguyen, D.-H.T.; Stapleton, S.C.; Yang, M.T.; Cha, S.S.; Choi, C.K.; Galie, P.A.; Chen, C.S. Biomimetic Model to Reconstitute Angiogenic Sprouting Morphogenesis in Vitro. *PNAS* **2013**, *110*, 6712–6717, doi:10.1073/pnas.1221526110.
494. Yamakawa, M.; Doh, S.J.; Santosa, S.M.; Montana, M.; Qin, E.C.; Kong, H.; Han, K.-Y.; Yu, C.; Rosenblatt, M.I.; Kazlauskas, A.; et al. Potential Lymphangiogenesis Therapies: Learning from Current Anti-Angiogenesis Therapies - A Review. *Med Res Rev* **2018**, *38*, 1769–1798, doi:10.1002/med.21496.
495. Paul, C.D.; Mistriotis, P.; Konstantopoulos, K. Cancer Cell Motility: Lessons from Migration in Confined Spaces. *Nat Rev Cancer* **2017**, *17*, 131–140, doi:10.1038/nrc.2016.123.
496. Zhang, J.; Goliwas, K.F.; Wang, W.; Taufalele, P.V.; Bordeleau, F.; Reinhart-King, C.A. Energetic Regulation of Coordinated Leader–Follower Dynamics during Collective Invasion of Breast Cancer Cells. *PNAS* **2019**, *116*, 7867–7872, doi:10.1073/pnas.1809964116.
497. Taufalele, P.V.; VanderBurgh, J.A.; Muñoz, A.; Zanotelli, M.R.; Reinhart-King, C.A. Fiber Alignment Drives Changes in Architectural and Mechanical Features in Collagen Matrices. *PLOS ONE* **2019**, *14*, e0216537, doi:10.1371/journal.pone.0216537.
498. Voutouri, C.; Kirkpatrick, N.D.; Chung, E.; Mpekris, F.; Baish, J.W.; Munn, L.L.; Fukumura, D.; Stylianopoulos, T.; Jain, R.K. Experimental and Computational Analyses Reveal Dynamics of Tumor Vessel Cooption and Optimal Treatment Strategies. *PNAS* **2019**, *116*, 2662–2671, doi:10.1073/pnas.1818322116.
499. Sleeman, J.P. The Lymph Node Pre-Metastatic Niche. *J. Mol. Med.* **2015**, *93*, 1173–1184, doi:10.1007/s00109-015-1351-6.
500. McLean, I.C.; Schwerdtfeger, L.A.; Tobet, S.A.; Henry, C.S. Powering Ex Vivo Tissue Models in Microfluidic Systems. *Lab Chip* **2018**, *18*, 1399–1410, doi:10.1039/C8LC00241J.
501. Meijer, T.G.; Naipal, K.A.; Jager, A.; van Gent, D.C. Ex Vivo Tumor Culture Systems for Functional Drug Testing and Therapy Response Prediction. *Future Sci OA* **2017**, *3*, doi:10.4155/fsoa-2017-0003.
502. Liu, T.; Zhou, L.; Li, D.; Andl, T.; Zhang, Y. Cancer-Associated Fibroblasts Build and Secure the Tumor Microenvironment. *Front Cell Dev Biol* **2019**, *7*, doi:10.3389/fcell.2019.00060.
503. Herman, H.; Fazakas, C.; Haskó, J.; Molnár, K.; Mészáros, Á.; Nyúl-Tóth, Á.; Szabó, G.; Erdélyi, F.; Ardelean, A.; Hermenean, A.; et al. Paracellular and Transcellular Migration of Metastatic Cells through the Cerebral Endothelium. *J Cell Mol Med* **2019**, *23*, 2619–2631, doi:10.1111/jcmm.14156.
504. Muller, W.A.; Luscinskas, F.W. Assays of Transendothelial Migration in Vitro. *Methods Enzymol* **2008**, *443*, 155–176, doi:10.1016/S0076-6879(08)02009-0.
505. Bertulli, C.; Gerigk, M.; Piano, N.; Liu, Y.; Zhang, D.; Müller, T.; Knowles, T.J.; Huang, Y.Y.S. Image-Assisted Microvessel-on-a-Chip Platform for Studying Cancer Cell

Transendothelial Migration Dynamics. *Sci Rep* **2018**, *8*, 1–14, doi:10.1038/s41598-018-30776-0.

506. Reese, B.E.; Zheng, S.; Evans, B.; Datar, R.H.; Thundat, T.; Lin, H.K. Microfluidic Device for Studying Tumor Cell Extravasation in Cancer Metastasis. In Proceedings of the 2010 Biomedical Sciences and Engineering Conference; May 2010; pp. 1–4.
507. Kwasny, D.; Kiilerich-Pedersen, K.; Moresco, J.; Dimaki, M.; Rozlosnik, N.; Svendsen, W.E. Microfluidic Device to Study Cell Transmigration under Physiological Shear Stress Conditions. *Biomed Microdevices* **2011**, *13*, 899–907, doi:10.1007/s10544-011-9559-x.
508. Podgrabinska, S.; Braun, P.; Velasco, P.; Kloos, B.; Pepper, M.S.; Jackson, D.G.; Skobe, M. Molecular Characterization of Lymphatic Endothelial Cells. *PNAS* **2002**, *99*, 16069–16074, doi:10.1073/pnas.242401399.
509. Bouta, E.M.; Wood, R.W.; Brown, E.B.; Rahimi, H.; Ritchlin, C.T.; Schwarz, E.M. In Vivo Quantification of Lymph Viscosity and Pressure in Lymphatic Vessels and Draining Lymph Nodes of Arthritic Joints in Mice. *The Journal of Physiology* **2014**, *592*, 1213–1223, doi:10.1113/jphysiol.2013.266700.
510. Somer, T.; Meiselman, H.J. Disorders of Blood Viscosity. *Annals of Medicine* **1993**, *25*, 31–39, doi:10.3109/07853899309147854.
511. Hope, J.M.; Greenlee, J.D.; King, M.R. Mechanosensitive Ion Channels: TRPV4 and P2X7 in Disseminating Cancer Cells. *The Cancer Journal* **2018**, *24*, 84, doi:10.1097/PPO.0000000000000312.
512. Broders-Bondon, F.; Ho-Bouldoires, T.H.N.; Fernandez-Sanchez, M.-E.; Farge, E. Mechanotransduction in Tumor Progression: The Dark Side of the Force. *J Cell Biol* **2018**, *217*, 1571–1587, doi:10.1083/jcb.201701039.
513. Agastin, S.; Giang, U.-B.T.; Geng, Y.; DeLouise, L.A.; King, M.R. Continuously Perfused Microbubble Array for 3D Tumor Spheroid Model. *Biomicrofluidics* **2011**, *5*, doi:10.1063/1.3596530.
514. Gunther, A.; Yasotharan, S.; Vagaon, A.; Lochovsky, C.; Pinto, S.; Yang, J.; Lau, C.; Voigtlaender-Bolz, J.; Bolz, S.-S. A Microfluidic Platform for Probing Small Artery Structure and Function. *Lab Chip* **2010**, *10*, 2341–2349, doi:10.1039/c004675b.
515. Abdi Dezfooli, Z. Vein-on-a-Chip: A Microfluidic Platform for Functional Assessments and Staining of Intact Veins. Thesis, 2015.
516. Biselli, E.; Agliari, E.; Barra, A.; Bertani, F.R.; Gerardino, A.; De Ninno, A.; Mencattini, A.; Di Giuseppe, D.; Mattei, F.; Schiavoni, G.; et al. Organs on Chip Approach: A Tool to Evaluate Cancer -Immune Cells Interactions. *Sci Rep* **2017**, *7*, doi:10.1038/s41598-017-13070-3.
517. Shanti, A.; Teo, J.; Stefanini, C. In Vitro Immune Organs-on-Chip for Drug Development: A Review. *Pharmaceutics* **2018**, *10*, doi:10.3390/pharmaceutics10040278.
518. Pavesi, A.; Tan, A.T.; Koh, S.; Chia, A.; Colombo, M.; Antonecchia, E.; Miccolis, C.; Ceccarello, E.; Adriani, G.; Raimondi, M.T.; et al. A 3D Microfluidic Model for Preclinical Evaluation of TCR-Engineered T Cells against Solid Tumors. *JCI Insight 2*, doi:10.1172/jci.insight.89762.
519. Nelson, G.M.; Padera, T.P.; Garkavtsev, I.; Shioda, T.; Jain, R.K. Differential Gene Expression of Primary Cultured Lymphatic and Blood Vascular Endothelial Cells. *Neoplasia* **2007**, *9*, 1038–1045.
520. Agliari, E.; Biselli, E.; De Ninno, A.; Schiavoni, G.; Gabriele, L.; Gerardino, A.; Mattei, F.; Barra, A.; Businaro, L. Cancer-Driven Dynamics of Immune Cells in a Microfluidic Environment. *Sci Rep* **2014**, *4*, doi:10.1038/srep06639.
521. Businaro, L.; De Ninno, A.; Schiavoni, G.; Lucarini, V.; Ciasca, G.; Gerardino, A.; Belardelli, F.; Gabriele, L.; Mattei, F. Cross Talk between Cancer and Immune Cells: Exploring Complex Dynamics in a Microfluidic Environment. *Lab Chip* **2013**, *13*, 229–239, doi:10.1039/c2lc40887b.

522. Mattei, F.; Schiavoni, G.; De Ninno, A.; Lucarini, V.; Sestili, P.; Sistigu, A.; Fragale, A.; Sanchez, M.; Spada, M.; Gerardino, A.; et al. A Multidisciplinary Study Using in Vivo Tumor Models and Microfluidic Cell-on-Chip Approach to Explore the Cross-Talk between Cancer and Immune Cells. *J Immunotoxicol* **2014**, *11*, 337–346, doi:10.3109/1547691X.2014.891677.
523. Schlereth, S.L.; Refaian, N.; Iden, S.; Cursiefen, C.; Heindl, L.M. Impact of the Prolymphangiogenic Crosstalk in the Tumor Microenvironment on Lymphatic Cancer Metastasis. *Biomed Res Int* **2014**, *2014*, doi:10.1155/2014/639058.
524. Dieterich, L.C.; Ikenberg, K.; Cetintas, T.; Kapaklikaya, K.; Hutmacher, C.; Detmar, M. Tumor-Associated Lymphatic Vessels Upregulate PDL1 to Inhibit T-Cell Activation. *Front Immunol* **2017**, *8*, doi:10.3389/fimmu.2017.00066.
525. Sackmann, E.K.; Fulton, A.L.; Beebe, D.J. The Present and Future Role of Microfluidics in Biomedical Research. *Nature* **2014**, *507*, 181–189, doi:10.1038/nature13118.